NOT FOR DISTRIBUTION

ONLY FOR INTERNAL USE

Hyper-Kamiokande

Technical Report

Version 1 (Dated: December 7, 2018)

List of Collaborators[1]

(Hyper-Kamiokande proto-collaboration)

[1] *List of Universities/Labs*

Abstract

Abstract to be written.

CONTENTS

LIST OF THE ACRONYMS

We introduce here the acronyms used throughout the document:

- AD: Avalanche Diode
- B&L: Box-and-Line dynode
- BSM: Beyond the Standard Model
- CC: charged currents
- CCSNe: Core-Collapse Supernovae
- CCQE: charge current quasi-elastic
- CE: Collection Efficiency
- CPL: Concrete Protective Liner
- DAQ: Data Acquisition
- DR: Design Report
- DT: deuterium-tritium
- EBU: Event Building Unit
- ECal: ND280 Electromagnetic Calorimeter
- FC: Fully Contained
- FCFV: Fully Contained in Fiducial Volume
- FGD: Fine Grained Detector
- FRP: Fiber Reinforced Plastics
- FV: Fiducial Volume
- GUT: Grand Unified Theory
- HDPE: High Density PolyEthylene
- HK: Hyper-Kamiokande
- HPD: Hybrid Photodetector
- HPTPC: High Pressure Time Projection Chamber
- HQE: High Quantum Efficiency
- Hyper-K: Hyper-Kamiokande
- IBC: International Board Representatives
- IBD: Inverse Beta Decay
- ID: Inner Detector
- INGRID: Interactive Neutrino GRID
- ISC: International Steering Committee

- IWCD: Intermediate Water Cherenkov Detector
- LAPPD: Large Area Picosecond PhotoDetector
- LBNE: Long Baseline Neutrino Experiment
- LAr: Liquid Argon calorimeter
- LD: Laser Diode
- LLDPE:Linear Low-Density PolyEthylene
- LV: Lorentz Violation
- MC: Monte Carlo
- MLF: Material Science Facility
- mPMT: Multi-channel Optical Module
- MR: Main Ring synchrotron
- NC: neutral currents
- ND280: Near Detector 280m
- NF: Nano Filter
- OD: Outer Detector
- PC: Partially Contained
- PE: Photo Electron
- PS: Power Supply
- PTF: Photosensor Testing Facility
- MH: neutrino mass hierarchy
- QA: quality assurance
- RBU: Readout Buffer Unit
- RO: Reverse Osmosis
- RCS: Rapid Cycling Synchrotron
- SK: Super-Kamiokande
- SM: Standard Model
- Super-K: Super-Kamiokande
- SUS: Stainless Steel (or Steel Use Stainless)
- TITUS: Tokai Intermediate Tank for Unoscillated Spectrum
- TPU: Trigger Processing Unit
- TS: Target Station
- UF: Ultra Filter
- UPW: Ultra Purified Water

- WAGASCI: Water Grid And SCIntillator detector
- WC: Water Cherenkov

EXECUTIVE SUMMARY

Part I

Overview

I.1. INTRODUCTION

This is the main introduction to the whole report. It comes at the start of the overview part.

I.2. BEAM AND NEAR DETECTORS

An overview of the JPARC beam and the Near and Intermediate sites.

I.3. THE HYPER-KAMIOKANDE DETECTOR

An overview of the far detector.

Part II

The Hyper-Kamiokande Near Site

The near site of the Hyper-K experiment includes the accelerator complex that delivers the high intensity proton beam, the primary neutrino beamline that extracts the proton beam and focuses the beam on the target, the target hall and secondary beamline where the neutrinos are produced and allowed to decay, and the near detector sites, where neutrino detectors monitor the beam and make measurements of the neutrino beam and interaction cross sections. The Hyper-K accelerator complex, primary beamline and target hall and secondary beamline used by Hyper-K will be upgrading from the existing accelerators and beamlines that have been operated for the T2K experiment up to a power of 485 kW. Hyper-K will also use the existing ND280 complex, which currently contains the INGRID and ND280 near detectors used by T2K. Potential upgrades to the near detectors and near detector complex will be carried out. Hyper-K also plans a new intermediate detector complex located $\sim$1 km off the J-PARC side where an intermediate water Cherenkov detector (IWCD) will be built.

Consistent with the T2K model, the upgrade and operation of the accelerator complex will be the responsibility of KEK and J-PARC. The upgrade and operation of the primary beamline and target hall and secondary beamline will be the responsibility of the Hyper-K collaboration, led by the KEK neutrino group. The upgrades of the near detectors, construction of the IWCD and operation of the near and intermediate detectors will be the responsibility of the Hyper-K collaboration, and significant contributions from international collaborators are expected. The IWCD detector facility will be constructed by KEK and J-PARC.

The accelerator and beamline have been successfully operated up to 485 kW beam power during T2K operations. The planned operating power for Hyper-K is 1.3 MW, which will be achieved increasing the repitition rate of the beam and increase the number of protons per pulse. This document describes the upgrades that are necessary to achieve 1.3 MW operation of the neutrino beamline.

The calculated neutrino flux produced by the beamline is a primary input to physics analyses in the Hyper-K experiment. The neutrino flux is calculated using inputs from proton beam current, position and profile monitors, horn current and field measurements, beamline geometry and alignment information, and external measurements of hadron interactions on material and at energies relevant for Hyper-K. This document includes a description experiments that will measure the hadron production.

The Hyper-K near detector conceptual design report (HKNDCDR) describes the physics requirements for Hyper-K near detectors and the conceptual design of near detectors for Hyper-K. The physics requirements and conceptual design are summarized here.

Quantitative requirements that have been identified by the Hyper-K Near Detector Working Group are:

- The uncertainty on the relative $\sigma(\nu_e)/\sigma(\nu_\mu)$ and $\sigma(\overline{\nu}_e)/\sigma(\overline{\nu}_\mu)$ cross section ratios should be measured with 4% precision or better.
- The wrong-sign contribution to the beam should be measured with 10% precision or better.
- The intrinsic $\nu_e(\overline{\nu}_e)$ and NC backgrounds should be measured with a relative uncertainty less than 4% for neutrino mode and antineutrino mode, and a correlated uncertainty of less than 12%.
- The cross section should be measured with 5% precision in the high-angle and backward regions ($\cos\theta < 0.2$).
- The off-axis angle, removal energy and contributions of non-QE components to the cross section should be measured precisely enough so that there is a 0.5% or less uncertainty on the average true or reconstructed neutrino energy in the appearance modes.
- The feed-down from non-QE interactions with true neutrino energy >700 MeV should be measured with XX% normalization uncertainty or better in the 400-800 MeV reconstructed neutrino energy range.

In addition to the above quantitative requirements, the following qualitative aspects are desired:

- The on-axis detector should be able to monitor the neutrino and antineutrino event rates to ensure stable beam operation.
- Near and intermediate detectors should cover the full phase space for neutrino interactions expected in Hyper-K and should include measurements on H_2O.
- Tracking detectors should aim to lower the threshold for proton track reconstruction so the recoil hadronic system can be studied with a goal of improving the understanding of nuclear effects in neutrino-nucleus scattering.

- The near and intermediate detectors should aim to measure neutrino interaction modes that are relevant for constraining atmospheric neutrino backgrounds for nucleon decay searches.

- The intermediate detector should be able to measure the multiplicity of neutrons produced in neutrino-nucleus scattering.

Based on these requirements, a near detector suite with a baseline of the following three detectors is required:

- An on-axis detector that will measure the beam direction with sufficient precision and monitor the neutrino event rate.

- An off-axis magnetized tracking detector that will separate the wrong-sign and right-sign components of the beam and be used to study the recoil hadron system.

- An intermediate water Cherenkov detector with off-axis spanning and Gd loading capabilities that will measure the intrinic ν_e and $\bar{\nu}_e$ backgrounds, the $\sigma_{\nu_e}/\sigma_{\nu_\mu}$ and $\sigma_{\bar{\nu}_e}/\sigma_{\bar{\nu}_\mu}$ cross section ratios, the neutrino energy vs. final state dependence and neutron multiplicities.

In the case of the on-axis detector, it is expected that the INGRID detector with minor upgrades will be sufficient. The off-axis magnetized detector is expected to be based on an upgrade of the T2K ND280 detector. T2K is carrying out an upgrade of ND280 for the T2K program, but it is expected that additional upgrades to the detector and infrastructure will be necessary for Hyper-K. The intermediate detector is a new detector that requires a new facility outside of the J-PARC site. The baseline design adopted for the intermediate water Cherenkov detector is that proposed by the E61 collaboration, where the intrumented portion of the detector can be moved to take measurements at varying off-axis angles.

Progress towards the technical designs of these detectors for Hyper-K are described in this document.

TABLE I. Main Ring rated parameters for fast extraction, with numbers achieved as of December 2017. The columns show (left to right): the currently achieved operation parameters, the projected parameters after the MR RF and magnet power supply upgrade, and the projected parameters for the maximum beam power achievable after the upgrade.

Parameter	Achieved	Doubled rep-rate	Long-term Projection
Circumference		1,567.5 m	
Beam kinetic energy	30 GeV	30 GeV	30 GeV
Beam intensity	2.45×10^{14} ppp	2.0×10^{14} ppp	3.2×10^{14} ppp
	3.1×10^{13} ppb	2.5×10^{13} ppb	4.0×10^{13} ppb
[RCS equivalent power]	[575 kW]	[610 kW]	[1 MW]
Harmonic number		9	
Bunch number		8 / spill	
Spill width		$\sim 5\,\mu$s	
Bunch full width at extraction	~50 ns	~50 ns	~50 ns
Maximum RF voltage	280 kV	560 kV	560 kV
Repetition period	2.48 sec	1.32 sec	1.16 sec
Beam power	485 kW[a]	750 kW	1340 kW

[a] As of 2018

II.1. THE NEUTRINO BEAM

Descriptions of the primary beamline, target hall and secondary beamline, and hadron production experiments can be found in the following sections. Neutrinos are delivered to the neutrino beamline by the J-PARC accelerator complex, directly from the 30 GeV Main Ring. The current and projected operating parameters of the accelerator are described in Tab. I. The upgrade of the Main Ring power to 750 kW will be achieved by an upgrade of the Main Ring RF and the magnet power supplies, which will allow the repetition rate to be doubled. Based on high intensity studies of the current accelerator performance, it is expected that 1-1.3 MW beam power can be achieved after these upgrades [**? ?**].

A. Primary Beamline

The role of the primary beamline is to stably deliver protons extracted from the main ring to the neutrino production target with the proper beam position, size and injection angle. The extracted proton beam is transported toward HK with an off-axis angle of 2.5°. The beam transport must be done with tolerable beam loss through the beamline in terms of both maintenance of the beamline equipment and the radiation level at the boundary of the radiation controlled area.

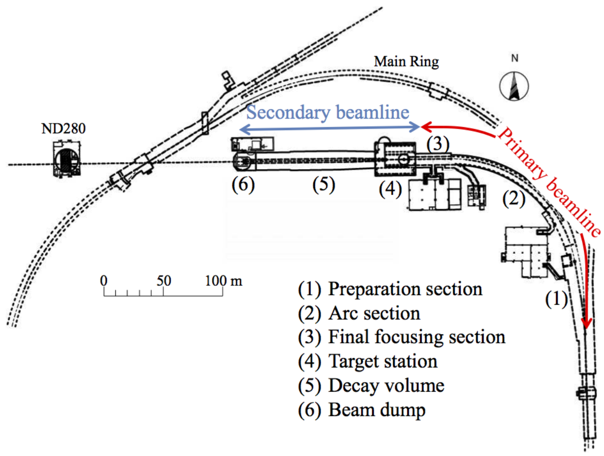

FIG. 1. Overview of the neutrino beamline.

There are three sections of the primary beamline: the preparation section, arc section and final focusing section (Fig. 1). The 30 GeV accelerated proton beam is extracted into the preparation section. The position and width of the extracted beam are tuned by normal-conducting magnets in order to match the beam optics in the arc section. The beam is then bent by 80.7° using super-conducting combined function magnets at the arc section. After the arc section, normal-conducting magnets are used to direct the beam downward by 3.647° and tune the position and size to focus the beam onto the center of the neutrino production target.

The primary beamline equipment consists of normal-conducting magnets and their power supplies, super-conducting magnets and their power supply and cryogenic system, beam monitors, beam plugs, collimators, and the vacuum system.

The primary beamline has operated stably during T2K operation and all components of the primary beamline are designed to be basically capable of accepting 1.3 MW beam power, provided that the beam loss is kept low as the present level.

TC: What does basically capable mean? Since potential upgrades for high power are discussed, should we assume that it means only minor upgrades will be needed?

KEK has been and will continue to be responsible for the primary beamline components. However, outside contributions, especially those including continued support, are welcome for any components.

1. Magnets and Magnet Apertures

The preparation section and the final-focussing section consist of 11 and 10 normal-conducting magnets, respectively. The arc-section sharply bends the beam using the world's first combined-function superconducting magnets, consisting of 14 doublets (focus/defocus) and 3 pairs (normal/skew) of steering magnets.

The aperture of some of the magnets may be too small for the desired increase in beam power. The beam size is the largest at PQ1 (the first quadrupole magnet after extraction) and at FQ2 and FQ3 (quadrupoles for focusing at the target). Beam sizes at FQ2 and FQ3 are sensitive to the beam emittance, and if the incoming beam emittance increases for higher beam power, a larger aperture may be required. The aperture of the steering magnet placed at the most upstream of the preparation section (PV1) may also need to be enlarged, for reasons described below.

TC: There are many references to magnets. Is there a drawing of the beamline that includes magnet labels?

If a magnet aperture needs to be increased, a large power supply for that magnet may also be required.

Any necessary aperture enlargement will be studied in the future by transporting beam from the MR with higher protons per pulse. Based on these future tests, a concrete plan for enlarging necessary magnet apertures will be considered.

TC: Is there a timescale for these tests? Would this upgrade be a significant impact on the budget?

If necessary, magnet upgrades will be the responsibility of KEK.

2. Beam Loss

The beam loss is measured by fifty Beam Loss Monitors (BLMs) installed along the primary beamline. Fig. 2 shows the beam loss distribution along the primary beamline. The residual radiation dose is also regularly measured. It has been found that the residual dose is within manageable levels, although the beam loss and residual radiation dose at the most upstream part of the preparation section are large even at 485 kW operation. One cause could be the small aperture of the PV1 magnet, where the beam halo from the MR may cause beam loss. This issue could be mitigated by enlarging the PV1 aperture, although enlargement of the MR apertures (or tuning of the MR beam) will probably be necessary before any neutrino beamline preparation section hardware upgrade.

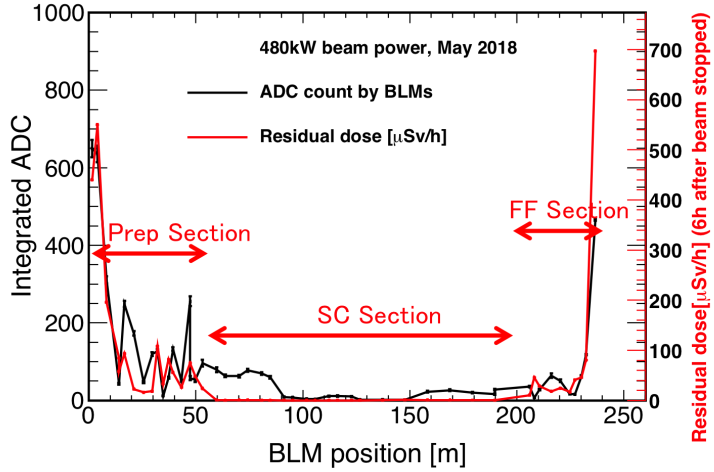

FIG. 2. Beam loss and measured residual radio-activity distribution along the beamline at present running condition with 480 kW. Horizontal axis is the distance from the extraction point.

The residual radiation dose is also high at the most downstream region of the final-focussing section. Upgrade plans around that area will be discussed in Sec. II.1 A 7.

3. Beam Ducts

In order to withstand the thermal shock stress due to a direct hit of mis-steered beam, the beam duct material should be either titanium or aluminum. There are still a few beam ducts made of stainless steel in some steering magnets (PH3, FH1, FV1 and FV2) due to financial reasons. These are the responsibility of KEK and will be upgraded for high beam power.

4. Collimators

Measurements during beam operation indicate that beam loss at the collimators is not large. On the other hand, fast-extraction magnet failures do occasionally occur. These failures result in off-orbit beam in the primary beamline, which may hit the target off-center, or may hit a beam duct, or, in the worst case, may hit the super-conducting magnets. Presently two collimators are installed, PC1 and PC4. The primary purpose of these collimators is not to scrape off the beam halo, but to block the off-center beam orbit in the case of a magnet trip, and the apertures of these collimators were determined as such.

Since the beam loss at the collimators is not large, they are presently cooled by conduction to the shielding iron wall.

However, the collimators do have a much smaller aperture compared to the magnets and are therefore very sensitive to the beam tail. At 485 kW operation, the beam halo is not significant: the collimators are not scraping off the halo and the heat load is negligible. 1.3 MW operation requires an increase in the protons per pulse, and the beam halo condition may change significantly. In that case, water cooling would be needed. This can be realized by replacing the copper bulk block inserted between the collimator jaw and the iron shield by a water-cooled copper block. Primary responsibility for new collimator design belongs to KEK, but this upgrade may be realized as a contribution for another institute.

5. Primary Beamline Configuration Change

Another possible primary beamline upgrade could be the modification of the most downstream configuration. Currently, the vertical beam position and angle at the target are measured by a fit to 3 beam monitors (SSEM18, SSEM19, OTR). However, uncertainty on this measurement is large, especially if the relative calibration between the 3 monitors has some uncertainty. Reducing the length of the most downstream vertical bending magnet, FVD2, could allow for installation of a 4th monitor to fit the vertical beam parameters at the target, which may significantly improve the proton beam vertical measurement. The magnet configuration change would be the responsibility of KEK.

TC: Are there any estimates of the cost for such a change or the timescale?

6. Proton Beam Monitors

The proton beam conditions are continuously monitored by a suite of proton beam monitors along the neutrino primary proton beamline, as shown in Fig. 3 and described in Ref. [**?**].

Five Current Transformers (CTs) are used to continuously monitor the proton beam intensity. Fifty Beam Loss Monitors (BLMs) continuously measure the spill-by-spill beam loss and are used to fire an abort interlock signal in the case of a high-loss beam spill. Twenty-one Electro-Static

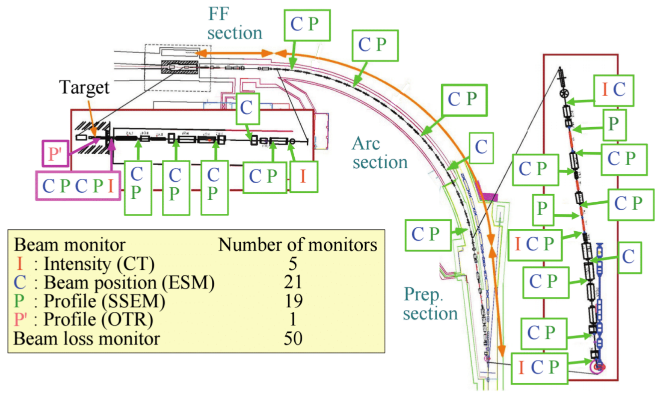

FIG. 3. Location of the beam monitors in the J-PARC neutrino beamline.

Monitors (ESMs) are used as Beam Position Monitors to continuously monitor the beam position and angle.

So far, these monitors have been running well and within the design precision and stability. These monitors were all designed to work continuously at high intensity (3.3×10^{14} protons per pulse), and we intend to continue to use them stably with minimal hardware upgrades for the foreseeable future. Regular calibration, improvements in calibration methods, and analysis improvements may be necessary for maintaining or improving the monitor stability or precision, and contributions to future analysis improvements for these monitors may be a contribution for other collaborators.

The proton beam profile (beam position and width) is monitored bunch-by-bunch during beam tuning by a suite of 19 Segmented Secondary Emission Monitors (SSEMs) [**?**] distributed along the primary beamline, where only the most downstream SSEM (SSEM19) is used continuously. An Optical Transition Radiation Monitor (OTR) [**?**], placed directly upstream of the production target, also continuously monitors the beam profile spill-by-spill, as described in Sec. II.1 A 8.

a. Segmented Secondary Emission Monitor (SSEM) Each SSEM sensor head consists of two thin (5 μm, 10^{-5} interaction lengths) titanium foils stripped horizontally and vertically (to measure the vertical and horizontal beam profiles respectively), and an anode HV foil between them. The strips are hit by the proton beam and emit secondary electrons in proportion to the number of protons that go through the strip, and compensating charge in each strip is read out as a pulse with positive polarity. The proton beam profile is reconstructed from the resulting charge distribution from all strips on a bunch-by-bunch basis.

Each SSEM causes 0.005% proton beam loss while in the beam. Therefore, the monitors can be remotely moved into and out of the beamline to eliminate additional loss during standard running. Eighteen of the SSEMs are only used to check the beam profile during beam tuning or after some expected parameter change, while the most downstream SSEM (SSEM19) and the OTR, which are located inside the monitor stack and Target Station respectively, and therefore in a high-radiation environment already, are used continuously. The continuous measurement of the beam width at the target by SSEM19 is required to safely run the neutrino beam.

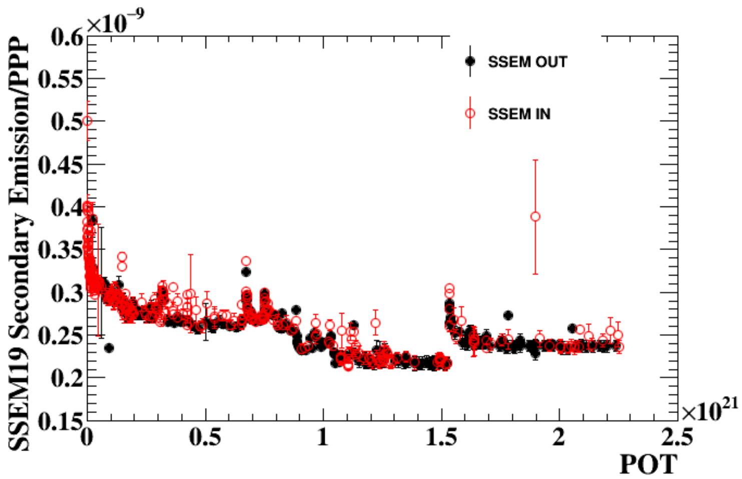

FIG. 4. Observed secondary emission of SSEM19 over the full T2K run so far. Jumps in normalized secondary emission appear to be correlated with changes in beam power. Points are shown when the other SSEMs are OUT (black) and IN (red).

Since bunch-by-bunch (and spill-by-spill) information from SSEM19 is necessary, potential degradation of the secondary emission signal should be carefully monitored. A potential ∼20% decrease in the secondary emission of SSEM19 has been observed after an integrated 2.3×10^{21} POT (with an average beam spot size of 4 x 4 mm), although the secondary emission stability at stable beam power (after an initial burn-in period) appears to be very good. The expected SSEM lifetime is not precisely known, however studies have indicated that the secondary emission efficiency of titanium is stable up to 10^{18}protons/cm^2. Although this integrated POT has already been exceeded at T2K, Fig. 4 shows that the SSEM19 secondary emission is basically stable after an integrated 1×10^{21} POT. However, SSEM19 must be periodically replaced if degradation begins to occur.

Since the SSEMs other than SSEM19 (SSEM1-18) have a relatively low total integrated incident number of protons, no issue with degradation is expected for SSEM1-18. SSEM1-18 are also installed in the primary beamline, which is much easier to access then the monitor stack (where

SSEM19 is installed). Therefore, the SSEM1-18 sensor heads can be relatively easily replaced by spares if any issues do occur.

b. Wire Secondary Emission Monitor (WSEM) Beam loss from secondary emission profile monitors can be reduced by switching from foils to wires intercepting the beam. A new Wire Secondary Emission Monitor (WSEM) has been jointly developed with the monitor group FNAL as part of the US/Japan collaboration, and prototype planes were built for the J-PARC primary neutrino beamline. This monitor consists of 2 planes with 25μm diameter twinned pure Ti (Grade 1) wires with 3 mm pitch. An anode plane between them, consisting of of 25μm single Ti wires with a 2- or 6-mm pitch, can be set to 100 V to sweep away electrons. All wires were mounted to the ceramic frame under a tension of 20 g/wire.

A prototype WSEM monitor has been fabricated and installed for testing in the neutrino primary beamline. The beam loss was measured to be $\sim$10x lower for the WSEM than for the neighboring SSEM. The beam position and width measurements and resolution and stability of the WSEM are consistent with the SSEMs.

Currently only SSEM19 can be used continuously, because it is installed in the high-radiation Target Station (TS). Since the beam loss due to a WSEM is $\sim$0.0005%, this monitor may be suitable to leave in the beam at all times even outside the TS.

SSEM18 has been replaced with WSEM in 2018, allowing for potential continuous operation with the WSEM inserted if SSEM19 becomes unusable. Other SSEM monitors may be replaced with WSEM in the future.

WSEM upgrades may also be possible – carbon wires may be more robust than Ti wires and optimization of the wire thickness and/or wire spacing could also potentially improve the measurement. There may also be some long-term advantage to adding additional WSEMs to the primary beamline or exchanging some SSEMs with WSEMs. KEK is currently responsible for the SSEMs and WSEMs, but WSEM upgrades can be a contribution from Hyper-K collaborators.

Periodic SSEM19 exchange would be the responsibility of KEK.

c. Beam Induced Fluorescence Monitor (BIF) A Beam Induced Fluorescence (BIF) monitor, which can continuously and non-destructively measure the proton beam profile, is under development [**?**].

TC: Citation is missing

In a BIF monitor, the beam profile is measured when the passing beam excites or ionizes some of the gas particles in the beamline. The particles then isotropically fluoresce when returning to the ground state, and the transverse profile of this fluorescence light will match the transverse profile of the proton beam. This light could then be observed from the bottom of the beampipe (to measure the beam horizontal profile) and from the side (to measure the beam vertical profile).

Studies show that a BIF monitor in the primary beamline would require the temporary local degradation of the vacuum level from $10^{-5} \sim 10^{-6}$ Pa to 10^{-2} Pa in order to detect ∼1000 BIF photons per beam spill at $\sim 2.5 \times 10^{14}$ protons per pulse (assuming reasonable acceptance and efficiency for the optical components).

The neutrino primary beamline has a ∼4-m-long empty duct in the final focusing section between bending magnets FH1 and FV2. We plan to replace this duct with a prototype BIF profile monitor. The current monitor design consists of :

- Two additional 500 L/s ion pumps
- A series of valves to inject pulsed N_2 gas into the beampipe
- Two composite quartz viewports (one at the bottom of the beampipe and one on the pathway side of the beampipe) to allow BIF light to exit the beampipe
- An optical system for transporting the light
- Photon detectors for light detection

R&D for the gas injection system, optical system, and light detection system is currently underway and a working prototype system is planned to be installed in the beamline in 2019. Future design improvements and upgrades may be necessary beyond 2019. If this monitor works well, installation of additional BIF monitors at other locations along the primary beamline may be desirable.

This R&D work is currently a joint effort between KEK and Kavli IPMU. Continued maintenance and operation will be a joint responsibility of both institues.

TC: General Question - Are any upgrades to the beam monitoring DAQ necessary for 1.3 MW operation?

7. Primary Beamline Maintenance Scenario

The original design concept of the primary beamline component maintenance scenario was hands-on work with quick-action devices. This includes quick-connections for the normal-conducting-magnet electric and cooling water lines, as well as quick-connections for the vacuum flanges. A remote hoisting tool and positioning keys are used for the removal and re-installation of the normal-conducting magnets. The intended use of these components is to finish hands-on maintenance work near the beamline within several minutes.

Except for at the most-downstream part of the final focusing section, the residual dose of the primary beamline components is less than we expected at the design stage. For the components placed at the preparation section, the arc section and the final focusing section other than the most-downstream part, we think the present scenario (hands-on maintenance with quick-action devices and semi-remote devices) will work even after 1.3 MW operation has been realized.

So far, maintenance work requiring removal and re-installation of beam monitors has been done by hand. Based on the present radio-activation levels, we expect this scenario is reasonable even after 1.3 MW has been achieved, again except for at the most-downstream part of the final-focusing section.

a. Maintenance scheme of the most-downstream part of the final-focusing section The most downstream part of the final focusing section, shown in Fig. 5, suffers from severe build-up of radio-activation due to back-scattering from the down-stream target station. At 470 kW operation, the maximum radio-activity is $\sim$6 mSv/h on contact 6 hours after the beam stop, and the level is reduced to $\sim$300 μSv/h at one foot one week after the beam stop. Re-positioning of the components in this section by hand will not be possible at 1.3 MW operation.

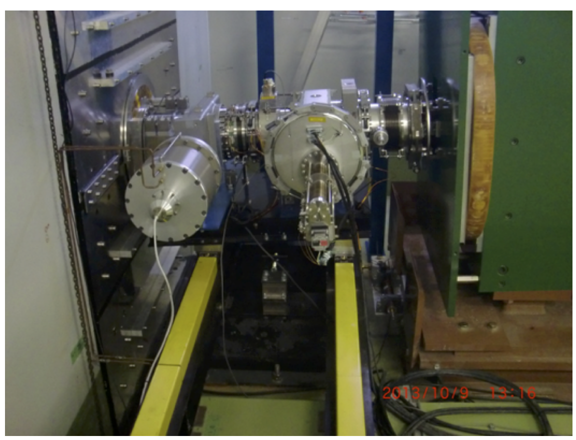

FIG. 5. The most downstream part of the final focusing section. The Target Station sits behind the wall on the left.

Initially, a line-out maintenance scheme was planned for this area, however the planned scheme is not feasible at the current residual radiation levels. Therefore, we will discontinue this line-out scheme and adopt a scheme of quick hands-on operation with positioning keys on the beamline, while components will be supported by over-head chain hoists. During the 2018 summer shutdown, we plan to re-build the stages of the currently-installed beam monitors and gate valve to have positioning key cones on the lower stages and key holes on the upper stages. We will also install quick bellows movers on the upstream bellows. This should allow for quick, semi-hands-on maintenance.

Eventual upgrades towards a fully-remote maintenance scenario are desired. Although the primary responsible institue will be KEK, work on these upgrades may be a good contribution from non-KEK collaborators, provided that those institutes will continue to contribute to maintenance and operation.

TC: Are there any details or examples of a fully-remote maintenance system that can be referenced? Is this a significant budget item?

8. Optical Transition Radiation Monitor (OTR)

The OTR uses optical transition radiation, light emitted from a thin metallic foil when a charged beam passes through it, to form a 2D image of the proton beam directly upstream of the neutrino production target.

The OTR active area is a 50-μm-thick titanium-alloy foil, which is placed at 45° to the incident proton beam. As the beam enters and exits the foil, visible light (transition radiation) is produced in a narrow cone around the beam. The light produced at the entrance transition is reflected at 90° to the beam and directed out of the Target Station (TS) He vessel by four aluminum 90° off-axis parabolic mirrors to an area with lower radiation levels. It is then collected by a charge injection device (CID) camera to produce an image of the proton beam profile spill-by-spill. The OTR foils are held in a rotating eight-position carousel; five of the mounted foils are designed to be used with continuous beam, one foil is exclusively for calibration, one foil is for low-intensity running, and the last position is empty to allow for background measurements, etc.

According to mechanical strength simulations, the OTR is designed to work at high beam intensity and should be able to withstand 3.3×10^{14} protons-per-pulse. So far there have been no major issues with the stability and precision of the OTR beam profile measurement, although damage of components after irradiation is a concern.

The OTR light yield vs. date from May 2014 is shown in Fig. 6 – a decrease in the OTR light yield of $\sim$85% after an incident 3.2×10^{21} protons total (1.4×10^{21} protons on the cross foil) has been observed. This yield decrease is probably due to radiation-induced darkening of the fiber optic taper coupled to the CID camera. Design upgrades to solve this problem are currently being considered, but one solution could be to use an easily replaceable (relatively cheap) fiber taper which would be periodically replaced. Another option could be to modify the optical focusing system to eliminate the need for a fiber taper.

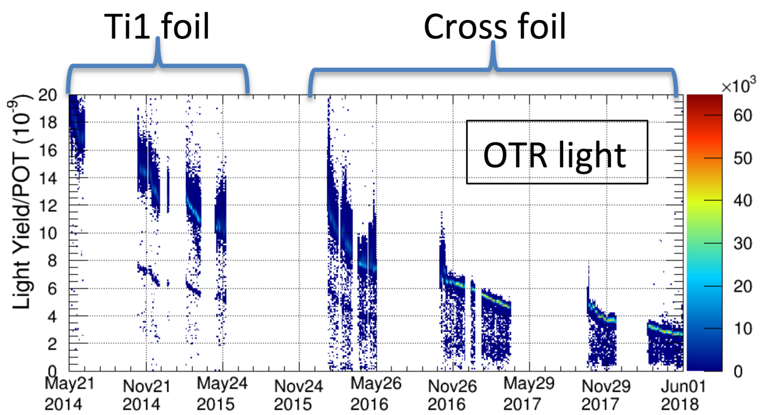

FIG. 6. Observed OTR light yield plotted as a function of date.

Periodic replacement of the OTR disk may also be required in the future. Studies to understand if there could be some benefit to using different foil materials in new disks are underway.

Upgrades to the OTR moving system and position-indicating microswitch are currently also required, but these upgrades will be carried out in the near future.

The OTR DAQ must also be upgraded to reduce the readout latency in order to run with <2.48 s beam spill repetition rate, as well as to improve the stability and robustness of the system. Presently, the OTR CID camera is read-out by a FastFrame 1303 PCI board in a Windows PC. Prior to the MR magnet PS upgrade, the readout scheme will be changed to use a Linux-based system and FPGA utilizing the USB2 interface of the camera.

The OTR is currently the responsibility of York University and TRIUMF, with contributions from the US and UK groups. Long-term continued support will be necessary (a responsible group for the HK era has not yet been confirmed).

B. Muon monitor (MUMON)

The secondary muon beam intensity and direction are monitored bunch-by-bunch by a Muon Monitor (MUMON) [**? ?**] which is located directly behind the beam dump. It consists of two 7×7 arrays of 25-cm interval sensors : an array of Si PIN photodiodes (Si) and an array of Ionization Chambers (IC). This configuration was adopted for redundancy and so far the Si-sensor array has been used to select good quality spills for the T2K analysis.

TC: The citations are broken

From initial beam tests, the expected lifetime of the Si sensors is $<8 \times 10^{20}$ POT at +250 kA horn current. However, in situ measurements at T2K so far show that the sensors do not degrade at that exposure level. A maximum ∼2% yield decrease after an exposure of $\sim 19 \times 10^{20}$ POT at +250-kA horn current equivalent has been seen. 8×10^{20} POT at +250 kA horn current corresponds to 20 days operation with +320 kA horn current at 1.3 MW. Since the actual Si lifetime is unknown, the baseline plan is to periodically check the Si sensor radiation damage and replace the sensors when damage is found. The expected check-and-replacement cycle is one or two months. Since the cost of the Si sensors is relatively cheap ($\sim 270,000$ Yen for one set), this plan is feasible during 1.3 MW operation with some extra cost for outsourcing of the replacement work.

TC: I updated this section to only mention 1.3 MW operation since that is what is planned for Hyper-K. Is the replacment plan still feasible? The beam time efficiency loss due to regular calibration runs should be considered. Should there be some statement about the results of the diamond sensor studies or any studies of more radiation hard silicon sensors?

Two gas types have been used in the IC: Ar with 2% N_2 is used for low-intensity beam, while He with 1% N_2 is intended for use at high intensity. The He configuration can be used during the HK operation, however He is found to have considerable after-bunch pileup induced by the movement of the He ions, which results in poor bunch-by-bunch resolution. Spill-by-spill IC information can be used at high beam power.

Currently, Electron Multiplier Tubes (EMT), custom made by Hamamatsu, are under investigation as a suitable sensor upgrade [**?**]. An EMT is equivalent to a Photo Multiplier Tube (PMT) without a photocathode and operates by multiplying secondary electrons produced by the passage of muons through the sensor. So far, tests of these new sensors in the T2K muon pit have been promising. A full plan for installation of new sensors will be further refined based on continued tests.

TC: Can test results be shown here?

Kyoto University is currently responsible for the MUMON and may be able to continue as the responsible group during Hyper-K. However, additional support would be welcome.

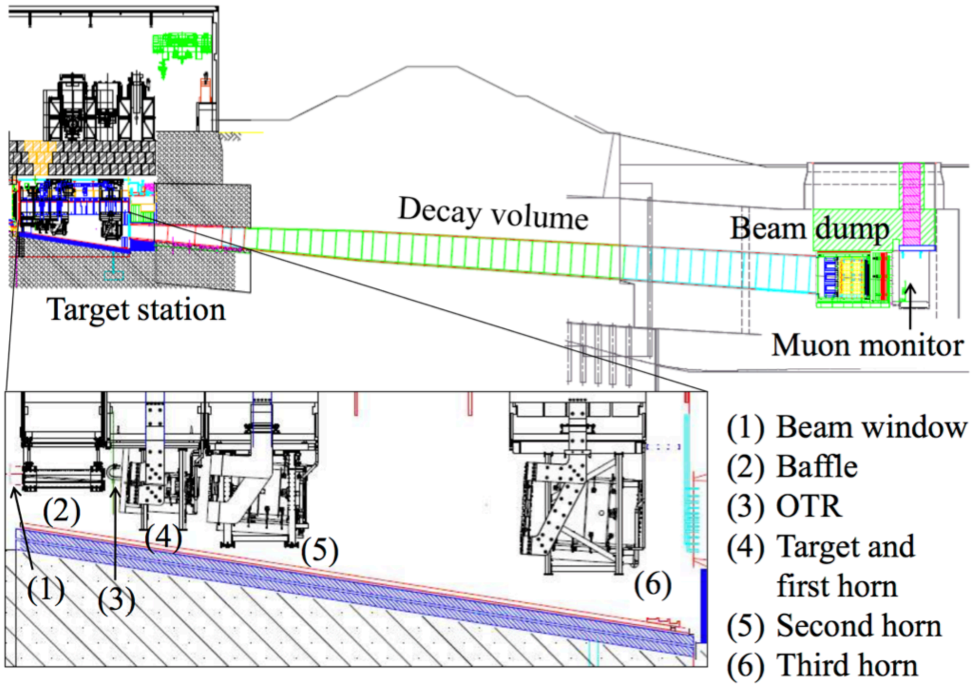

FIG. 7. Side view of the overall secondary beamline. The proton beam enters from the left side of this figure.

C. Secondary Beamline

1. Overview

The delivered proton beam strikes a neutrino production target to produce secondary particles, mainly pions and kaons, which are focused along the beamline by magnetic horns and decay in flight into muon neutrinos and muons in a 94 m long decay volume. The purpose of the secondary beamline is to produce intense, narrow band neutrino beams with the so-called off-axis method.

The secondary beamline consists of the Target Station, Decay Volume, Beam Dump, and Muon Monitors. Figure 7 shows side view of the overall secondary beamline. All the secondary beamline equipment other than the Muon Monitors are contained in a gigantic helium vessel, whose volume is 1,500 m^3, filled with helium gas at atmospheric pressure in order to suppress pion absorption and to reduce the production of tritium and nitrogen oxide (NOx). The most upstream part of the helium vessel is located beneath the Target Station which is a facility building to handle the target, magnetic horns, and related peripherals. The Target Station helium vessel contains an upstream beam window, a graphite collimator (called a Baffle), an optical transition radiation (OTR) monitor, the target, and the three magnetic horns in order from upstream, as shown in

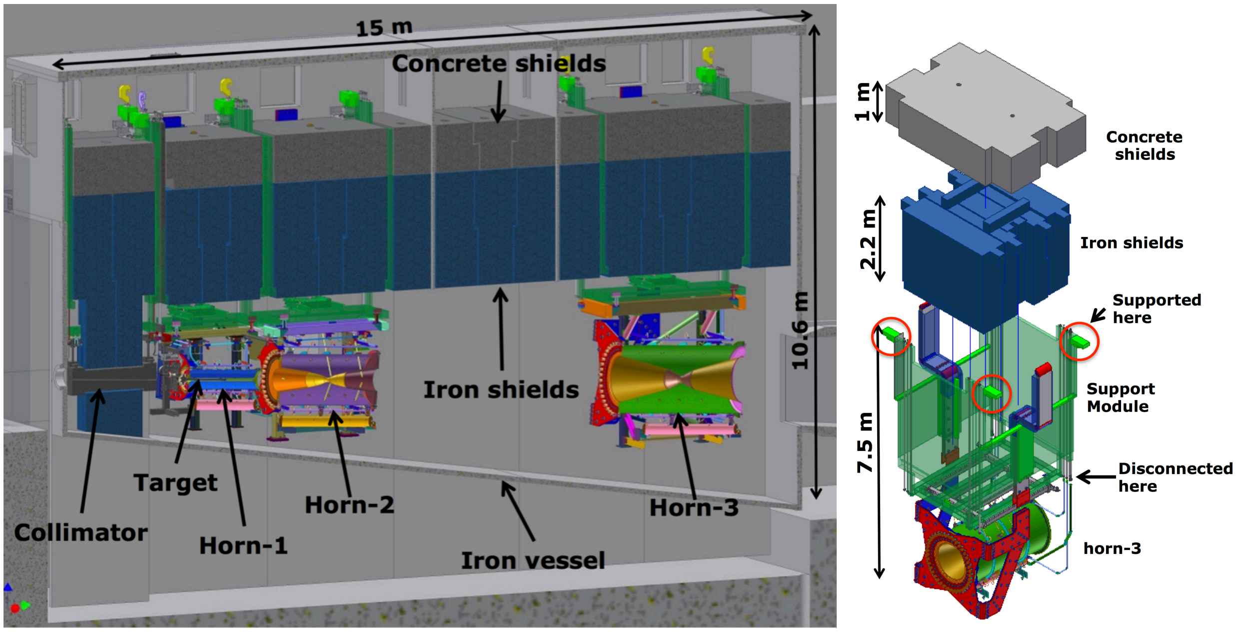

FIG. 8. Schematic view of the secondary beamline equipment inside the helium vessel (left). The beam comes from left side. The horns are supported beneath a box-shaped iron structure called a support module. Both iron and concrete shields are inserted in the inner space of the support module (right).

Fig. 7. A detailed schematic view of the secondary beamline equipment at the Target Station helium vessel is shown in Fig. 8. Since all of these equipment become highly radioactive at $O(10 \sim 10^2)$ Sv/h on their surface due to the high intensity beam operation, they are replaceable by using an automated overhead crane and remote-controlled hoisting attachments.

2. Beam Window

A beam window separates the atmospheric pressure helium environment of the target station vessel from the primary beam line vacuum. In addition to withstanding this differential pressure, the window must survive intense heating and the resulting thermal stresses and radiation damage from interaction with the pulsed proton beam. The window consists of two thin concentric partial hemispheres of titanium alloy cooled by helium flowing between the two skins. Sealing between the target station and the primary beamline is achieved using inflatable bellows seals on both the upstream and downstream sides of the beam window. The beam window assembly can be replaced by venting and evacuating the bellows seals and lifting the window assembly from the beamline using a remotely operated lift mechanism.

Titanium alloy was chosen due to its high strength and high thermal shock resistance resulting

FIG. 9. (upper) Stress in beam direction as function of time (ns) at window centre for 1.3 MW beam operation, with window thickness = 0.3, 0.4, 0.5, and 0.7 mm. (lower) Stress in the beam window as a function of thickness, after the final (8^{th}) bunch of a full beam spill at 1.3 MW operation. Z Stress represents through thickness stress and X Stress shows radial stress, respectively.

from a low thermal expansion coefficient and moderate Youngs modulus. It also has a low density meaning that the beam heating is relatively low. It has a low thermal conductivity compared with beryllium, the only other candidate material, hence it requires direct surface cooling, but for a low frequency pulsed beam such as at J-PARC it is the preferred candidate. The window material has three sources of stress operating at different timescales. The static stress due to the pressure load is reduced to a low level by the partial spherical profile. A transient stress caused by beam heating generates a compressive stress at the centre of the beam window. Finally, the 8-bunch structure within the 5 microsecond beam spill can generate a stress resonance between the surfaces of the window material. The next beam window under construction has been upgraded from 0.3 mm to 0.4 mm thick to increase the tolerance to this stress resonance effect. Figure 9 shows how this has been achieved, by ensuring that the bunch-to-bunch stress waves destructively interfere as they resonate between the two surfaces, and allowing for the properties to vary with the temperature increase during the beam spill.

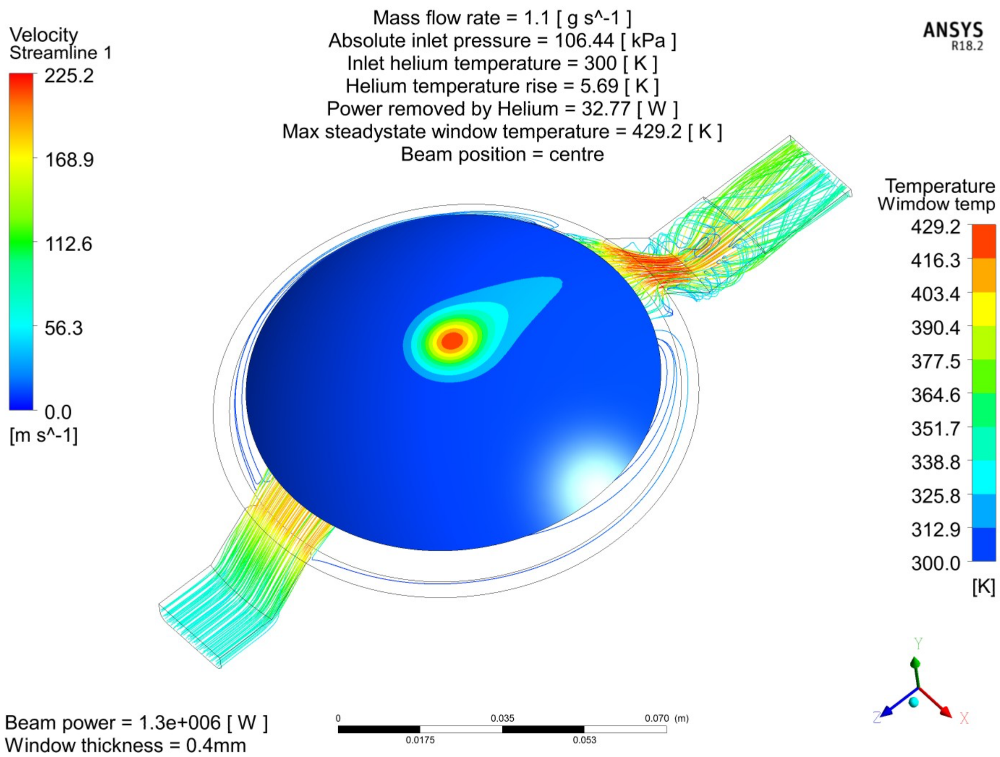

FIG. 10. Helium flow streamlines for 0.4 mm-thick beam window by ANSYS CFD Analysis for 1.3 MW beam. Current operating mass flow rate of 1.1 g/s is used in this analysis.

Figure 10 shows the helium velocity streamlines and temperatures in the titanium alloy material from an ANSYS CFX steady-state simulation for 1.3 MW operation.

TC: Is there an estimate for how long the beam window will last before replacement is necessary during Hyper-K operation?

3. Baffle

A baffle/collimator, as shown in Fig. 11, is required to protect the magnetic horns and Beam Dump from a mis-steered beam and to reduce the activation of components in the final focusing section upstream of the target. The existing baffle is a four interaction length (1700 mm long) Carbon Lorraine 2191 isotropic graphite block situated in the Target Station helium vessel between the beam window and the target. The 30 mm diameter bore for the proton beam is slightly larger than the diameter of the target rod and is precisely aligned with the target and horn axis. This arrangement protects the downstream components without the baffle interacting with the tails of the proton beam which would produce a high energy neutrino background. The graphite baffle block is incorporated into the Target Station to create a labyrinth with the steel shielding

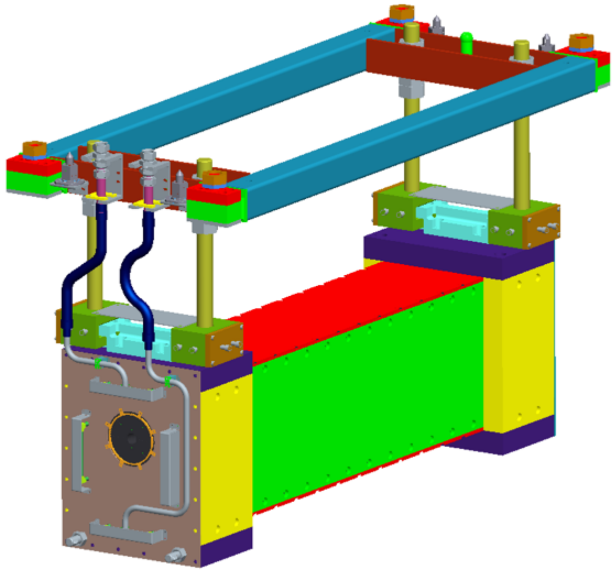

FIG. 11. Baffle.

and reduce backscattering from the target to the final focusing section. The 3.5 kW heat load estimated at normal 1.3 MW operation is easily removed by thin stainless steel water cooling tubes clamped to the outside of the baffle block by zinc coated steel plates. A full beam strike would deposit around 700 kJ causing a local temperature rise of around 200°C, compared with a long term maximum service temperature of over 700°C for the nuclear grade graphite in helium. An array of thermocouples around the upstream and downstream ends of the bore monitors the baffle temperature and gives an indication of proton beam position from the back-scattered heat load. Since the protons per pulse and consequent temperature jump and thermal shock from a full beam strike at 1.3 MW will remain the same as at 750 kW, the existing baffle is suitable for 1.3 MW operation and does not need to be upgraded.

TC: Are the protons per pulse for 750 kW and 1.3 MW really the same? According to Table 1, there is a 60% increase.

4. Target

The T2K target is a two interaction length (900 mm long) graphite rod (26 mm in diameter) sealed inside a titanium alloy container and cantilevered within the bore of the first magnetic horn. The polycrystalline nuclear graphite used is a low Z, low modulus, low thermal expansion coefficient and relatively high thermal conductivity refractory material making it particularly resilient to the intensely pulsed proton beam. Less than 5% of the beam power is deposited as heat in the target,

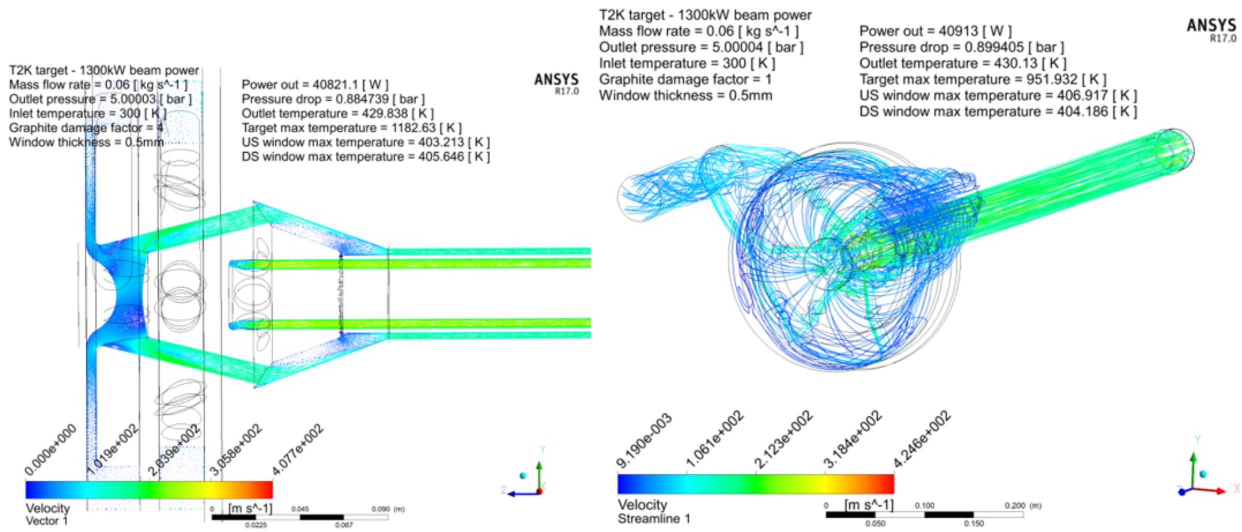

FIG. 12. Velocity flow lines in current T2K target geometry operating at 5 bar outlet pressure and 1.3 MW beam power.

and this enables it to be cooled by gaseous helium. Helium cooling permits the graphite to run at an elevated temperature thereby reducing the effects of radiation damage, minimises activation of the coolant and eliminates any pulsed-beam induced shock waves that would be generated in an incompressible liquid coolant such as water. In order to prevent oxidation of the graphite from any trace oxygen in the target station, it is sealed within a thin titanium alloy container which includes thin single skin entry and exit windows. The target and its container walls are cooled by a single circuit of high purity, high velocity helium. The alloy Ti-6Al-4V is used for the container and windows since it has a relatively high strength and heat capacity and low thermal expansion coefficient making it one of the few structural materials able to withstand the shock wave stresses generated within it by the pulsed proton beam. It is also known to retain its mechanical properties albeit with a reduction of ductility at proton fluences up to 10^{20} p/cm^2 [3]. However as with all metals, titanium loses strength at elevated temperatures and it is necessary for the helium to cool both the entry and exit windows before cooling the target rod without generating an excessive pressure drop over the complete circuit. Figure 12 shows the cooling flow path that has been devised and optimised to achieve this.

TC: The citation above appears to be missing.

The helium inlet enters an annular buffer volume in the target head before flowing across the entry window. The helium then flows through 6 angled holes in the graphite head to an outer annulus, cooling the titanium outer tube along the length of the target before performing a 180°

TABLE II. Comparative results between the existing 0.75 MW design and a potential 1.3 MW upgrade solution.

	0.75 MW (existing design)	1.3 MW (upgraded design)
Heat load	23.5 kW	40.8 kW
Helium mass flow	32 g/s	60 g/s
Helium inlet pressure	1.6 bar	5.9 bar
Pressure drop	0.72 bar	0.88 bar
Max helium velocity	560 m/s	425 m/s
Upstream window temp. (average)	107 °C	130 °C
Downstream window temp. (average)	117 °C	132 °C
Target core maimum temp. (new graphite)	620 °C	680 °C
Max graphite temp. (for 1/4 conductivity due to radiation damage)	750 °C	910 °C

turn at the downstream window and then returning along an inner annular channel cooling the target rod. The hot helium flows out through the graphite head to an annular outlet manifold via 6 angled holes interspaced between the 6 inlet holes.

Incremental developments to the target design are required to enable it to operate at a higher beam power. The main change is a requirement to increase the helium mass flow rate by increasing the helium pressure. Table X shows some comparative parameters for the current target operating at 750 kW and a suitable modified design. It is shown that with a mass flow rate of 60 g/s the target core temperature is nominally the same (∼50 °C) as the current design. Therefore oxidation of the graphite should be about the same as the current target if O_2 levels in the helium are similar. The table also shows how increasing the system pressure reduces the pressure drop and maximum velocity in the target. Keeping the pressure drop down is an important consideration for the helium compressors physical size and power requirements. Table II shows comparative results between the existing 0.75 MW design and a potential 1.3 MW upgrade solution.

TC: The first table appears to be missing. Can it be combined with the second table comparing 0.75 MW and 1.3 MW?

If the target outlet pressure is increased from 0.9 bar to 5 bar then it is possible to double the helium coolant mass flow rate without a significant increase in overall pressure drop. This means that in principle the existing target design may be able to dissipate the heat load deposited by a 1.3 MW beam. A velocity vector plot of a CFD simulation of this case is shown in Fig. 12.

This elevated pressure generates an increase in the mechanical stresses in the titanium alloy

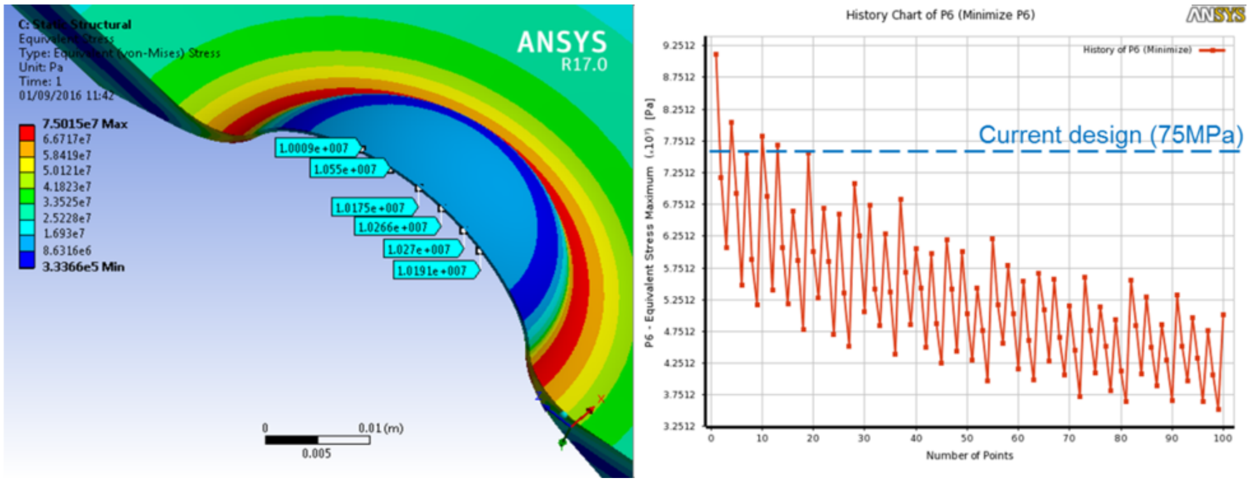

FIG. 13. Von-Mises equivalent stresses in the existing upstream target window operating at 5 bar helium pressure (L) and the history chart (R) of the parameterized re-optimization of the design

enclosure, particularly the upstream and downstream windows, which have now been re-optimised. Fig. 13 shows some results of these simulations using a parameterised model and a genetic algorithm for the upstream window to reduce the stress at 5 bar gauge pressure from 75 MPa to 34 MPa by a relatively modest increase in the outer plate thickness outside the beam footprint which therefore will have no impact on pion production performance.

The elevated heat load also generates a modest increase in thermal gradients and consequent stresses in the graphite material, but these effects are moderated by the graphite operating at an elevated temperature.

TC: What steps need to be taken to confirm that the updated titanium alloy enclosure design and 5 bar operation are sufficient for Hyper-K?

Studies have shown that a higher-Z core within the graphite target rod would increase the production of (anti)neutrinos from right-sign, while reducing the background from wrong-sign pions. SiC may be a candidate refractory material and SiC coated graphite is one of the materials being tested in a BLIP irradiation run as part of the RaDIATE collaboration. However, incorporating a new material such as this would increase the heat load and complexity of the target and no feasibility study has yet been conducted of such a design concept.

TC: Will work in this area continue to proceed? Are further physics studies needed?

TABLE III. Typical dimension of magnetic horn conductors.

Parameters	horn1	horn2	horn3
Inner diameter	54 mm	80 mm	140 mm
Outer diameter	380 mm	1,000 mm	1,330 mm
Length	1,495 mm	2,036 mm	2,536 mm

5. *Horns*

The three magnetic horns (horn1, horn2, and horn3 in order from upstream) are placed downstream of the target. Each magnetic horn consists of two coaxial (inner and outer) aluminum conductors which encompass a closed volume. The inner conductors are 3 mm thick to reduce interactions of secondary particles, while the outer conductors are 10 mm thick.

The horns are designed for a 320 kA pulsed current to maximize focussing of the secondary particles with low momentum and high emission angle [**?**]. The maximum magnetic field of 2.1 T is generated at 320 kA operation. The horn system focussing increases the neutrino flux at the peak energy of 0.6 GeV by a factor of 16. A pulsed current of 32 kA with 2 ms width is generated by a horn power supply and transferred through power cables to a pulsed transformer which amplifies the current by a factor of ten. The output current of 320 kA is then transferred through aluminum striplines to the horn conductors. The polarity of the horn current can be changed to allow for focussing of positive or negative secondary particles.

The typical dimensions of the horn conductors are shown in Table III. The horn conductors are made of an aluminum alloy A6061-T6, which is commonly used for a horn conductor material. The alloy A6061-T6 has the tensile strength of 310 MPa (at 25 °C), which is degraded by repetitive forces and whose fatigue strength is estimated to be 68.9 MPa for 97.5% confidence that the material will not fail in 2×10^8 cycles. The material strength is also affected by a corrosion compared to an air environment. An empirical factor of 0.43 is taken from the experience of MiniBOONE horn operation. Allowable stress on the horn conductors is 29.6 MPa by taking these reduction factors into account. The material strength also depends on temperature. Since the strength degradation is large above 100 °C, the allowable temperature is set to be 80 °C for the aluminum conductors so that the temperature effect can be small.

TC: Why does the corrosion in air environment matter if the horns operate in a He environment?

The aluminum conductors suffer from heat deposition by beam exposure and Joule loss. The heat deposition at the horn conductors for 1.3 MW operation is summarized in Tab. IV. Instanta-

TABLE IV. Summary of heat deposit at each horn. Heat deposit from beam exposure is based on beam intensity of 3.2×10^{14} protons/pulse for 1.3 MW. Joule heating of each horn is estimated for pulse widths of 2.0 ms. The calculation of the total heat deposit in units of kW is based on 1.16 s cycle.

Heat deposit	horn1		horn2		horn3	
	Inner	Outer	Inner	Outer	Inner	Outer
Beam (kJ)	12.1	10.5	2.8	9.7	1.0	1.9
Joule (kJ)	9.7	0.5	3.3	0.3	2.4	0.3
Total (kJ)	32.8		16.1		5.6	
Total (kW)	28.3		13.9		4.8	

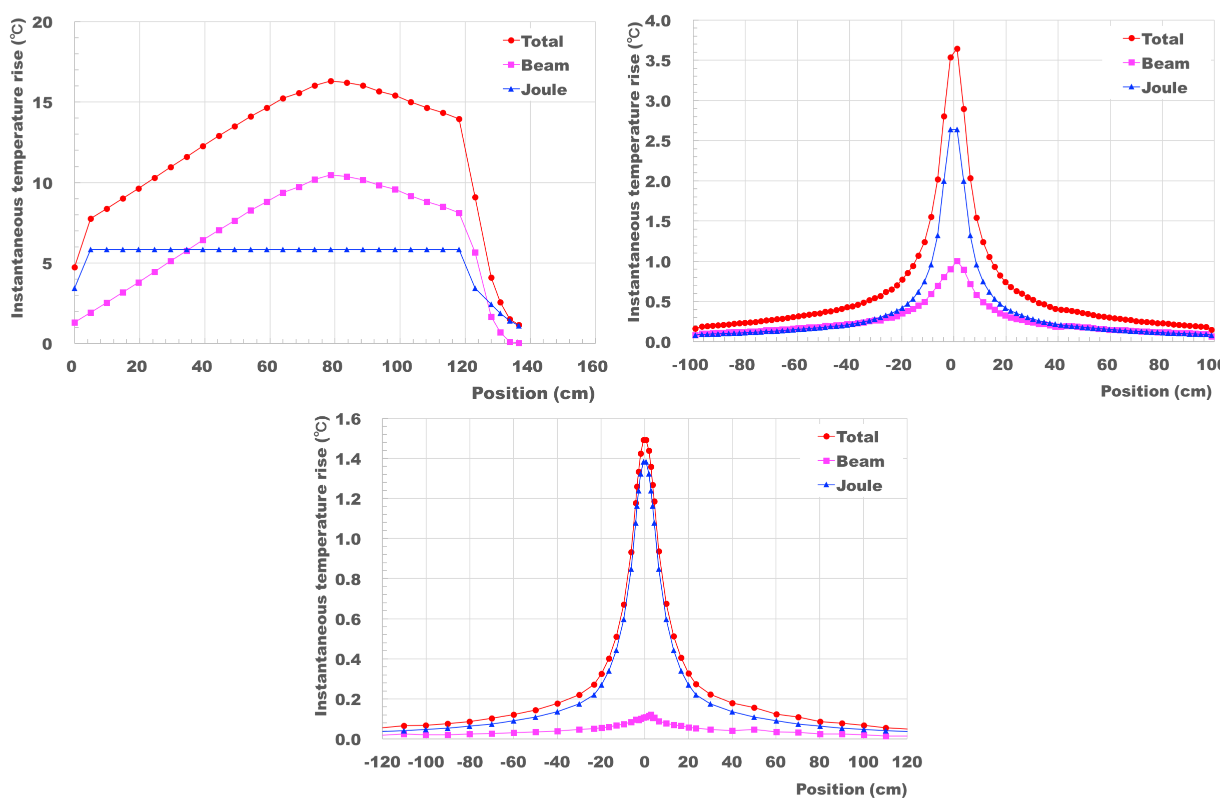

FIG. 14. Instantaneous temperature rise at inner conductors for 1.3 MW case as a function of longitudinal position for horn1 (top left), horn2 (top right), and horn3 (bottom). The instantaneous temperature rise due to beam exposure and Joule heating are represented by rectangles and circles, respectively. The total instantaneous temperature rise is also indicated by dots.

neous temperature rise at the inner conductor is also shown in Fig. 14. The heat load at the inner conductor of horn1 is largest and the instantaneous temperature rise is estimated to be 16.3 °C. Although the total heat load at the outer conductors are comparable to or larger than those at

TABLE V. Estimation of maximum temperatures at horn1, horn2, and horn3 for 1.3 MW operation. Numbers shown are in unit of °C.

Items	horn1	horn2	horn3
Instantaneous temperature rise	16.3	3.6	1.0
(beam exposure)	10.5	1.0	0.1
(Joule loss)	5.8	2.6	0.9
Steady state temperature rise	19.1	22.1	5.8
Coolant water temperature	25.0	25.0	25.0
Maximum temperature	60.4	55.3	31.8

TABLE VI. Summary of the heat flux at the striplines by beam exposure and Joule loss. Beam exposure is based on 3.2×10^{14} protons/pulse for 1.3 MW. Joule heating is estimated for pulse width of 2 ms. The current helium flow speed and the acceptable beam power relevant to the stripline cooling are also shown.

Heat flux per stripline plate	horn1	horn2	horn3
Beam heating (J/m^2)	164	1042	123
Joule heating (J/m^2)	50	24	18
Total (J/m^2)	214	1066	141
Helium flow speed (m/s)	2.7	2.7	2.2
Acceptable beam power (MW)	2.10	0.75	2.04

the inner conductors, because of their large volume, local heat deposit at the outer conductors is quite small (instantaneous temperature rises for horn1, horn2, and horn3 are 0.4 °C, 0.08 °C, and 0.01 °C, respectively). The inner conductors are cooled by water sprayed from nozzles attached at the outer conductors. From the past measurements at several bench tests, typical heat transfer coefficients for the horn inner conductor cooling were measured to be 7.9 kW/m^2·K (horn1), 1.0 kW/m^2·K (horn2), and 1.3 kW/m^2·K (horn3). Then the maximum temperatures at the horn conductors for 1.3 MW operation are estimated as summarized in Table V. The estimated maximum temperatures are well below the allowable temperature of 80 °C. The cooling performance of the horns is satisfactory for 1.3 MW operation. However, the cooling capacity of the horn water cooling system should be increased for 1.3 MW.

TC: By how much does the cooling capacity need to be increased. Is this upgrade a significant cost?

Striplines near the horn conductors also suffer from heat load by beam exposure and Joule loss, as summarized in Table VI. The largest heat load is expected at the horn2 striplines because defocused secondary particles by horn1 pass through the horn2 striplines. The stripline conductors are covered by aluminum ducts and the conductor plates are cooled by forced helium gas flow through the ducts. The helium flow speeds at the exit of the stripline ducts, where the highest heat load is expected, are estimated from the measured flow rate at the inlet for each horn as shown in Table VI. The acceptable beam power of 750 kW for horn2 is lower compered to the other horns (∼2 MW) due to the larger heat load. A different cooling scheme, a water cooling method, will be developed. The new water cooled striplines will be adopted to the horn2 for the beam power over 750 kW.

The proposed operation cycle for 1.3 MW beam is 1.16 s. A new horn electrical system, including power supply, transformer, and striplines, has been developed to satisfy 320 kA operation at 1 Hz.

The concentration of hydrogen produced by water radiolysis is as high as 0.7% at 1 week operation at 485 kW, with the hydrogen level controlled by a hydrogen recombination system. In addition, weekly helium gas flushing can keep the hydrogen concentration well below the requirement of 3% for 485 kW operation. However, it is found that the hydrogen production rate depends on the condition of the ion-exchanger operation and the lifetime of the ion-exchanger is affected by the existence of hydrogen peroxide. Therefore, reinforcement of the hydrogen recombination system will be performed to achieve safe and reliable operation for 1.3 MW or higher beam power.

In the following paragraphs details of the upgrades toward 1.3 MW are described.

a. Electrical system upgrade The 1 Hz operation requires a shorter charging time, while 320 kA operation requires higher operation voltage than that for 250 kA. Lower voltage operation is desirable to reduce a risk of failure, especially for some semi-conductor switching devices. Therefore the input load for one power supply should be as small as possible. To meet these requirements, the following are adopted.

- Separate power supplies for each horn to reduce the input load
- Energy recovery system (i.e., recycling electrical charge returned from the horns) to shorten charging time
- New striplines that have lower inductance and resistance than the current ones
- A new transformer that has the rated current of 320 kA. Three transformers are needed. Because of the limited space, these transformers should be compact compared to the existing transformers.

A schematic figure of the three-power-supply configuration is shown in Fig. 15. The stripline structure was already modified to reduce both inductance and resistance. The thickness is increased

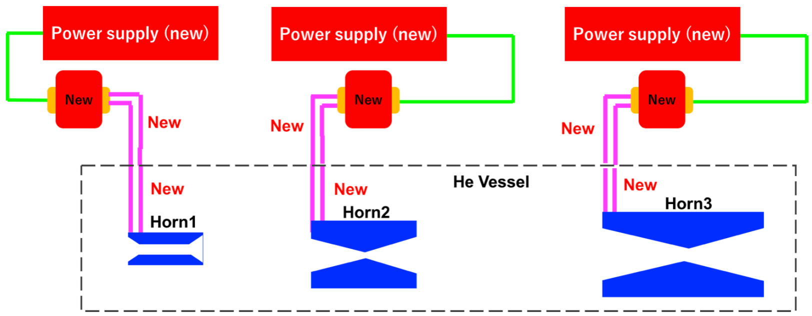

FIG. 15. Schematic figure of the three-power-supply configuration for 320 kA and 1 Hz operation.

TABLE VII. Comparison of the input load between the old and new electrical circuits.

Old configuration						
Components	horn1		horn2 + horn3			
	L (μH)	R (mΩ)	L (μH)	R (mΩ)		
Horn	0.47	0.100	0.46+0.53	0.035+0.023		
Striplines	0.28	0.100	0.60	0.210		
Transformer	0.30	0.040	0.30	0.040		
Total	1.05	0.240	1.89	0.308		
New configuration						
Components	horn1		horn2		horn3	
	L (μH)	R (mΩ)	L (μH)	R (mΩ)	L (μH)	R (mΩ)
Horn	0.47	0.100	0.46	0.035	0.53	0.023
Striplines	0.15	0.056	0.17	0.060	0.18	0.065
Transformer	0.25	0.025	0.25	0.025	0.25	0.025
Total	0.87	0.181	0.88	0.120	0.96	0.113

from 10 mm to 12 mm and the gap is reduced from 20 mm to 15 mm. The widths of the striplines at the horn are increased from 400 mm to 500 mm and from 400 mm to 600 mm above the support modules. A comparison of the input loads between the old and new electrical circuits is also shown in Table VII.

TC: So no further upgrade of the striplines is necessary for 1.3 MW operation?

The specification of the new power supply is summarized in Table VIII. The schematic diagram of the new power supply is shown in Fig. 16. The energy recovery system with full-bridge circuits was already adopted in the previous T2K power supply [?]. The polarity of capacitor bank is alternated pulse by pulse but the output current should have the same polarity at every discharge.

TABLE VIII. Summary of specification of the new power supply.

Item	Value
Rated operation voltage	7 kV
Rated charging current	7 A
Charging unit	50 kW
Rated operation cycle	1 Hz
Total capacitance	4 mF
Capacitor bank configuration	
(original design)	2S16P (0.5 mF×32)
(modified)	2S24P (0.335 mF×48)
Pulse width	2 ms
Rated output current	32 kA
Stored energy	98 kJ

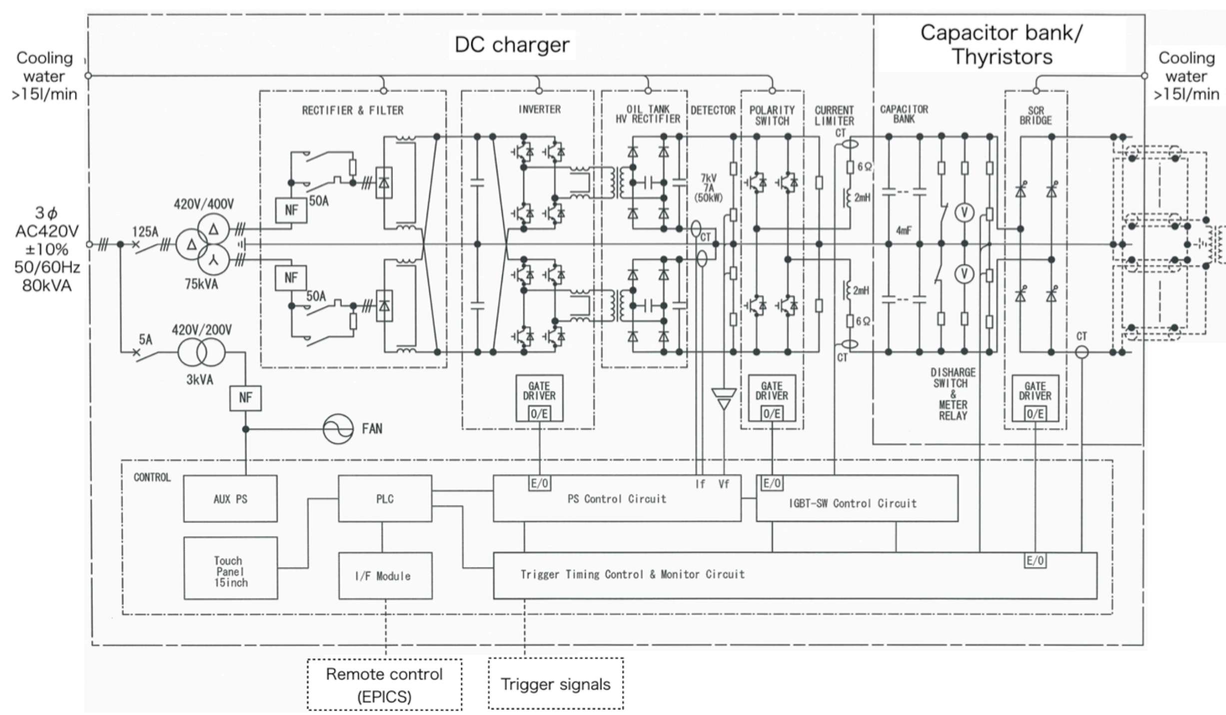

FIG. 16. Schematic diagram of the power supply circuit.

A full-bridge IGBT circuit, "polarity switch", is employed between charger and capacitor bank to control the polarity of charging current. Also used is a full-bridge thyristor circuit to control the polarity of output current to be the same at every pulse. Many semi-conductor switches are used in this system. Any malfunction of such high voltage semi-conductor switches can cause critical

TABLE IX. Simulated operation parameters for the new horn electrical system.

Parameter	horn1	horn2	horn3
Operation current	323 kA	323 kA	323 kA
Operation voltage	5.85 kV	5.72 kV	5.91 kV
Returned voltage	4.60 kV	4.78 kV	5.00 kV
Voltage recovery rate	78.6 %	83.6 %	84.6 %
Pulse width	2.00 ms	2.01 ms	2.08 ms
Charging time	0.71 s	0.54 s	0.52 s

damage of the power supply, which results in a long downtime of the experiment. In the new power supply, a safety system, "current limiter", is adopted to avoid a large current flow to the charging circuit by introducing an inductive load of 2 mH between the polarity switch and the capacitor bank. The current limiter can successfully reduce a reverse current flow to below the rated current of 600 A even though all the current flow to the current limiter. Therefore, the IGBTs are protected by this limiter. Circuit simulations were performed based on these new parameters. The obtained operation parameters are summarized in Table IX.

For all horns, the operation voltage is expected to be 5.7∼5.9 kV for 320 kA operation. The pulse width is also expected to be 2.0∼2.1 ms. Thanks to the low input load, the returned voltages are 79%∼85% of the operation voltages and thus the charging time can be reduced to less than 0.71 s. It is expected that the requirement of 320 kA and 1 Hz can be satisfied with the new configuration.

Two of the new power supplies and all the new striplines inside the helium vessel have been produced and installed in 2014. They have been operated stably at 250 kA so far, although 5∼10% capacitance drop of the capacitor bank was observed. One of the new transformer was also produced and installed in 2017. All the necessary upgrades were made for horn1 and then 320 kA operation of horn1 was tested. The measured operation parameters were as following: the measured peak current was 321.4 kA with the charging voltage of 6.05 kV, and the measured pulse width was 1.98 ms. The measured voltage (pulse width) was slightly higher (narrower) than the expectation, which is consistent with the observed 5 ∼ 10% decrease of the capacitance. A short-term continuous operation for 24 hours was also performed, although the operation cycle was 2.48 s, and steady-state temperatures at several places of the new transformer were measured. The maximum temperature was measured to be 35.3 °C at the secondary copper busbar, whereas the cooling water temperature was 26 °C. For 1 Hz operation the maximum temperature is expected

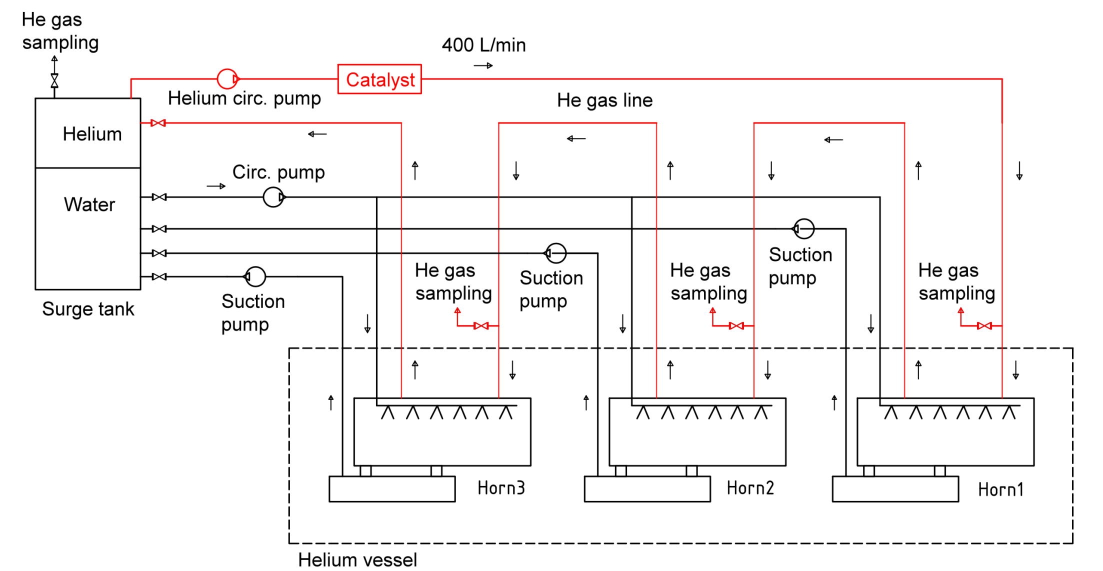

FIG. 17. Schematic diagram of water circulation system for horns. The hydrogen recombination system is shown in red.

to be at most 49.1 °C, which is well below the temperature limit of 60 °C at the transformer. Therefore the feasibility of 320 kA and 1 Hz operation is confirmed.

TC: Is the capacitance drop of the capacitor bank a continuing trend? Will a test a 0.86 Hz be made?

Remaining upgrade items are the production of one new power supply, two new transformers, and new striplines outside the helium vessel (for horn2 and horn3). All the capacitors with the countermeasures against the electro-corrosion must be produced and installed to the existing power supplies.

TC: What is the timescale for these upgrades?

b. Improvement of the hydrogen removal system The hydrogen recombination system is connected to the horn cooling water circulation system as shown in Fig. 17. The system has a catalyst (alumina pellet with 0.5% paradium) which recombines hydrogen and oxygen into water (i.e., H_2 + $1/2O_2 \rightarrow H_2O$). The horn inner volume and the cover gas region of the surge tank are connected and the helium gas is circulated by helium circulation pump at flow rate of 400 L/min. All three horns are connected in series in this helium circulation loop. The total volume of helium gas is approximately 5.5 m^3. The helium gas is flown through the catalyst that is kept at 60 °C by heater in order to increase the hydrogen recombination rate. In-situ gas chromatography system can measure gas contamination in the helium atmosphere by remotely sampling the helium gas from the circulation loop.

The measured production rate of the hydrogen at 485 kW beam power is 260 L (or 4.7%) per 10^{19} POT without the operation of the hydrogen recombination system. The hydrogen concentration is reduced to 0.1% per 10^{19} POT by the recombination system. The hydrogen concentration is gradually increased to 0.7% at one week operation at 485 kW, which corresponds to 1.9% for 1.3 MW operation. The hydrogen explosion limit in an air environment is 4% and the limit can be higher in the helium atmosphere. A risk of the hydrogen explosion may be very low with a lack of oxygen. However, the hydrogen concentration is kept below 4% in our operation to further reduce the risk. To satisfy this requirement, helium gas flushing is performed at weekly maintenance days and the hydrogen concentration can be reduced to 0.1% after the flushing. If we restrict the hydrogen concentration below 3%, it corresponds to the acceptable beam power of 2 MW.

TC: Are there any lab or legal limits on the hydrogen concentration. Can the maximum level for the helium environment be quantified?

The main final products from water radiolysis are hydrogen, hydrogen peroxide, and oxygen, and production rate of oxygen is quite smaller than that of hydrogen or hydrogen peroxide [**? ?**]. However, since the hydrogen peroxide is unstable and naturally decomposed into water and oxygen (i.e., $H_2O_2 \rightarrow H_2O + O_2$), the oxygen from the hydrogen peroxide can be a source of the hydrogen recombination. The remaining hydrogen peroxide was measured at a concentration of 10 mg/L at 485 kW operation, and it can corrode the ion exchange resins due to oxidization of the resins, reducing their lifetime to less than 1 year with the current system. In order to avoid this degradation, a newly developed Paradium-overlaid ion exchanger will be adopted in addition to the usual ion exchangers. The utilization of the Paradium-overlaid ion exchangers are supposed to help reliable ion exchanger operation even at 1.3 MW.

TC: The citations are broken. You say that the new paradium-overlaid exchangers will help reliable operation at 1.3 MW. Can this be quantified? Can the degradation time at 1.3 MW operation be estimated?

With these improvements, the water cooling system with hydrogen removal scheme can be operated with higher reliability and stability for 1.3 MW.

c. Improvement of stripline cooling The stripline ducts near the horn conductors, where the heat load is largest, are open-end and there is a difficulty in estimating the exact helium flow rate. In addition, there is another difficulty to achieve much higher acceptable beam power by the forced helium flow scheme.

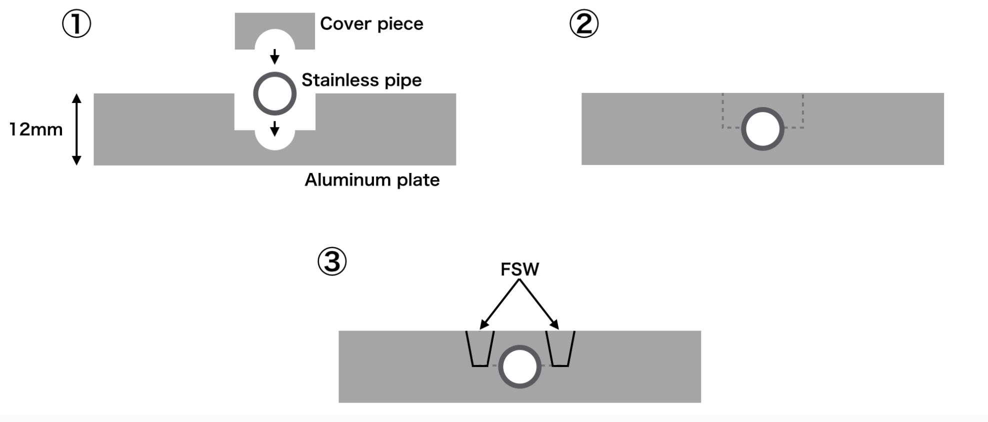

FIG. 18. Schematic figure showing water cooling method by FSW technique.

TABLE X. Summary of the measured effective heat transfer coefficients at several water flow rates.

Water flow rate (L/min)	Effective heat transfer coefficient (kW/m^2·K)
1.0	2.38
3.0	3.48
4.3	4.05

TC: This section isn't very clear. From this it is not clear why a helium cooling system can't work.

A new water cooling scheme is developed, where the integration of the cooling pipe is achieved by using a welding technique called Friction Stir Welding (FSW), as shown in Fig. 18. A 12 mm thick aluminum plate is machined to have a groove for a stainless pipe. A 1/4 inch stainless pipe that is put in the groove is covered by an aluminum piece and both ends of the cover piece are welded by FSW. The FSW technique has been used for welding of the stripline plates and is a well established technique. A merit of this technique is that a cooling path can be flexibly placed in the two-dimensional plane. Cooling performance of this technique was investigated with a simple test piece. The measured effective heat transfer coefficients are summarized in Table X. The effective heat transfer coefficient depends on water flow rate. Since the diameter of the stainless pipe that is embedded in 12 mm-thick aluminum plate is only 1/4 inch (inner diameter is 4.35 mm), the water flow rate achieved in this test was only 4.3 L/min. A mockup of the water cooled stripline was produced to check the actual water flow rate as shown in Fig. 19.

TC: What does a mockup mean in this case? Was the piece built and the water flow tested?

Estimation of stripline temperature at 1.3 MW operation was performed using a two-dimensional

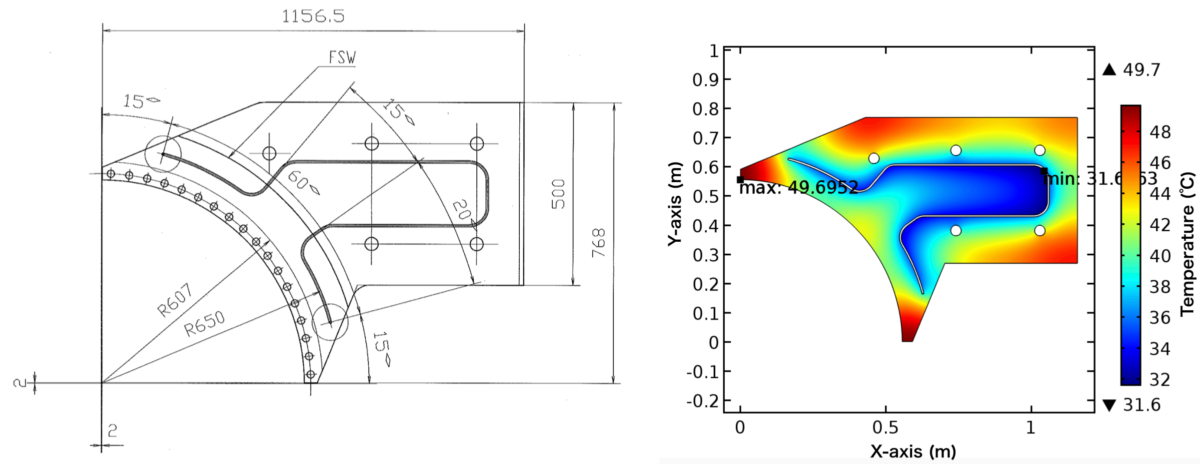

FIG. 19. (Left) Drawing of the mockup of the water cooled striplines. (Right) Estimated temperature distribution at the water cooled stripline for 1.3 MW beam operation.

FEM simulation. Adopting a heat transfer coefficient of 3 kW/m^2·K for the water cooling path and input heat load for 1.3 MW operation, the temperature distribution at the stripline was calculated as shown in Fig. 19. The maximum temperature is estimated to be 49.7 °C, which is well below the allowed temperature of 80 °C. With the assumed heat transfer coefficient of 3 kW/m^2·K, the acceptable beam power is estimated to be approximately 3.3 MW. Great improvement on the stripline cooling performance can be achieved with the proposed water-cooled striplines.

The remaining study items for the water-cooled striplines are as following.

- Tolerance against vibration due to Lorentz force should be well considered. For example, a special care should be paid to the design of inlet and outlet connection structure. In order to investigate the vibration tolerance, operation test with mockup water-cooled striplines will be performed.

- Design of water plumbing connecting to the water-cooled striplines should be done. Since several-hundred volts are applied to the striplines, electrical insulation must be considered.

The water-cooled striplines will be adopted to only horn2. Before the new horn2 is prepared, a current testing of the water-cooled striplines is planned with the spare horn1. Although the shape of the mockup water-cooled stripline for horn1 is different from the actual one for horn2, it is supposed that very useful outputs can be obtained from the current testing with horn1, such as investigation of the vibration tolerance and plumbing design around the water-cooled striplines (insulation structure) and so on. The current testing with spare horn1 will be performed in JFY2019

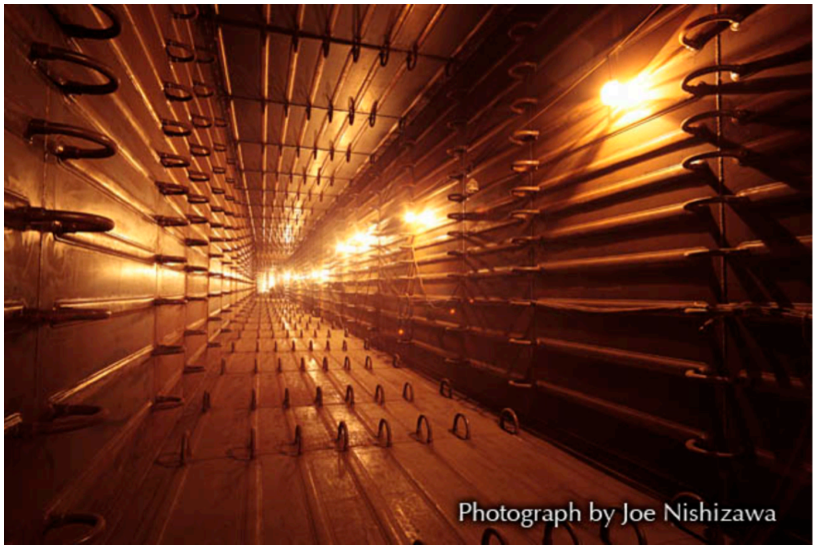

FIG. 20. Picture of the Decay Volume.

and JFY2020. After that, current testing with horn2 will be performed in JFY2020 and JFY2021. The actual production and installation will be done in FY2021.

6. *Decay Volume*

The Decay Volume is a 94 m-long tunnel with a vertically elongated rectangular cross section allowing variation of the off-axis angle to the far detector from 2.0° to 2.5°. The secondary beamline is directed 3.637° downward to have the same off-axis angle of 2.5° to both Super-Kamiokande and Hyper-Kamiokande. The whole structure of the helium vessel is composed of 10 cm-thick iron plates where water cooling channels, called plate coils, are welded on the wall to cool the wall and surrounding concrete shielding below 100 °C, as shown in Fig. 20. The helium vessel, which is inaccessible due to the high radioactivity after beam exposure, is designed to survive thermal stress from 4 MW beam. For the Target Station helium vessel, temperature increase of the iron wall should be limited to 30 °C in order to suppress thermal expansion of the wall below 1 mm, which can cause an uncertainty on alignment of the target and the horns.

TC: A requirement is given, but is it achieved with the current design?

7. *Beam Dump*

The remnant proton beam is deposited in a hadron absorber (beam dump) at the downstream end of the decay volume. The absorber is required to dissipate approximately one third of the

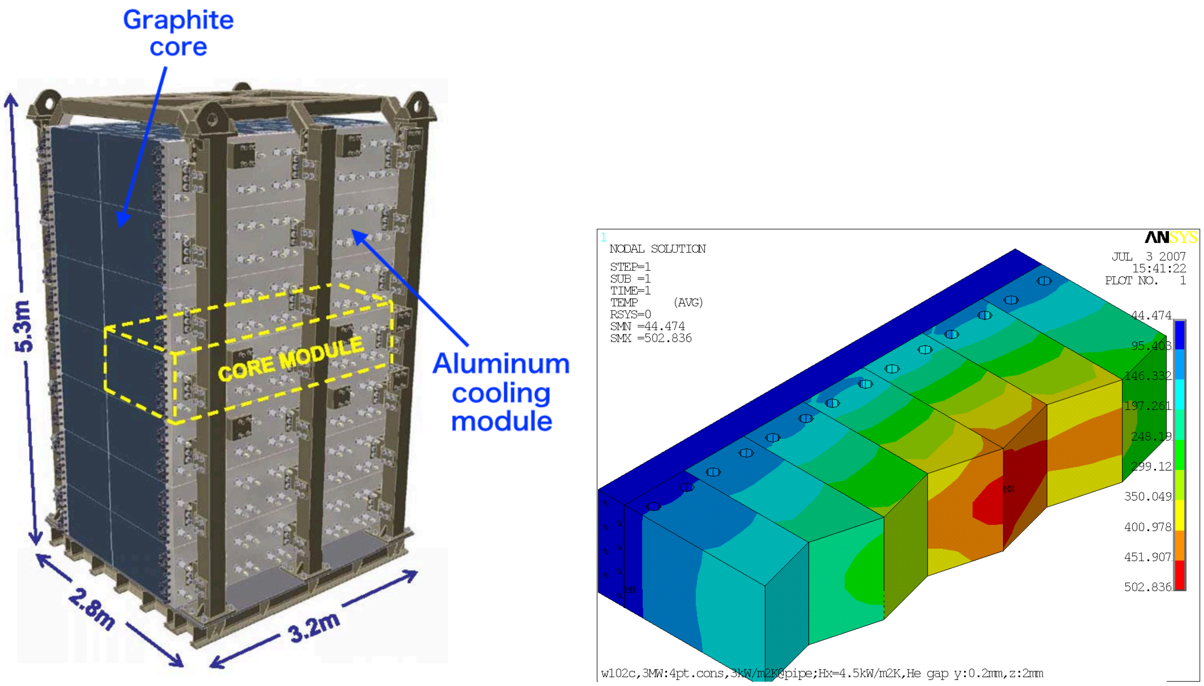

FIG. 21. Schematic figure of the Beam Dump (left) and temperature distribution from MARS and ANSYS FEA simulations for 3 MW beam power, along centre division of a half layer of graphite (right).

total beam power and the core comprises a 3.2 m length of graphite followed by a total length of 2.4 m of steel. The hadron absorber is contained within the helium-filled decay volume in order to minimise oxidation of the graphite at the operating temperature, to minimise activation of the surrounding air and to avoid the technical risk of a large beam window at the downstream end of the decay volume. Due to its inaccessibility and high radioactivity after operation it is not possible to repair or replace the hadron absorber. Consequently it has been designed to accommodate the full potential beam power of 3-4 MW and to survive the lifetime of the facility. The graphite core is 2 m wide to accommodate the majority of the disrupted hadron shower and is 4.7 m high in order to permit the facility to accommodate tuning of the off-axis angle between 2 degrees and the current 2.5 degrees. Graphite is chosen for the absorber since it is robust to thermal shock and able to operate at temperatures up to the level where oxidation from the trace oxygen in the helium atmosphere may become an issue. It consists of 7 layers of 14 blocks of PSG-324 extruded graphite supplied by SEC Co, clamped to external water cooling modules comprising steel pipes cast within aluminum blocks. Figure 21 shows a schematic figure of the Beam Dump and simulated temperature distribution for 3 MW beam power.

TC: Is there any risk of failure during Hyper-K operation?

TABLE XI. Devices maintained remotely in the Target Station.

Device	Readiness of remote handling system	Experience of actual remote handling
Beam monitor	Under development	No
Beam window	Yes	Yes
Baffle	No	No
Target	Yes	Yes
Horns	Yes	Yes

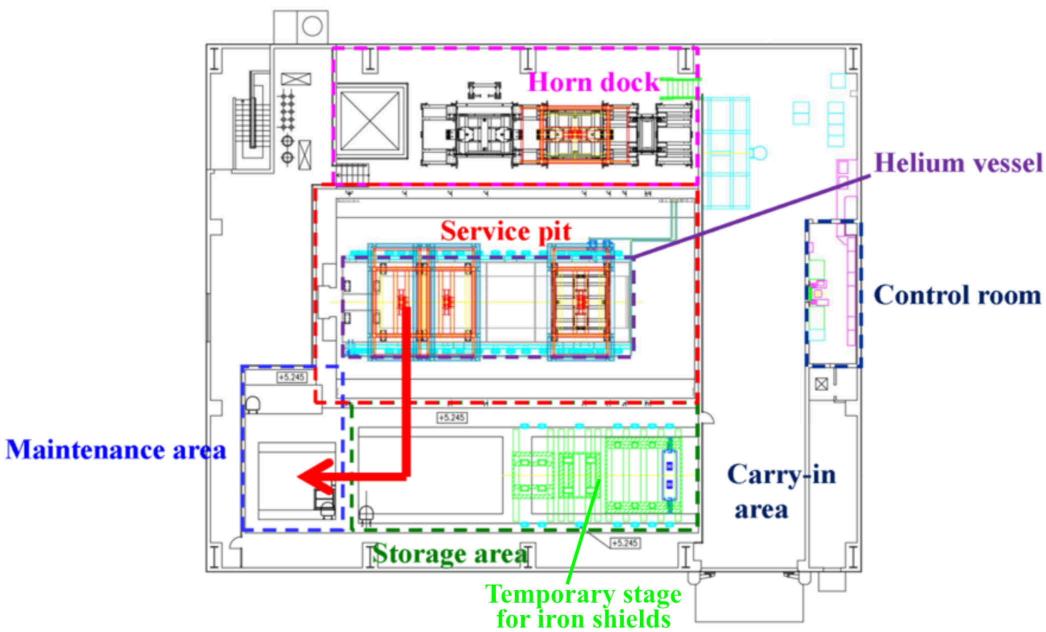

FIG. 22. Top view of the Target Station.

8. *Remote Handling*

a. Overview The secondary beamline devices become highly radioactive by beam operation and must be handled remotely with considerable caution. The Target Station has specially designed systems for remote maintenance. Table XI shows the devices maintained remotely in the Target Station. Figure 22 shows the top view of the Target Station. The Target Station consists of the following area.

- Service pit where the helium vessel with the target and the magnetic horns is installed
- Machine room (underground floor below the horn dock area) where the cooling systems for the target, the magnetic horns, the helium vessel, and the decay volume is installed

- Horn dock area where the new magnetic horns are tuned
- Maintenance area where the devices handled remotely are replaced
- Storage area where the radioactive devices are stored
- Carry-in area where the devices are carried into the Target Station from outdoor

Since concrete shielding blocks are stacked above the service pit, the maintenance area, and the storage area during beam operation, it is necessary to remove the concrete shields before maintenance of any of the devices in the beam line. All devices can be accessed only from the top.

There are two master-slave manipulators and a lift table for the replacement work in the maintenance area, and those devices can be operated and viewed through a lead glass window from a neighbouring shielded area with human access. Devices maintained remotely in the Target Station are transported from the beam line to the maintenance area where they are replaced. The used devices are put into a shielding casket and stored in the neighbouring storage area. Thus every remote maintenance system consists of following three components.

- Handling machine which carries the device from the beam line to the maintenance area and installs it into the beam line again
- Exchanger which replaces the device with a new one
- Casket in which the used device is stored/disposed of.

The handling machine is attached to the crane and controlled remotely from the crane control room in the target station.

The crane in the Target Station is operated by a 3-dimensional control system. All motion systems (traveling, traversing, lifting, rotating) are duplicated. If one motor fails, the work can be continued by switching to another motor. Because all control boards of the crane are in the crane control room, they are not only shielded from radiation during remote maintenance work, but also they can be repaired in this room should they fail. The operator operates the crane and the handling machine while watching not only the coordinate and the values of sensors (tilt, load, and so on) but also the camera images. For example, 40 cameras are used when the magnetic horn is carried from the beam line to the maintenance area.

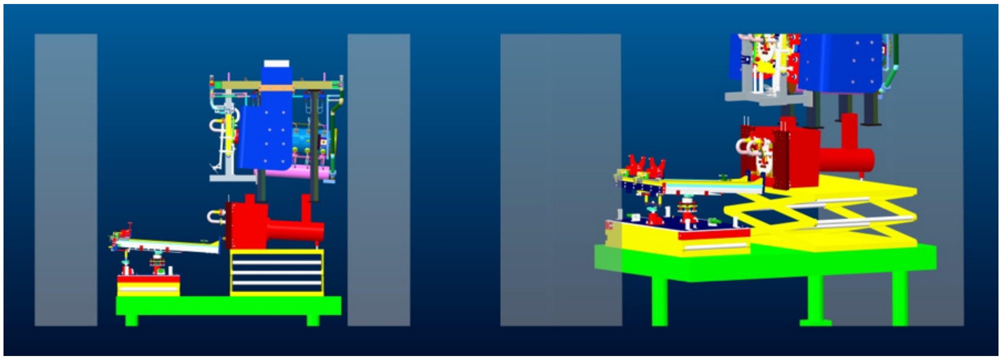

FIG. 23. Horn, target exchanger and installation/disposal cask installed on lift tables in Remote Maintenance Area of Target Station.

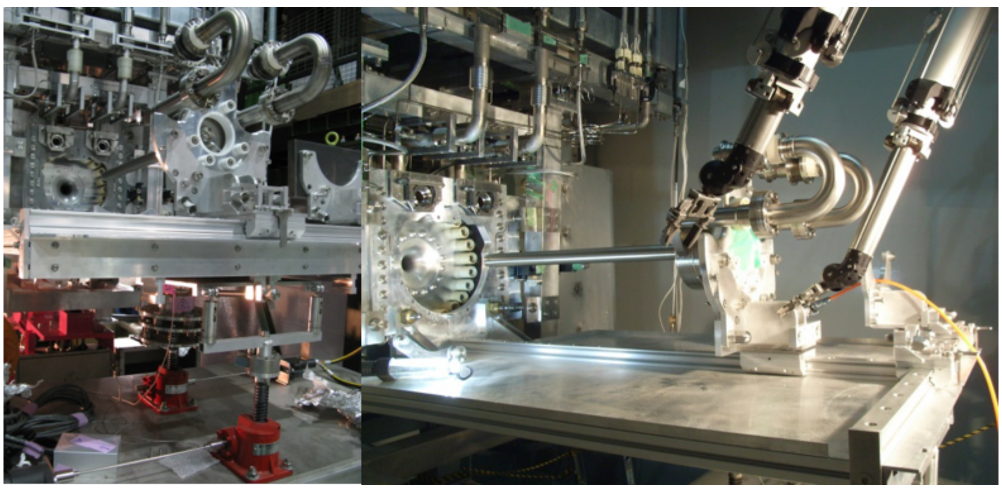

FIG. 24. Photographs (Left) of target on exchanger docked to horn, showing red screw jacks and suspension protection used to dock to horn at correct height and angle, and (Right) target installation using manipulators in remote maintenance area of Target Station.

b. Target As the beam power increases, target failures due to radiation damage are expected to occur more frequently than magnetic horn failures. A failed target can be replaced within the 1st magnetic horn in the Remote Maintenance Area (RMA) of the Target Station, permitting the horn to be re-used. In order to do this, a replacement target is first installed in the RMA and loaded onto a bespoke target exchange mechanism mounted on an independent lift table. The horn containing the failed target is then lowered into the RMA beneath its support module. Figure 23 shows a 3D CAD model of the horn, the target container and the target exchanger installed in the Remote Maintenance Area. The target exchanger is then raised on its lift table and carefully docked to the horn as shown in Fig. 24 using the master-slave manipulators which are incorporated in the RMA. The failed target is removed from the horn and replaced with the new target using the

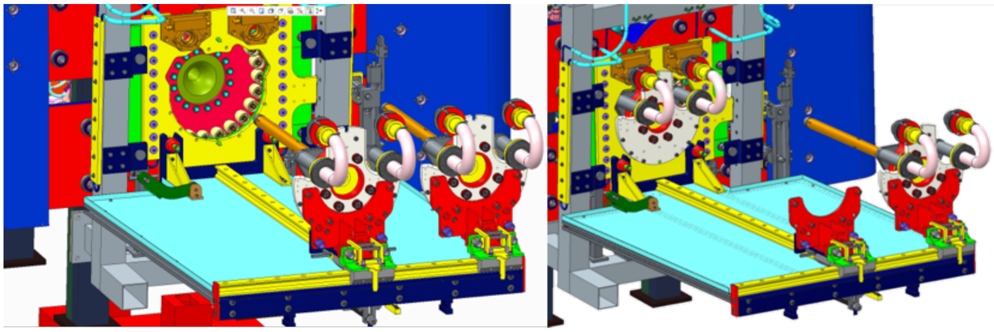

FIG. 25. CAD models of target exchange procedure showing the longitudinal Z-rail used to install/withdraw targets and a cross-rail (X-rail) to exchange.

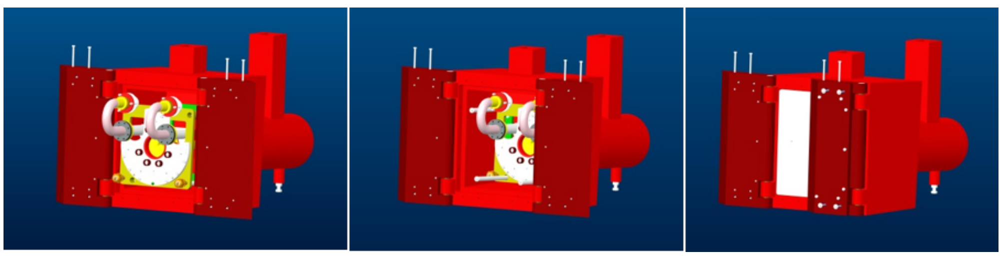

FIG. 26. Target as installed in shielded Installation/Disposal cask (Left), pushed back on internal rail system (Centre) and containment and shield door closure (Right).

target exchange mechanism as shown in Fig. 25. The target exchanger is then disconnected from the horn which, complete with the replaced target, is then lifted from the RMA and re-installed in the beam line. Figure 26 shows the failed target installed in shielded cask which is then loaded into a larger shielded cask for storage in the morgue and eventual disposal. Figure 27 shows pictures of the shielded Installation/Disposal cask.

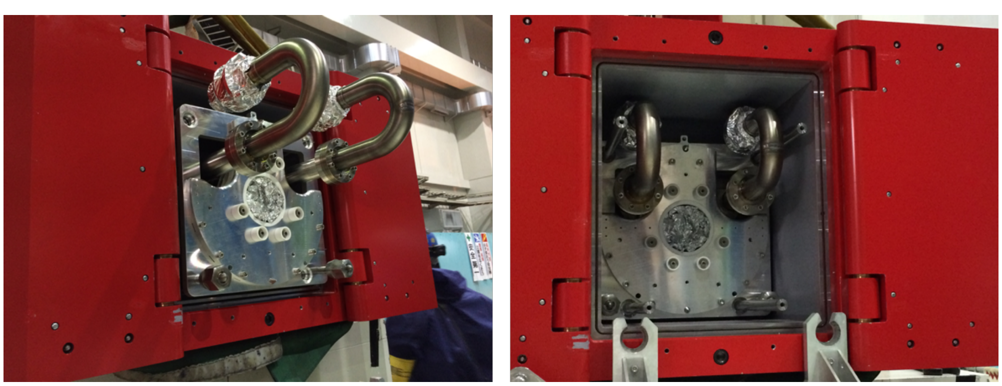

FIG. 27. Pictures of the shielded Installation/Disposal cask. Left: target is set inside the cask. Right: target is fully contained.

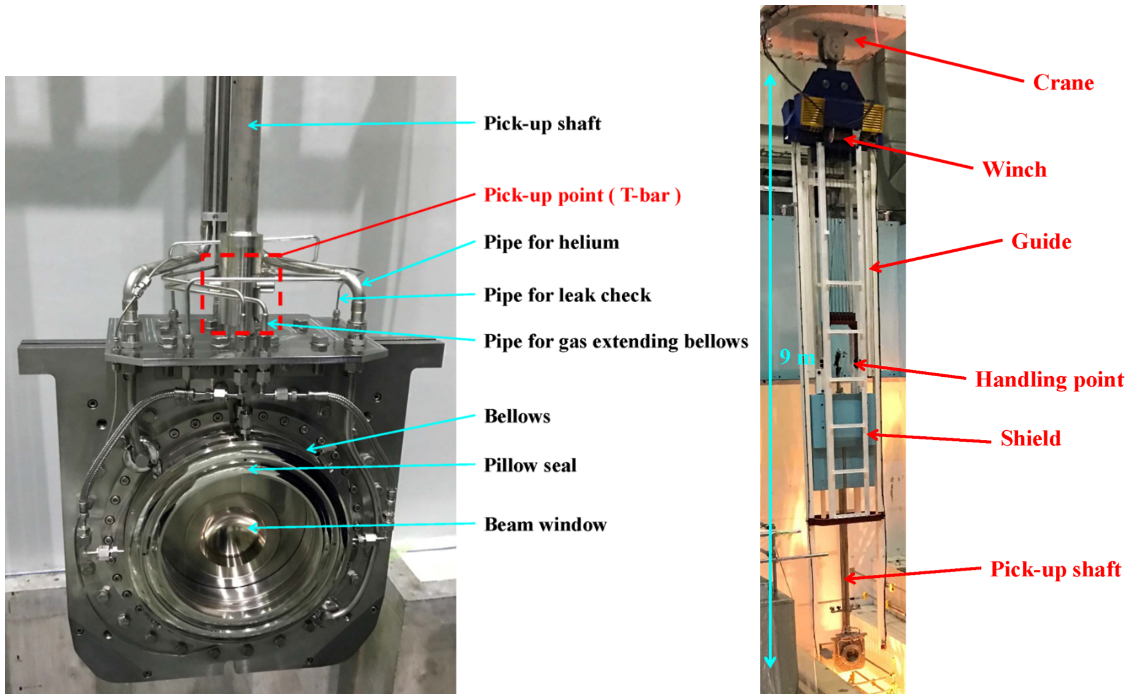

FIG. 28. Picture of the beam window (left) and its remote handling device (right).

Access to the Remote Maintenance Area is only possible when the beam is shut down for a long enough period for the top layers of concrete shielding to be removed, which is a costly and time consuming process. Consequently opportunities to rehearse and develop the target exchange procedure have been relatively limited. It has never been possible to entirely exclude personnel from the 'active' side during the installation and set-up of non-activated components for fully realistic rehearsal purposes. Nevertheless every individual procedure for the remote target replacement as described above has been tested in the Target Station Remote Maintenance Area using the master-slave manipulators to perform manual operations. The only exception is the target disposal sequence, where a failed target is installed in its shielded cask, for which a complete rehearsal was not possible due to a lack of time available. Confidence in the use of the target exchange mechanism has been gained by using it to replace a leaking target helium pipe performed in 2015. This was not a task that was originally envisioned and required a special modification of the mechanism.

c. Beam window The beam window separates the vacuum in the monitor stack (upstream side) from the helium vessel (downstream side) using inflatable bellows vacuum seals (called pillow seals) to seal against mirror flanges. This system enables the window to be easily disconnected and replaced when required. Figure 28 shows a picture of the beam window and its remote handling device.

The pillow seal is a kind of metal seal, and composed of a pillow and a mirror flange. The pillow is attached to a bellows which can expand by applying pressure from outside in order to obtain a contact pressure on the mirror flange. A nominal pressure during the beam operation is +0.3 MPa. In case of beam window replacement, the pressure is released to shorten the bellows in order to make a gap between the pillow and the mirror flange. The mirror flanges are attached to the monitor stack and the helium vessel. The pillows can be exchanged with the beam window replacement, but the mirror flanges still remain. So it is important to keep the surface of the mirror flanges clean. Because vacuum is kept by metal touch between the pillow and the mirror flange, damage and pollution on the surface of the pillow and the mirror flange influence seal performance. Some visual inspection devices and cleaners for the mirror flanges are developed for this purpose.

The beam window has a pick-up point (called T-bar) at the top and is handled with the pick-up shaft here. Because the beam window is installed on the beamline, which is 4 m below the service pit floor where workers access, the height of the pipes (2 pipes for cooling helium, 4 pipes for gas extending bellows and 2 pipes for leak check) is also 4 m. The beam window is carried together with these pipes into the maintenance area and the pipes are removed from the beam window there.

A shield (called upper-shield) is placed above the beam window during beam operation in order to shield radiation from the beamline. The upper shield is removed before the replacement work and installed again after the replacement.

Figure 28 also shows a handling machine for the beam window, which can be attached to the crane hook. The handling machine is very long and narrow, because the beam window is 4 m below from the service pit floor. A set of guide poles, which are placed on the service pit floor, ensure the alignment of the handling machine. Once the bottom of the handling machine touches down the guide poles and its alignment is fixed, the pick-up shaft can vertically move along the guide frames by a winch. The handling machine can also handle the upper-shield. The sky-blue shield in Fig. 28 (called handling-machine-shield) shields radiation in the work after removing the upper shield and is removed from the handling machine when the upper-shield is handled. The pick-up shaft for the beam window is hung on the top of the shield, and a worker rotates the shaft to lock or unlock the beam window over the shield, as shown in Fig. 29 . Once the beam window is picked up, the pick-up shaft is moved upward by the winch. Then the handling machine with the beam window is transported to the maintenance area and the irradiated beam window is inserted into a casket. The new beam window is thereafter installed to the beamline in the opposite procedure.

The first replacement work by remote control was done in August, 2017. There was no trouble.

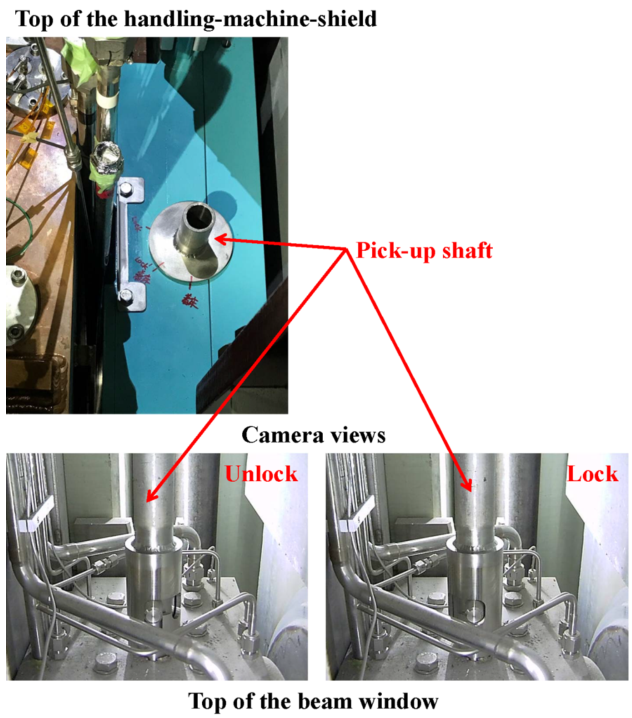

FIG. 29. Beam window is picked up.

The leak rate of the new beam window after the replacement work is the same as that of the old beam window before the replacement work. The new beam window is used at the present beam operation.

d. Horn When one of the horns is broken, it is moved to the maintenance area. Then the horn itself is disconnected from its support module and moved to the storage area and stored inside a cask for temporary storage. Thereafter a new horn is set up in the maintenance area and connected to the support module. The support module is designed to be reused even if the horns are broken. After connection, the new horn is moved to the helium vessel.

There are iron and concrete shields in the helium vessel, which are placed very tightly with only 3 cm gaps between all the neighboring elements for radiation shielding. During insertion into or extraction from the helium vessel, it is important to avoid for each component to hit the neighboring components even with such small gaps. To ensure that the equipment is safely moved upward or downward, a guide system, composed of guide frames and a special remote handling machine, was developed as shown in Fig. 30. Two guide frames are placed both at the top of the helium vessel and at the maintenance area. The remote handling machine has several guide rollers at each corner which ensure a smooth movement along the guide frame. Before the horn transportation, the guide frames are aligned very precisely based on the position of the horns and

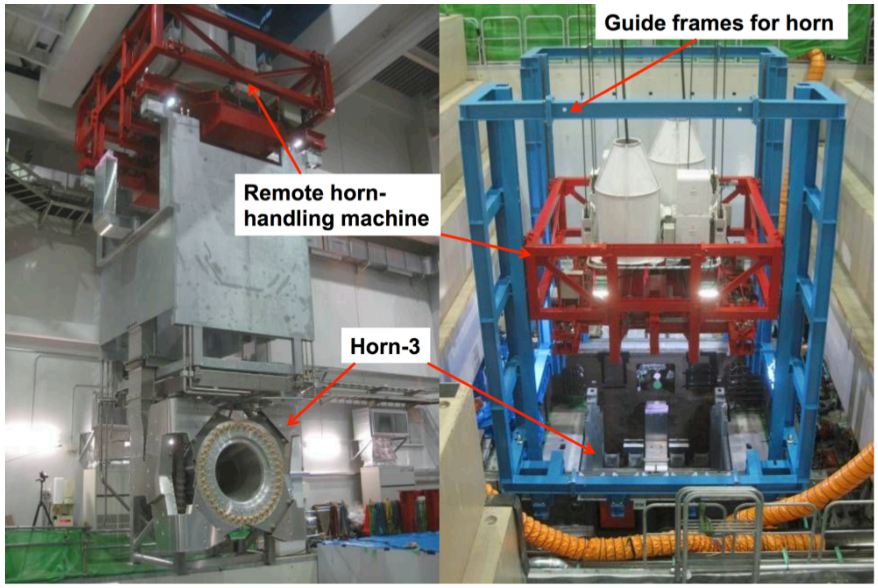

FIG. 30. Pictures of the remote handling machine for the horns. The horn3 hanged by the special remote handling machine (left) and the remote handling machine lowering in the guide frame placed on top of the helium vessel (right).

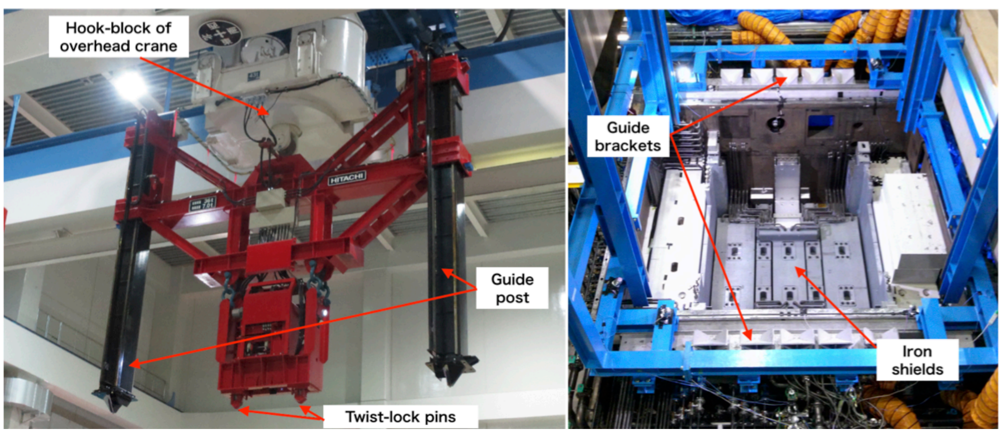

FIG. 31. Pictures of the remote handling machine for iron and concrete shields (left) and its guide brackets located on the edge of the helium vessel (right).

horizontal position within a few mm precision can be secured during the upward and downward movements. Since the horns and the support module are 10 m-high at maximum and the center of gravity is horizontally off by a few cm from the supporting point, it is important to adjust the perpendicularity. Some counter weights are attached at the top of the support module and its perpendicularity when hung by the remote handling machine is adjusted by using an angle meter which can be monitored remotely even during the transportation. There is also a dedicated remote handling machine for the iron and concrete shields as shown in Fig. 31. This machine has two

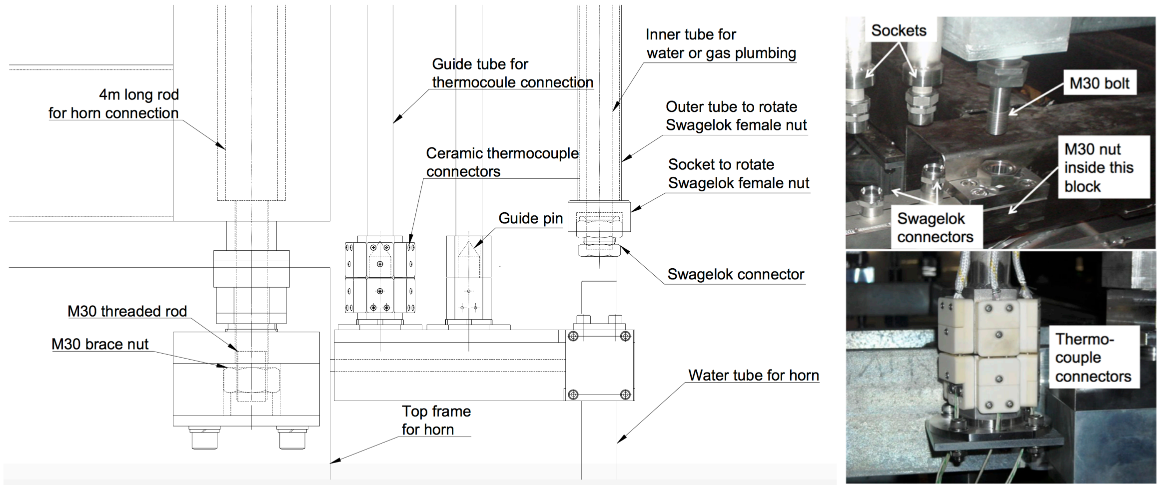

FIG. 32. A drawing (left) and pictures (right) of the remote connection for the horn attachment, the water/helium pipes, and the thermo-couples.

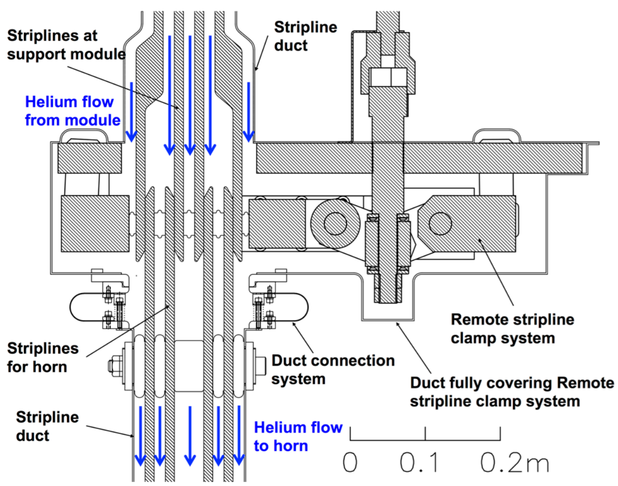

FIG. 33. A drawing of the remote connection for the striplines.

guide posts and their corresponding guide brackets are located on the both edges of the helium vessel to ensure relative alignment between the shields and the remote handling machine.

Once the irradiated horns are placed in the maintenance area, the exchange of the horns is performed. The horns and their support module can be disconnected with a semi-remote manner. The remote connection/disconnection must be done for the attachment of horn itself, the striplines, the water and helium pipes, and the thermo-couples. The detailes of those remote connection mechanism are shown in Figs. 32 and 33. The basic concept for the horn remote connection is to perform the connection/disconnection of each item by using its dedicated long shaft that is rotated by a worker who stands on the concrete shield inserted inside the support module. The support

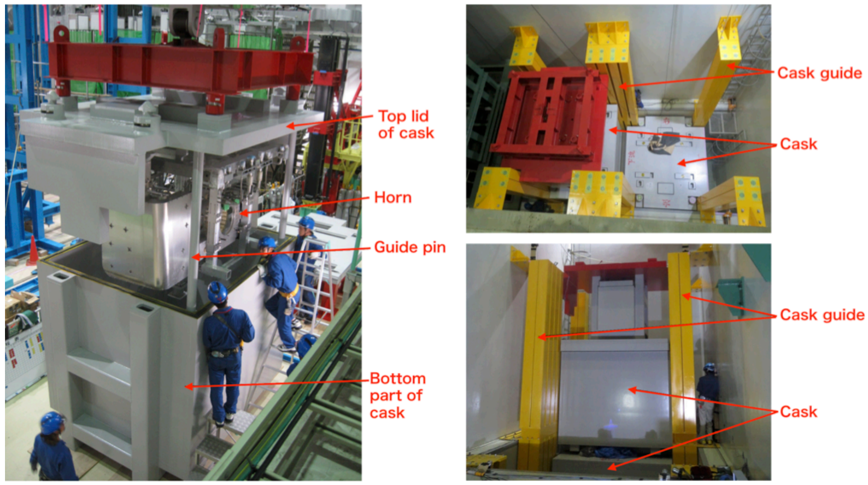

FIG. 34. Pictures of the cask for the horns taken during an insertion test of non-irradiated horn (left) and cask and cask guide placed in the storage area (right).

modules have many through-holes where the long shafts are inserted. For the horn attachment, 4 m-long stainless shafts that have M30 thread at the bottom end are adopted in the support module and corresponding M30 brace nuts are located at the horn side. By rotating the long shaft from the top of the support module, the connection of the horn to the support module is performed. For the connection of the water/helium pipes, commercial Swagelok connectors are used. The coaxial pipes penetrate the through-holes of the support module. The inner pipe is used as water/helium plumbing and the outer used as a rotation tool for the Swagelok connectors. The nut of the Swagelok connecter can be tightened/loosened by rotating the outer pipe from the top of the support module. Ceramic connectors are used for the connection of thermo-couples. The connectors are aligned by using guide pins and guide holes. Striplines are also detachable at the bottom of the support module. Figure 33 shows the remote stripline clamp system where the rotation of the long shaft changes torque to a horizontal force. It can clamp the stripline plates by 15 tons of force equivalent to 5 MPa contact pressure on the stripline surface. The relative alignment between the horn and the support module is achieved within 0.3 mm accuracy by a set of guide pins and guide hole/slit.

The detached irradiated horn is then transported to the storage area and stored inside a cask made of thick iron plates. A picture of the horn cask is shown in Fig. 34. The top lid of the horn cask can hang the horn by using twist-lock system which manually operated on the lid. The thickness of the lid is 30 cm to reduce radiation dose during the work. The horn hung by the top lid is moved to the storage area with remote operation of the crane. For the insertion to the cask,

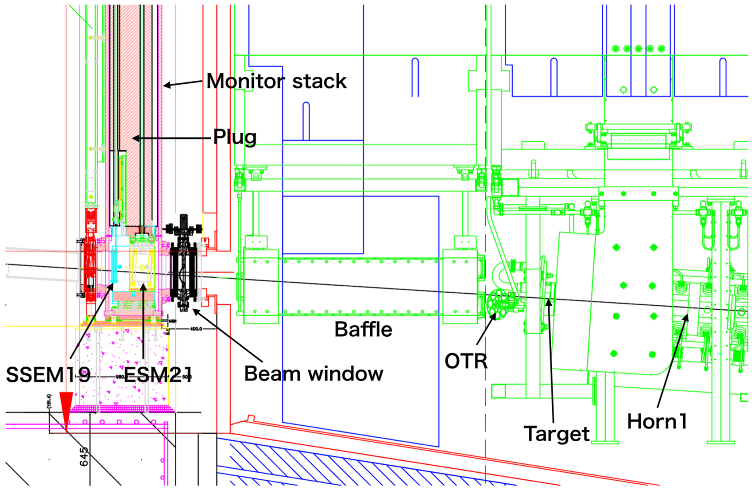

FIG. 35. Side view of the three proton beam monitors in the Target Station.

the top lid is guided by guide columns to ensure the alignment as shown in Fig. 34. Then a new horn is connected to the support module and transported to the helium vessel.

In the past, the first remote transportation of the irradiated horn was performed in 2011 for inspection of the horns after the Great East Japan Earthquake. There was a trouble occurred due to the perpendicularity and then the improvement described above was adopted. During the installation of the second-generation horns in JFY2013, remote exchange of all three horns has been conducted without any problem. The remote maintenance of the horns was established.

e. Beam monitors The three proton beam monitors, the beam profile monitor (SSEM19), the beam position monitor (ESM21), and OTR, are located in the Target Station, as shown in Fig. 35. SSEM19 and ESM21 are installed in the vacuum chamber (called monitor stack) set in the upstream side of the helium vessel. OTR is attached to the frame of the magnetic horn 1.

SSEM19 and ESM21 are attached to the bottom of the plug of the monitor stack and carried to the maintenance area with the plug. They are removed from the plug by manipulators there. The handling machine serves both for the plug and the beam window. The exchanger for SSEM19 and ESM21 is under development.

The OTR is carried to the maintenance area with horn1 and exchanged by manipulators there. OTR-I was removed by manipulators from the horn 1 at the replacement work of the horn in 2014. There is no experience in which we attached OTR to horn1 by manipulators.

f. Disposal scenario of the irradiated equipment Used devices replaced at the remote maintenance work are stored with their casket in the storage area of the Target Station. The area is the size of 5 m in width, 18 m in length, and 13 m in height. There are the magnetic horns with their

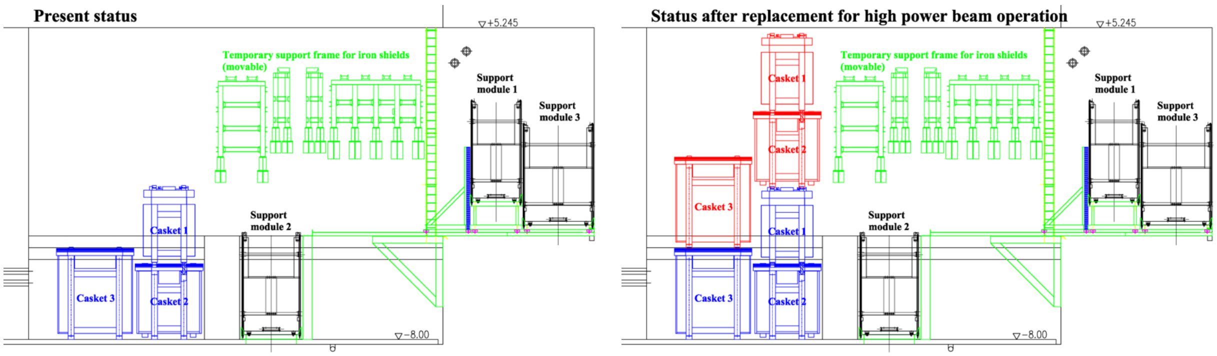

FIG. 36. Current (left) and future (right) layout of the storage area in side view. Currently three caskets are stored in the storage area as shown in blue. After the third-generation horns are installed, the old three horns are stored in the storage area as shown in red.

caskets at the upstream side and the other devices at the downstream side in the storage area. As shown in Fig. 34, the cask guide pillars to prevent the caskets from toppling over are installed in the storage area, and the caskets are piled up on the correct location along them (maximum 4 tiers). The storage area has the capacity containing 8 caskets for the horn1, 8 caskets for the horn2, or 6 caskets for the horn3. Figure 36 shows the present and future status of the storage area (side view). We replaced all three horns in JFY2013, and there are three caskets in this area. Figure 36 (right) shows the expected situation after horn replacement with third-generation is performed and the second-generation horns are stored in the storage area. There may be some space for one or two more caskets. If we need further space for more caskets, we have to carry the oldest caskets to outside of the Target Station. There is the building to store the radioactive devices from all facilities in J-PARC. Used targets and used magnetic horns are carried into the building and stored after several years storage in the Target Station.

9. *Other Upgrade Items*

a. Water cooling system Figure 37 shows the schematic diagram of the water cooling system in the secondary beamline. There are two water cooling systems in the Target Station. One is for the magnetic horns, the target cooling helium gas, and the baffle (called target-horn line). And another is for the helium vessel, the iron shields above the horns, the upstream part of the decay volume, and the collimator for the decay volume (called iron line). There is a water cooling system for the downstream part of the decay volume, the beam dump core, the iron shields in the beam dump, and the vessel for the beam dump in the neutrino utility building No.3 (called NU3). Every

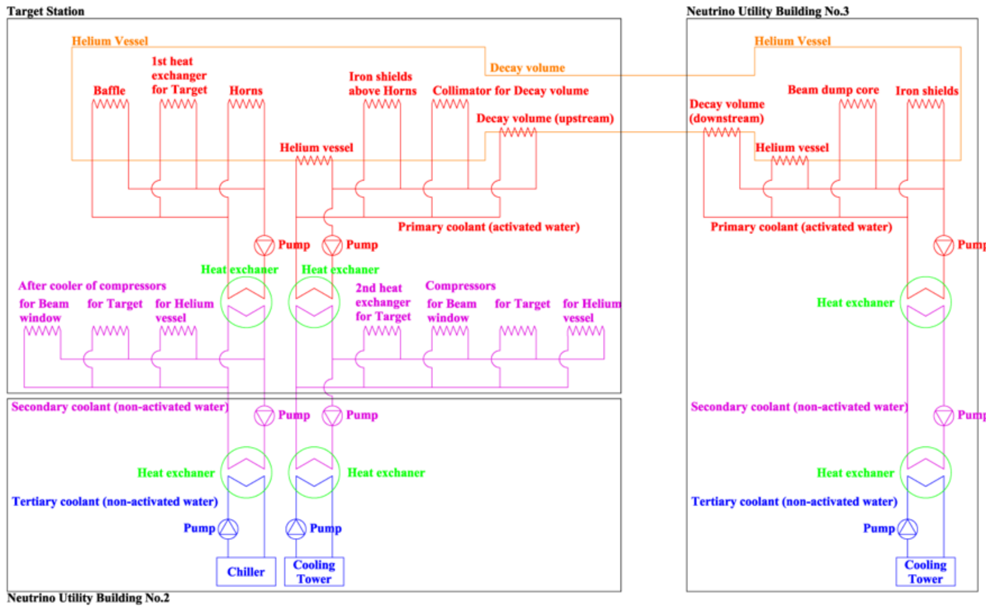

FIG. 37. Schematic diagram of the water cooling system in the secondary beamline.

system consists of three stages and the stages are coupled by the heat exchangers, so that the activated water does not mix into the tertiary coolant if one of the heat exchanger breaks. The circulation pumps and the heat exchangers are in the machine room, which is next to the beam line area (called service pit) separated by a concrete shield wall. The target-horn line, the iron line in the Target Station, and the iron line in the NU3 have each one set of the pump and heat exchanger.

The helium vessel, the decay volume, the collimator for the decay volume, the iron shields in the beam dump, and the vessel for the beam dump are cooled by cooling water through the iron channels called plate coils, as shown in Figs. 38, 39, and 40. The water cooling pipes made of the carbon steel are cast into the iron shields above the horns, as shown in Fig. 41. The beam dump core is made of graphite and cooled with the attached cooling modules. The cooling module is made of aluminum alloy, and the water cooling pipes made of the carbon steel are cast into the module. The plate coils and the cooling water pipes have several watercourses, and it is possible to change the watercourse by switching the valves. Several channels are connected in series at present to suppress the total flow rate, but it is designed in order to remove heat load at 4 MW beam operation by connecting in parallel. The present connection is for 750 kW beam operation. It is necessary to increase the total flow rate in parallel connection.

TC: Can this be done with just the switching valves? Is it enough for 1.3 MW operation?

Cooling water pipes in the beam line area are designed in order to accommodate 4 MW beam

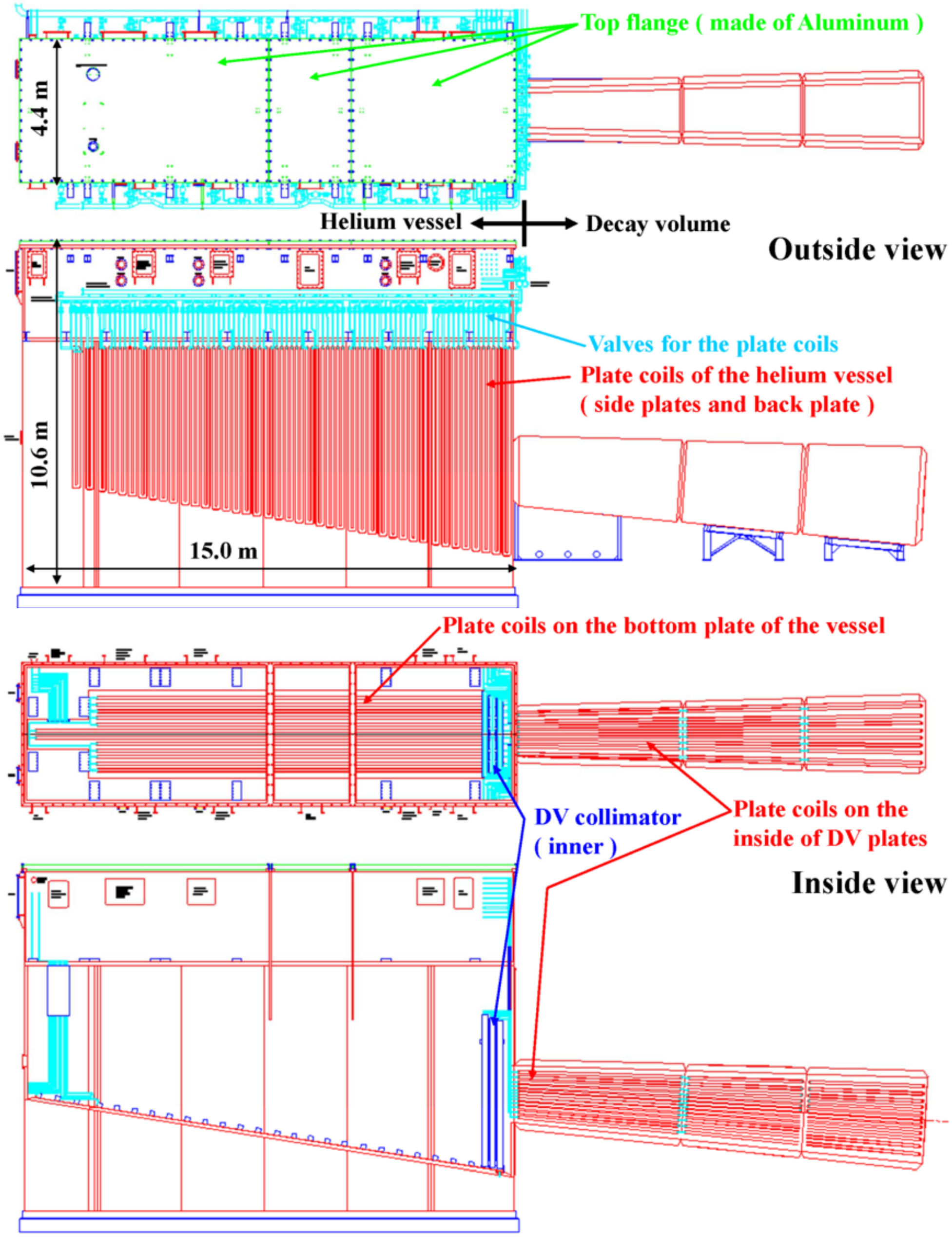

FIG. 38. Water cooling channels for the helium vessel and the Decay Volume.

operation, but pipes in the machine room are designed for 750 kW beam operation. The flow velocity of the cooling water in the pipes on the machine room side rises with increase of the total flow at the 1.3 MW beam operation, but it is not necessary to replace the pipes. It is required to replace the circulation pumps, the heat exchangers, chillers, and cooling towers to larger capacity ones, because they were designed based on 750 kW beam operation.

The capacity of the pumps and the heat exchanger in the primary coolant for the target and

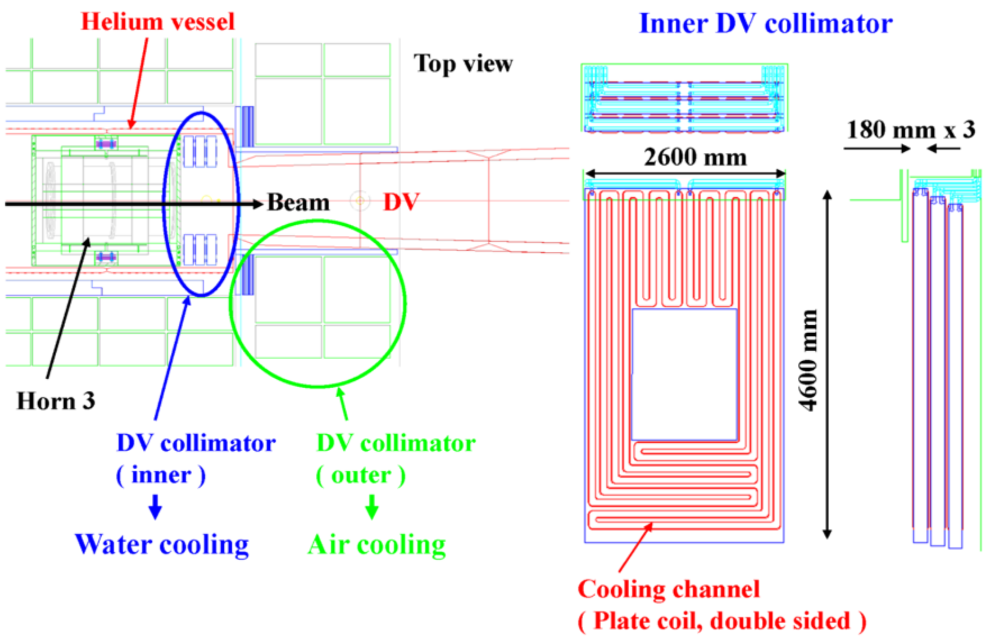

FIG. 39. Water cooling channels for the collimator for the Decay Volume.

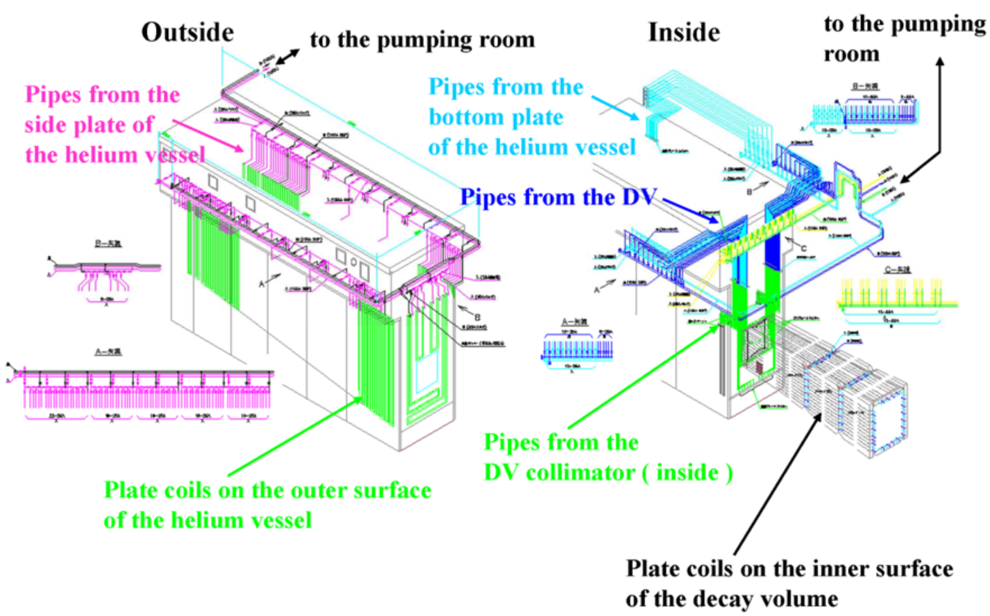

FIG. 40. Water cooling lines in the Target Station.

the horns is enough, but it is necessary to increase the heat removal in the secondary coolant by increasing flow rate or lowering the coolant temperature. It is possible to lower the temperature of the secondary coolant to 12 °C from the present operation temperature of 25 °C, because there is a margin to lower the temperature sufficiently. However, when lowering the temperature, it is necessary to install heat insulation for dew condensation prevention to the pipes. In case of

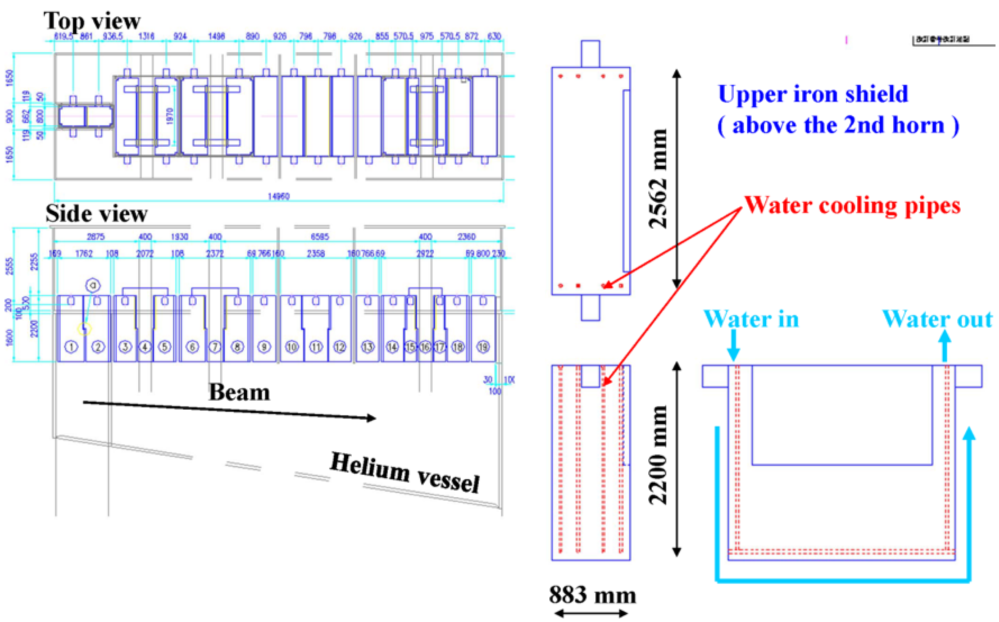

FIG. 41. Water cooling pipes for the iron shields above the magnetic horns.

TABLE XII. Measured maximum temperature rise (ν beam operation).

	Present (410 kW, ν)	Extrapolation (750 kW, ν)	Calculated value (750 kW, ν)
Helium vessel (side wall)	7.1 °C	13 °C	22 °C
Iron shields above horns	8.7 °C	16 °C	22 °C
Decay volume	7.3 °C	13 °C	34 °C
DV collimator	11.0 °C	20 °C	38 °C
Beam dump core	36.9 °C	68 °C	-
Vessel for BD core	7.5 °C	14 °C	-
Iron shields behind BD	20.1 °C	37 °C	-

increasing the flow rate of the secondary coolant, it is necessary to replace the pump to a larger capacity one.

TC: When can the upgrades be made?

Tables XII and XIII show measured maximum temperature rises of iron line devices at 410 kW neutrino beam and 450 kW antineutrino beam operations with calculated values, respectively. The calculated value is by ANSYS heat simulation, supposing heat transfer coefficients on the plate coils and pipes and inputting heat loads calculated using a 2-dimensional mode by MARS simulation. Figure 42 shows a sample of ANSYS heat simulation (for helium vessel). The input heat transfer coefficient is conservative in this simulation. The temperatures of iron line devices are

TABLE XIII. Measured maximum temperature rise (anti-ν beam operation).

	Present (450 kW, anti-ν)	Extrapolation (750 kW, anti-ν)	Calculated value (750 kW, ν)
Helium vessel (side wall)	7.8 °C	13 °C	22 °C
Iron shields above horns	7.5 °C	12 °C	22 °C
Decay volume	11.9 °C	20 °C	34 °C
DV collimator	13.3 °C	22 °C	38 °C
Bema dump core	20.5 °C	34 °C	-
Vessel for BD core	6.0 °C	10 °C	-
Iron shiedls behind BD	18.0 °C	30 °C	-

TABLE XIV. Measured heat removals (ν beam operation).

	Present (410 kW, ν)	Extrapolation (750 kW, ν)	Calculated value (750 kW, ν)
Helium vessel	40 kW	73 kW	158 kW
Iron shields	11 kW	20 kW	29 kW
Decay volume	42 kW	77 kW	85 kW
DV collimator	40 kW	73 kW	105 kW
TS Total	133 kW	243 kW	377 kW
NU3 Total	129 kW	236 kW	332 kW

kept below 60 degree (temperature rises are kept below 30 degree). This condition is important in particular of the side wall of the helium vessel, because the side wall supports the magnetic horns. When the temperature of all parts of the side wall rises 30 degree, the position of the magnetic horn becomes 1mm higher.

Tables XIV and XV show heat removals of iron line devices at 410 kW neutrino beam and at 450 kW anti-neutrino beam operation with design values, respectively. Measured values are calculated from measured values of temperature rises and flow rates of the coolant. Design values were determined by heat loads from 2D-Mars simulation. Heat load is higher at anti-neutrino beam operation than at neutrino one in the Target Station, on the other hand, it is higher at neutrino beam operation in the NU3. The measured total heat removal in the Target Station at 450 kW anti-neutrino beam operation is 179 kW, and it becomes 289 kW when it is extrapolated at 750 kW. It is 77% of the design value 377 kW. When extrapolating using this factor, the cooling system becomes effective up to a beam power of 980 kW. The measured total heat removal in NU3

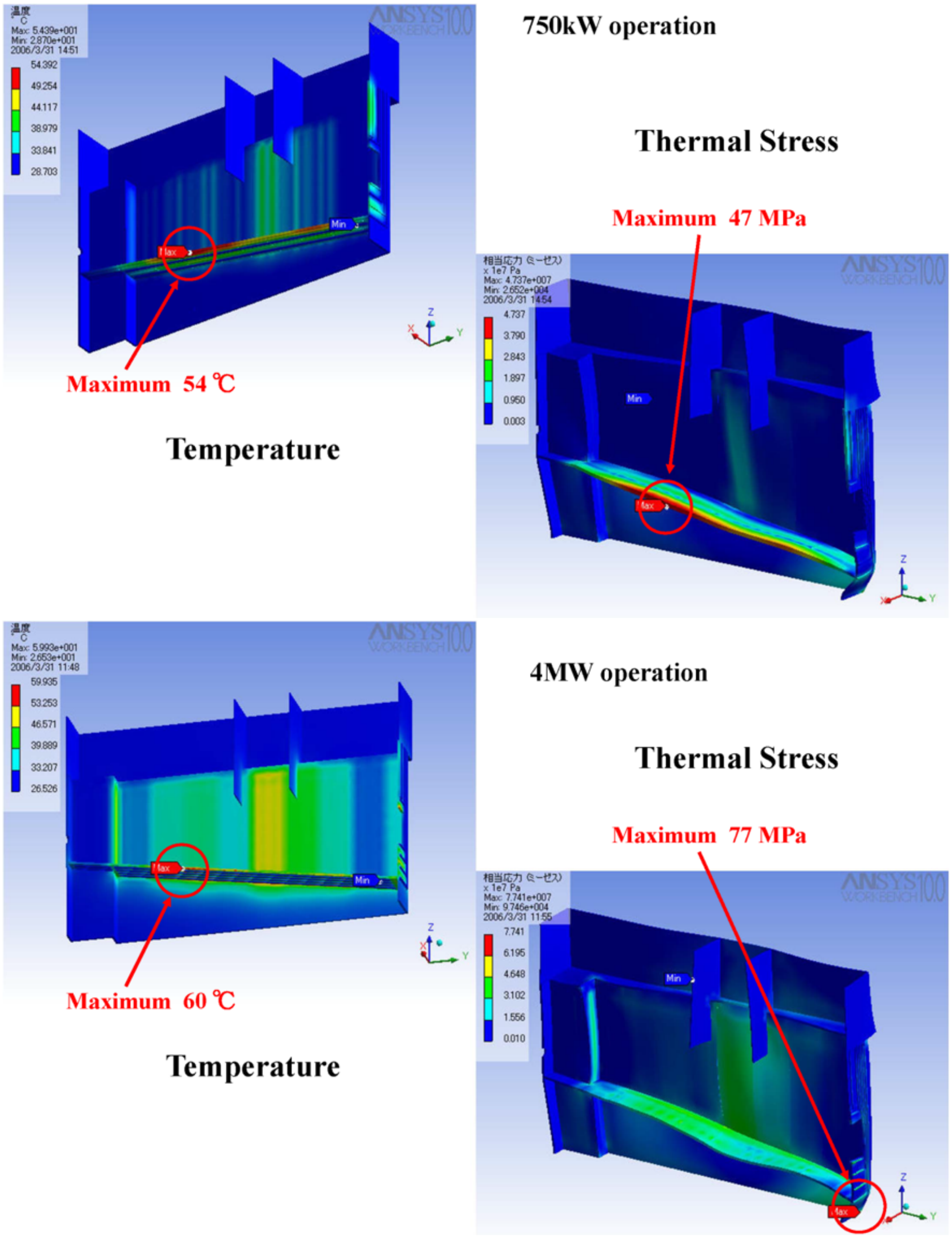

FIG. 42. A sample of ANSYS heat simulation (for helium vessel).

at 410 kW neutrino beam operation is 129 kW, and it becomes 236 kW when it is extrapolated to 750 kW operation. It is 71% of the design value, 332 kW. When extrapolating using this factor, the cooling system becomes effective to a beam power of 1060 kW.

TC: How will operation at 1.3 MW be achieved?

The oxygen density of the cooling water is suppressed to avoid the formation of rust in the pipes using a deoxidation device with deaeration films, because the material of pipes is carbon steel in

TABLE XV. Measured heat removals (anti-ν beam operation).

	Present (450 kW, anti-ν)	Extrapolation (750 kW, anti-ν)	Calculated value (750 kW, ν)
Helium vessel (side wall)	54 kW	90 kW	158 kW
Iron shields	19 kW	32 kW	29 kW
Decay volume	52 kW	87 kW	85 kW
DV collimator	55 kW	92 kW	105 kW
TS Total	179 kW	289 kW	377 kW
NU3 Total	101 kW	168 kW	332 kW

iron line. The deoxidation devicess are installed in the Target Station and NU3. Because the black layer of steel inside the pipes is left intentionally in order to prevent making rust, the deaeration films are filled with the black powder from the black layer. Therefore the deoxidation devices has filters, but it is necessary to exchange the filters periodically. It is also necessary to exchange the deaeration films periodically. The amount of the black powder which collects on the deoxidation device increases according to the beam power according to measurements, so when operating at beam power beyond the current state, it is necessary to add the deoxidation devices and the filters.

In summary, except the deoxidation devices, the present water cooling system of the secondary beam line is capable up to 750kW beam operation, but it is necessary to do the following upgrade in case of the operation beyond 750 kW.

- Lowering the secondary coolant temperature in the target-horn line
- Replacement of the circulation pumps and the heat exchangers to larger capacity ones in the iron line
- Adding chillers and cooling towers in the iron line

For the deoxidation devices, it is necessary to add the deoxidation devices and the filters as soon as possible.

TC: Are all of these upgrades sufficient to achieve 1.3 MW operation?

b. Radiation shielding Figure 43 shows the cross section of the Target Station. The iron shields surround the helium vessel in which the target and the magnetic horns are installed, and the concrete shields surround the iron shields. At the side and bottom part, concrete serves both as a shield and a skeleton structure of the Target Station building and iron shields are fixed to the building. At the upper part, all the shields are movable. There are 19 iron shield blocks and 10

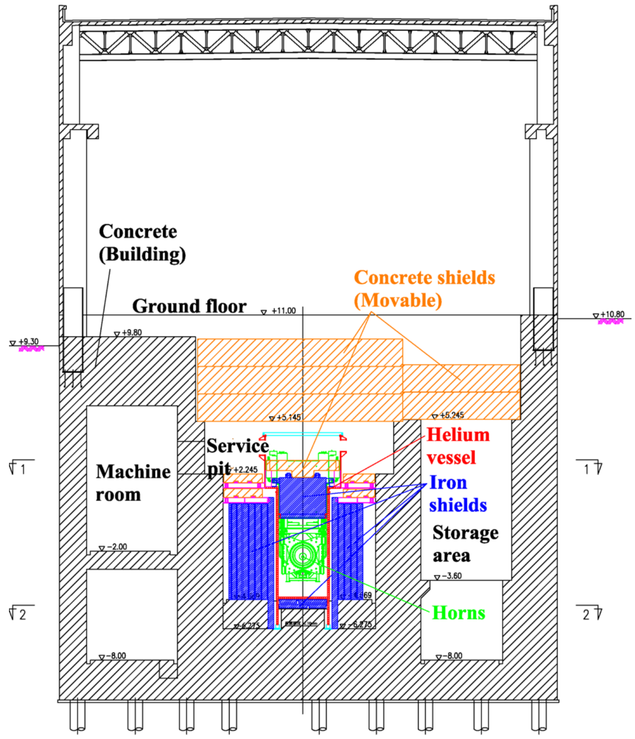

FIG. 43. Cross section of the Target Station.

TABLE XVI. Thickness of shields.

	Iron shields	Concrete shields
Top (outside helium vessel)	-	4,500 mm Movable
Top (inside helium vessel)	2,250 mm Movable	940 mm Movable
Side (machine room side)	2,200 mm	4,000 mm
Side (storage area side)	1,600 mm	5,000 mm
Bottom	500 mm	4,770∼7,190 mm

concrete shield blocks inside the helium vessel, and 147 concrete shield blocks above the helium vessel. Table XVI shows total thickness of shields.

The radiation level has to be below the legal limit of the off-limits area (< 25 μSv/h) for a person to be able to enter the ground floor of the Target Station even during beam operation. The thickness of the upper shield was determined by calculation as the maximum radiation level on the ground floor is below the half of the legal limit (12.5 μSv/h) at 750 kW beam operation. The thicknesses of the side shield and the bottom shield were determined by calculation as the maximum radiation level is below 5 mSv/h at the boundary with soil. Cord MCNP was used for

TABLE XVII. Measured radiation level on the ground floor of the Target Station.

	Present (460 kW)	Extrapolation (750 kW)	Extrapolation (1.3 MW)
Neutrino operation			
γ	0.7 μSv/h	1.1 μSv/h	2.0 μSv/h
neutron	1.3 μSv/h	2.1 μSv/h	3.7 μSv/h
total	2.0 μSv/h	3.3 μSv/h	5.7 μSv/h
Anti-neutrino operation			
γ	0.7 μSv/h	1.1 μSv/h	2.0 μSv/h
neutron	1.2 μSv/h	2.0 μSv/h	3.4 μSv/h
total	1.9 μSv/h	3.1 μSv/h	5.4 μSv/h

calculation.

Table XVII shows the measured radiation level on the ground floor (above the beam line) of the Target Station at 460 kW beam operation and the extrapolation values (750 kW and 1.3 MW).

The extrapolation value indicates that the radiation level is below the specified value (12.5 μSv/h) even at 1.3 MW beam operation, in other words that it is not necessary to add more shields. However, we have to determine whether we add more shields based on the calculation, because the application to Nuclear Regulation Agency is based on calculation. So we have to redo radiation calculation at 1.3 MW beam operation.

c. Radioactive water disposal Radioisotopes originated from cooling water are mainly created by neutrons hitting oxygen atoms in the water. In the cooling water, some other materials, like iron from steel pipes and aluminum from the magnetic horns, are resolved in water. Radioisotopes are also produced from breaks of those metals. Among them, all radioisotopes except ^{3}H can be removed by ion-exchangers.

Table XVIII summarizes the information on the water circulation system in the secondary beamline and the expected amount of ^{3}H production for future high power beam operation. ^{3}H accumulated in the neutrino beam line are disposed by two methods. One is the drainage of the radioactive water, and the other is disposal using tank truck. For drainage, radioactive water are moved to disposal tanks and are diluted by industrial water. The effective volume of the NU2 and NU3 disposal tank are 84 m^{3} and 17 m^{3} respectively. From a regulation, concentration of ^{3}H in the disposal water must be less than 60 Bq/cc. Because of the safety reason, the radiation safety section requires that the concentration should not exceed 42 Bq/cc. Accordingly, total ^{3}H disposed from NU2 and NU3 disposal tank in one drainage cycle are 3.53 GBq and 0.72 GBq, respectively.

TABLE XVIII. Cooling water system in the neutrino beamline. Name of the system, volume of cooling water, objects for cooling, drainage system for cooling water are listed. Total ^{3}H produced by 750 kW $\times$ 10^7 seconds and by 1.3 MW $\times$ 10^7 seconds are also shown.

Cooling system	Total volume of water (m^3)	Objects for cooling	drainage	Total ^{3}H (GBq) 750 kW x 10^7s	Total ^{3}H (GBq) 1.3 MW x 10^7s
Horn	2.7	3 magnetic horns	NU2	126	218
TS32 °C	7.8	Helium vessel	NU2	150	260
		decay volume (upstream)			
NU3-32 °C	10.0	decay volume (downstream)	NU3	60	104
		beam dump			

At present, one cycle of drainage from the disposal tank takes every three business days. This schedule is arranged from following constraints;

- Local government request that the drainage should be done in business day morning
- Overnight operation is needed to measure the concentration of ^{3}H
- One business day is needed for paper work related to permission of drainage

The back-end section of JAEA provides a service to take over radioactive water by a tank truck. The takeover by the tank truck in NU3 started, successfully. This can also be done in NU2 after a change of the water circuit. In one-day tank truck service, about 10 GBq of ^{3}H can be taken over. The maximum frequency of the tank truck service is once every month, or 10 times per year. If the present agreement between the neutrino group and JAEA is considered, radioactive water containing 100 GBq can be taken out by the tank truck service.

The procedure of the radioactive water drainage is schematically shown in Fig. 44. During beam operation, cooling water in the Target Station building become highly radio-activated. Nominal contaminations of ^{3}H are $\sim$6000 Bq/cc for horn cooling water and $\sim$2500 Bq/cc for TS32 cooling water after 470 kW$\times$1 month beam operation. An access to the cooling water system is done during periodical maintenance period. Fresh water is supplied to the system, and radioactive water is sent to the buffer tank which is placed in NU2. The effective volume of the buffer tank is 18.2 m^3. After the replacement dilution, beam operation can be resumed.

TC: It is not clear what the "replacement dilution" means. Does this mean the dilution processes must be completed before the operation can be resumed?

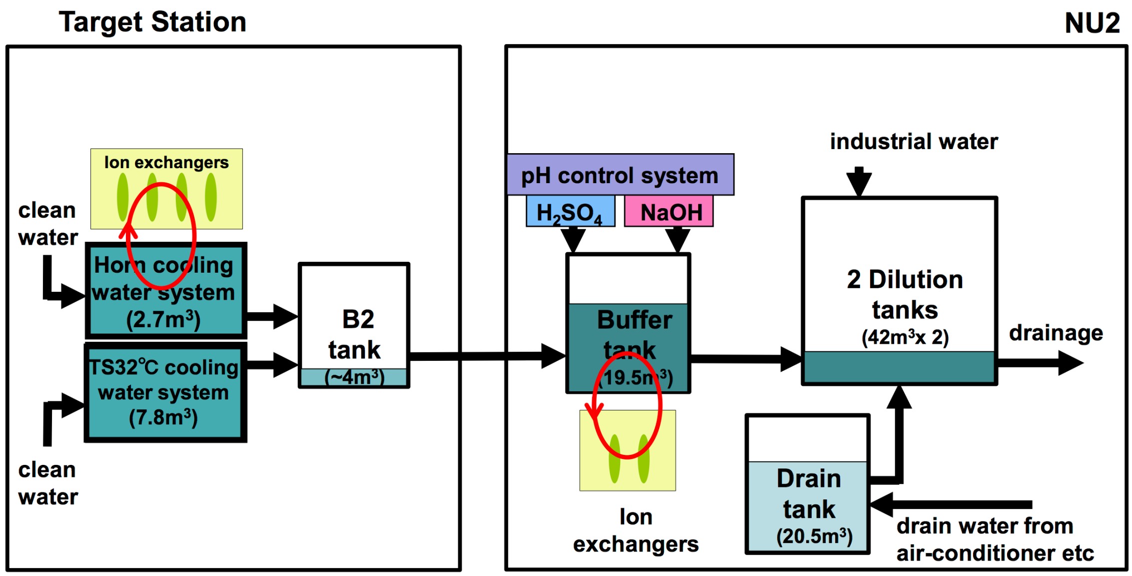

FIG. 44. Schematic view of the drainage for horn and TS32 °C radioactive water.

The NU2 building is not an off-limit area even during the beam period. First, radioactivities except ^{3}H are removed by the ion-exchangers. It is known that radioactivities can be removed effectively for acidic water. Sulfuric acid and sodium hydroxide are occasionally used for pH control. After radioactivities except ^{3}H are removed, the dilution/disposal process starts. In the usual case, the ^{3}H concentration of radioactive water in the buffer tank exceeds 1000 Bq/cc. Drainage of radioactive water is permitted if the ^{3}H concentration is less than 42 Bq/cc. A small volume (a few m^3) of radioactive water is sent to the dilution tank, where industrial water is added, and the radioactive water is diluted to be less than 42 Bq/cc. After the measurement of the radioactivities and paper works, the water is disposed. It takes 3 business days for one cycle of the drainage. By $\sim$10 times of the dilution/drainage procedure, radioactive water in the buffer tank can be completely disposed. It will take more than one month.

In 1.3 MW$\times 10^7$ second operation, 104 GBq of ^{3}H are produced in the NU3 building. Most of them can be disposed by the tank truck. However, the tank truck quota for the neutrino facility is almost full for the NU3, and no quota is left for NU2. In NU2, 478 GBq of ^{3}H must be disposed. It corresponds to 135 times of dilution/drainage. Because the quota of tank truck disposal will be fully used by NU3, the ^{3}H from NU2 must be disposed by the dilution/drainage from the disposal tank. For upgrade beyond 1.3 MW beam, larger disposal tanks are certainly necessary. Construction of $\sim$400 m^3 disposal tank was proposed and the budget request was submitted to

KEK. Based on the MR upgrade schedule the construction of the new disposal tank should be completed before starting high repetition rate operation (1.3 s) with the upgraded MR magnet power supplies from JFY2022.

TC: For the upgraded system, what is the dillution and disposal time for one month of 1.3 MW operation?

D. Hadron Production Measurements

The high energy neutrino flux passing through the Hyper-K detector will primarily be produced at J-PARC neutrino beam facility and by cosmic rays in the atmosphere. These neutrinos are produced in decays of hadrons and muons. Since the neutrino flux cannot be easily directly measured, we rely on Monte Carlo models to predict production of hadrons and therefore predict the neutrino flux. Different models predict significantly different fluxes. In the case of T2K, hadron production measurements were performed in the NA61/SHINE [**?**] experiment at CERN to resolve this issue. The NA61/SHINE data [**? ? ? ?**] have been successfully used to re-weight Monte Carlo predictions and the more detailed explanation can be found in Ref. [**?**]. Generally, there are two types of hadron production measurements: measurements with a thin nuclear target (a couple of percent of interaction length) and measurements with a replica target. The thin target measurements are used to constrain interaction probability and hadron production in interactions of a single hadron species at desired momentum with a chosen material. An example of such measurements is NA61/SHINE proton-carbon measurements at 31 GeV/c (see Ref. [**?**]). On the other hand, the replica target measurements include all interactions in the target and give the total number of hadrons emitted from the replica target surface per protons on target. A combination of both approaches needs to be used to constrain the Hyper-K neutrino flux.

We can infer which additional hadron production measurements need to be done for Hyper-K from the current limitations of the T2K experiment. The NA61/SHINE hadron production measurements reduced the T2K hadron production uncertainty from $> 20\%$ to around 5% (see figure 45). Currently, there are three factors limiting the precision of hadron production uncertainty in T2K:

1. uncertainty of the replica target measurements,

2. difference in fluxes estimated with the thin and the replica target data, and

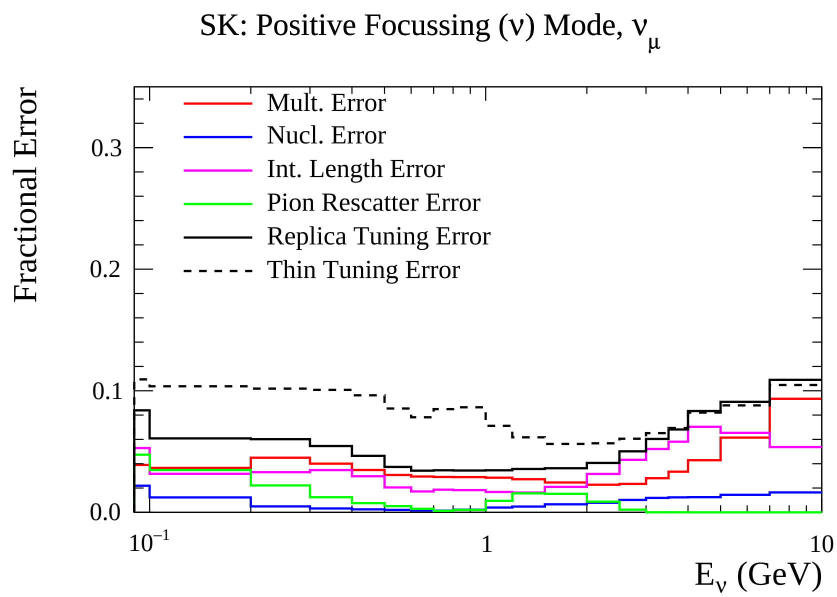

FIG. 45. Hadron production uncertainty of the neutrino flux at SK in neutrino mode [?]. The solid black line shows the total uncertainty after using the NA61/SHINE replica target data. The dashed black line shows the same uncertainty after using only the NA61/SHINE thin target data. At higher energies, neutrino flux is produced by kaon decays, and the replica target measurement of kaon yields have not yet been implemented yet. After implementation of the kaon data, a similar value of 5% is expected at high neutrino energies.

3. low momentum pion and kaon reinteractions outside the target for which hadron production data does not exist.

The three limiting factors can be addressed by performing additional measurements in NA61/SHINE and EMPHATIC experiments.

NA61/SHINE Experiment

NA61/SHINE is a hadron spectrometer which consists of four large TPC chambers, four small TPC chambers in the forward region and a forward time-of-flight wall. Two of the large TPCs are located in the magnetic field of the superconducting magnet. The measured momentum resolution is typically better than 1%. Particle identification is achieved with energy loss and time-of-flight measurements. The NA61/SHINE experiment provides replica target data in bins of outgoing hadron momentum, polar angle and longitudinal position of the exit point on the target surface. The most recent NA61/SHINE replica target measurements [?] quote the total uncertainty of the pion yields at around 4% in the majority of the bins. As seen in the figure 46, systematic

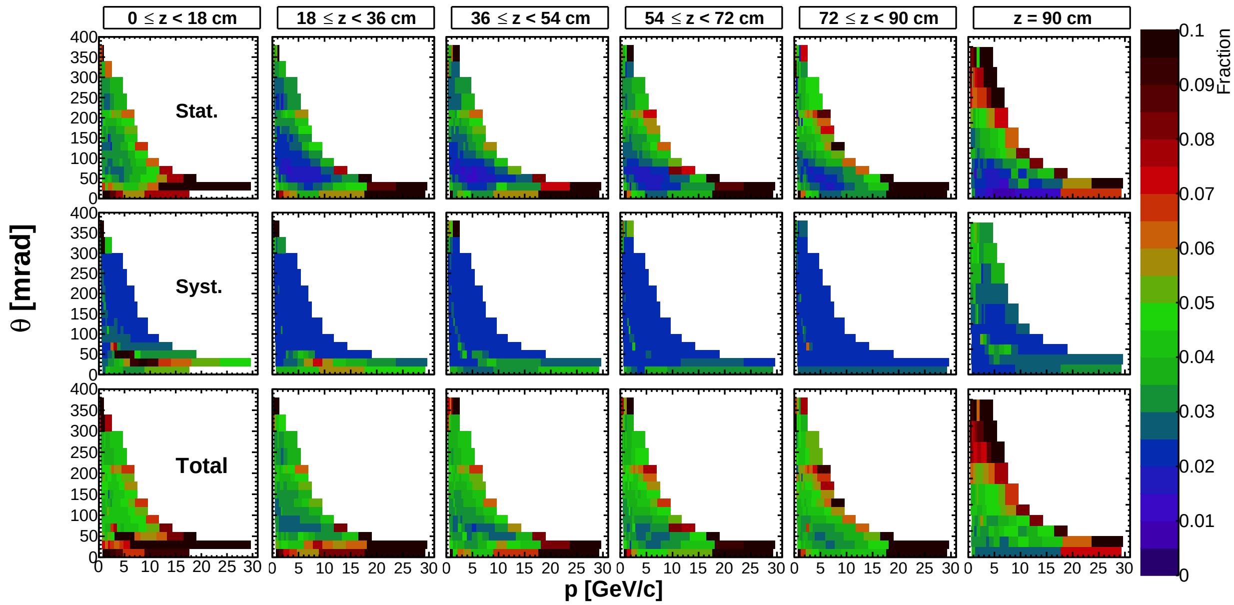

FIG. 46. The uncertainty of the NA61/SHINE π^+ yields coming from the replica target surface. The first row shows statistical uncertainty, the second row shows systematic uncertainty and the third is the total uncertainty. Each column presents different longitudinal bin, while each panel shows the uncertainty as a function of the momentum and polar angle. Similar figures for π^-, $K^\pm$ and p can be found in Ref. [?].

and statistical uncertainties are similar in size in regions from 50 mrad to 200 mrad which mostly contribute to the neutrino flux. The dominant systematic contribution in these bins is caused by uncertainty in the reconstruction algorithm and calibration of the TPCs. In the most upstream longitudinal bin and the downstream target face, the total uncertainty is limited by systematics. Possible biases in track extrapolation from the TPCs to the surface of the replica target cause this error.

Three steps are identified towards the improvement of the replica target measurements for Hyper-K:

1. Better understanding of the NA61/SHINE detector and track reconstruction,

2. Development of the detector system which measures track position close to the target surface and improvement of the detector forward acceptance,

3. Increase in the statistics.

The first point requires improved simulation of the NA61/SHINE detector which is already developed and in use. The reconstruction uncertainty is conservatively assigned to be 2% in all measured bins, and by doing careful studies of the efficiency of the reconstruction algorithm, it can be significantly improved. The second point requires the installation of the tracking planes around the replica target to reduce track extrapolation systematic uncertainty. The possible technology is still under discussion. The forward acceptance has already been improved by installing a set of additional forward TPCs in 2017. These can measure the surviving beam proton without additionally increasing the magnetic field and losing low momentum particles below 5 GeV/c. In the latest replica target measurements, the total number of protons on target after the selection was around 6.5×10^6. A Hyper-K study is needed to determine the number of bins necessary in the future measurements and the corresponding required statistics.

Improvements described above are necessary conditions for the future measurements. However, two additional improvements are possible. The Hyper-K collaboration can provide complete replica target. The equivalent for T2K would be to take measurements with the target including titanium casing and cooling lines instead of just with the graphite core. The feasibility of this approach will be known after the design of the new target is completed. A second possible improvement is related to the dependence of the measured replica hadron yields on the beam profile. If the narrow beam is used in the replica target measurement, hadron yields coming from the upstream part of the target are suppressed. It is a consequence of interactions vertexes being further away from the target surface, and therefore hadrons cannot exit the target in the upstream longitudinal bins. The suppression also depends on the polar angle of the produced hadrons. If one assumes that this is a purely geometrical effect, data and Monte Carlo ratios used in the re-weighting procedure would be independent of the beam profile, provided that Monte Carlo simulation uses the same beam profile (see Ref. [**?**]). From Monte Carlo studies in T2K we know that if the beam profile in the data changes, the flux varies within 1%. NA61/SHINE attempted to get the same beam properties as the J-PARC proton beam in the previous replica target measurements. The J-PARC beam profile changes with time and NA61/SHINE uses secondary beam which removes any possibility of a complete match between the two beam profiles. Instead, the replica target measurements can be done with a wide beam profile. The beam profile can be binned in radial bins, and hadron yields from the replica target surface can be measured for each beam radial bin separately. A linear combination of the hadron yields for all beam bins would give better agreement with the J-PARC beam at any given moment. However such measurement would introduce more complexity in already complex replica target data analysis, and the required statistics would be much larger. Additionally, improved tracking of the beam before it hits the replica target is necessary.

If the Hyper-K target material changes, NA61/SHINE can also perform additional thin target measurements. Currently, thin target measurements are necessary to constrain out-of-target interactions, mainly pion and kaon interactions in the aluminum. The NA61/SHINE beam is not capable of going below 13 GeV/c per nucleon. An upgrade of the beamline is only possible during Long Shutdown 3 (LS3), and it would be expensive. For this purpose, a tabletop experiment called EMPHATIC is designed to be complementary to NA61/SHINE.

TC: Are there any measurements in the > 13 GeV/c range that should be made by NA61 for out-of-target interaction tuning, or should these be made by EMPHATIC?

EMPHATIC Experiment

The Experiment for Measurement of Production of Hadrons At a Testbeam In Chicagoland (EMPHATIC) is a future tabletop hadron production experiment designed to measure cross-sections and hadron yields for the variety of beams (p, $\pi^{\pm}$, $K^{\pm}$) and targets (C, Al, Fe). The experiment will use silicon strip detectors for tracking, gas and aerogel Cherenkov detectors for beam particle identification and an aerogel ring imaging Cherenkov (ARICH) detector for the identification of the produced particles. The Testbeam Facility in Fermilab can provide secondary beams from 2 GeV/c to 120 GeV/c. This is ideal for measuring $\pi^{\pm}$+C interactions at low momenta. The aim of EMPHATIC is to reduce the flux uncertainty coming from untuned interactions both in J-PARC and NuMI beams. First hadron production measurements will be done in 2019 and continued in 2020. However, the first beam test was already done in January 2018. The setup included silicon strip detectors and the scattering angle of the incoming protons on carbon, steel, aluminum and empty targets was measured. These measurements can be used to estimate the cross-section and compare the results with NA61/SHINE measurements. The crosscheck is of the NA61/SHINE cross-section result is needed because Monte Carlo re-weighted with the thin target measurements cannot reproduce replica target results. In fact, replica target results prefer about 5σ lower p+C production cross-section. The neutrino flux after re-weighting with the replica target data becomes lower, as it can be seen in Fig. [**?**]. Future EMPHATIC measurements include measurements of the beam survival probability with various target lengths to study differences in interaction probability. This discrepancy should be resolved before Hyper-K.

Although EMPHATIC is designed to be complementary to NA61/SHINE, one of the EMPHATIC goals is related to the atmospheric neutrino physics. Atmospheric neutrinos in the sub-GeV sample are sensitive to CP violation phase (δ_{CP}). The size of the effect is a couple of percents and the measurement is limited by the hadron production uncertainty at low energies. For this

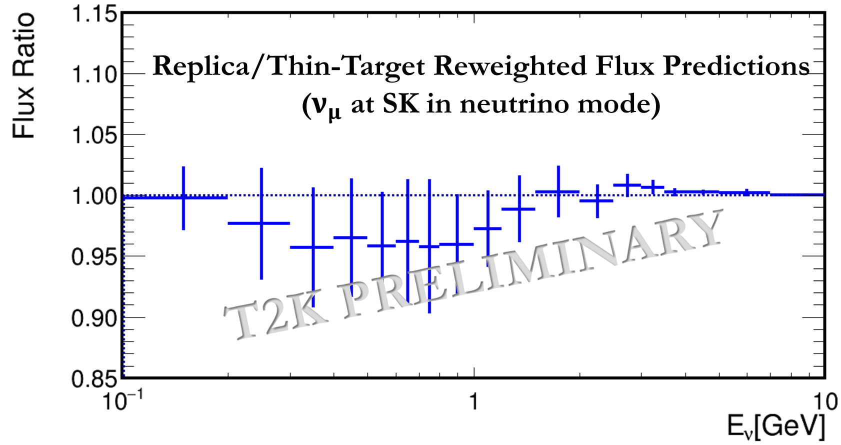

FIG. 47. Ratio of the T2K neutrino flux re-weighted with the NA61/SHINE replica target measurements and the flux re-wighted with the NA61/SHINE thin target measurements [**?**].

purpose, measurements with boron, boron nitride, and boron oxide target will be performed. Boron can be subtracted to get hadron production measurements in air. Such measurements will be used to reduce systematics related to the atmospheric neutrino flux in Hyper-K.

II.2. NEAR DETECTORS AT THE 280 M COMPLEX

For the case of all existing detectors, a description of the human resource requirements for operation should be given, and the plan for handover of the detector operation from T2K to Hyper-K should be described.

A. The INGRID On-axis Detector

The INGRID (Interactive Neutrino GRID) is the T2K on-axis near detector located 280 m downstream of the production target [**?**]. The main purpose of INGRID is to measure the neutrino beam direction with a precision better than 1 mrad and monitor the neutrino event rate. The spatial width (1σ) of the neutrino beam at 280 m from the target is about 5 m. In order to sufficiently cover the neutrino beam profile, INGRID is designed to sample the beam in a transverse section of 10 m $\times$ 10 m, with 14 identical modules arranged in two identical groups along the horizontal and vertical axes, as shown in Fig. 48. Each of the modules consists of nine iron target plates and eleven tracking scintillator planes, as shown in Fig. 49. They are surrounded by veto scintillator planes to reject charged particles coming from outside of the modules. The dimensions of each iron target plate are $124{\times}124\text{cm}^2$ in the horizontal and vertical directions and 6.5 cm along the beam direction. The total iron mass serving as a neutrino interaction target is 7.1 tons per module. Each tracking scintillator plane consists of two scintillator layers. Each layer has 24 scintillator strips, making a plane of $120{\times}120\text{cm}^2$ in the horizontal and vertical directions and 1.0 cm along the beam direction. One layer is placed perpendicular to the other layer in a tracking scintillator plane so that it is sensitive to both horizontal and vertical positions. The veto scintillator plane consists of one scintillator layer which is made up of 22 scintillator strips segmented along the beam direction, in order to identify the incoming charged particles produced by neutrino interactions outside of the modules. Scintillation light is collected and transported to a photodetector with a wavelength shifting fiber (WLS fiber) which is inserted in a hole at the center of the cross section of the scintillator strip. The light is read out by a Multi-Pixel Photon Counter (MPPC) attached to one end of the WLS fiber.

TC: Can a description of the readout electronics and power systems be added? Do the electronics require active cooling? What is the failure rate for these systems?

TC: Are the veto layers sufficient, or is there any need for improvement?

INGRID identifies neutrino events by detecting muon tracks from ν_μ or $\bar{\nu}_\mu$ charged-current

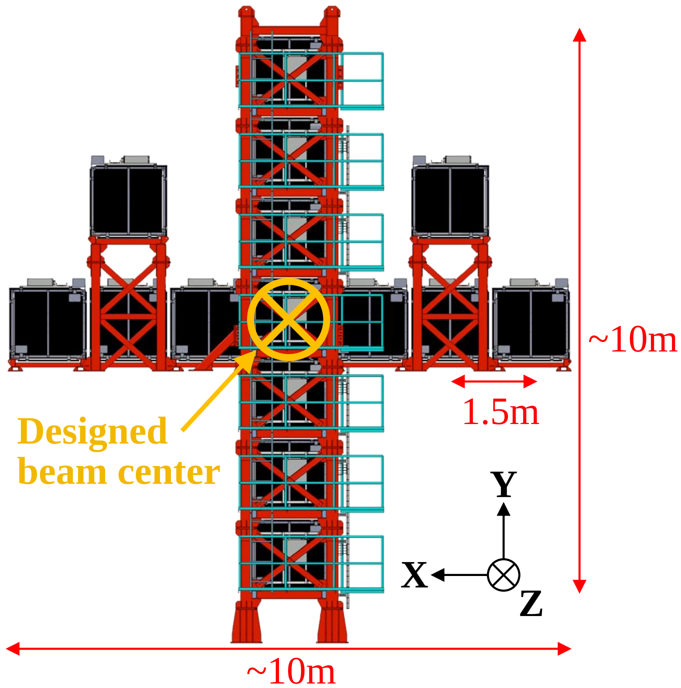

FIG. 48. Front view of the INGRID detector.

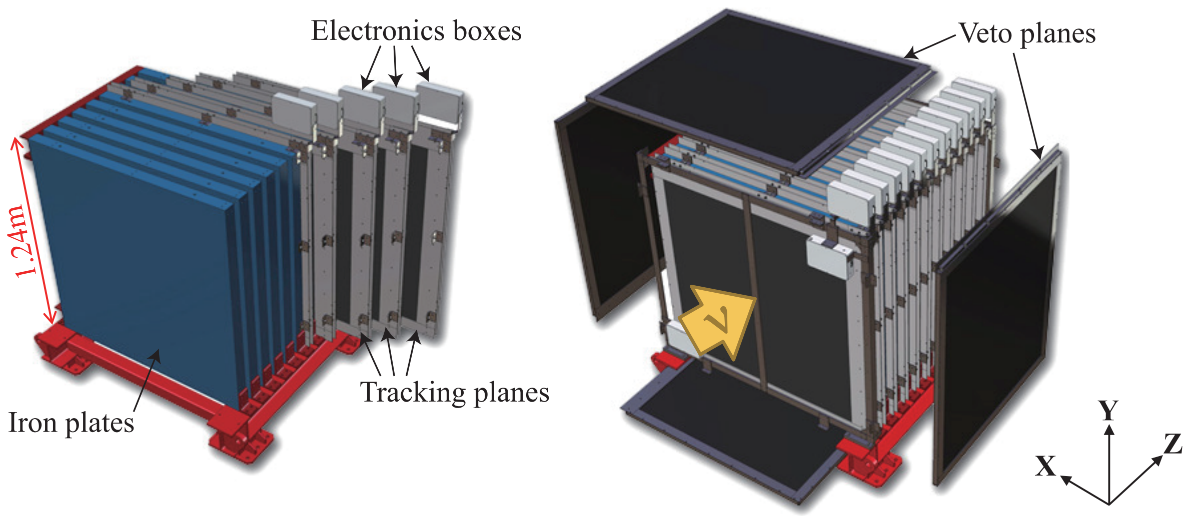

FIG. 49. Exploded view of an INGRID module.

interactions on the iron target. The neutrino event rate is calculated from the total number of the neutrino events divided by POT. The neutrino beam profile is reconstructed from the number of the neutrino events at each module. The neutrino beam direction is calculated from the reconstructed beam center position in the INGRID location.

TC: I edited out the beam direction measurement plots as that can be covered in the near detector

CDR.

The current systematic errors are 1% on the number of selected events and 0.1-0.2 mrad on the measured neutrino beam direction. Thus, INGRID operates with better accuracy than the original requirement of 1 mrad. However, issues of the scintillator aging and the dead channels appeared during the long-term operation. The scintillator light yield decreased by 13% in nine years. The number of dead channel increased from 11 to 68 out of 8360 channels in nine years. The effect of these issues on the INGRID beam measurement is not significant for now. Even if these issue become more significant in the future, the effect can be corrected in the analysis. Thus, it is currently not expected that special upgrades of INGRID for Hyper-K are needed and need.

TC: Can time dependent plots of the light yield reduction and dead channel accumulation be added? Are there any advantages of adding new more sensitive and better performing SiPMs to counteract the light reduction?

TC: Can you add an estimate of the human resources that are necessary to keep the detector running? Are any of the INGRID T2K groups willing to commit to keeping the detector operating for Hyper-K?

B. The ND280 Off-axis Detector

The ND280 off-axis detector was constructed in 2009 for the T2K experiment. The original detector consists of five subdetectors described in Section II.2 C. Several aspects of the original ND280 detector are planned to be replaced and ready to receive data in 2021 by the T2K experiment. This upgrade will be described in section II.2 D. An extensive beam test programme took place at CERN during summer 2018.

The aims of the original and upgraded ND280 detector remain the same. Its purpose is to measure neutrino flux and interaction rates before oscillations, with measurements of final state particle kinematics and reconstrucction of exclusive final states identified by the charge and type of final state particles. At the time of construction, there was not a single detector technology that could achieve all of these measurements and so it was necessary to develop a hybrid near detector.

Any off-axis ND280 detector design must be able to measure the signal and background processes from beam interactions that are relevant to neutrino oscillation measurements. These processes include

- Charged current interactions with no detected pion in the final state (CC0π).

- The intrinsic electron (anti)neutrino component of the beam, which is a background for the electron (anti)neutrino apperence signal
- Wrong-signed charged current processes, which are a background to the CP violation measurement.

TC: Removed the NC background since this can be measured at the IWCD or the far detector.

Further to this, any off-axis near detector should be capable of

- Measuring the intrinsic ν_e and $\bar{\nu}_e$ backgrounds and their cross sections.
- Reconstructing final states with low momentum thresholds.
- In order to study energy reconstruction through the hadronic recoil system, tracking or calorimetric reconstruction of low energy hadrons and detection of neutrons is necessary.
- Identifying the charge of the final state particles
- Covering a 4π phase space with high efficiency at all angles.

The efficiency of the original ND280 design is not flat and is relatively low for angles $> 40°$ with respect to the beam's direction. This is discussed in Section II.2 C. Planned upgrades to the off-axis near detector for T2K and T2K-II will help further improve the selection efficiency, as discussed in Section II.2 D

Though upgrades to the original detector hardware will help significantly, they may not meet the requirements of the Hyper-Kamiokande experiment and further upgrades may be required.

C. Original ND280 detector design

Fig. 50 shows the original design of the off-axis ND280 detector. As of 2018, this design is still current, though an upgrade is planned for 2021. The original off-axis detector comprises of an inner tracking region surrounded by an upstream Pi-Zero detector (PØD) [**?**], Electromagnetic Calorimeter (ECal) [**?**] and Side Muon Range Detector (SMRD) [**?**].

The tracker region of the detector consists of three Time Projection Chambers (TPCs) [**?**], separated by two Fine Grained Detectors (FGDs) [**?**]. All of the detectors are contained inside a magnet, which provides a 0.2 T field. Details of the magnet are given in Section II.2 F.

The T2K collaboration has successfully developed methods to fit the near detector data using parameterized models of the neutrino flux and interaction cross sections [**?**]. Without constraints

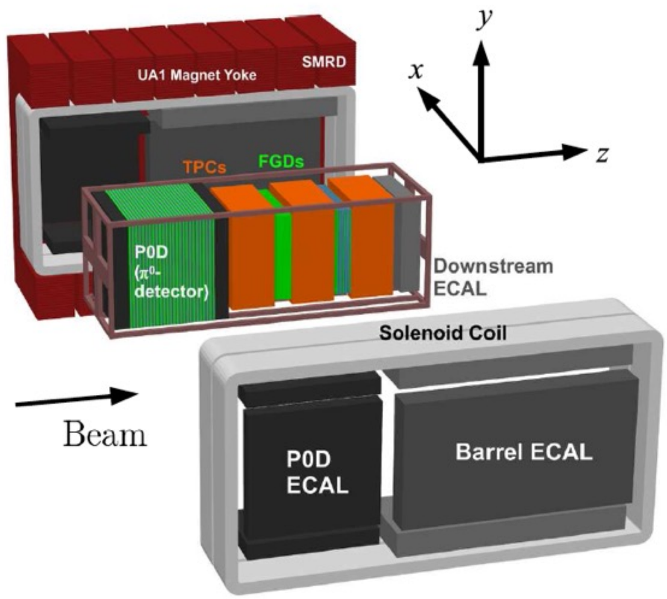

FIG. 50. Cross section of the original ND280 off-axis design [**?**]. Each subdetector is labelled using the acronyms defined in the main text.

from the near detectors, the projected uncertainties in the T2K far detector, Super-Kamiokande, would be $10-12\%$. However, further improvements will be needed to achieve the $1-2\%$ required for the Hyper-Kamiokande experiment.

Charged current interactions are selected by identifying a charged lepton in the off-axis near detector. In the original ND280 design, charged leptons were selected by looking for an interaction vertex in one of the fine-grained detectors and using the Time Projection Chamber immediately downstream to identify the lepton. This led to a selection that was highly efficient in the forward region, but very low at high angles ($> 40°$). This is shown in Figure 51. Inclusion of high angle samples REF TN has helped improve the selection efficiency, but it is still far from the uniform, 4π efficiency of a water Cherenkov detector.

Each sub-detector was designed to fulfil a specific purpose. The PØD is located at the upstream end of the ND280 detector. It is a tracking detector composed of layers of scintillator and lead. The downstream portion of the PØD contains additional passive layers that can be filled with water, thus allowing a measurement of neutrino interaction rates on oxygen (water) [**? ?**]. The PØD was designed to have a large fiducial mass and a high reconstruction efficiency for low-energy gamma rays. The PØD will be replaced as part of the ND280 upgrade for T2K-II.

Immediately downstream of the PØD is the tracker region. The TPCs provide particle iden-

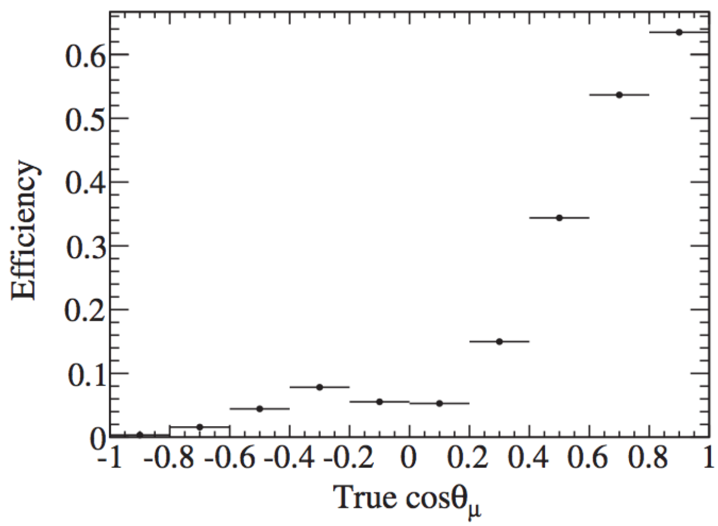

FIG. 51. Angular efficiency of Charged Current events with no pions from T2K ND280 measurements of neutrino CC interactions on C_8H_8 [?].

tification via energy loss measurements (dE/dx) and momentum and charge measurements via curvature of charged particle tracks in the magnetic field. The FGDs lie between the three TPCs and provide a neutrino interaction target. Both FGDs are constructed from extruded polystyrene bars (dimensions XX cm by YY cm by ZZ cm), arranged into layers. In the downstream FGD, XX scintillator planes are replaced with passive layers that are filled with water to allow on-water interaction measurements [?]. Both the TPCs and FGDs will be retained in the T2K-II ND280 upgrade.

The Electromagnetic Calorimeter (ECal) surrounds the central tracker region. Its primary purpose is to identify any electromagnetic particles that escape detection in the tracker region. In addition, the ECal is an active veto, shielding the tracker region from particles produced by neutrino interactions in the surrounding material (e.g. the magnet). Alternating planes of scintillator and lead form the ECal, the number of layers of each depends on the ECal module. The tracker ECal is surrounded by the barrel and downstream ECal modules and the PØD is enclosed by the PØD ECal.

Muons exiting the tracker and ECal regions are tagged using the SMRD, which also provides an accurate way of detecting cosmic rays which are used for detector calibration and an additional veto of out of detector neutrino interactions. The SMRD is constructed from scintillator planks that were inserted into gaps in the magnet yolk.

Each of the FGD, PØD, ECal and SMRD make use of plastic scintillator and wavelength-shifting fibre readout. Each fibre is coupled to one or two customised 667-pixel Hamamatsu Multi-Pixel Photon Counters (MPPCs) with a sensitive area of 1.3×1.3 mm^2. Approximately 64,000 MPPCs were custom produced for ND280. Signals from the MPPCs are processed by a set of custom built electronics (discussed in sections II.2 C 1) and read out via the Data Acquisition (DAQ) systems (section II.2 C 3).

When charged particles pass through the TPCs, ionization electronics are produced in the argon-based drift gas. The ionisation electrons in the gas, drift from the central cathode towards a readout plane. At the readout plane, the electrons are multiplied and sampled with bulk micromegas detectors. The arrival time of the ionisation electrons at each micromegas detector are combined to give a complete 3D image of the charged particle's track. Signals from the micromegas detectors are received by custom electronics (section II.2 C 1) and read out via the DAQ systems.

1. Readout Electronics

Two distinct custom designed front end electronics designs are used in the off-axis ND280 detector. The PØD, ECal and SMRD use identical electronics to process signals produced by the MPPCs. The electronics for these subdetectors is based upon the Trip-T ASIC **REF** and are referred to as the "Trip-T" electronics. The TPC and FGD utilise an different design that AFTER system is used for the FGD and TPC readout. The Trip-T electronics is also used to distribute the timing and trigger to all sub detectors in the off-axis detector.

An overview of the ND280 electronics systems is shown in Fig. 52.

In the Trip-T system, up to 64 MPPCs are read out by custom-designed Trip-T front end boards (TFBs) that contain four Trip-T ASICs. The Trip-T chip integrates the charge from each connected MPPC in a programmable integration window that is synchronised with the neutrino beam timing. The Trip-T chip can store data from 23 integration cycles in a capacitor array. Following each integration cycle, there is a programmable reset time which has a minimum length of 50 ns. The TFB is controlled by an FPGA which timestamps a discriminator output, assembles the data and sends it to a back-end board for buffering.

The back-end of the Trip-T electrons consists of several different modules; Readout Merger modules (RMMs), Cosmic Trigger Modules (CTMs), Slave Clock Modules (SCMs) and a Master Clock Module (MCM). The different modules are deployed on identical hardware but run different firmware, which determines their module type. The Trip-T backend boards contain a Xilinx Vertex II Pro FPGA, clocked at 100 MHz.

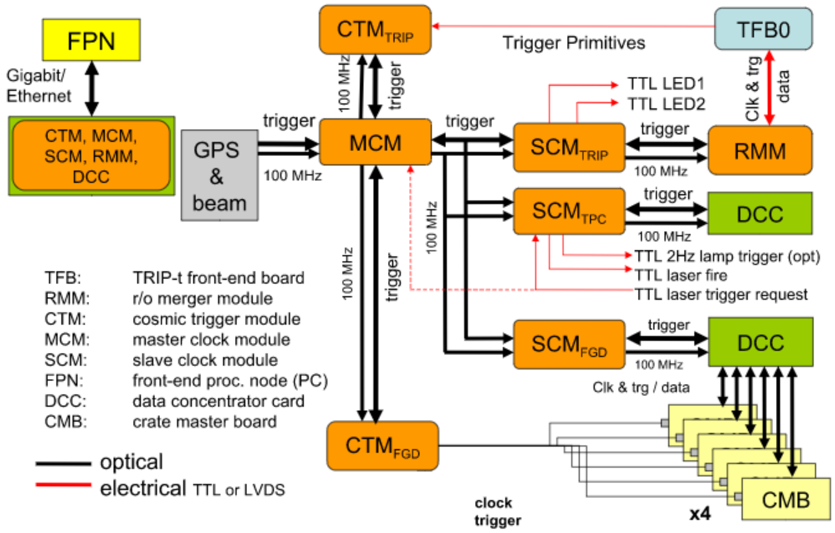

FIG. 52. An overview of the electronics layout for the original ND280.

Up to 48 TFBs are connected to each RMM via Cat 5e cables. The RMM communicates with each TFB, controlling it, distributing clock/trigger signals and collecting its data. Data is sent asynchronously to the DAQ systems via a Gigabit Ethernet link. Each RMM receives a clock and trigger signal that is transmitted via RocketIO-driven optical link from its associated SCM.

Trigger and clock signals are distributed to the SCMs from the MCM. There is one SCM for each subdetector (5 in total), which allows each detector to run individually. When running individually, the SCM acts as an MCM for that particular subdetector. When running in global mode, the SCMs fan-out signals from the MCM to their respective subdetector. The MCM is responsible for coordinating the clock and trigger distribution for the ND280 off-axis detector. Information about the beam-spill arrival time is received from the accelerator via a RocketIO 2.25 GHz optical link. The MCM can generate sequences of triggers, with beam spill as highest priority. Trigger and clock signals are distributed to the SCMs via RocketIO-driven optical links. Each sub-detectors signals its busy state to the MCM during readout to prevent triggers being issued during deadtime.

Two cosmic trigger modules (CTMs), one for the Trip-T systems and another for the FGDs, are connected to the MCM. The CTMs receive signals from up to 192 TFBs or 48 crate master boards (FGD). The CTM uses the signals to determine where a cosmic ray passed through the detector and trigger the readout accordingly.

Signals from the FGD's MPPCs are collected by front-end boards, held in a mini-crate. EAch mini-crate has a crate master board (CMB) which can read out up to 240 MPPCs. The front-end boards use an AFTER ASIC to shape and digitize photosensor signals at 50 MHz. The Waveform is stored in a 511-deep switched capacitor array. Data from each CMB is transmitted to Data Collector Cards (DCCs) via optical fibre links.

The AFTER ASIC is also used in the TPC readout. Six front-end cards, each containing four custom AFTER ASICs, sample and digitize signals from 1728 micromegas pads. Each AFTER ASIC shapes and digitizes signals from 72 pads and stores them in a 511-deep switched capacitor array. The six front-end cards transmit their data to a single front-end mezzanine card which performs zero suppression and sends data to the DAQ via an optical link.

2. Timing and trigger distribution

More details here?

3. DAQ systems and Data transfer

The ND280 DAQ systems use a common architecture based upon the MIDAS framework and operate on commercially available computing hardware running Scientific Linux 6. The MIDAS framework provides standard components for operation and interfaces with the detector hardware via custom C/C++ applications. DAQ nodes are interconnected via commercial Gigabit ethernet switches.

To provide flexibility and partitioning of detectors, the MIDAS processes are distributed across a number of computing nodes. Two additional MIDAS instances are implemented, one each for the TPCs and FGDs. The two additional MIDAS instances assemble data from the TPC and independently from the FGD and transmit it to the global DAQ.

The Trip-T detectors are connected to front-end processor nodes (FPNs) via point-to-point Gigabit ethernet links. Each FPN controls and reads out up to two Trip-T back-end boards. The FPN consists of three separate processes, interconnected by shared memory buffers. Electronics hardware readout and configuration is undertaken by the Readout Task (RXT). Data readout across electronics boards is parallelised in a multithreaded manner and buffered to allow access by the Data Processing Task (DPT). The DPT's primary role is to reduce the total data volume transmitted to DAQ and thus written to disk. Prior to zero-suppression, the DPT produces per-channel histograms of signal amplitudes, which are inserted into the data flow at a programmable rate. In addition to the histograms, the DPT performs pedestal subtraction, applies zero suppression and formats the data for output. The final FPN task is the MIDAS Front End task (MFE), which implements the MIDAS functionality. Processed data from the DPT is buffered and dispatched to the DAQ back-end via this process. Additionally, the MFE task is responsible for the correct number of triggered events and event fragments are read out and inserted to the data flow.

Data fragments from each FPN, the TPC and FGD are delivered to the event-building process, which performs basic consistency checks and writes the fully assembled event to disk. Custom data archiving software transfers copies of completed files to local on-site storage and off-site storage (KEK HPSS) for offline processing. Figure 53 shows an overview of the off-axis DAQ systems.

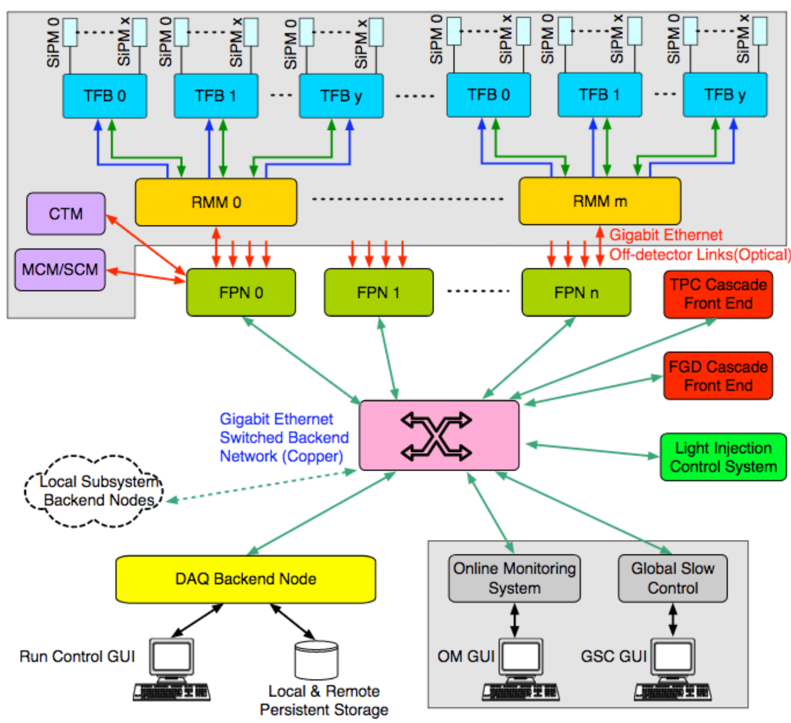

FIG. 53. An overview of the ND280 off-axis detector DAQ systems.

4. Performance of the ND280

The first components of the ND280 off-axis detector began operation in 20XX, and the barrel ECal was added in 20XX. As of summer 2018, XX POT in FHC and XX POT in RHC mode have been collected by the off-axis detector.

To date, the FGD has suffered no significant electronics problems, with only one fibre optic cable and several power supplies needing to be replaced. There are sufficient spare electronics boards on site in case any replacement is needed. In 201X, one of the water layers in the downstream FGD failed as a result of human error during annual maintenance. The missing target was felt to have no detrimental effect on the T2K data, so was not replaced. The target will not be replaced for the ND280 upgrade, but its replacement should be considered if the FGD is retained for Hyper-K. The ageing of the FGD scintillator bars has been studied and is monitored throughout each T2K data-taking period.

No particular ageing is expected for the TPCs. Since installation in 2009, none of the micromegas has broken and only 3 out of 72 Front-End Mezzanine (FEM) have required replacement. Sufficient spares are on site for any future issues.

For the Trip-T systems, 2 of the 366 ECal TFBs were lost during the 2011 Tohoku earthquake. Replacement of the failed boards would require removal of all of the North ECal barrel modules, a costly operation and one that would present a significant risk to the ECal. Therefore, it has not been attempted. Of the two failed TFBs, one read out a single-ended bar which left a dead region in the detector and the other read out one end of a double-ended scintillator bar, resulting in slight loss of efficiency in those bars. Replacement of the two failed TFBs should be considered for Hyper-K.

Only 1 out of 128 SMRD TFBs have been replaced. All TFBs for INGRID are accessible and should not present an issue if replacement is needed in future. The failure of PØD TFBs has been somewhat higher with 12 out of 174 boards being replaced to date (September 2018). The relatively high failure rate of PØD TFBs is likely related to the removal and reinstallation of the P0D electronics when the water bags and sensors were replaced. The total failure rate of front end boards is around 2% for the ND280 Trip-T systems. There are currently 20 spare TFBs on-site and a further 48 in the UK. Removal of parts of the P0D for the ND280 upgrade will provide additional spares.

There has been only one backend board failure in the Trip-T system, corresponding to a failure rate of 2.7%. Though it is not conclusive what caused the ECal RMM to fail, the most likely reason is overheating due to a poor connection between the cooling block and Xilinx chip. All of the ECal RMMs have had their cooling subsequently upgraded. On-site there are 12 spare boards and a further 2 boards in the UK. As with the TFBs, removal of the P0D will provide an additional set of spare boards.

Across all subdetectors, a small number of MPPCs (¡1%) have failed. Some of these MPPCs could be replaced, but this is not thought to be essential as they do not impact the detector performance significantly.

5. Scintillator ageing

Look up technical notes

D. Upgraded ND280 design

An upgrade to the ND280 off-axis detector has been proposed [?] in order to reach a systematic uncertainty of around 4% for the second phase of T2K (T2K-II). Assuming that the 4% uncertainty is achieved, T2K-II should provide a 3 σ exclusion of CP conservation for 36% of the phase around $\delta_{CP} = -\pi/2$ [?].

One of the limitations of the original ND280 design was that the phase space sampled by the near and far detectors was not the same. Figure 51 shows that the original ND280 design sample favored forward going interactions with high efficiency but had little sensitivity to backward-going or high angle events. Interactions selected in the far detector cover the phase space more evenly, indicating that the near and far detectors are not sampling the same parts of the neutrino beam spectrum and interaction. When extrapolations of the near detector spectrum are performed to obtain the predicted far detector spectrum, there is greater reliance on the underlying neutrino interaction models, leading to larger uncertainties. These must be reduced for both the T2K-II and Hyper-K projects, hence the need for the ND280 upgrade.

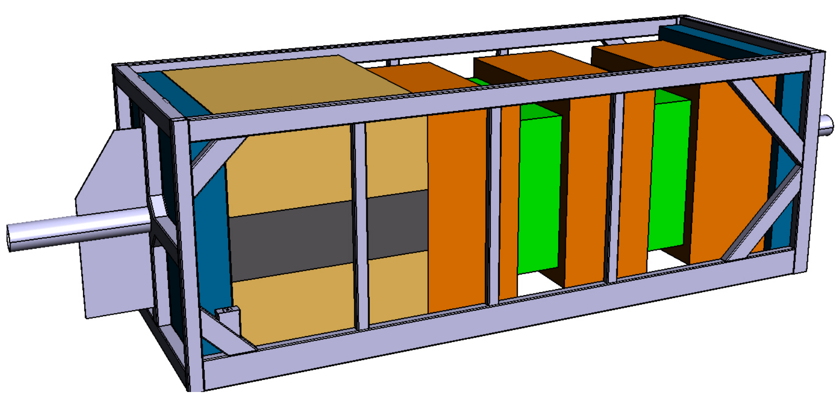

FIG. 54. Schematic of the upgraded ND280 detector [?].

A schematic of the proposed upgrade detector is shown in Figure 54 . A major part of the PØD will be removed to allow installation of a new tracker system. The new tracker will consist of a high granularity "SuperFGD" scintillator detector sandwiched between two horizontal High-Angle TPCs (HA-TPCs), one above and one below, to measure the tracks produced at high angle. The whole new tracker will be surrounded by a Time-of-Flight (ToF) detector providing a good time resolution to precisely measure their direction and possibly improve the particle identification.

Following the upgrade, a significant proportion of the original off-axis detector will remain unchanged. No changes to the FGDs, TPCs, ECal and SMRD are planned. The upstream calorimeter part of the PØD will be retained primarily as it forms part of the cosmic ray trigger and it provides an excellent veto for particles coming from the upstream material. In addition, the DAQ systems, clock and timing systems will remain unchanged. All of the new detectors will be integrated into the existing T2K DAQ and software framework and will participate in the current trigger and timing scheme.

1. *SuperFGD*

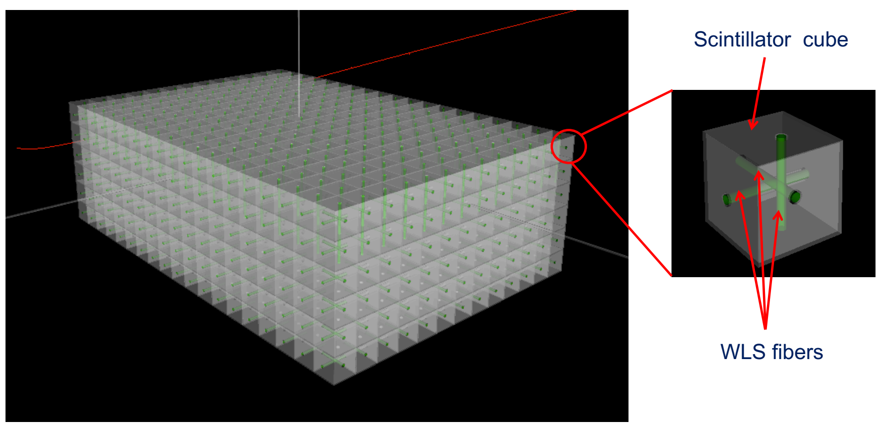

FIG. 55. Schematic of SuperFGD. It will consist of many cubes of plastic scintillator with 1 cm^3 size. Each cube will be read out by wavelength shifting fibers from three directions.

A fine-granularity plastic scintillator detector will be used as the active neutrino target. It will provide sufficient mass to produce neutrino interactions, a large acceptance to the charged particles that are measured in the surrounding TPCs and will be able to reconstruct the short tracks produced by neutrino interactions.

A novel detector concept called SuperFGD [**?**] will be employed in the upgrade of ND280. It consists of a fully-active fine-grained plastic-scintillator detector made of many 1×1×1 cm^3 cubes. Each cube has three 1.5 mm holes and 1 mm diameter Y11(200) Kuraray wavelength shifting (WLS) fibers along the three orthogonal directions that read out the scintillation light and provide three views (XY, XZ and YZ), instrumented on one end with a Multi-Pixel Photon Counter (MPPC). Because SuperFGD will provide projections of charged particle trajectories onto three planes without inactive regions, it will provide us significantly more information on the neutrino interaction compared to the existing FGD, which consists of plastic scintillator bars aligned in either X or Y direction. The dimensions of the SuperFGD will be approximately 1.8(W)×2.0(L)×0.6(H) m^3 for a total mass of about 2 tons. The number of read out channel will be about 60,000. The electronics will be based on the CITIROC ASIC, which is designed for the readout of SiPM devices.

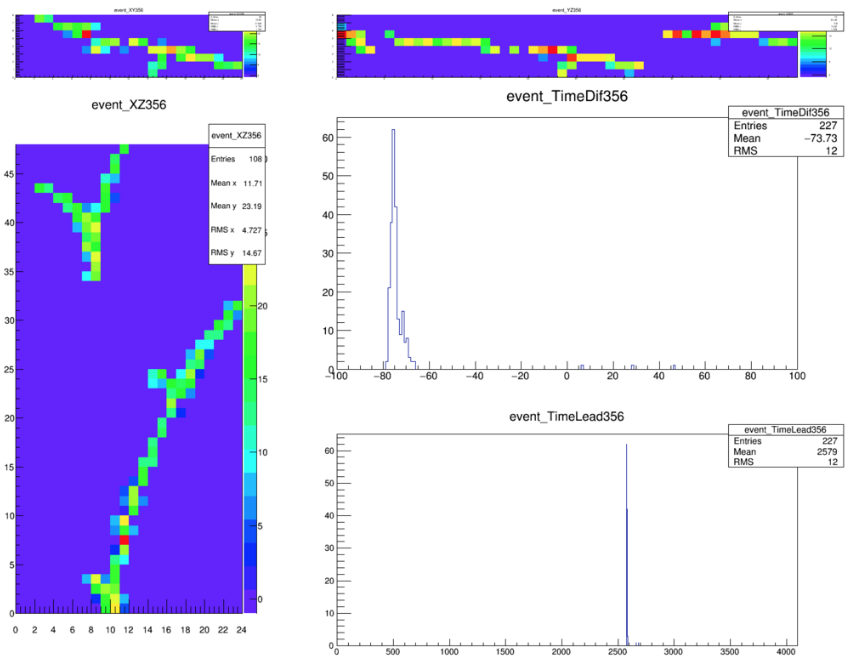

FIG. 56. Event display from the 2018 beam test at CERN. The event consists of an electron bent by the magnetic field and a bremsstrahlung photon converted into an electron-positron pair. The colors indicate the time the charged signal is above a defined threshold, corresponding to the light yield.

In summer 2018, test beams were performed at CERN with a prototype of the size of 24(W)×8(H)×48(L) cm^3. Figure 56 shows an event display with an electron and a bremsstrahlung photon converted into an electron-positron pair.

2. High Angle TPCs

The HA-TPCs will provide 3D track reconstruction, charge measurement, momentum measurement, and particle identification by dE/dx for those tracks produced at high angles. The requirements for HA-TPCs are almost the same as those for the current TPCs in ND280. A

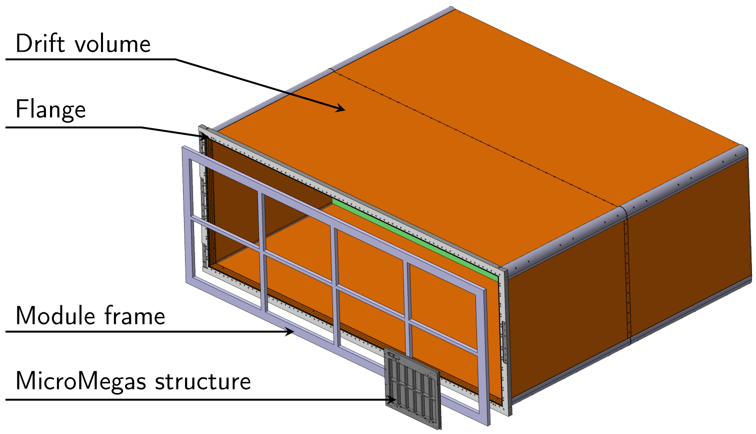

FIG. 57. Schematic of a High-Angle TPC module. Two HATPC detectors will be constructed and placed above and below the superFGD detector.

schematic of HA-TPC is shown in Fig. 57.

In order to maximize the acceptance to tracks exiting the SuperFGD, we will build a thin field cage, about 2 cm thick and $\sim 2\%$ of a radiation length, following the scheme developed for the ILC experiment [**?**] or used in the HARP experiment [**?**]. The Micromegas detector will be constructed with the "resistive bulk" technique [**?**], that naturally introduces a spread in the charge on the anode plane, thereby allowing in principle a lower density of readout pads. This technique allows also to eliminate the discharges (sparks) and therefore the protecting diodes on the front end cards are no longer necessary. Each HA-TPC will have a drift length of ~ 80 cm and about 32,000 readout channels. The same frontend ASIC as the existing TPCs, AFTER chip [**?**], will be employed for the readout of HA-TPC.

3. Time of Flight detectors

The new tracker will be surrounded by a TOF detector consisting of plastic scintillator bars. It will consist of approximately $12\times1\times230$ cm^3 EJ-200 cast plastic scintillator bars and be read out at both ends with an array of eight 6×6 mm^2 SiPMs. Based on the results from a prototype [**?**], the expected timing resolution is about 100 ps.

4. *Expected performance*

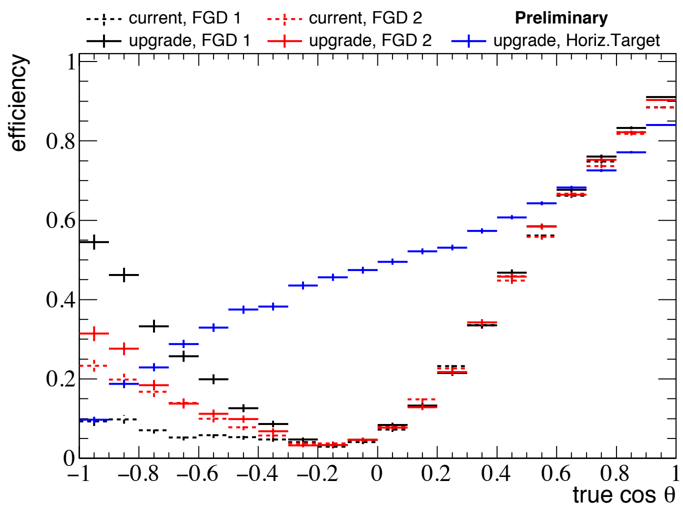

FIG. 58. The ν_μ-CC event selection efficiency as a function of the true muon angle with respect to the z direction. The curves are shown for neutrino interactions in FGD1 (black), FGD2 (red) and SuperFGD (blue).

The performance of the ND280 upgraded detector has been evaluated with simulations [**?**]. As an example, Fig. 58 shows the selection efficiency for Charged-Current (CC) inclusive ν_μ events in neutrino enhanced mode as a function of the muon angle with respect to the neutrino beam direction. As expected, the upgraded ND280 drastically improves the angular acceptance for muons produced at high angles.

E. Options for Hyper-Kamiokande

At the beginning of the Hyper-Kamiokande experiment, parts of the ND280 off-axis detector will be XX years old. The approximate age and spares status are given in Table XIX. A significant portion of the electronics will be with a limited number of spare parts, even before the start of the Hyper-Kamiokande experiment. It is therefore likely that any components that are retained by Hyper-Kamiokande will need new readout electronics, which will come with a significant cost. The subdetectors most likely to be retained are the SMRD and ECal. Replacing the ECal electronics would require removal of all of the ECal modules (13 in total), a significant engineering operation requiring the use of specialist frames, scaffolding a use of a crane. It is likely to exceed XXXX.

Replacing the SMRD electronics is more straightforward as both the front and backend boards are external to the magnet. They can therefore be easily replaced, providing that any replacement

Component name	Subdetector used	Number of spares	Comments
Trip-T backend boards	ECal, PØD, SMRD, Timing/trigger		Cannot make any new boards as Xylix chip no longer available. Would require redesign.
Trip-T frontend boards	ECal, PØD, SMRD		Cannot manufacture new boards as components no longer available
AFTER electronics	FGD, Original TPCs		Could replace with new readout electronics used for vertical TPCs

TABLE XIX. Component age and spares status for the off-axis ND280

is compatible with the MPPC connector. As the SMRD scintillator planks and MPPCs are not accessible (CHECK THIS) they cannot be replaced unless the magnet is removed completely.

Removal of ECal costs incl. electronics TBD

Replacement of SMRD incl. electronics TBD

Comment on Trigger/timing replacement

Lifetime of the basket?

To achieve a constraint of $1-2\%$ for Hyper-Kamiokande, a completely new design of near detector may be required. On such possibility is to replace the tracker region with a High Pressure TPC (HPTPC). The existing ND280 basket could accommodate an HPTPC with an 8 m^3 fiducial volume, held at a pressure of 10 bar. At such a pressure, a significant number of CC interactions would be accumulated. An HPTPC would provide a full 4π coverage of events at the near detector as well as precision identification of low momentum protons and other charged particles. A further advantage of an HPTPC is that the detector could be operated with a variety of gases including He, CH_2, Ne, Ar, CF_4 and N_2:CO_2 mixture with 60% oxygen by mass. The data obtained from operation with different gases would help break degeneracies arising from neutrino-nucleus interaction models.

Emulsions would also provide 3D tracking, sensitivity to protons down to 20 MeV and 4π sub micrometer precision through offline scanning ***REF***

Upgrades to the DAQ system would be required and it is likely that the framework developed for the Hyper-Kamiokande detector would be used for the off-axis ND280 detector and intermediate detector.

F. Infrastructure at the ND280 Complex

The operation of detectors at the ND280 complex relies infrastructure systems that are currently supported by collaborating T2K institutes, but may be supported in the future by the host lab. These include the ND280 magnet and its systems, the gas systems for operation of Time Projection Chambers (TPCs) and the water systems for detector electronics cooling.

1. *The ND280 Magnet*

The ND280 detector is immersed in a 0.2 T magnetic field provided by the recycled UA1 magnet [**?**]. The magnet consists of water-cooled aluminum coils and a flux return yoke. The aluminum bars that compose the coil have a 5.45 cm$\times$5.45 cm cross section with a 23 mm diameter bore through which the cooling water flows. The four coil elements and yoke are shown in Fig. 50.

The magnet power supply was designed and manufactured by Bruker to provide the DC current to energize the magnet. The nominal current is 2900 A with a voltage drop of 155 V. For T2K the requirements for the current resolution and stability were 300 ppm and 1000 ppm over a 24 hour period respectively. The power supply is controlled locally or remotely by the magnet control system (MCS).

The magnet cooling system was built by MAN Ferrostaal AG (D), and it provides up to 750 kW of cooling power through two independent cooling circuits of de-mineralized water. The cold source in the cooling circuit is a glycol circuit maintained at 8 °C by a chiller built by Friotherm, D. The secondary pumping circuit units, heat exchangers, water purification units and main panel controller are mounted in an ISO container. The secondary circuit has a flow 30 L/s at a pressure of 10 bar to compensate for the 7 bar pressure drop across the coil bore holes.

a. Operational Experience of T2K T2K experienced two major periods of ND280 downtime due to failures in the magnet chiller and power converter systems.

A chiller problem caused poor cooling of the magnet and an increase of the magnet operation temperature, forcing the magnet to be switched off. Two issues were discovered during the repair work by FrioTherm (Germany). Solenoid valves that control the freon pressurized system were found to be faulty. Also, the timer switch breaker that stages the start of the compressors to avoid large current spikes on the supply line was faulty.

The power converter (PC) problem was caused by a faulty resistor in a power line filter at the input of the PC. This short caused the main facility transformer to trip and the PC to trip safely.

The problem was discovered and fixed by the engineer from the company that built the PC.

In both cases, the failures were attributed to aging of parts and poor maintenance in the past. In the case of the chiller, it was also found that the heat exchange component is corroded in several places due to operation in proximity to the ocean. In both cases, weeks of downtime were incurred as it was necessary to bring technicians from Europe to J-PARC for the repair and replacement parts had to be produced.

Among the solutions to mitigate these failures in the future, more active support of the magnet systems by J-PARC, KEK and Japanese companies are being investigated. For the PC, the full system should be replaced to allow for maintenance by a Japanese company. The specifications for the hardware are being collected and a cost estimate will be made. The replacement of the chiller with a Japanese provided system would be a major undertaking. Investigation of a Japanese produced system will be undertaken, but a maintenance scheme of the original system built by MAN will also be investigated.

There are additional minor issues with the magnet systems that should be addressed for Hyper-K. The slow control system uses an outdated release of Windows, which created issues with the internet safety regulations in J-PARC. It has also shown a lack of flexibility to adapt to new developments and requirements. The system should be migrated to a more modern and maintainable Linux-based system. Additional human resources are needed for this work.

The water manifolds have been operated for many years and the system requires a revision. The check of this system will be done during the next shutdown.

The moving system was inherited from the HERA-B experiment at DESY and suffers from some aging. The main two issues are a crack in one of the hydraulic pistons, producing small a leak, and an outdated control system based on very old components. The system requires a serious refurbishment, and discussion with RWTH is on going to identify possible solutions to both problems. Possible solutions include the acquisition of a brand new system or adapting a much modern system.

TC: Can a estimate of the human and monetary resources needed for regular maintenance and operation be added?

II.3. THE INTERMEDIATE WATER CHERENKOV DETECTOR

The intermediate water Cherenkov detector (IWCD) is located 0.75-1.8 km away from the neutrino source, requiring a new site outside of J-PARC. The detector is designed to be moveable in a vertical shaft that is filled with water up to the detectors position, allowing for the measurement of neutrino interactions at different off-axis angles. The nominal off-axis angle range of 1°-4° provides neutrino spectra with peak energies ranging from 0.4 GeV to 1.0 GeV. The IWCD will use multi-PMT modules consisting of high resolution 3-inch PMTs housed in a pressure tolerant vessel with the readout electronics and high voltage circuits. The major design and technical challenges for the IWCD are selection of the detector site and excavation of the vertical shaft, design and construction of the lifting mechanism to move the detector in the vertical shaft, design and construction of the multi-PMT photosensors, and design and construction of the calibration systems necessary to achieve percent level calibration of the detector.

A. The IWCD Detector Structure

1. Detector Design

Figure 59 shows the experimental setup of the intermediate water Cherenkov detector (IWCD). The instrumented detector is contained in a cylindrical tank of 8 m height and 10 m diameter made of stainless steel. The height of the detector may change depending on the baseline at which the detector is deployed. The tank is filled with Gd-loaded water for neutron tagging. The water tank is optically separated by the PMT support frame and black sheet into the cylindrically shaped inner detector (ID), with 6 m height and 8 m diameter, and the outer detector (OD), which surrounds the ID with 1 m thick water layer. The size of the ID is determined to contain up to $\sim$1 GeV muons generated in the fiducial volume and to accumulate enough statistics for precise measurements. On the other hand, the upper constraint is set to suppress pile-up[1] and reduce the cost for construction. The OD layer is necessary for two purposes: (1) to identify muons or other charged particles entering or exiting the ID, and (2) to shield the ID against neutral particles such as gamma rays and neutrons. Both entering muons generated from neutrino interactions in upstream rock and exiting muons from the ID must be identified in order to select fully contained neutrino events produced in the ID. Thickness of the OD is determined to identify muons with $\sim$ 100% efficiency and reduce entering gamma rays and neutrons to the level well below ν_e and

[1] Multiple interactions in the same beam bunch, which Cherenkov rings are difficult to separate.

neutron capture signals. The PMT support frame is equipped with 685 multi-PMT (mPMT) modules, each contains 19 inward facing PMTs to detect Cherenkov light from the ID. Figure 60 shows a schematic drawing of the PMT frame, with an outdated multi-PMT design that views the OD as well. As discussed in Section II.3 F, independent photo sensors for the OD will be deployed. Digitization electronics and high voltage power supply are encapsulated inside the multi-PMT module to reduce the number of cables, which results in suppression of weight, cost and dead space.

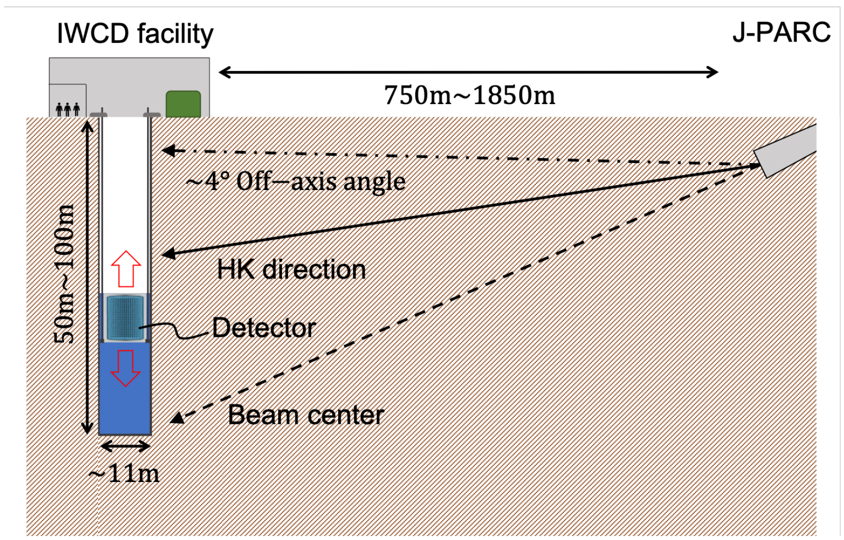

FIG. 59. Experimental setup of intermediate water Cherenkov detector.

As was confirmed in Super-Kamiokande (SK), performance of event reconstruction in a water Chrenkov detector is typically worse for charged particles generated around the edge of the detector and facing toward the wall. This will be a serious issue for the small water Cherenkov detector due to the detector size. 3-inch diameter PMTs ar therefore employed instead of large 20 inch PMT used in SK and the past 1kton detector in K2K, to improve the resolution of the Cherenkov ring image.

TC: Removed discussion of cross sections since it should be covered in the CDR.

2. Off-axis spanning capability

Neutrino interactions with varying peak energies are measured by varying the position and hence off-axis angle of the IWCD. Vertical pit with a depth of 50 m to 100 m is excavated at a location between 700 m and 2 km from neutrino beam target (see Section II.3 B) and the pit is

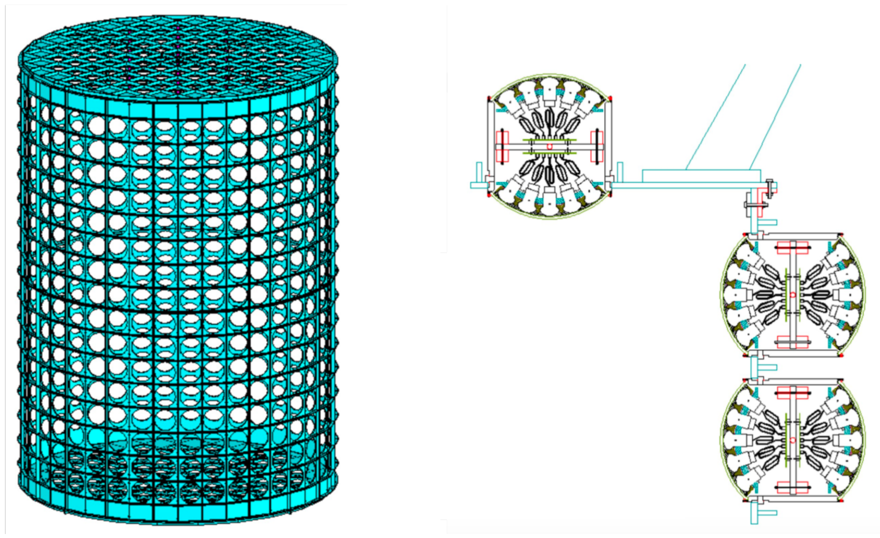

FIG. 60. Schematic drawing of proposed intermediate water Cherenkov detector (left), PMT support frame (middle) and attachment of mPMT modules (right). *TC: Update the multi-PMT drawing.*

filled with water. The cylindrical detector tank is put inside the pit by a crane set on the surface. The detector tank is water sealed so that Gd-loaded water inside the tank is not leaked outside. The quality of water outside of the detector tank is not required to be pure, *i.e.* contamination of ground water is acceptable. Therefore, the vertical pit is not tightly water sealed. A lifting mechanism is equipped to realize the off-axis spanning method in which the vertical position of the detector inside the pit can be adjusted. The neutrino beam direction is tilted downward as shown in Fig. **??**, and the direction to HK is pointed southward relative to the average beam direction, as shown in Fig. 61. The depth of the pit is chosen to range from 1° at the bottom to 4° at the top which as at ground level.

Figure 62 shows a conceptual design of lifting mechanism with an oil-hydraulic cylinder jack and rod system. Rods with a few meters lengths are connected and attached to stainless steel water tank. The water tank is lifted up or down with an oil-hydraulic cylinder jack set on the surface. The rods are attached or removed after lifting up or down the detector by the length of single rod. The water level in the pit is controlled to be at the top of the detector by adding or draining pit water. This will allow services on the top of the detector such as calibration devices and the lifting mechanism to operate without being submerged in water.

The position of the detector can be changed during beam-off accelerator maintenance days. Assuming one maintenance day every week, the detector must be moved by up to 5 m so that the detector position covers from the top to the bottom in one year of operation (20 weeks $\times$ 5 m =

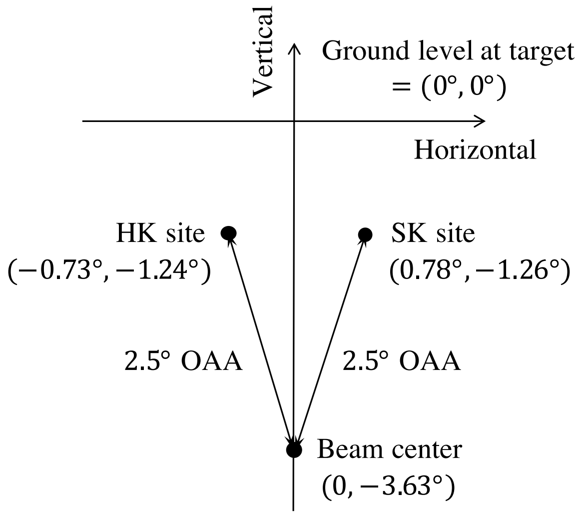

FIG. 61. Direction of beam center, Super-Kamiokande and Hyper-Kamiokande from beam target.

2097 100 m). This requires flow rate of 20 ton/hour for pouring and draining to keep the pit water level
2098 at the top of the detector. In case the required flow rate is not feasible with a reasonable cost, a
2099 buffer tank will be built to control the flow rate.

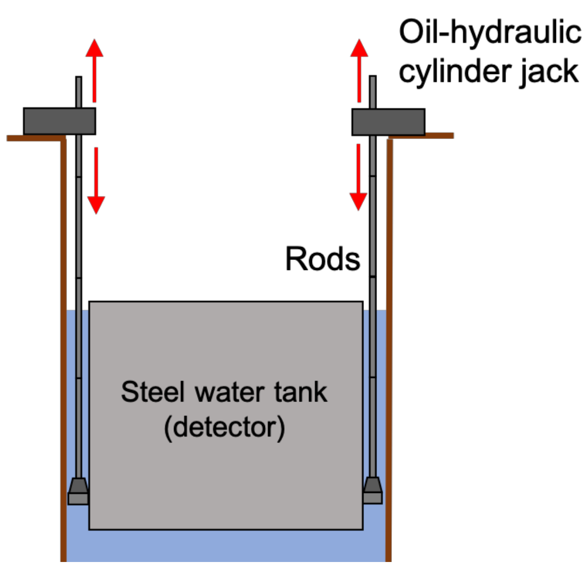

FIG. 62. Conceptual design of lifting mechanism with oil-hydraulic cylinder jack and rod system.

3. Water

The composition of Gd-loaded water will be identical to SK-Gd so that neutron multiplicity measurements with high statistics neutrino and antineutrino beam data can be used for calibration of the measurements in SK-Gd and HK. The Gd-loaded water is circulated during operation with the water purification system based on the same mechanism as SK-Gd. The water temperature in the tank must be kept below about 14 °C by circulating cooled water to prevent growth of bacteria and keep water transparency stable during operation. The underground temperature below 5 m in Tokai is 15 $\sim$ 16 °C and stable all year around.

B. The IWCD Site and Facility

C. Site selection

Figure 63 is a map of Tokai village along the J-PARC neutrino beam. Yellow, red and blue lines show the direction of beam center, the direction toward HK at the Tochibora site and the direction toward SK, respectively. The candidate site of IWCD should be selected to satisfy the following conditions:

- The if possible, the IWCD should be located along direction from neutrino beam target to HK to monitor the neutrino flux along the same direction.
- The distance from neutrino beam source to IWCD should be between 700 m and 2 km. At the shorter distance, the energy spectrum of neutrino flux is different from HK even at the same direction due to the flight length of pions. In addition, more than one neutrino interaction can occur in the same bunch (pile-up) for most cases if the distance is much shorter than 700 m. As the minimum size of the detector is defined to contain up to $\sim$1 GeV muons, this pile-up issue sets the lower limit to the baseline for IWCD. While, at a longer baseline, a larger volume of the detector is required to accumulate enough statistics of neutrino data for precise measurements. In addition, the pit must be excavated deeper at longer baseline to reach 1° and 2.5° OAA. Both of these directly affects the cost for construction.
- Availability of the ground must be also considered. A large fraction of the land along the neutrino beam is occupied with rice fields, which are considered to be difficult to use for other purposes. This is mainly due to license system for rice fields in Japan. Locations owned by Tokai village are favored, while privately owned ground can be still considered.

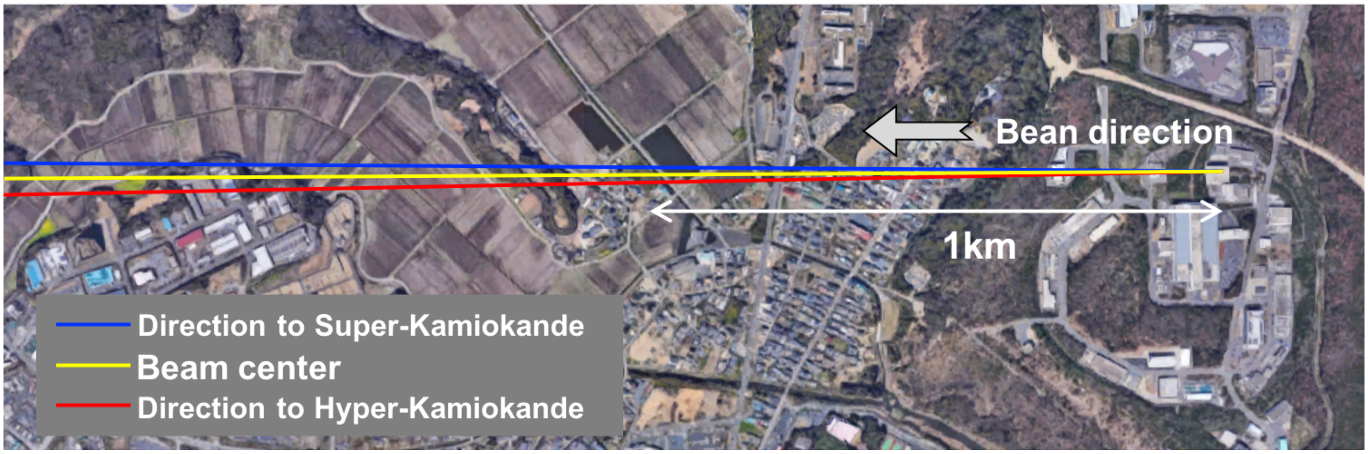

FIG. 63. Map of Tokai village along J-PARC neutrino beam. Yellow, red and blue lines show the direction of beam center, direction toward Hyper-Kamiokande (Tochibora site) and Super-Kamiokande, respectively.

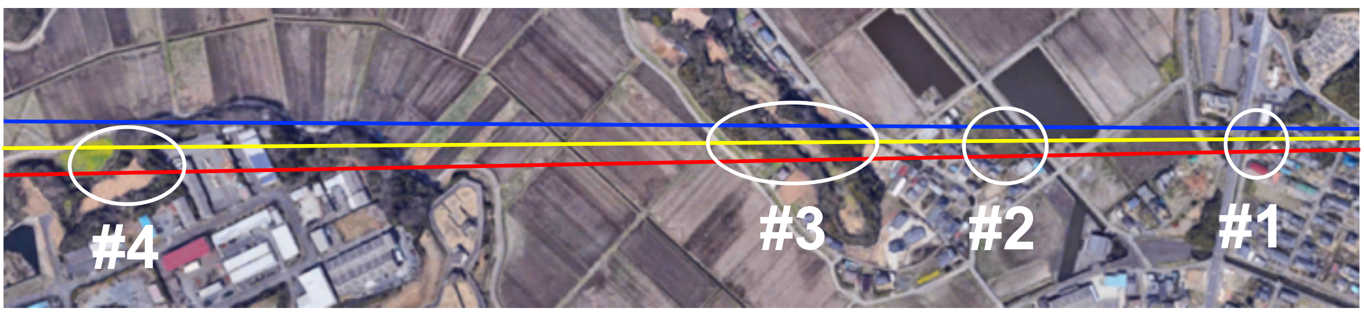

FIG. 64. Four candidate locations for IWCD. Yellow, red and blue lines show the direction of beam center, direction toward Hyper-Kamiokande (Tochibora site) and Super-Kamiokande, respectively.

Considering these conditions, four candidate locations shown in Fig. 64 are selected for consideration as the IWCD site. The advantages and disadvantages for each site are evaluated.

Table XX summarizes the position, baseline, depth to reach 1° OAA for the four candidate locations currently considered. The numbers (#) do not represent the priority but they are assigned for discussion. The depth of the pit ranges from 47 m to 107 m depending on the baseline. Feasibility, methods, and cost for excavation are currently investigated.

Table XXI summarizes the pros and cons for each candidate. Large flat space with a wide access road is suitable for construction, and moderate distance around 1 km is favored for physics where neutrino beam flux is almost identical to HK and pile-up is well suppressed. Ownership of the ground is also important to acquire the ground or get permission for construction. Among the four, candidates #1 and #4 are owned by Tokai village. The underground rock condition is also

TABLE XX. Summary of four candidate locations considered for IWCD facility.

#	Baseline (m)	Latitude (°)	Longitude (°)	Elevation (m)	Surface OAA (°)	Depth (m)
1	749.0	36.449096	140.595995	9.0	4.44	47.2
2	993.1	36.449083	140.593265	3.9	3.95	53.0
3	1239.1	36.449071	140.590515	10.1	4.17	70.5
4	1845.7	36.448821	140.583736	9.0	3.99	107.0

TABLE XXI. Pros and cons for each candidate locations.

#	Baseline (m)	Depth (m)	Pros	Cons
1	749.0	47.2	· Owned by Tokai village · Shallow pit to reach 1° OAA · Direct access with R245	· Narrow space · Conflict with R245 extension · HK direction is not available (to be built at SK direction) · Undulation (need retaining) · Close to nearby residents
2	993.1	53.0	· Flat space · Moderate distance	· Privately owned · Need extension of access road · Limited space for HK direction · Close to nearby residents
3	1239.1	70.5	· Flat open space · Moderate distance	· Privately owned · Need extension of access road · Specified as archaeological site
4	1845.7	107.0	· Owned by Tokai village · Large open space · Isolated from nearby residents · Requires only small extension of access road	· Need excavation of deep pit results in a large cost

considered for evaluating the method excavation and construction of the pit.

Figure 65 show a map around candidate #1 and the design of the facility including a retaining wall to create a level site for the detector. The circles on the map indicate an 11 m diameter pit. The widest road in Fig. 65 (candidate #1) is R245. It must be noted that there is a concrete plan to extend the width of R245, which is currently 9.6 m, to 22 m. The HK direction is not available in # 1 location and and the narrow space of candidate #1 will be a serious issue.

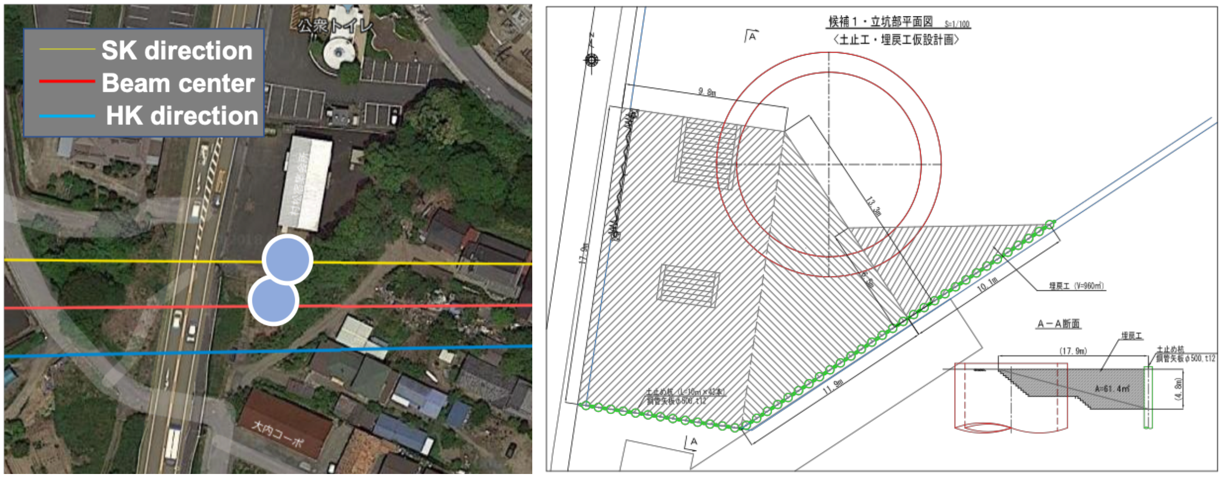

FIG. 65. Map around candidate #1. Yellow, red and blue lines show the direction toward SK, beam center and direction toward HK (Tochibora site), respectively. Circles indicate the size of 11 m diameter pit although the position is not precisely fixed. Right-hand drawing is the conceptual design for construction with retaining shown by hatched area.

Figure 66 show the maps around candidate #2 and #3. These locations are privately owned and the availability is not confirmed. For candidate # 2, there is not enough space to excavate the pit and construct the lab buildings along the HK direction. The construction consulting company confirmed that the extension of an access road is necessary to reach the site with heavy vehicles. The east side of candidate # 3 is not possible for this reason. The extension of the access road to candidate #2 and the west side of #3, requires negotiations with nearby residents and Tokai village in addition to the acquisition of the ground for the facility (shown in right-hand of figure 66 for candidate # 2).

Figure 65 show maps around candidate #4, the required extension of the access road, and the conceptual design of the facility and soundproof wall. Candidate #4 has the advantage of a large open space on HK direction owned by Tokai village and isolated from nearby residents. This site requires minimum construction of an access road, and there is flexibility of the route so that negotiation will be easier. The major issue is the cost for the excavation of deep pit required do to the long baseline.

In order to evaluate feasibility, methods, and cost for excavation for each candidate, the underground rock condition must be investigated by boring or, as alternative approach, the rock conditions must be assumed from the extrapolation of available boring data considering the nearby geographical features. Figure 68 shows the rock conditions along the neutrino beam direction

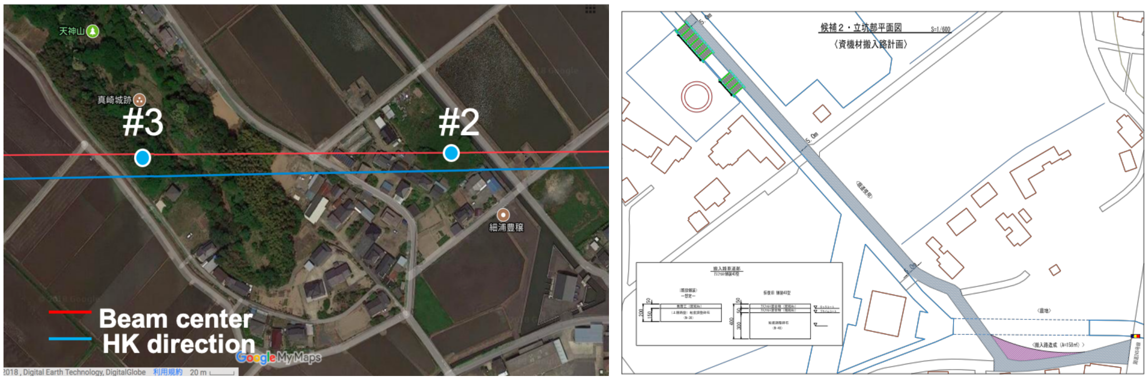

FIG. 66. Map around candidate #2 and #3. Red and blue lines show the direction of beam center and direction toward Hyper-Kamiokande (Tochibora site), respectively. Circle indicate the size of 11 m diameter pit although the position is not precisely fixed. Right-hand figure shows the extension of access road required to reach candidate # 2 (provided from construction consulting company).

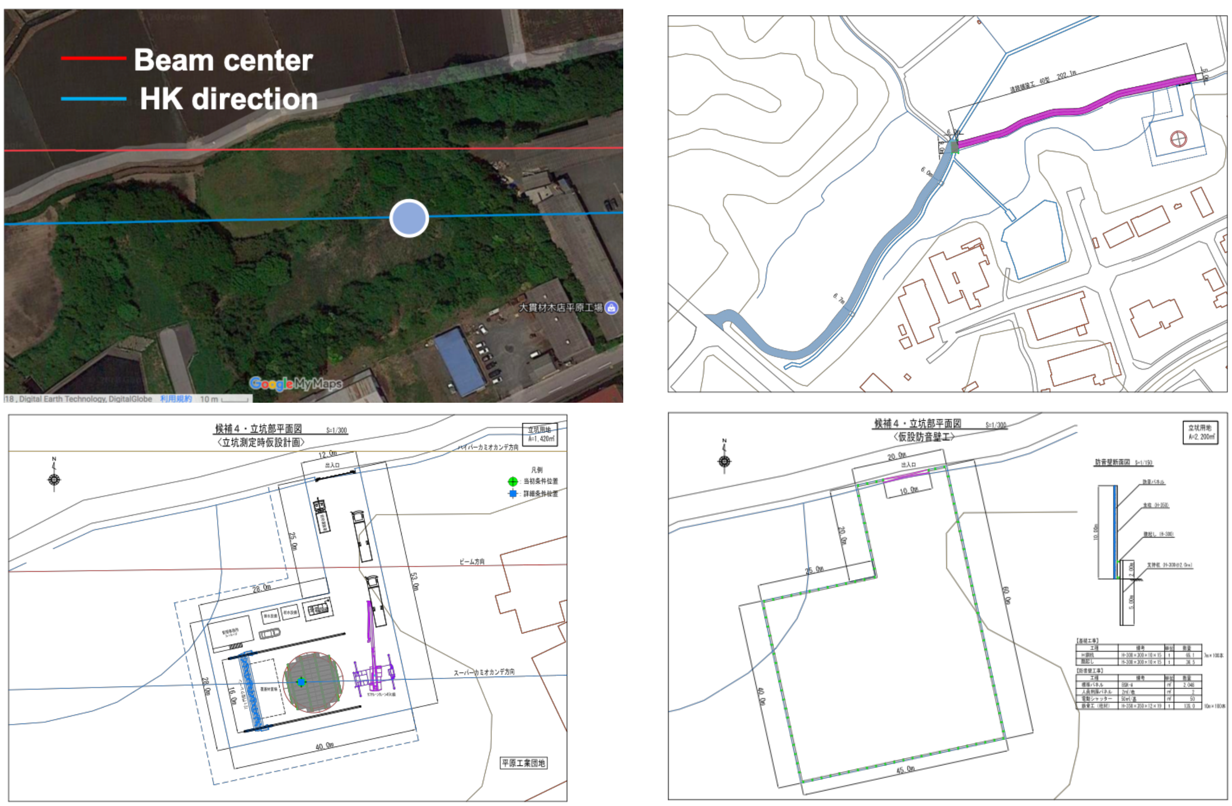

FIG. 67. Left-top: map around candidate #4. Red and blue lines show the direction of beam center and direction toward Hyper-Kamiokande (Tochibora site), respectively. Circle indicate the size of 11 m diameter pit although the position is not precisely fixed. Right-top: extension of access road for candidate # 4. Left-bottom: conceptual design for construction. Right-bottom: design of soundproof wall.

by such assumptions based on existing nearby boring data of J-PARC[2], publicly available boring data around the 1 km distance and dedicated boring data taken for the past 2 km site investigation. Based on the rock conditions, optimized excavation methods for each candidate location are determined for cost evaluation. In general:

- If the ground is composed of solid rock and does not contain ground water, the rock is excavated and pit walls are secured with rock bolts (anchors): NATM
- If the ground is composed of sand or soft soil, the structure of the pit wall must be created: opened caisson
- For a deeper pit (typically >40 m), the wall structure must be stronger to sustain the pressure: pneumatic caisson (expensive)

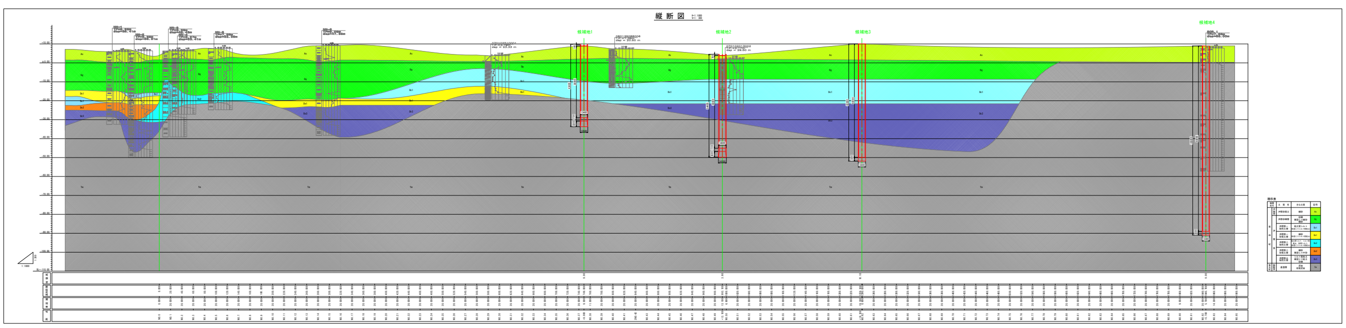

FIG. 68. Rock conditions along neutrino beam direction based on boring data and assumptions from the nearby boring data and geometrical feature. Vertical pit for candidate #1, #2, #3 and #4 are drawn by red colors.

D. Facility

Figure 70 shows the layout of IWCD facility. The water tank is assembled on surface and the detector components (PMT frame, mult-PMT modules, cables, etc.) are installed inside the laboratory building using a 1 ton crane. The detector water tank is then moved into the vertical pit with air-float. As the HV power supply and digitizer are included in mult-PMT modules, small electronics hut is sufficient on the surface. All DAQ computers and electronics can be stored with three racks.

[2] Many boring data exists in J-PARC for construction of accelerator and other facilities.

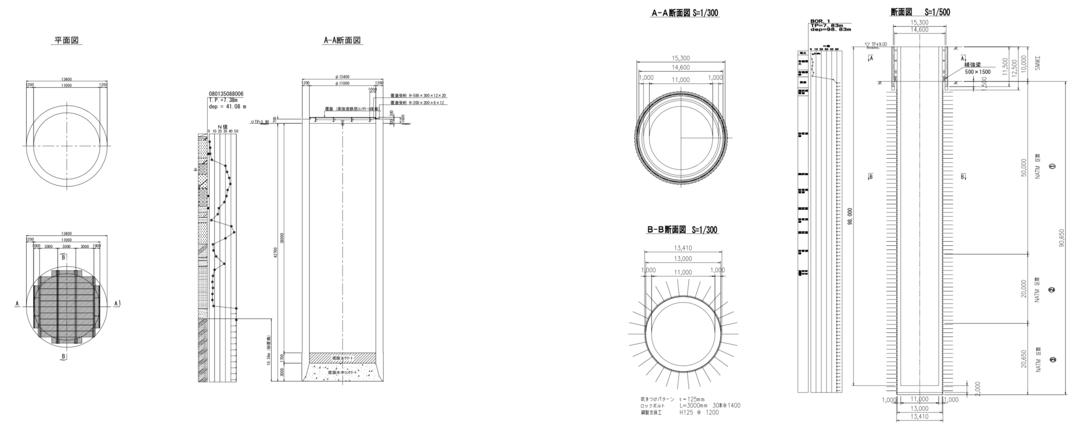

FIG. 69. Conceptual design of vertical pit for candidate #1 and #4, excavated by open caisson for candidate #1 and NATM for candidate #4.

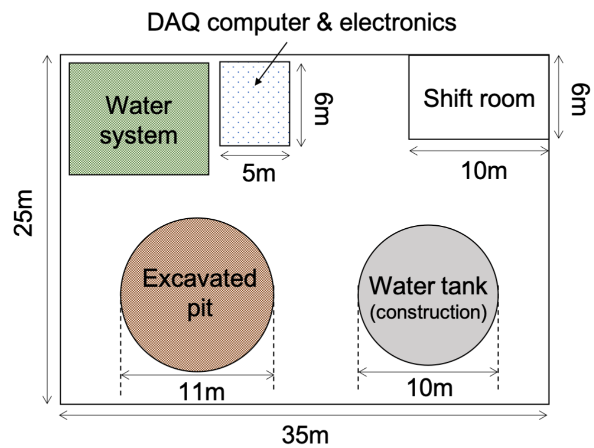

FIG. 70. Layout of IWCD facility.

E. Cost

Table XXII shows tentative estimates of the costs for IWCD facility.

TC: We need some discussion that summarizes the facility and cost and suggests how to proceed on the site investigation.

F. The IWCD Photosensors

The IWCD will deploy mult-PMT photosensors to detect Cherenkov photons produced in the inner detector and small PMTs surrounded by by wavelength shifting plates to detect photons in

TABLE XXII. Tentative estimates of the costs for IWCD facility. 8% tax is included. Unit is 1,000,000 Yen ($\sim$ 10,000 US Dollar).

	# 1	# 2	# 3	# 4
Ground acquisition[a]	0	81	81	0
Excavation[b]	814	1,129	1,263	3,486[c]
Lab. building[d]	133	133	133	133
Infrastructure[e]	64	64	64	64
Lifting mechanism	TBD	TBD	TBD	TBD
Total (w/o lifting mechanism)	1,051	1,406	1,540	3,683

[a] Ground acquisition costs assuming 2000 m^2 and average price in Tokai. Cost for use of Tokai village property is not accounted.
[b] Excavation costs include excavation, access road construction, retaining, construction and removal of soundproof wall, while ground acquisition cost for access road is not included.
[c] 2,227 for shallower pit at candidate # 4 with 70 m depth.
[d] Cost for laboratory building is from phase-0 surface detector with 18 m $\times$ 24 m area and 1 ton crane.
[e] Cost for infrastructure is from phase-0 surface detector in J-PARC.

the outer detector.

1. *multi-PMT design*

The multi-PMT is described in detail in Sec. III.8. The current design, shown in Fig. 132, has 19 PMTs facing into both the inner detector. This design is currently under development at TRIUMF.

2. *multi-PMT design changes for the IWCD*

The multi-PMT design for the IWCD is largely unchanged from the Hyper-K design. Potential differences are listed below:

- Mounting procedure - due to the different tank construction and PMT support structure this may differ from the Hyper-K approach. This will be better understood once the IWCD tank and support structure has been finalised.
- Penetrator design - the IWCD multi-PMT will include electronics for the OD PMTs, whereas for the Hyper-K OD PMTs this has not been decided. The IWCD penetrator would then have to include space for two additional cables for the OD PMT power and signal.

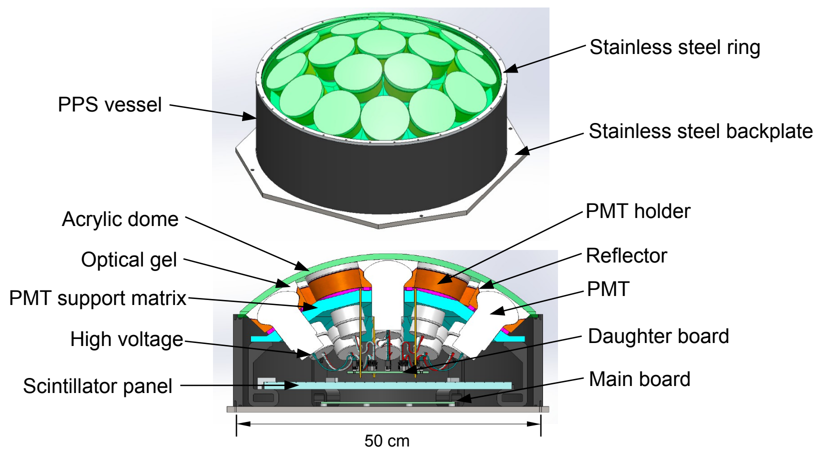

FIG. 71. Current design for the multi-PMT

- PMT HV polarity - The IWCD does not require as low dark noise rates as Hyper-K, so the PMTs may be run with a negative high voltage. In this case an HA coating will be applied to the PMT.

These small difference are not expected to impact the multi-PMT design or production schedule.

3. OD photosensor

The OD photosenor design is described in Sec. III.7 and is not expected to differ for the IWCD.

4. Electronics

The multi-PMT electronics design for the Hyper-K multi-PMT are described in Section III.8 B. Ideally we would re-use most or all of the Hyper-K multi-PMT electronics for the IWCD multi-PMT electronics. Two issues make this difficult. First, as noted above the IWCD does not require low dark noise rates, so it may be preferable to go with the simpler negative high voltage for the PMT.

Second, the IWCD detector will experience much higher event rates than HK. Up to 10% of bunches will have two fully contained events (after outer detector veto) for the most on-axis position. Single PMTs will often get hit multiple times in the same spill and sometimes multiple times in the same bunch. This imposes a stricter requirement on the mult-PMT electronics to be able to cleanly distinguish between different hits in different bunches and possibly between different hits in the same bunch. This requirement would suggest favouring the FADC digitization design for the IWCD multi-PMT electronics.

5. mPMT + OD assembly

Details about the multi-PMT assembly procedure are given in Sec. III.8 D. The most significant difference for the IWCD is the number of modules required, which will be between 500 and 1000 depending upon the height of the detector.

For the OD PMTs the assembly and production is discussed in Sec. III.7 D. There are not expected to be any differences between the HK OD PMTs and those for the IWCD.

G. The IWCD Data-Acquisition

The DAQ for the IWCD encompasses the systems for electronics readout, data storage, event building, triggering and time distribution for the detector. The DAQ software used to build and control these systems will be built on a scalable and modular framework called ToolDAQ and run on commercial computer hardware.

1. Electronics readout readout

The front end boards of the mult-PMTs will be read out using standard Ethernet connections of $\approx$100 Mb/s via either UDP or TCP protocols. These connections will be routed through commercial router hardware to allow redundancy in the destination of the data. Connected to this network will be $\approx$6 DAQ servers with 10 Gb/s connections designed to readout continuously the $\approx$2.5 GB/s of hit data made by the 685 multi-PMTs (this number can be reduced if the electronics can be remotely triggered to output only at beam spills). These machines will buffer and catalogue the data by timestamp and when a positive trigger decision is received the will write the data disk.

2. Triggering

Triggering of the detector will be achieved by beam spill information received from J-PARC. This will be read by another piece of electronics and the trigger signal sent to the readout machines to tell them to save that segment of the detector data to disk. Further data windows can be opened to collect cosmic ray data as well as calibration data as needed. If the multi-PMT electronics boards can also receive external trigger signals this could then be further relayed to them to initiate readout.

TC: How is the trigger signal transfered to the IWCD site?

3. Timing

A GPS receiver will be used to generate a timing signal, which will then be distributed to the front end and readout electronics. There are a couple of possibilities as to how achieve this distribution of the timing. We could either use a white rabbit variant to pass the timing signal down the data network connection lines or use a separate pair of cables to and the 1pps of the GPUS with an oscillator circuit to produce a common clock. This second method could be achieved with commercial time distribution hardware.

TC: Can you expand on the second approach? It is not clear from the text.

4. Computing requirements

The on-site computing requirements for the DAQ are:

- 6 DAQ servers with 10 Gb/s connections.
- 2 gateway servers
- 2 servers for command and control webserver and SQL
- 1 disk server for onsite data backup.

H. The IWCD Calibration Systems

The IWCD is a water Cherenkov detector and its calibration system uses similar calibration methods as the Hyper-K detector, such as the diffused/collimated light sources on the wall and deployment of a laser ball, Ni source, and AmBe source. Special consideration is required for the smaller scale of the IWCD detector. The fiducial volume is relatively small compared to the full volume, making stringent requirements on the vertex reconstruction. Characterizing the detection efficiency also becomes a challenge as most of the active volume is near the volume where the efficiencies of event reconstruction and particle identification varies. Finally, we need to develop the calibration system on the moving platform of IWCD.

There are examples of water Cherenkov detectors similar to the IWCD in size (1kton), such as Kamiokande, IMB, the K2K 1kton water Cherenkov, and SNO. The systematic errors on efficiency are several % or more, which is significantly larger than what is required for IWCD of 1-2%. As a matter of fact, this is one of the most challenging aspects of IWCD and a critical point for the success of the Hyper-K project. The SNO experiment did the most precise measurement among small water Cherenkov experiments. They observed their efficiency error is limited by the uncertainties in the angular responses of PMTs and the positions of each PMT in the vessel, which are tightly related.

In addition to the calibration sources similar to SK/HK on the moving platform, the IWCD will use geometrical calibration by photogrammetry and ex-situ calibration of angular response at the photosensor test facility (PTF). In order to calibrate against the physics process, such as the response to hadron interaction and light scattering in the detector, a beam test is planned to establish this state-of-the-art calibration for the smaller scale water Cherenkov detector.

1. Calibration sources and their deployment system

The depoyment system considered is a manipulator arm deployed from the top of the tank. The system is similar to the ones used by KamLand, a manipulated bar, or a manipulated source like Daya Bay and SNO. The former has an advantage of providing a well defined scale between multiple source positions. The deployment system will be mounted on the tank that moves up and down the shaft. Since we cannot access to the deployment system, a grab box similar to other experiments would not work. An automated source exchange system or multiple deployment systems for each sources, would be required. The deployment system will deliver the diffuser ball, Xe ball, Ni source, and Am-Be sources at various positions in the detector. It will also deploy the camera for photogrammetry, as discussed below. There will be fixed LED light sources developed for HK on the walls to provide both focused and diffused lights.

2. Geometrical calibration by photogrammetry

The photosensors will receive large buoyancy force when filled with water and their position shifts. The force will also cause the distortion of the support structure. The displacement was as large as several centimetre for SNO, and the distortion of the tank was apparent by eye in the case of 1kton for K2K. For both SNO and K2K analyses, analysis was done without taking the displacements into account, since there was not a good way to measure them. SNO+ developed a new technique of monitoring the PMT positions using photogrammetry. High resolution digital camera images can be used to reconstruct the 3D image of the object (photogrammetry). With a 12M pixel camera, SNO+ tests in a swimming pool achieved 0.5-1 cm precision in reconstructing the image. Six camera's are currently installed in SNO+ detector. For the IWCD, 50M pixel to 120M pixel camera will be deployed with a manipulator system, providing pictures of the detector at various positions and angles. By fitting the image with camera positions and angles, a 3D image of the inner surface of the detector can be reconstructed, similar to what is done by free 3D photogrammetry softwares.

3. Ex-situ calibration of mPMT angular response

The angular response of the photosensor is one of the biggest systematic uncertainties, in particular when it is coupled with the displacement of the photosensors. At photosensor test facility, detailed angular response of the photosensor can be mapped by injecting light at various positions and angles.

4. Water Cherenov Beam test

Physics description of the Monte Carlo simulation is not perfect, and the only way to test it is to inject well understood particle and measure the detector response. For the water Cherenkov, the particles go through interaction with the water such as hadronic interactions for hadrons, electromagnetic interactions such as delta ray production, and Cherenkov light scatterings in the water. A beam test of a prototype water Cherenkov detector would provide an opportunity to test these physics processes, along with the detailed detector calibration discussed above to demonstrate and establish the state-of-the-art calibration required for IWCD. A test of a 3-4 m diameter and 3-4 m tall detector in available test beams at Fermilab and CERN is feasible. Fig. 72 shows a conceptual configuration of the test beam experiment and an example design of the detector instrumented with 132 multi-PMT modules.

TC: The IWCD schedule and total budget should be added.

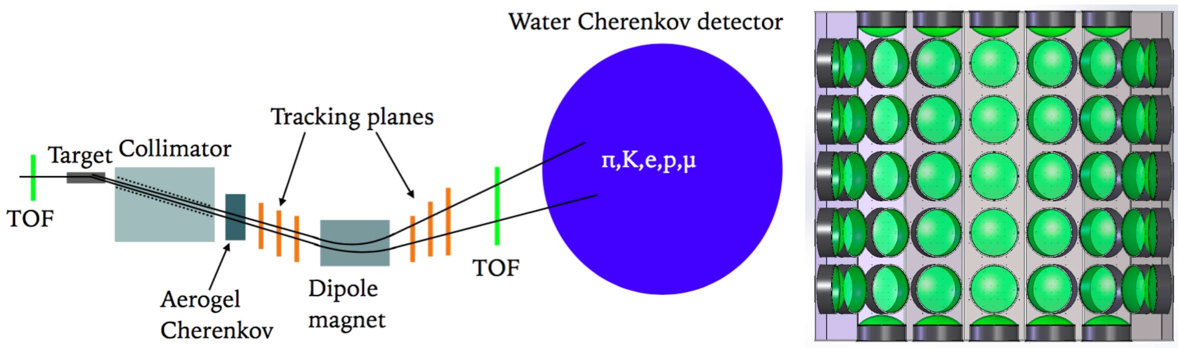

FIG. 72. Left: conceptual design of the beam for the water Cherenkov test experiment. Right: View of half of the detector for the design of the test experiment detector with 132 multi-PMT modules.

Part III

The Hyper-Kamiokande Far Detector

TC - This text is transferred from p.52 of the DR. Should also add Figures 17 & 18 from the DR.

The Hyper-K far detector site is located 8km south of the Super-K site. It is in the Tochibura mine of the Kamioka Mining and Smelting Company (KMS), near Kamioka town in Gifu prefecture, Japan. The J-PARC neutrino beam is designed so that the existing Super-K detector has an off-axis angle of 2.5°, and the Hyper-K site is chosen to have the same off-axis angle, but on the opposite side of the beam axis in the North-South direction. The Hyper-K experiment will be accessible via a drive-in access tunnel in a similar way to Super-K. This horizontal tunnel will be ≈2.5km long. The detector will lie under the peak of Nijuugo-yama, with a rock overburden of 650 metres, equivalent to 1,750 metres of water (m.w.e). It is at an altitude of 514m above sea level, with geographical coordinates Lat. 36°21'20.015"N, Long. 137°18'49.137" E.

The site is surrounded by several faults, and the caverns and their support structure are placed so as to avoid a conflict with the known faults. The site has a neighbouring mountain, Maruyama, just 2.3km away, whose collapsed peak enables us to dispose of more than 500k m^3 of rock from the detector cavern excavation.

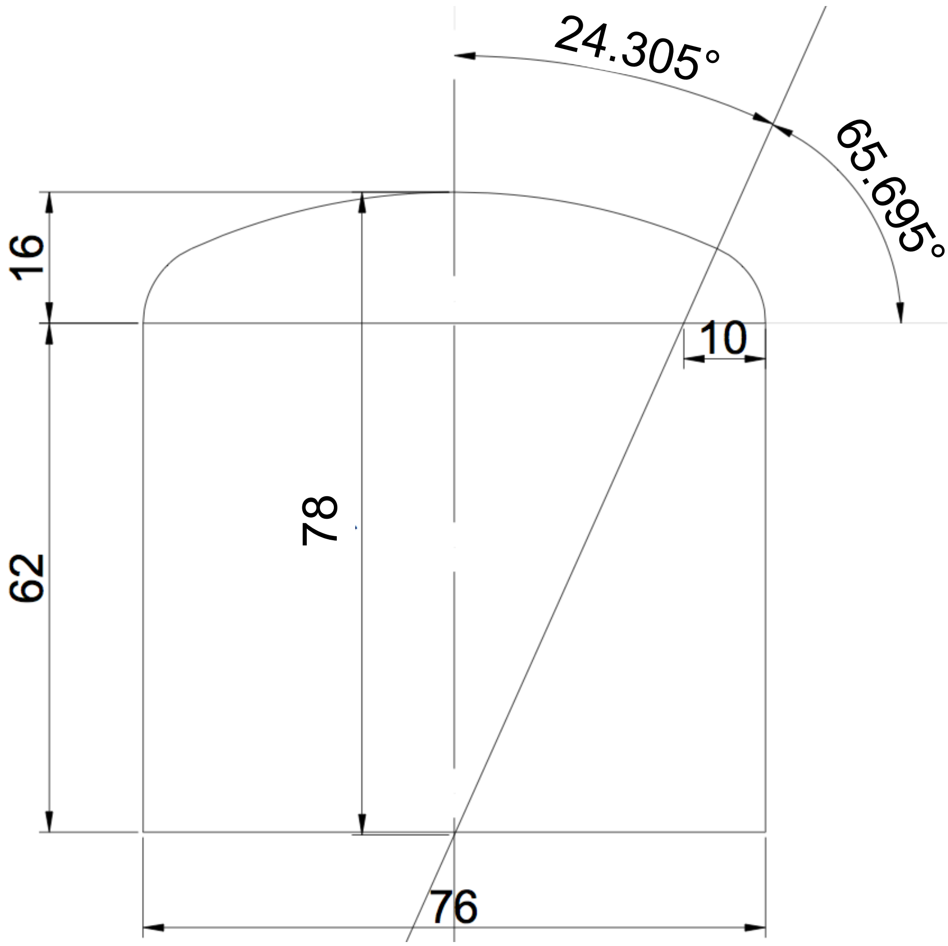

FIG. 73. The dimensions of the Hyper-K cavern in the baseline design. The units are metres.

III.1. DETECTOR CAVERN

TC - Note that possible changes in these dimensions were presented at the Collaboration Meeting, which might reduce the cost. The cavern excavation is the largest single cost driver for the realisation of Hyper-K, and also has the longest timescale for completion. Preliminary costings and timelines were shown at the Collaboration Meeting, and both costs and timelines should be added to this document in due course. This section will need updating after further discussions with the construction companies.

The huge cavern for the Hyper-K detector will be excavated under the peak of Mt. Nijuugo-yama. In the baseline design, the cavern has a cylindrical portion of 62 m in height and 76 m in diameter under a 16 m high dome-shaped space (see FIG.73). The total volume of the cavern is approximately 330,000 m^3.

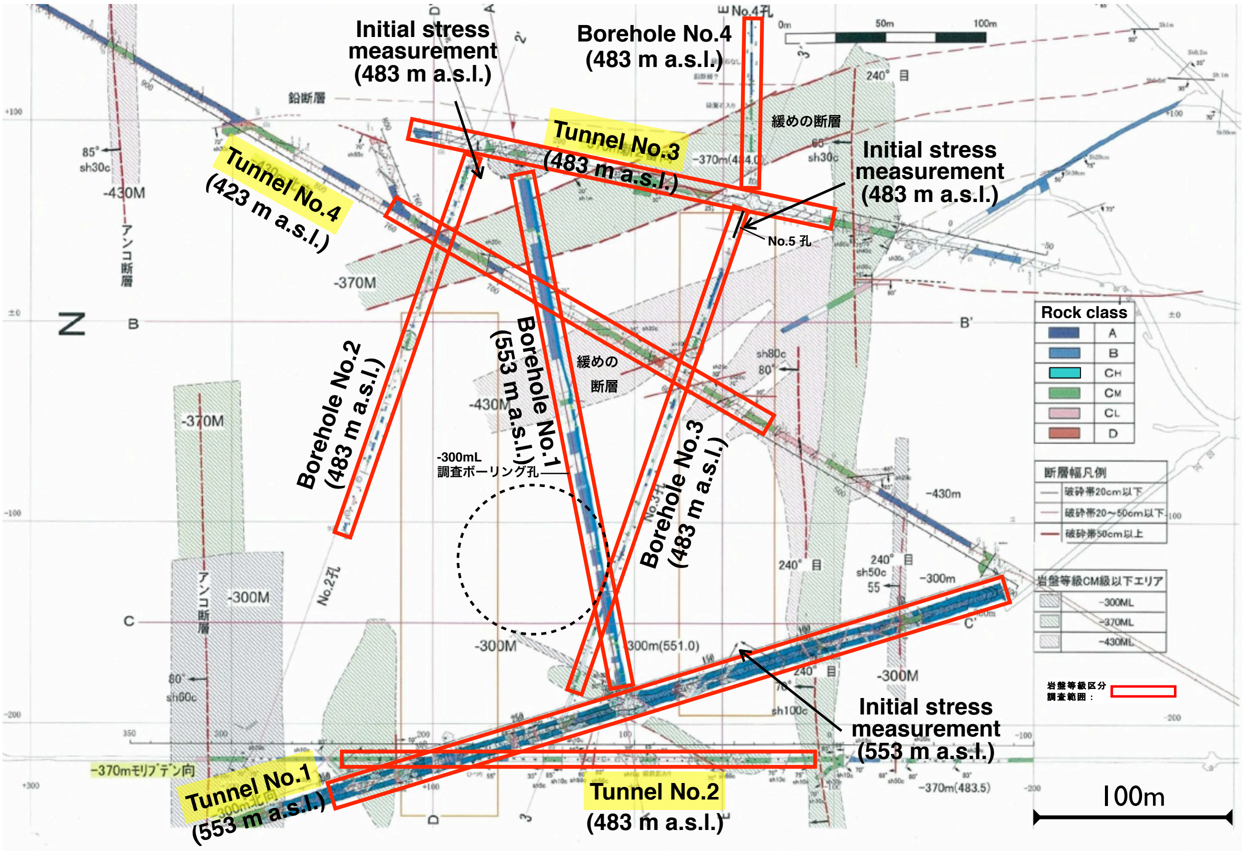

FIG. 74. The rock class distribution at the Hyper-K cavern site obtained by the tunnel and boring geological survey. Horizontal tunnels and boreholes located at various vertical levels (a.s.l.) are projected onto a horizontal plane and represented by the red rectangles. The dashed circle indicates the planned position of the Hyper-K cavern.

A. Geological Survey and Excavation

TC - Here it would be useful to add Table VIII from P.55 of the DR

The rock quality at the detector site has been investigated by examing the wall surface of existing mine tunnels and by sampling borehole cores. Figure 74 shows the rock quality in these tunnels and boreholes classified according to the DENKEN system as A (Solid), B (Very Good), CH (Good), CM (Fair or Medium), CL (Poor or Weak) and D (Very Poor/Very Weak), according to the method developed by the Central Research Institute of Electric Power Industry (CRIEPI). The fraction of the good rock (A, B and CH) is about 95% in the tunnel No.1 and the borehole No.1, which are located at the level of the shoulder of the cavern (553 m above sea level). In contrast, the tunnels and boreholes located at the level of the cavern bottom (483 m above sea level) have a lower fraction of the good rock, about 80% in the borehole No.3 and about 60% in

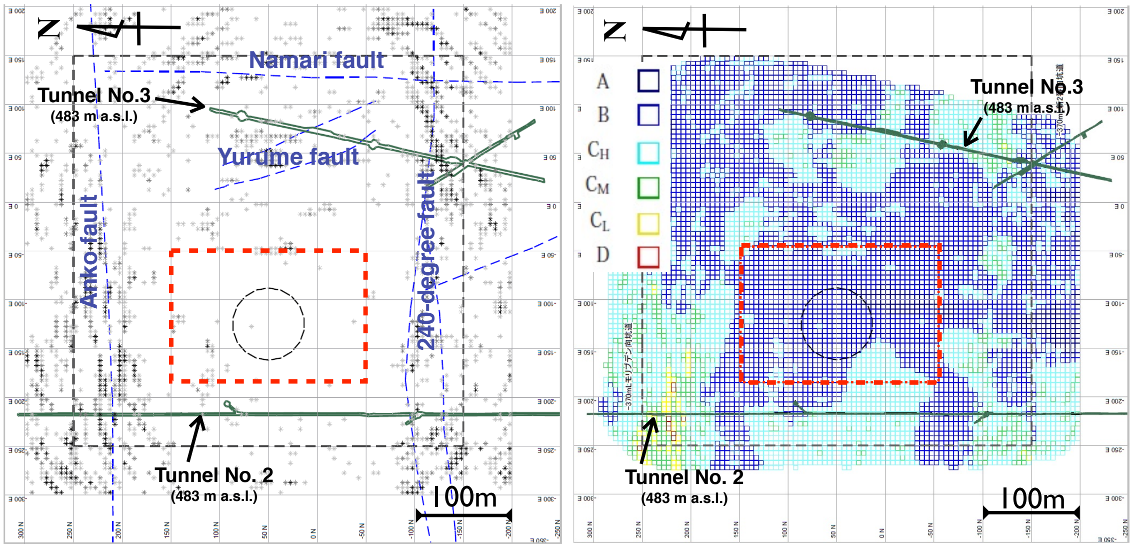

FIG. 75. Results from the seismic prospecting at the Hyper-K cavern site. The left-hand figure shows a horizontal slice at 483 m above sea level of the reflection point distribution, and the right-hand one shows the rock class distribution in the same horizontal slice. The black dashed circle in each figure indicates the size of Hyper-K cavern, and the red boxes show the best candidate region obtained by the seismic prospecting.

the other tunnels and boreholes.

To identify the best candidate region which has good rock quality and no fault/fracture zones, a wide-area 3D seismic survey was carried out using existing mine tunnels. Seismic prospecting uses artificially generated elastic waves. These waves propagate faster (slower) through harder (softer) rock, and they can be reflected if there is a discontinuous or uneven structure. The left-hand plot in Fig.75 shows the reflection point distribution at 483 m above sea level. The results indicate that there should be no major fault/fracture zones in the central region of the candidate area. The right-hand plot in Fig.75 shows the rock class distribution derived from the measured velocity of the elastic waves and the reflection amplitude at each point. Based on the results from the seismic prospecting, the best candidate region for the Hyper-K cavern excavation is identified as shown by the red dashed boxes in the figures.

The support of the Hyper-K cavern surface wall is designed based on the geological information obtained by the surveys. Figure 76 shows the plastic region in the cavern wall without any support. Here, the cavern is assumed to be surrounded by uniform CH-class rock. The depth of the plastic region is estimated to be 12 m at most, and the structural stability of the cavern can be achieved by using existing cavern construction technologies.

While the geological surveys that have been completed already show the feasibility of the re-

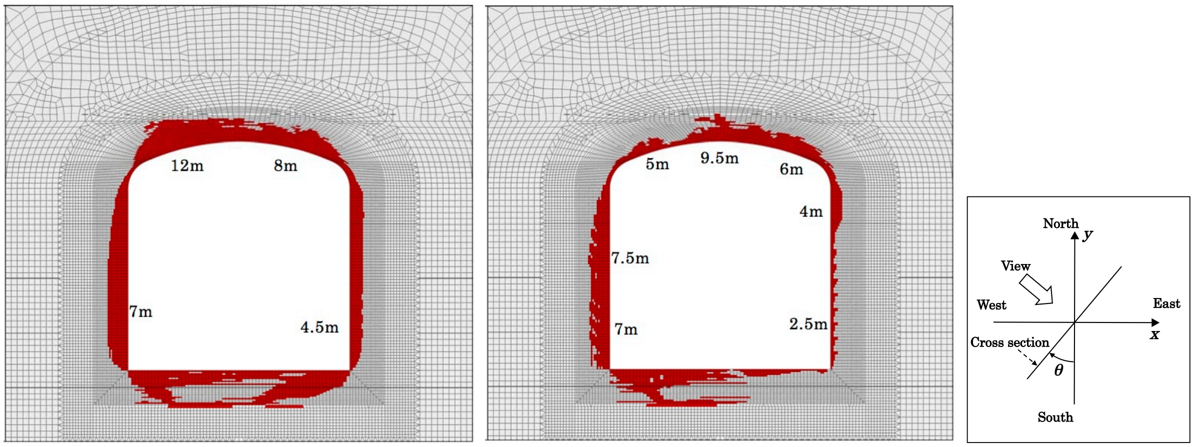

FIG. 76. The plastic region at 45 degree (left) and 105 degree (middle) slices with an assumption of the uniform CH-class rock distribution. The right-hand figure shows the definition of the view angle.

quired cavern construction, further detailed surveys in the vicinity of the candidate site will be conducted for the final determination of the cavern location and to support the design work before starting the cavern excavation.

B. Access Tunnels

TC - Alternative designs for the main access tunnel were shown in the Collaboration Meeting, so this section may need updating.

A 2.5 km-long access tunnel needs to be constructed from the entrance at Wasabo to the Hyper-K site. This access tunnel is used to transport heavy machinery, for dump trucks extracting the rock, and for other infrastructure necessary for the Hyper-K detector construction. Figure 77 shows the proposed layout of the access tunnel.

Since the Hyper-K access tunnel is a "dead end", it is desirable to have a second access tunnel making a connection to another mine entrance. If Hyper-K has a physical connection to an existing KMS tunnel, it secures an additional evacuation route from underground in case of emergency. It would also make it possible to have a natural flow of air, and to supply electrical power by a more direct route. At the moment there is no agreement between KMS and Hyper-K to make a connection to an existing KMS tunnel, and to use it for the installation of infrastructure for the cavern.

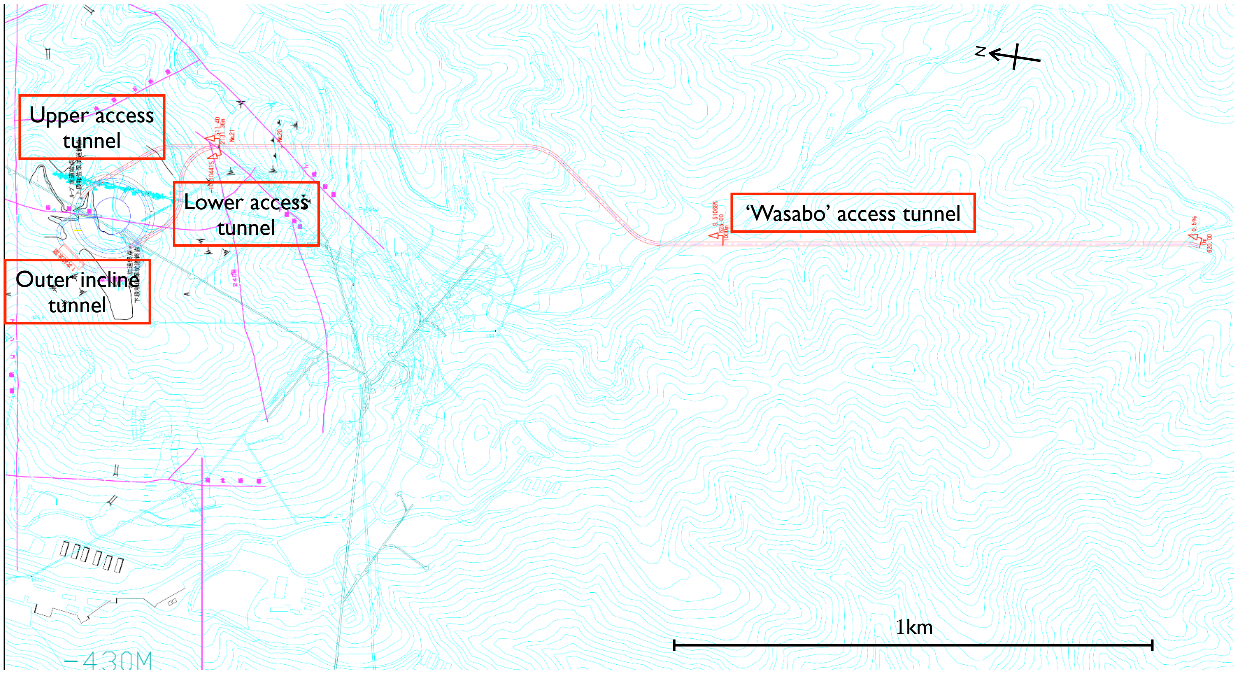

FIG. 77. Overview of the access tunnels.

C. Waste Rock Disposal

Approximately 570k m^3 of excavated rock from excavations of the access tunnel and Hyper-K cavern will be transported from the mine entrance (Wasabo) to Maruyama by dump trucks and disposed of as an accumulated pile in a sinkhole on the top of Maruyama. At the Wasabo site the excavated rock needs to be sampled for chemical analysis to ensure the heavy metal content in the excavated rock is less than a threshold defined by laws and regulations.

For transportation of the excavated rock, the existing roads (a prefectural road and KMS's private road) will be used, but they need to be improved and reinforced to allow smooth traffic of a huge number of dump trucks. In addition to the improvement of the existing roads, two new sections of road are planned to be constructed. Figure 78 shows the route of the excavated rock transportation.

TC - Much better pictures of this route were shown in the Collaboration Meeting, although one of them is marked as Confidential. A pity that no details of the environmental survey of Maruyama are given here. There is a lot of detail on geological surveys of the Maruyama site, and of the proposed design of the rock disposal place in the DR. This should be added to this section.

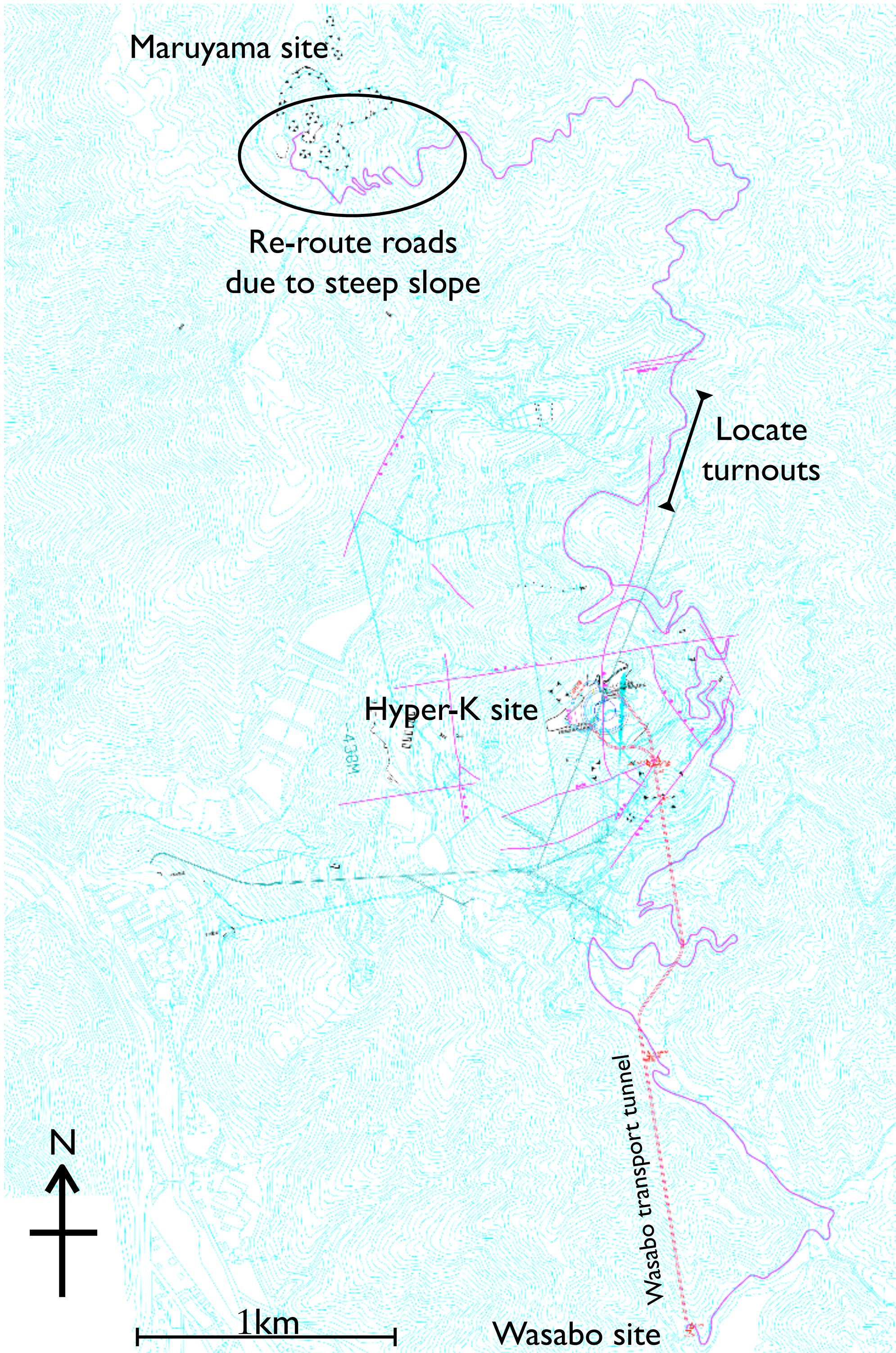

FIG. 78. Overview of the excavated rock transportation routing from the Hyper-K site to Maruyama. The magenta line denotes the transportation route from the Wasabo entrance to the Maruyama rock disposal site.

Before the construction work of the route and the rock disposal at Maruyama can begin, permission and agreement from local governments (Gifu prefecture, Hida city) are required.

D. Entrance Yard

TC - Some better figures of the design of the entrance yard were shown in the Collaboration Meeting.

An entrance yard of approximately 10,000m^2 needs to be constructed in front of the access tunnel. This entrance yard will be used as the base for the tunnel/cavern excavation work. The candidate site for the yard is the area around the exit of the transport tunnel in the Wasabo accumulation site which is managed by the mine company. Figure 79 shows the Wasabo accumulation site and the planned entrance yard.

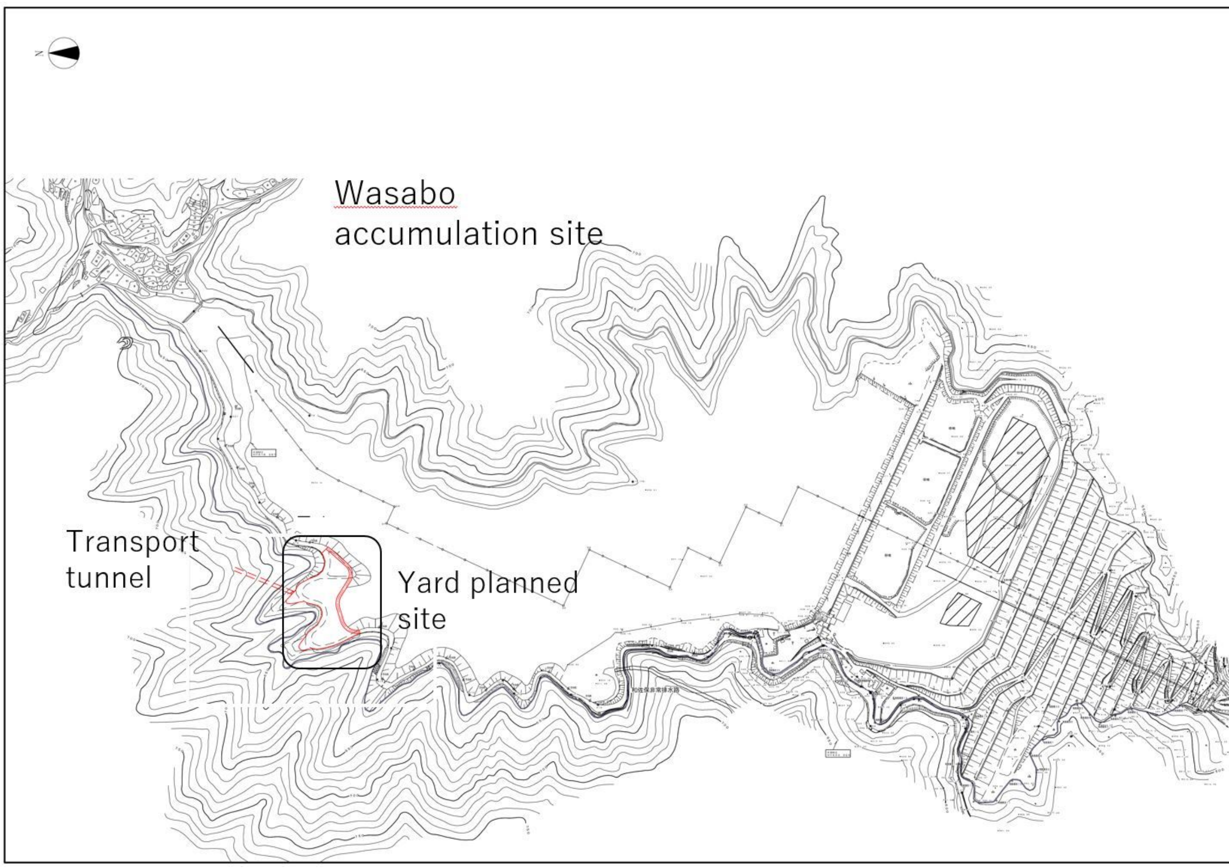

FIG. 79. The Wasabo accumulation site and the planned entrance yard.

To make a firm ground for the yard, the removal of the accumulated material and the re-filling of earth are planned. A prefectural road cuts through the candidate site for the yard. To avoid interference with the frequent passage of construction vehicles, it is required to relocate this road to the outside of the yard. We need to discuss this with the local governments, comme up with the detail design and get the necessary permissions.

To complete the design of the yard a detailed survey and ground investigation are needed. These are ongoing.

TC - Details of these to be added later.

E. Waste Water Treatment

We need to construct a system for supplying the water necessary for drilling, and for the drainage and treatment of the waste water. This system will be located in the Wasabo entrance yard. The water is taken from and drained into the Wasabo river. For the drainage water, we need to get the permissions from the relevant organisations.

The requirement for the supply water is 90t/h for drilling and other activities during the excavation period. This supply needs to be prepared before the start of the access tunnel excavation. The expected amount of waste water includes some additional spring water, as well as the supply water from the river. The waste water for which drainage treatment is required is 100t/h during the excavation of the access tunnel. A significant increase in the amount of spring water is expected during the period of the main cavern excavation. For this we need to increase the drainage capacity to 300t/h. Figure 80 shows the present plan for the supply and waste water facility capacities related to the excavation schedule.

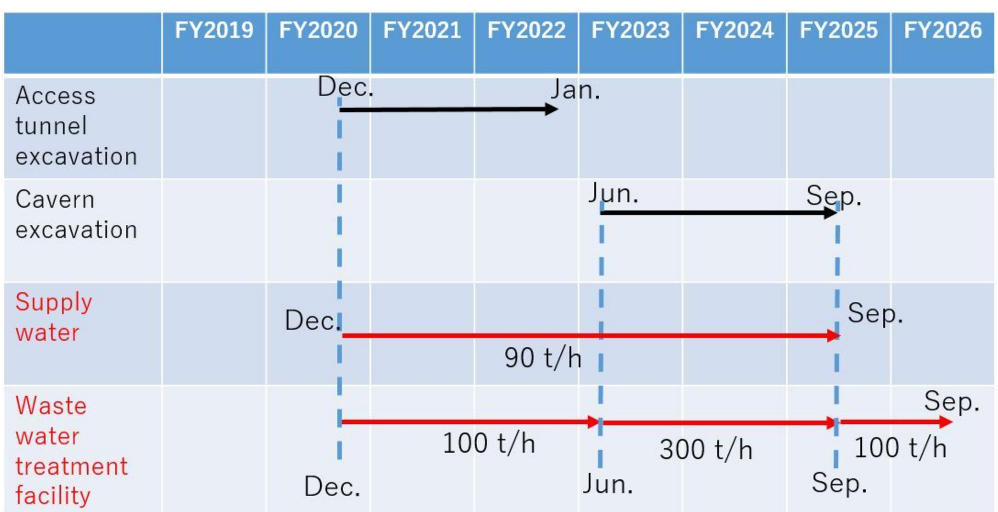

FIG. 80. Present schedule of the supply and waste water facility capacity.

F. Infrastructure

The infrastructure that is needed for the cavern construction has to be prepared before the start of the construction. It consists of the following items:

- Electricity supply.
- A fresh air transportation system.
- An air conditioning system.
- A telephone line.
- A network connection.
- Water and sewer services.
- Environmental monitors for O_2, CO_2 and Radon.
- A mine entrance system.

After the cavern construction this infrastructure will be needed for the installation and operation of the Hyper-K far detector. At this point it will to be necessary to enhance the infrastructure to provide additional power for the detector operation, better networking for data handling, and to provide more reliable systems for continuous detector operation over many years.

1. Electricity Supply

The expected electricity usage during construction is 900kW for the access tunnel, and 1700kW for the cavern excavation. The tank construction requires 400kW, and the fresh air system 500kW. The detector water system requires 1100kW for continuous circulation, 1200kW when filling the tank, and a further 120kW outside the mine for pumping the source water from the well to the main water system. The electronics and DAQ, including the HV for the photosensors is estimated to require 300kW, and the local computing resources require 1000kW. These expectations are maximum estimates, and may decrease depending on the eventual cavern construction method and schedule. For detector operations the electronics assumes full coverage of the inner detector with 20" PMTs.

TC - The sum of the contributions during continuous operation is 1100+500+300+1000=3000kW. This is inconsistent with the 2000kW specified for the power line in the subsequent figure and text.

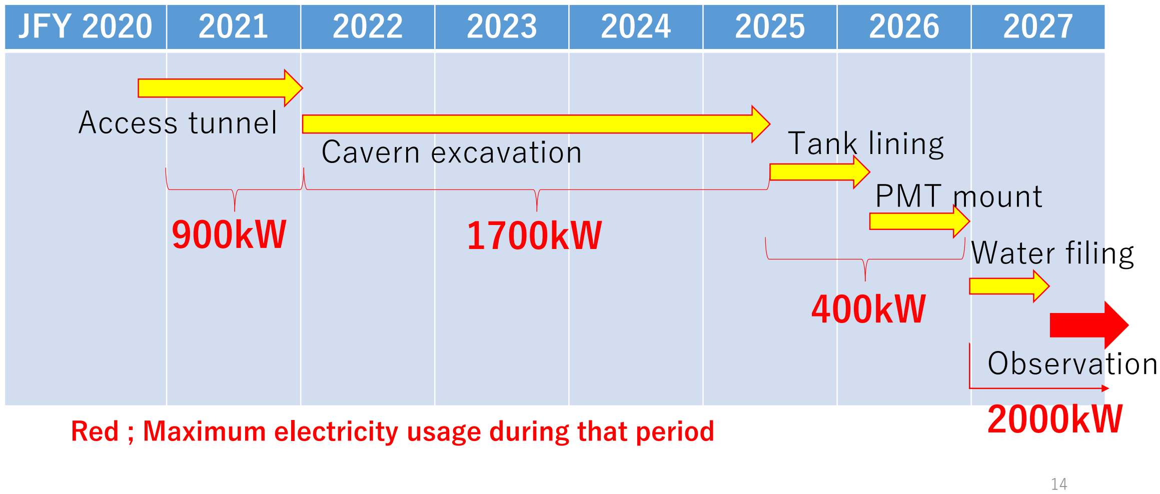

FIG. 81. Expected electricity usage vs. time

In this subsection, we mostly discuss how to prepare the electricity supply inside the mine, since this is the most urgent and difficult item. Figure 81 shows a time chart of the expected electricity usage during and after the construction. As shown in this time chart, a new power line which can send 2000kW needs to be prepared. Figure 82 shows the planned power lines to the Hyper-K detector. Electricity during the construction phase will be sent via the red dashed line, and electricity during the observation phase will be sent via the red solid line. Note that the first step of the construction is to make the access tunnel from the Wasabo entrance yard, so electricity for the construction needs to be received at the yard at the beginning of the construction phase. The proposed supply route is along the prefectural road 484 which is a relatively small road, and power cuts due to fallen trees might happen some times, especially during the winter. For the observation phase it is better to have a more reliable power line via a tunnel from the Shikama entrance in order to keep stable detector operations. Making a new tunnel from the Shikama entrance is still under discussion with KMS, and the plan is not fixed yet. Therefore we assume that at the begining of our observational phase, electricity might still be sent via the Wasabo yard.

Electricity for the construction needs to be ready by October 2020 in our current schedule. In order to get authorisations, we have already started discussions with Gifu prefecture and Hokuriku Electric Power Company, which will do the actual construction of the power poles and supply line. According to them, we need an authorisation to put new poles in the preservation area which is shown as a yellow area in figure 82, and another authorisation to put poles and do constructions along the prefectural road 484. In case the process takes too long, we are also discussing with KMS to see if they could supply us with electricity as a backup plan. To do this KMS would need to upgrade their electricity facility to send 2000kW for Hyper-K, at a cost of more than $5M.

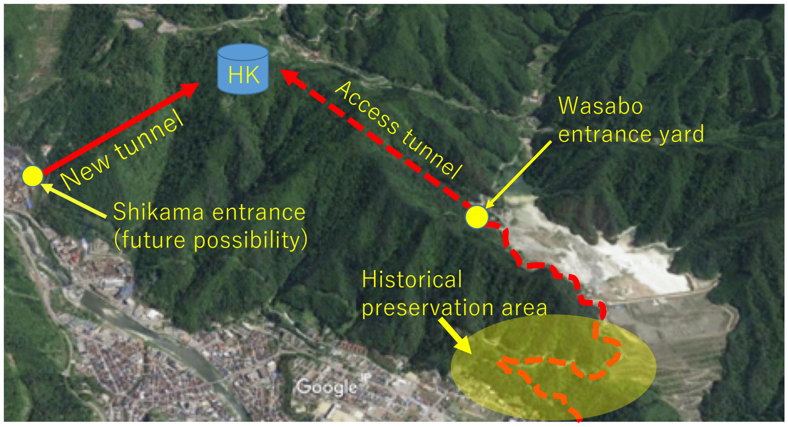

FIG. 82. Planned power lines for Hyper-K

2. Other systems

A fresh air transportation system is very important for ventilation, and to keep low Radon levels in the detector cavern. Super-K is currently sending fresh air to the detector cavern at about 100m^3/min. If we scale this with the detector volume, we will need 500m^3/min of fresh air in case of Hyper-K. The Super-K system has been maintained by the US group, so we consider this system to be a possible foreign contribution for Hyper-K as well.

Environmental monitors can be also prepared by foreign collaborators.

TC - This section comes to an end here, without describing any details about the other items on the infrastructure list.

III.2. WATER TANK

TC - A general introduction to the tank has been added, mostly taken from the DR. It would be useful to add some of the tank figures from the DR.

The walls of the excavated cavern are covered with a watertight lining to contain the ultra-pure detector water (including the Gadolinium, if we decide to add this). The lining consists of a backside concrete layer, onto which are attached polyethylene sheets. The cavern is divided into a cylindrical volume which will be filled with water, and a dome section at the top of the cavern known as the "on-deck" area, where calibration systems, huts for shifters, electronics and computing systems are located.

The dimensions of the water volume are 74.0m in diameter and 60.0m in height, giving a total water mass of 258kt. This volume is segmented into an inner detector (ID) of 70.8m diameter and 54.8m height (216kt), used to measure neutrino interactions and proton decays, and an outer detector (OD) region used to veto incoming muons, with a thickness of 1m in the barrel region, and a thickness of 2m in the top and bottom endcaps. Between the ID and the OD regions there is a "dead space" of 0.6m thickness occupied by the ID and OD photosensors, their support structure, and the front-end readout electronics. The photosensors and readout electronics are described in Section III.6 (ID photosensors), Section III.7 (OD photosensors) and Section III.9 (electronics).

A. Tank Lining

TC - Should add some figures of the tank lining, e.g. those from the DR.

The tank lining covers the inner surface of the Hyper-K cavern, and contains the ultra-purified water which may have added gadolinium sulfate $Gd_2(SO_4)_3$. The lining structure should prevent any leakage of the detector water and any inflow of external water into the tank from the surrounding rock. The lining structure should also act as a barrier to radon entering the tank from the rock, and should prevent any dissolution of other impurities into the medium. The durability of the tank lining should be ~ 30 years. A plug manhole made of stainless steel should be built at the lowest part of the side wall for future maintenance work. There also need to be holes in the bottom and top of the tank for the pipes for filling, draining and circulating the water in the tank.

TC - How will seals be made between the HDPE and these holes?

The lining structure is to be constructed inside the cavern bedrock by first coating the rock

Material property	Nominal value
Thickness	5.00 mm
Density	0.94 g/cm^3
Yield strength	15.2 MPa
Elongation at break	500%
Carbon black content	2−3%
Pigment content	1.5−2.5%
Notched constant tensile load	400 hours
Thermal expansion coefficient	1.20×10^{-4}/C°
Low temperature brittleness	−77 C°
Dimensional stability in each direction	±1.0%
Water vapour transmission	$<$ 0.01 g/m^2/day
Typical roll dimension	2.44m × 59.73m

TABLE XXIII. Properties of a candidate CPL taken from the specifications by Studliner, GSE Environments. *TC - This table has been added from the DR.*

with a shotcrete layer. Between the shotcrete and the inner tank lining a backfill of concrete is used. A waterproof sheet is installed between the shotcrete and backfill concrete with the aim of conveying away water coming either from small leakages from the tank through the inner lining and backfill concrete, or from water from the bedrock penetrating through the shotcrete.

The tank lining material is a Concrete Protective Liner (CPL) made of High Density PolyEthylene (HDPE). The material properties of a candidate CPL are given in Table XXIII. It consists of between 2mm and 5mm thick sections of HDPE with a number of studs protruding from one side, that lock the liner into the surface of the backfill concrete to prolong the service life of the concrete structure. HDPE is a thermoplastic resin, containing a linear polymer prepared from ethylene (C_2H_4) by a catalytic process. The absence of branching results in a closely packed structure with a high density (greater than 0.94), which is harder, more opaque, has a higher chemical resistance, and a higher temperature resistance (120° Celsius for short periods, 110° Celsius continuously), than Low Density Polyethylene.

The elution of impurities from HDPE and the change of light absorbance were tested both in ultra-purified water and in a 1% gadolinium sulfate solution. A certain amount of material elution was observed (organic carbon, anions, and metals), and an increase of the absorbance was measured at wavelengths lower than 300nm. Since the PMTs are sensitive to wavelengths between 300nm and 650nm, the effect of this change in absorbance on the experiment is limited. In any case it is anticipated that we will add titanium dioxide (TiO_2) or a reflective layer of Tyvek on top of the HDPE to improve the veto performance of the OD.

We have made breakdown tests by applying localised water pressure. This looks at possible situations where there are cracks or holes in the backfill concrete wall. The HDPE lining survived these tests without breaking. Tests for tensile and share stress were also performed by making deformations with a 1mm gap or step in the backfill concrete, and no damage or leakage was observed in the HDPE lining. Although the lifetime of HDPE is expected to be more than 500 years at 15° Celsius, actual tests of the long term stability are being considered.

The plan for the installation of the tank lining is to install the CPL sheet and the waterproof sheet at the same time as pouring the backfill concrete, which is set to the inside of moulds. Adjacent CPL sheets are joined together using an extrusion welding method in which molten HDPE filler is fed into the joint from the barrel of a mini hand-held extruder based on an electric drill.

A leakage detection and drain system has to be installed. Holes in the CPL sheets with size of >0.5mm, including those on the welded seams, can be identified by a high-voltage pin-hole test and by a negative pressure test. The effect of holes in the CPL sheets <0.5mm in diameter can be measured by collecting and controlling the amount of leakage water. HDPE plastic mouldings are embedded together with the CPL in the backfill concrete. These work as partitions at a pitch of 10m in the direction of the circumference of the tank. Water leaks from the CPL(s) or seam(s) in each partition are collected individually, so that detectors installed at the bottom can identify which partition has a leakage problem. Water leaks from the outside bedrock can be separated from water leaks through the CPL and cracks in the backfill concrete by the waterproof sheets. These external water leaks will be drained separately.

B. Geomagnetic Compensation Coils

TC - This brief summary is taken from the equivalent section of the DR.

The photon collection efficiency of the ID photosensors decreases when a magnetic field is applied, especially in a direction perpendicular to the PMT. For the 20" B&L PMTs these decreases have been measured to be ≈1% at 100mG, increasing to ≈3% at 180mG. In contrast no decrease is observed when applying 200mG parallel to the PMT. The goal of the geomagnetic compensation coils is to reduce the Earth's magnetic field of 470mG (320mG Horizontal, 360mG Vertical), to

<100mG in the directions perpendicular to the PMTs.

The compensation coils will either be attached to the surface of the water containment tank lining, or they will be embedded in the backfill concrete layer (this has yet to be decided). The coils are assumed to be a combination of vertical rectangular coils and horizontal circular coils. For simplicity the spacing between the coils has been set to be 2m in both directions. Constant currents I_V and I_H are applied to all the coils except for the top and bottom horizontal coils which have some additional windings in the coils to increase the current. This helps to reduce the perpendicular field in the top and bottom tank corners.

Studies have determined the optimal currents to be I_V =60A, I_H =67A, giving a typical value of $B_\perp$ =50mG, and a fraction of ID PMTs with $B_\perp$ <100mG of 97.8%. The worst affected PMTs are in the upper and lower corners.

The power consumption of the compensation coils is estimated to be about 10 kW, assuming a 4-conductor cable with 0.491Ω/km. This is 50% higher than the equivalent system in Super-K, but is still reasonable.

C. Photosensor Support Frame

TC - Need to add an updated table of the loads. Also need figures showing the arrangement of the suspension points at the top, and the attachment points at the bottom.

The structural framework on which the ID and OD photosensors are mounted is made of commercially available SUS304 shaped steel. The supporting frameworks for the top endcap and barrel parts are truss structures hung from the ceiling, while the support for the lower endcap is freestanding on the bottom of the tank. This differs from Super-K where the barrel part was also freestanding on the ground. The reason for this change in Hyper-K is that a suspension structure can be built with relatively thinner and lighter steel members, resulting in a lower construction cost, while a freestanding structure needs thicker and heavier members to avoid buckling. The anchor bolts for the suspension points for the top endcap and barrel structures are embedded in the ceiling rock during the excavation of the dome part of the cavern. In Table XX, the weight loads are listed.

The support frame is designed to support the weight of the photosensors with their covers and associated front-end electronics.

When the tank is filled with water, the overall load to the framework is reduced by the buoyancy

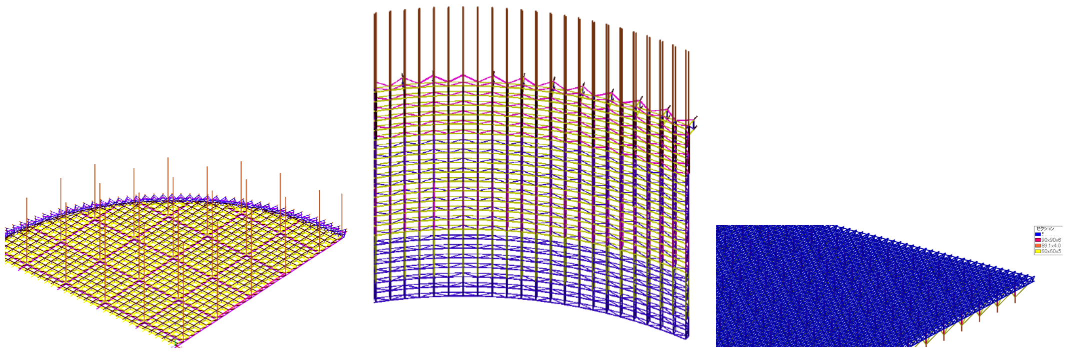

FIG. 83. The frame structure of the the deck (left), the barrel (center), and the bottom part(right)

ID photosensor	(/PMT)
50 cm PMT	13 kg
Protective cover	39 kg
Cable for readout/power supply 10m	2 kg
OD photosensor	(/PMT)
20 cm PMT	2 kg
Protective cover	8 kg
Wavelength shifting plate	5 kg
Cable for readout/power supply 10m	2 kg
Underwater electronics (for readout/power supply)	47 kg/unit
Network cables connecting adjacent underwater electronics	2 kg/unit
Water system pipes (65A PVC)	1.4 kg/m
Calibration system (with 200A SUS pipe holes)	1000 kg/m^2 $\times$ 4
	100 kg/m^2 $\times$ 16
Other distributed load on the roof	100 kg/m^2

TABLE XXIV. List of major weight loads taken into account for designing of the supporting framework.

of the various components. This buoyancy is a very important factor in determining the design of the framework. In order to make full use of the economic advantages of the hanging structure for the barrel, it is designed so that almost no load is applied to the framework by buoyancy when the tank is full of water. If the buoyancy is too large, it is necessary to attach a weight to the lower part of the framework so that it does not float. When a heavy load is applied to the framework, on the contrary, it is necessary to adjust the framework stainless steel to a thicker one to support the full weight when the tank is empty. It is necessary to pay attention to the loading condition

	Design report case	medium weight case	light weight case	heavy weight case
Number of ID PMT (BL type)	40,716	20,358	20,358	20,358
PMT wight	12.8 kg	9 kg	9 kg	9 kg
Cover weight	38.7 kg	23 kg	13 kg	31 kg
Light collector wight	0 kg	3 kg	0 kg	6 kg
Cable weight	2 kg/10 m	2 kg/20 m	2 kg/20 m	2 kg/20 m
Attachment wight	3.1 kg	0.9 kg	0.9 kg	0.9 kg
Buoyancy (1/PMT)	-70.1 kg	-73.4 kg	-74.1 kg	-76.5 kg
Number of ID multi-PMT	0	6,786	0	10,030
PMT wight	0 kg	44 kg	0 kg	61 kg
Buoyancy	0 kg	-46 kg	0 kg	-30 kg
Number of OD 8" PMT	6,822	6,822	6,822	6,822
Weight including light collector *etc.*	19.3 kg	11.4 kg	11.4 kg	18.9 kg

TABLE XXV. The condition of the test three cases.

on the structural framework, such as the numbers of PMTs and the design of the PMT covers, and to design the framework accordingly. We conducted three case studies to see this buoyancy issue. The three conditions are 1) medium wight, 2) light weight, and 3) heavy weight case. In all of the cases, two thousand box-and-line (BL) type PMTs and 67 hundred 8" OD PMTs are assumed. In the medium case, stainless steel covers and light collectors are added to the BL type PMTs and 67 hundreds of the muti-PMTs are mounted for ID. In the light case, resin covers are added to the BL type PMTs. In the heavy case, heavy stainless steel covers and light collectors are equipped to the BL type PMTs and one thousand of multi-PMTs and OD PMT covers are assumed. The details are listed in Tabe III.2 C. In each case, proper frame structure is calculated based on the each load condition. The resultant frame structure weight and the net load when the tank is filled with water are shown in Table III.2 C. In the medium case, the net load to the barrel part is negative, -47 ton, and some weight needs to be added to compensate the buoyancy. In the light case, both of the net loads to the barrel and bottom parts are negative. Especially for the barrel part, -230 ton, and it means that the condition is too light to construct without putting counter balance, and it leads cost increase.

TC - Isn't it necessary to be able to support the full weight of the PMTs when the tank is empty and there is no buoyancy correction? -¿ YK: This is stated explicitly above.

The PMT supporting framework in the tank bottom part is constructed on the floor, inde-

	Design report case	medium weight case	light weight case	heavy weight case
Frame weight	1,451 ton	1,339 ton	1,377 ton	1,398 ton
Net load to the barrel at full tank	positive	-47 ton	-230 ton	positive
Not load to the bottom at full tank	positive	positive	-38 ton	positive

TABLE XXVI. Frame weight and the net load when the tank is filled with water for the three test cases.

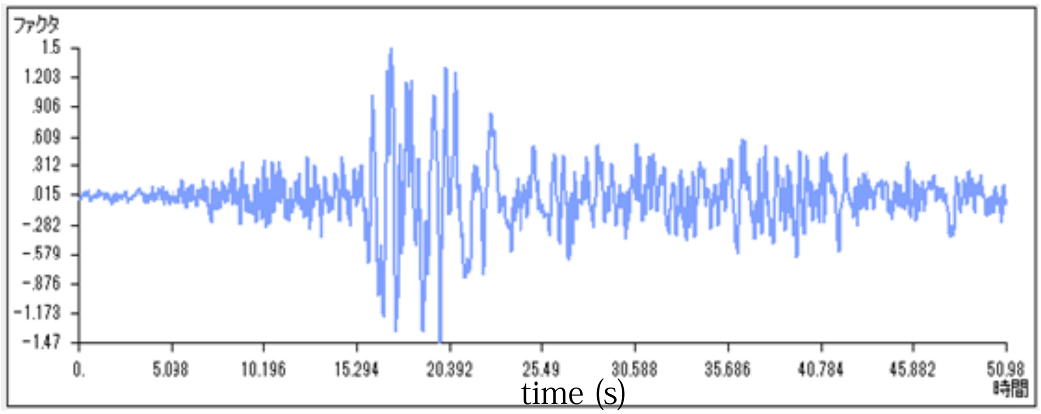

FIG. 84. The wave form of Hachinohe earthquake on the ground surface.

pendently from the top and barrel frameworks, and has struts placed directly on the watertight HDPE tank-lining. The specific method of fixing these struts on the HDPE while keeping the lining waterproof is still to be determined.

The support framework also needs to be able to withstand a horizontal load in the event of an earthquake. There is no official regulation for considering the effect of an earthquake in the Law on Special Measures related to Public Use of Deep Underground. A peak horizontal acceleration of 0.15g is assumed, as was used for designing the Super-K water tank. This is a conservative assumption derived based on the Seismic Design Code for High-Pressure Gas Facilities of Japan, a standard for facilities on the ground. Since the Hyper-K tank is built deep underground, the actual displacement of the framework during an earthquake is expected to be much smaller.

For the design of the tank structure, a seismic response analysis is performed to estimate the maximum displacement of the tank structure during an earthquake assuming various seismic waveforms. For the three test cases as well as the design report case, the displacements are less than the reference value, 50 cm. The maximum displacements in a long term earthquake, Hachinohe earthquake shown in Fig. 84, are 41.5 cm, 22.5 cm, 41.2cm, and 23.7cm for the design report case, the medium, the light, and the heavy case, respectively. There are no straightforward relation between the load conditions and the maximum displacement. One reason is that not only on the load on the barrel frame but also on the weight and rigidity of the frame itself affect the specific time-period of the frame, which is one of the important factors to estimate seismic responses. The seismic response analysis, therefore, needs to be conducted after the load condition on the structural framework is determined. The analysis is also demanded if the load condition is changed, for example even in the case of HK upgrade in some future. To ensure the safety of people working inside the narrow outer detector layer if there is an earthquake, we are considering putting some temporary spacer structures for securing a safe space in the outer detector, but this would only be done during tank construction and future detector maintenance periods.

D. On Deck Facilities

The top roof of the tank is supported at the edges contacting the side concrete wall of the cavern, and is designed so that people can walk on it, and structures such as electronics huts can be placed on it. It is not supposed to support heavy objects, such as the LINAC, for which a separate small cavern is foreseen. This top deck is made of stainless steel plates placed on a truss framework which is separated from the top part of the photosensor support framework by the 2m thickness of the OD region.

In both the top deck and the top of the photosensor support framework there need to be a number of holes for access:

- Calibration holes are required for the LINAC beam and for the deployment of sources and light injection systems, which are described in Sec. III.11.

  TC - add some links to the relevant calibration and installation sections. YK: added

- Water pipes are needed for the circulation of the tank water. See Sub-sec. III.3 E.

  TC - add link to the relevant water flow section. YK: Added.

- Holes for cables from the front-end electronics to the outside of the tank.

  TC - add links to the relevant electronics sections. YK: The holes for the cables are not decided as far as I know. They should be determined.

  In Hyper-K the HV/signal cables from the individual PMTs are routed to 24-fold front-end modules, and optical fibres are used from the front-end modules to the outside. This reduces the space required for cables by a significant amount compared to Super-K, where individual PMT cables are routed to the outside.

- The suspension structures for the top and barrel photosensor support frameworks need to be fed through the top deck.

Finally, there needs to be enough of an air space at the top of the tank, below the top deck, so that the water can slosh around during an earthquake without damaging the detector components.

III.3. WATER SYSTEM

TC - This text was a direct copy from the DR. An edit has been done for readability.

Water is the target material for the neutrinos, as well as being the source of protons that might decay. It is also the detection medium, where large numbers of Cherenkov photons are produced by charged particles. To achieve good detection efficiency in a large water Cherenkov detector an excellent transparency is the highest priority, so the water must be ultra-pure.

The main backgrounds for low energy neutrino studies come from radon emanating from the photosensors, the photosensor support structure materials, and the surrounding rock. These backgrounds can be reduced by preventing radon from passing from the OD into the ID, but it is also indispensable to have an efficient radon removal system as part of the water circulation system. In Super-K the water purification system has been continually modified and improved over the course of the experiment. As a result, the transparency is now very stable and can be kept above 100m, and the radon concentration in the ID is held below 1mBq/m^3. The Hyper-K water system design will be based on the success that is been achieved with the current Super-K water system.

A faster water circulation is naturally more effective when trying to keep huge amounts of water clean and clear, but the increasing costs limit this straightforward approach, so a compromise between transparency and re-circulation rate must be found. In Super-K, 50kt of water is processed at the rate of 60t/hour in order to keep the attenuation length for visible photons above 100m. A supply of 20Nm^3/hour of radon free air is generated for use as a purge gas in degas modules, and as gas blankets for both the buffer tanks and the Super-K tank itself. Scaling these numbers up for the 258kt of water the Hyper-K tank, we need a water circulation of 310t/hour and 50Nm^3/hour of radon free air generation.

A. Source Water Line

The rate of at which the tank can be initially filled with water is restricted by the amount of available source water. In Mt. Nijuugo-yama, the baseline location of Hyper-K, the total amount of spring water is about 600t/hour. It varies seasonally between 300t/hour and 800t/hour and is above 600t/hour except in Winter (December-March). However, the mine company KMS uses all of the 600t/hour of spring water for their smelting factory, so the availability of spring water for Hyper-K is limited and cannot be allocated at this point.

To fill the tank the plan is to get 105t/hour of source water from outside the mine, and use

Water Quality	Units	Kamioka(snow melt)	Tochibura(spring)	Mozumi(spring)
Temperature	°C	11.9	11.0	12.0
pH (25°C)		7.1	7.8	7.8
Conductivity	μS/cm	101	170	221
Turbitidity	degree (Kaolin)	<1	<1	<1
Acid consumption (pH 4.8)	mg $CaCO_3$/l	27.9	40.0	75.8
Total organic carbon	mg/l	<0.1	<1	<1
Phosphate	mg/l	<0.1	<0.1	<0.1
Nitrate	mg/l	3.0	1.0	1.6
Sulphate	mg/l	4.4	36.4	30.2
Fluoride	mg/l	<0.1	0.3	0.4
Chloride	mg/l	8.6	1.6	1.8
Sodium	mg/l	4.6	4.9	6.2
Potassium	mg/l	0.8	0.5	0.5
Calcium	mg/l	12.3	25.2	32.0
Magnesium	mg/l	1.5	1.5	2.9
Ammonium	mg/l	<0.1	<0.1	<0.1
Ionic silicon dioxide	mg/l	12.8	17.1	11.8
Iron	mg/l	<0.01	<0.01	<0.01
Copper	mg/l	<0.01	<0.01	<0.01
Zinc	mg/l	–	0.09	<0.01
Lead	mg/l	<0.1	<0.1	<0.1
Aluminium	mg/l	<0.01	<0.01	<0.01
Boron	mg/l	<0.01	<0.01	0.2
Strontium	mg/l	–	0.18	0.52
Barium	mg/l	<0.01	<0.01	0.03

TABLE XXVII. Comparison of the purity of the source water from the Kamioka snow melt with spring water in the Tochibura and Mozumi mines. *TC - This table has been added from the DR.*

this to make 78t/hour of ultra-pure water. This enables us to fill the Hyper-K tank in 180 days. The source water site that has been identified is the storage well for the snow-melting system in Kamioka town next to Oshima public hall. Table XXVII compares the purity of the snow melt water with the spring water in the Tochibura and Mozumi mines (the Mozumi spring water is used for filling Super-K). The well is about 5km away from the tank position. Hida city is supportive of our use of the well, and Gifu prefecture is also helping to decide the route for the transfer pipes from the well to the entrance of the Tochibora mine. Serious investigations and negotiations are ongoing with these local governments.

B. Cooling Water

We need to remove heat generated by the photosensors and electronics in the tank, and also to compensate for heat generated by the water purification system. Precise control of the water temperature is essential for controlling the water flow inside the tank, so it is necessary to cool the pure water both when filling and during recirculation.

The primary option is to cool the pure water using the mine water and a heat exchanger. In order to fill the tank at 80t/h and to recirculate it at 310t/h, about the same amount of cooling water is necessary. We are currently negotiating with KMS to provide that amount of cooling water, which they can then reuse afterwards.

An alternative option is to cool the pure water using a chiller. For this option, the required electricity is 96kW for filling water and 372kW for the recirculating water. These numbers are scaled up from the current performance of the EGADS chiller, which uses 200V$\times$30A=6kW to cool 5t/h.

C. Purification System

TC - Updated and more detailed figures of the circulation system(s) were shown in the Collaboration meeting.

The main Hyper-K water purification system consists of a 1st stage system for filling the tank, and a 2nd stage system for recirculation of the water as shown in Figure 85. The processing power that can be delivered by the 1st stage system is 78t/h, and accordingly it takes 138 days to fill the tank without consideration of any stops for maintenance during the filling process. In reality it may take up to 180 days to fill the tank. The processing power of the 2nd stage system for the recirculation is 310t/h, which has an electric power consumption of 1425kW. It is assumed that half of the water system costs will be provided through international contributions to the experiment.

Figure 86 shows the layout of the water systems in the cavern, and their space requirements.

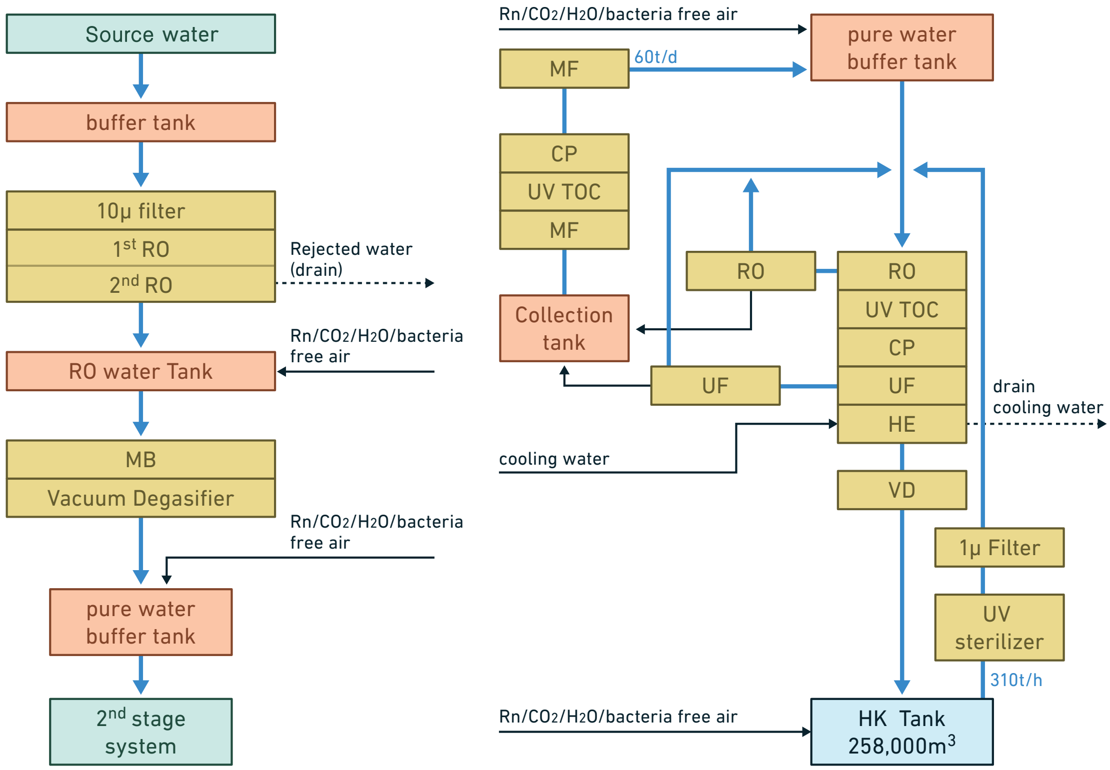

FIG. 85. 1st stage system for filling the tank and 2nd stage system for recirculating the water: MF = Membrane Filtration, MB = Melt Blown Filtration, CP = Constant Pressure Boost, TOC = Total Organic Carbon reduction, UF = Ultra Filtration, HE = Heat Exchanger, VD = Vacuum Degassifier.
(TC - This key has been added to help the reader, please correct if there are mistakes.)

D. Radon Free Air System

A supply of 50Nm^3 of radon free air is necessary as the cover gas for the water system, the buffer tanks, and for the Hyper-K tank itself. The IPMU radon free air system which has an ability of producing 18Nm^3 of radon free air (<1mBq/m^3) is shown in Figure 87. Scaling this system up by a fact or three for Hyper-K, the necessary electric power consumption is 80kW.

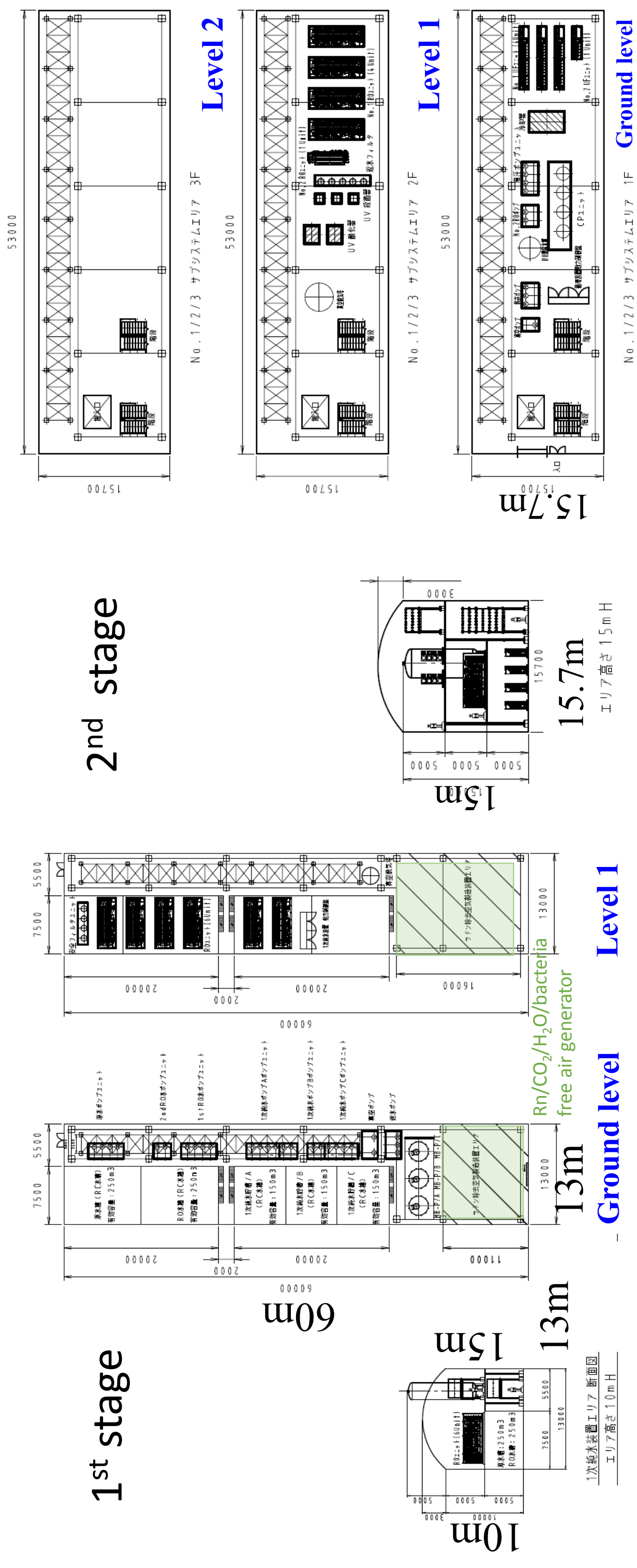

FIG. 86. Necessary space for the main water systems.

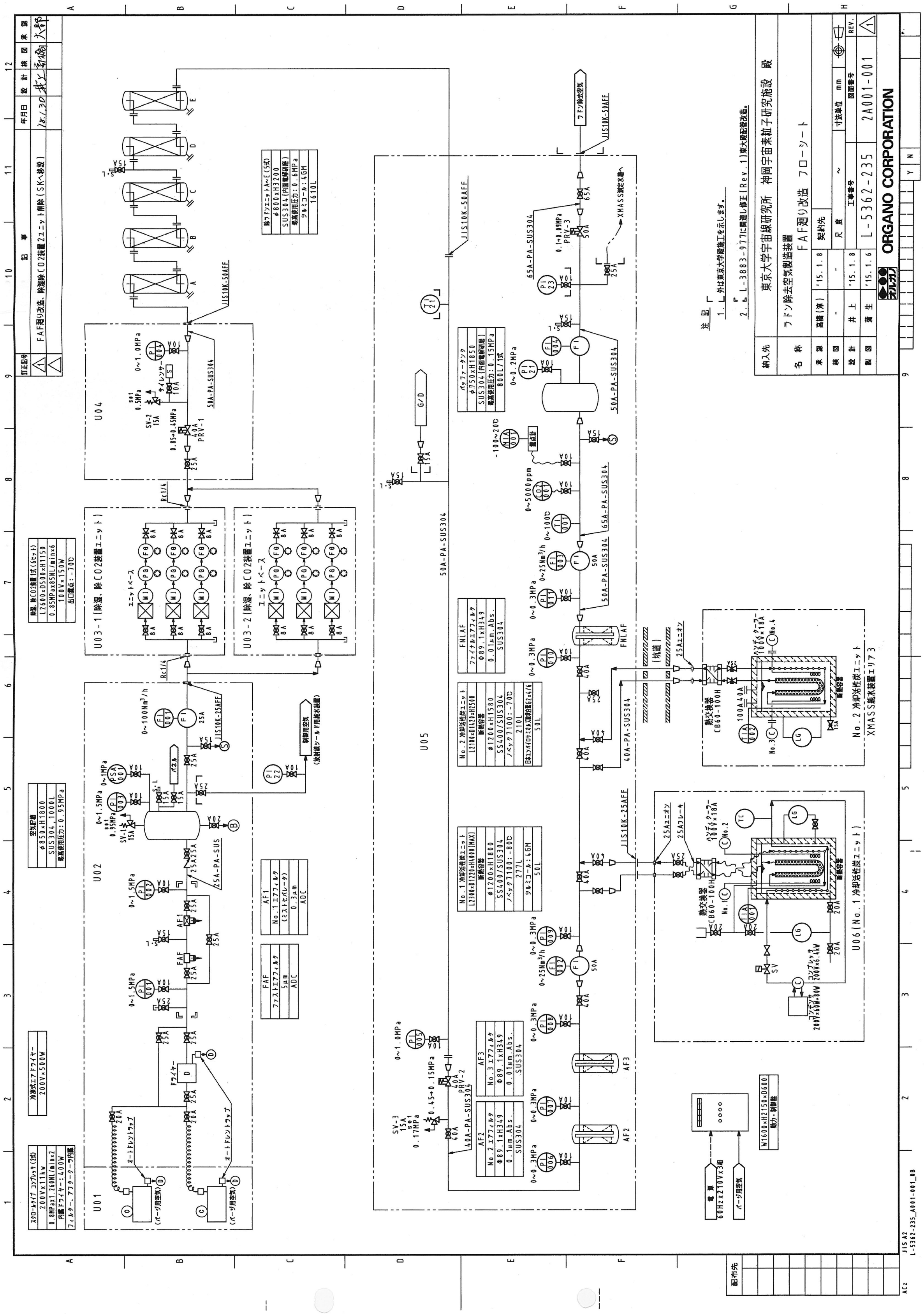

FIG. 87. One third of the required radon free air system

E. Water Flow

The water flow in the tank directly affects the distribution of impurities and their impact on the physics performance of the detector. Simulations of the water flow have been conducted. The flow does not only depend on the total water flow rate, but also on a number of other factors which include: the geometry of the photosensors and their support structure, the distribution of heat sources inside the tank, the configuration of water inlets and outlets, the supply water temperature, and the surrounding rock temperature. The input parameters for the simulations are summarised in Table XXVIII, and the main results are shown in Figure 88. When cold water is supplied from the bottom of the tank, convection in the tank is suppressed and the flow becomes laminar, resulting in effective water replacement. When cold water is supplied from the top of the tank, large convection is evoked and the water quality in the tank becomes uniform, spoiling effective water replacement. This behaviour has been confirmed in the 50kt Super-K tank, and seem to be common to all cylindrical tanks. The conclusion is that the water flow in Hyper-K should be controlled in the same way as in Super-K.

Input Parameter	Value
ID flow rate	271.8t/h
OD flow rate	37.9t/h
Inlets/Outlets	65A×37/65A×37
ID boundary condition	Inlet: 0.61m/s, 13°C; Outlet: 0Pa
OD boundary condition	Inlet: 0.67m/s, 13°C; Outlet: 0Pa
Supply water temperature	13.0°C
Top level rock temperature	16.7°C
Bottom level rock temperature	17.7°C
Heat flux from the PMTs+electronics	3.2W/m^2
Total heat from ID top or bottom	2100W
Total heat from ID wall	6502W
Total heat from OD wall(rock)	5384W
Water density	999.4 kg/m^3 @13°C, 998.4 kg/m^3 @19°C
Water heat conductivity	0.587 W/m/K @13°C, 0.597 W/m/K @19°C
Water viscosity	0.0012 kg/m/s @13°C, 0.0010 kg/m/s @19°C

TABLE XXVIII. Input parameters for the water flow simulations.

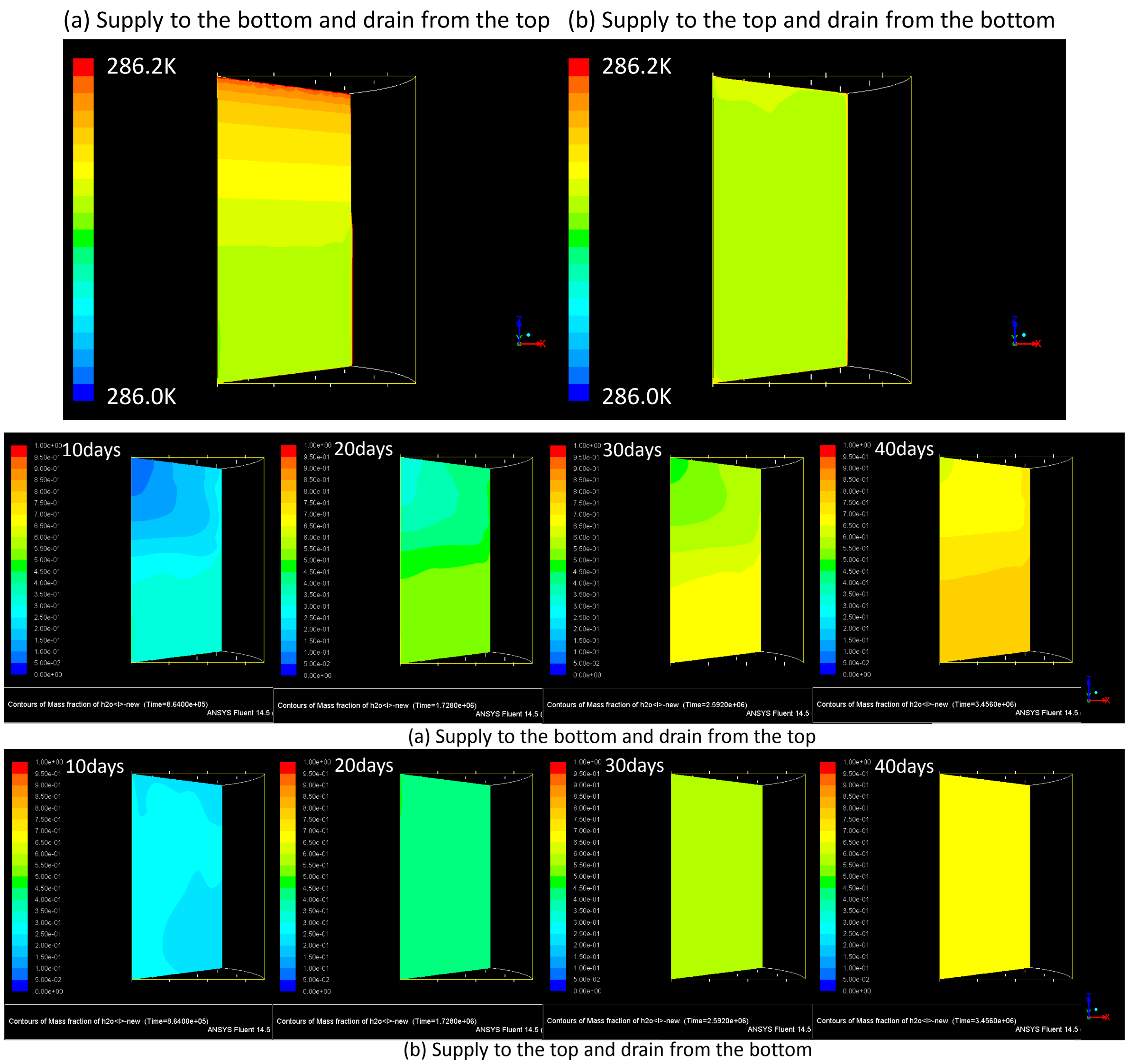

FIG. 88. Water temperature distributions (top) and water replacement efficiencies (bottom) for two different water flow simulations: (a) supplying water from the bottom of the tank and draining water from the top of the tank; (b) supplying water from the top of the tank and draining water from the bottom of the tank. Only 1/6 of the tank is shown, since the tank has a cylindrical shape, the water inlets and outlets are distributed symmetrically at the top and bottom, and there are symmetric boundary conditions. In the bottom plots the elapsed days since the recirculation of water was started are indicated. In this simulation, at first the tank was filled with old water (= 0, blue), then new water (= 1, red) was supplied to the tank, therefore the colour scale corresponds to the water replacement efficiency. After 40 days (a) is more reddish at the bottom, but (b) is more uniform.

III.4. RADON MITIGATION

Radon (^{222}Rn) is a radioactive noble gas, with a half-life of 3.8 days. It occurs as a daughter nuclide in the ^{238}U decay scheme, via the decay of ^{226}Ra with $\tau_{1/2} = 1599$ years. Small but finite quantities of ^{226}Ra exist in all materials and therefore every material can produce ^{222}Rn. As a gaseous isotope, ^{222}Rn can easily escape from the materials used in the construction of Hyper-K, so the radioactivity content of construction materials must be carefully screened.

The decay of ^{222}Rn produces several daughter isotopes, but the decays of most of these are not sufficiently energetic to produce Cherenkov light in the Hyper-K detector. The most serious background for low energy measurements is the daughter ^{214}Bi which decays via beta emission with a Q-value of 3.27 MeV and a half-life of 20 minutes. This limits the energy threshold of the solar neutrino measurements in which a neutrino-electron elastic scattering reaction is used.

In the same energy region, ^{208}Tl, produced in the ^{232}Th decay scheme, could become another source of background, with a Q-value of 2.61 MeV, and a half-life of 3 minutes. However, from a radon assay with special detectors [**? ?**], the contamination of ^{220}Rn from the thorium series looks to be much smaller than that of ^{222}Rn in the Super-K water. So, we discuss only background from ^{222}Rn in this section.

A. Environmental Radon Monitoring

In order to estimate the Rn concentration to be expected inside the Hyper-K detector, several measurements were performed in two locations, −300m and −370m in the Tochibora mine, around the candidate site for Hyper-K. The amounts of ^{238}U and ^{232}Th in the rock have been measured from rock samples using Ge detectors, and the Rn concentration in the air has been measured with a 1-L Rn detector [ref 10.1093/ptep/pty091 to be published] in each location.

The air measurement was performed over about one week, and the results can be see in Figures 89 and 90. The radon concentration has been measured to be around 1200 Bq/m^3 in both locations, which is consistent with the observations in the tunnels of the Mozumi mine at the same period (around SuperK). At the −300m location, the air flow is expected to be negligible and a stable Rn concentration is expected. However, a continuous decrease can be observed in Fig. 89. This feature is not well understood and could be explained by several environmental factors, e.g. a displacement of the air due to the installation of the detector. A longer deployment is needed to understand the situation. At the −370m location, the air flow is expected to be significant,accounting for the

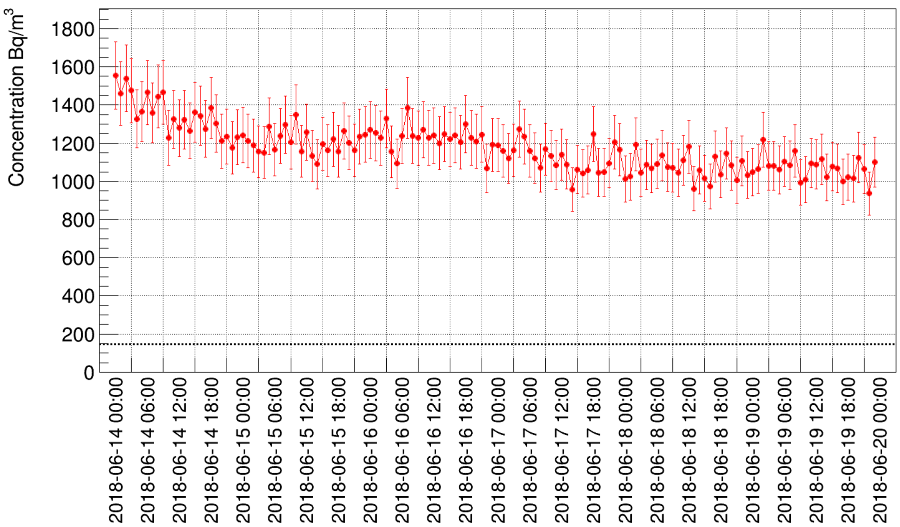

FIG. 89. Radon concentration measured at −300m from 2018/06/14 to 2018/06/19

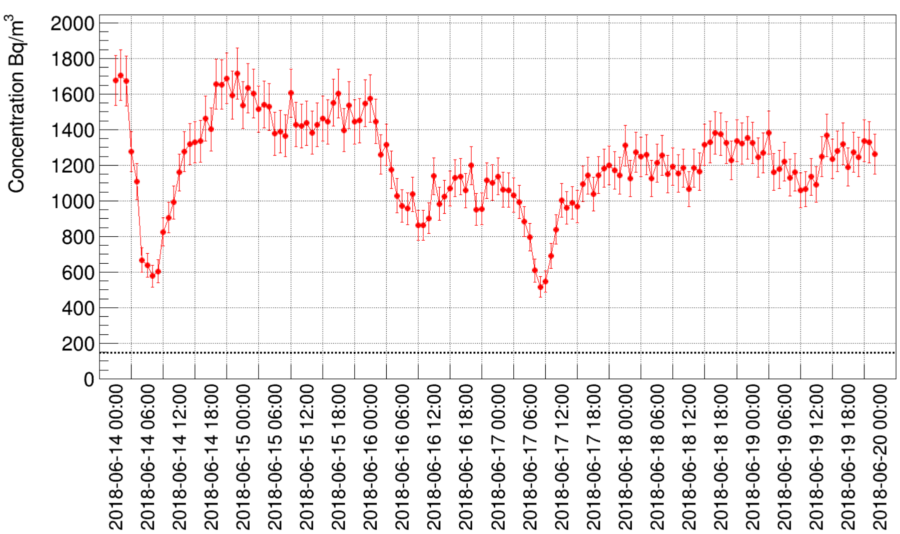

FIG. 90. Radon concentration measured at −370m from 2018/06/14 to 2018/06/19

fluctuations observed in Fig. 90.

The rock sample measurements can be see in Tables XXIX and XXX. The highest value from the ^{238}U-chain middle estimation will be used to determine the expected radon concentration in the outer part of the Hyper-K tank. This estimation will be done with and without the HDPE tank-lining. It will allow us to determine if the current plan for a radon reduction of 3 orders of magnitude at the boundary between the OD and ID volumes is sufficient for our low energy physics goals.

Samples	Floor	Wall a	Wall b	Wall c
U-chain middle (^{226}Ra-^{210}Pb)	$2.14^{+0.05+0.22}_{-0.05-0.64}$	$13.3^{+0.1+1.4}_{-0.1-4.0}$	$7.51^{+0.07+0.75}_{-0.07-2.26}$	$7.34^{+0.07+0.74}_{-0.07-2.21}$
U-chain upper (^{243}Th)	$3.09^{+0.39+0.31}_{-0.39-0.93}$	$18.2^{+0.8+1.9}_{-0.8-5.5}$	$9.35^{+0.48+0.94}_{-0.48-2.81}$	$8.57^{+0.61+0.86}_{-0.61-2.58}$
Th-chain (^{228}Ra-^{208}Tl)	$0.85^{+0.04+0.09}_{-0.04-0.26}$	$15.2^{+0.1+1.6}_{-0.1-4.6}$	$5.51^{+0.05+0.56}_{-0.05-1.66}$	$6.10^{+0.06+0.62}_{-0.06-1.83}$
^{40}K	237^{+2+24}_{-2-72}	342^{+2+35}_{-2-103}	163^{+1+17}_{-1-49}	307^{+2+31}_{-2-93}

TABLE XXIX. Rock sample measurement from the −300m location. Values are in Bq/kg.

Samples	Wall a	Wall b
U-chain middle (^{226}Ra-^{210}Pb)	$19.8^{+0.1+2.0}_{-0.1-6.0}$	$14.1^{+0.1+1.5}_{-0.1-4.3}$
U-chain upper (^{243}Th)	$18.9^{+0.8+1.9}_{-0.8-5.7}$	$18.1^{+0.7+1.9}_{-0.7-5.5}$
Th-chain (^{228}Ra-^{208}Tl)	$20.0^{+0.1+2.0}_{-0.1-6.0}$	$21.7^{+0.1+2.2}_{-0.1-6.5}$
^{40}K	457^{+1+46}_{-1-137}	410^{+2+41}_{-2-123}

TABLE XXX. Rock sample measurement from the −370m location. Values are in Bq/kg.

B. Fresh air system

The typical radon concentration in the mine air at the Mozumi site is $\sim 1200\text{Bq/m}^3$ [?], similar to what has been measured at the Tochibora site. In order to reduce radon concentration around the Super-K detector, including the water purification systems, fresh air is always supplied to cover these experimental areas. The fresh air system for Super-K consists of an air pump, a dehumidifier system, and about 2km of piping. The pump and dehumidifier system are located in a "Radon hut" at the Atotsu entrance to the Mozumi mine. The system was built and is maintained by US collaborators in the Super-K collaboration.

The flow rate of the fresh air into the Super-K dome area is $\sim 10\text{m}^3\text{/min}$ [?]. This keeps the radon level below $\sim 100\text{Bq/m}^3$. A similar fresh air system will be necessary for Hyper-K, but presumably with a larger flow rate scaled for the larger volume of the dome. The fresh air system for Hyper-K is expected to be built with an international contribution.

C. Studies of Radon Emanation

Radon emanation from the photosensors themselves could be the dominant source of radon at the edges of the ID volume. The Super-K group measured the radon emanation from one of their 20" PMTs to be 2mBq/day, giving 10mBq/photosensor at equilibrium [SK note 97-5]. With 11129 PMTs and 50kt of water, the average radon concentration due to emanation from the PMTs is calculated to be 2.2mBq/m^3. This value is close to the measured value in the ID region of the Super-K detector [?].

The situation is likely be similar in the Hyper-K detector, but efforts are being made to reduce the radon emanation from the new 20" PMTs in order to improve the low energy physics reach of the experiment. The current requirement on the radon emanation of a photosensor in the Hyper-K detector is $<$10mBq. With this limit the expected radon concentration due to the emanation from 40k photosensors into the 258kt of water would be $<1.6\text{mBq/m}^3$.

In addition to the photosensors, it is necessary to assay the radon emanation of each major detector component separately. These include the photosensor covers, the mPMT modules (if used), the cables and front-end electronics modules, the photosensor support structure, the ID/OD separation materials, and the HDPE tank-lining itself. To perform these radon assays, we are going to use the special radon detectors developed for Super-K [? ? ?]. For example, to measure radon emanation from a 20" photo sensor, a 700L radon detector will be used as a vessel for the sensors.

This is then connect to 80L radon detectors to measure the radon concentration in the system. For smaller detector components, an 80L radon detector and an electropolished stainless steel vessel with an insulated concrete form (ICF) will be used.

D. Permeability of Tank Lining

A major difference between the Super-K and Hyper-K detectors is the tank-lining material. In Hyper-K a 5mm thickness sheet of HDPE will be used instead of stainless steel. The typical radon permeability through a HDPE sheet has been reported by various groups as $O(10^{-8})$ to $O(10^{-7})\text{cm}^2/\text{s}$ [**? ? ? ? ?**].

For Hyper-K we have estimated the radon concentration in the OD water due to permeation through the tank-lining from outside the detector to be $O(10)\text{mBq/m}^3$. This is similar to the radon level observed in the Super-K Outer Detector. This estimate uses as inputs the following assumptions:

- The radon permeability of the HDPE sheet is $10^{-8}\text{cm}^2/\text{s}$.
- The radon concentration in mine water is 10^3Bq/m^3.
- There is no water flow between the ID and OD regions ("hermetic" separation).
- The volume of mine water contributing to this effect is far larger than the volume of the OD water.

TC - Why are these assumption expressed in terms of mine water rather than rock? The Hyper-K site is above the Tochibura water table.

In order to reduce the uncertainty in this estimation, we are measuring the radon permeability of a Hyper-K HDPE sheet. The performance of the assay system is still being tuned, but the current sensitivity of the system in air is $O(10^{-9})\text{cm}^2/\text{s}$ for a 1mm thickness sheet. A device to assay radon permeation in water is under development in Kamioka. The preliminary results of the measurements are shown in Table XXXI. A higher sensitivity measurement under water is now ongoing.

Thickness of HDPE sheet [mm]	environment	permeation
0.50	air	$(0.60 \pm 0.07) \times 10^{-7}\mathrm{cm}^2/\mathrm{sec}$
0.96	air	$(0.52 \pm 0.08) \times 10^{-7}\mathrm{cm}^2/\mathrm{sec}$
0.50	water	$< 0.49 \times 10^{-7}\mathrm{cm}^2/\mathrm{sec}$ (90% C.L.)
0.96	water	$< 0.86 \times 10^{-7}\mathrm{cm}^2/\mathrm{sec}$ (90% C.L.)

TABLE XXXI. Preliminary results of radon permeation measurements of the HDPE sheet.

III.5. GADOLINIUM LOADING

An important feature of the Hyper-K detector is its ability to detect neutrons which are produced in the MeV range, and then thermalised in the water until they are captured after $\approx 100\mu$s. The production of neutrons by charge exchange can distinguish between neutrino and antineutrino interactions. This is particularly useful for the measurement of supernova neutrinos (both relic and burst). The absence of neutrons in the final state can also be used to reduce the background from atmospheric neutrinos in the search for proton decays.

In Hyper-K neutrons can be identified from the 2.2MeV gamma rays emitted after capture on hydrogen. This is a very low energy event, giving only a few Cherenkov photons from Compton scattered electrons. To detect this signal requires a large number of photosensors with high quantum efficiency. From Monte Carlo studies it is expected that about 50% of the captures can be identified with 40% photosensor coverage. In Super-K with lower quantum efficiency photosensors, the efficiency for seeing neutron captures on hydrogen is about 25%.

The addition to the water of gadolinium sulphate, $Gd_2(SO_4)_3$, would significantly improve the neutron detection efficiency. The neutron capture cross-section on gadolinium is large, so the capture time is reduced by an order of magnitude, and the capture produces about 8MeV of energy as a gamma cascade, which gives a Cherenkov signal equivalent to an $\approx$4.5MeV electron. This option has already been extensively studied for Super-K, which is currently being prepared for the addition of 100t of gadolinium sulphate. In Super-K the neutron detection efficiency is expected to improve to 85% with this mass loading of 0.2% of gadolinium sulphate. In Hyper-K with the same loading the efficiency would be even higher with 40% coverage and the higher quantum efficiency of the photosensors. This would require a bit more than 500t of high-purity gadolinium sulphate, plus some significant additions to the water system hardware, which will be described below.

The cost of Hyper-K can be significantly reduced if the gadolinium loading is reduced by an order of magnitude to 0.02%, and the photosensor coverage is reduced to 20%. At this loading half of the neutrons would capture on gadolinium and half on hydrogen, and with 20% photosensor coverage they would be detected with efficiencies of 85% and 25% respectively, giving an overall neutron detection efficiency of $\approx$55%. The necessary production facilities and additional water systems required to add about 50t of gadolinium sulphate to Hyper-K are already quite well-developed for Super-K. It is possible to increase this loading by up to a factor of five if a higher neutron detection efficiency is needed.

A. Purification of Gadolinium Sulphate

The radioactivity of the gadolinium sulphate powder developed for Super-K is shown in Table XXXII. A company can produce a 500kg batch of this high purity powder in one week. To produce 50(500)t of gadolinium sulphate, corresponding to 0.02(0.2)% loading in Hyper-K, would take 2(20)years with the current system . However, the company has said that if they upgrade their facilities, it is not unrealistic to have a production rate of 100t/year, including the time for procurement of the raw material.

Chain	^{238}U		^{232}Th			^{235}U	
Isotope	^{238}U	^{226}Ra	^{232}Th	^{228}Ra	^{228}Th	^{235}U	^{227}Ac/Th
Goal	< 5	< 0.5	< 0.05	< 0.05	< 0.05	< 3	< 3
Achieved	< 0.04	< 0.2	0.02	< 0.3	< 0.3	< 0.4	< 1.7

TABLE XXXII. Radioactivity of gadolinium sulphate powder, $Gd_2(SO_4)_3.8H_2O$, in units of mBq/kg. The goals are set by the background requirements for low energy events with a 0.2% gadolinium loading.

TC - Should we worry about the ^{232}Th daughters, or are there some missing zeroes in this table?

B. Gadolinium Recirculation

The gadolinium sulphate to be loaded into Hyper-K must first be dissolved and passed through a pre-cleaning stage before being sent to the detector. Such a system has already been designed and built for Super-K by Organo, as depicted schematically in Figure 91. Since it is intended for the full SK loading of 0.2% gadolinium sulphate (100t), this design could simply be reproduced for use in Hyper-K, if the final goal is only 0.02% gadolinium sulphate (50t).

Once the gadolinium has been added to Hyper-K, a specialized water recirculation system will be required capable of maintaining the exceptional water transparency, while at the same time maintaining the desired level of dissolved gadolinium. This means the Gd-loaded water must be continuously recirculated and cleaned of everything *except* gadolinium sulphate.

Starting in 2007 with a 0.2t/hour prototype at the University of California, Irvine, and then in 2009 with the Kamioka-based EGADS project, we have shown that such a selective water filtration technology, known as a “molecular band-pass filter”, is feasible at 3t/hour. It removes unwanted impurities while simultaneously and indefinitely retaining the desired levels of both the gadolinium and sulphate ions. It continuously improves and then maintains the transparency of water loaded with gadolinium sulphate at the ultra-pure level required by Super-K and Hyper-K.

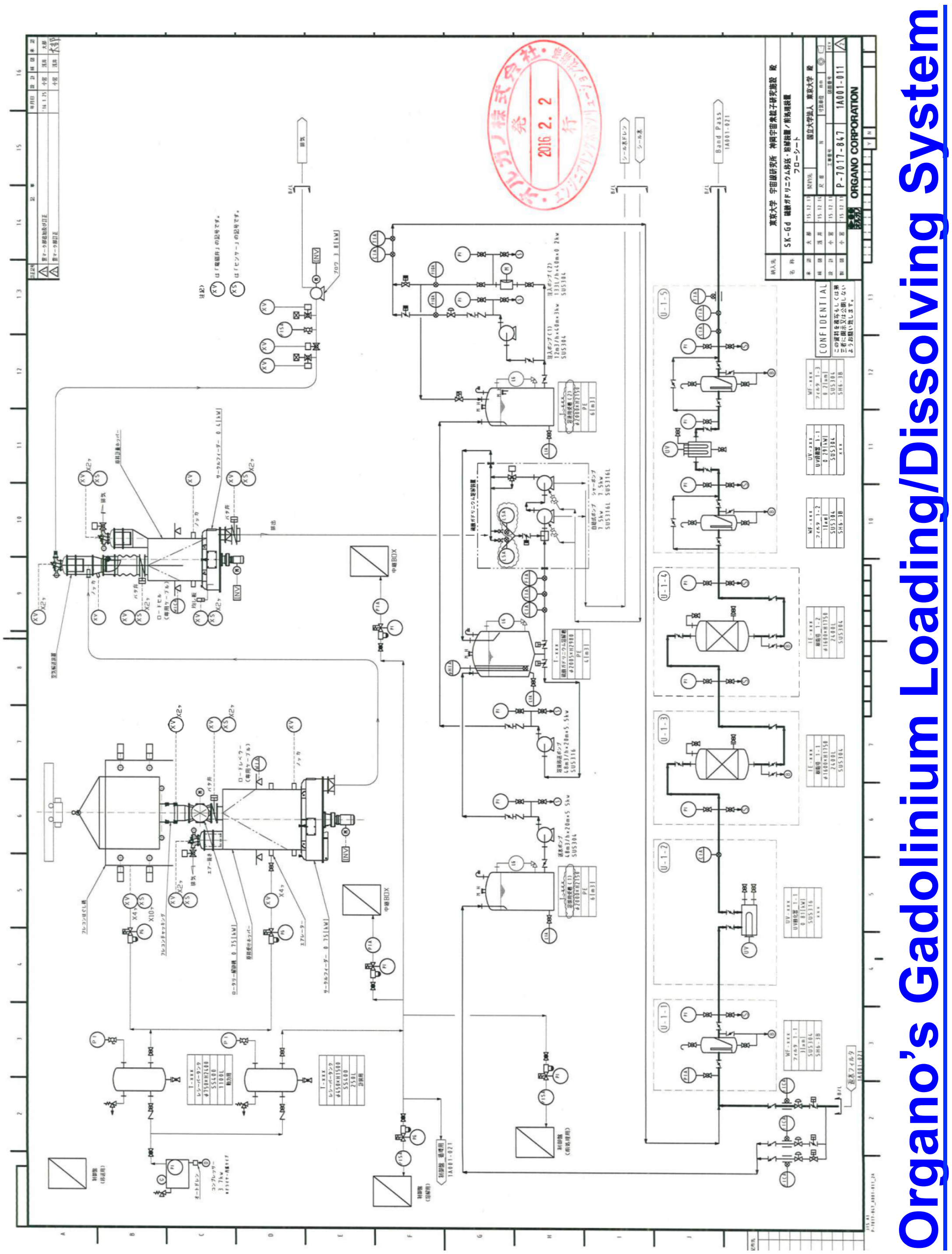

FIG. 91. Super-K's gadolinium dissolving and pretreatment system. This is capable of dissolving and cleaning 100t of gadolinium sulphate, making it suitable for a 0.02% loading of Hyper-K.

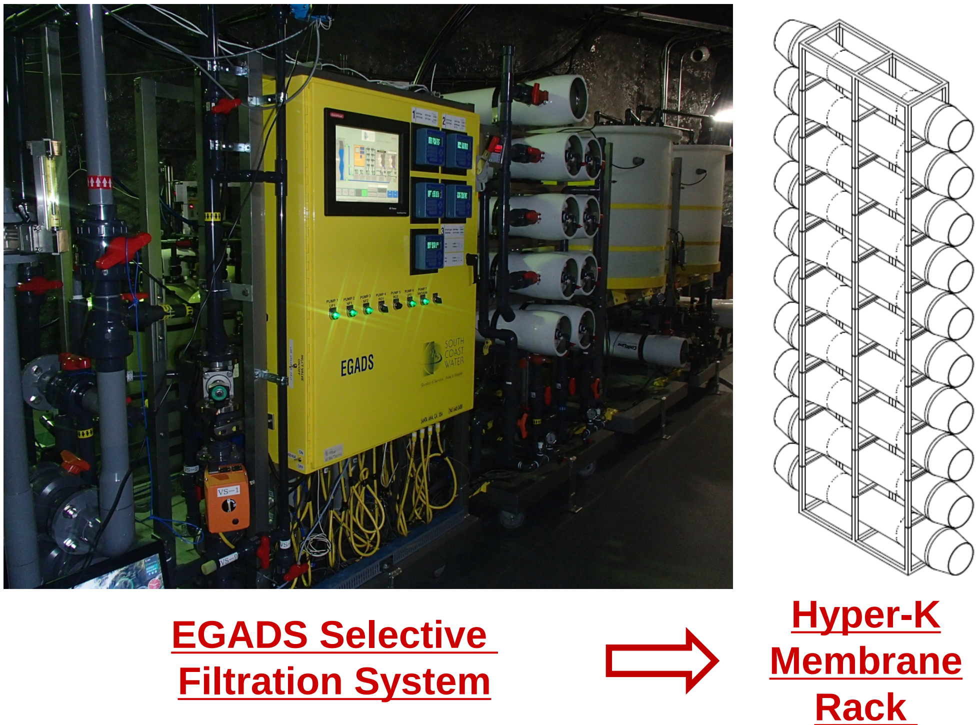

FIG. 92. Scaling the modular EGADS selective filtration band-pass for Hyper-K. One rack of filtration membrane housings is shown here.

Since EGADS was built specifically to show that gadolinium loading would be feasible in Super-K, scalability was always an important design criterion. Therefore, from the beginning the EGADS band-pass system was conceived of as a modularized design. It uses cost-effective, readily available components operating in parallel to achieve the desired throughput and assure serviceability. As the band-pass design is modular and uses off-the-shelf equipment, albeit in novel ways, it is straightforward to scale it up from the current 3t/hour to 60t/hour for Super-K, or even to 310t/hour for a full loading of 0.2% in Hyper-K. Figure 92 indicates one rack of filtration membrane housings, the modular unit around which the band-pass system is based.

Figure 93 depicts South Coast Water's vision of how the modular rack from Figure 92 may be duplicated and operated in parallel to provide the needed throughput. Further design simplification and cost savings are achieved by using a standardized membrane housing array and filling the housings with a variety of filter membranes, each of which handles a different cleaning task. These components include nanofilters (NF), ultrafilters (UF), and reverse osmosis (RO) membranes. Note that the layout shown in Figure 93 is schematic in nature. Due to space constraints underground the illustrated system is likely to be split into two or more levels, placed on top of each other.

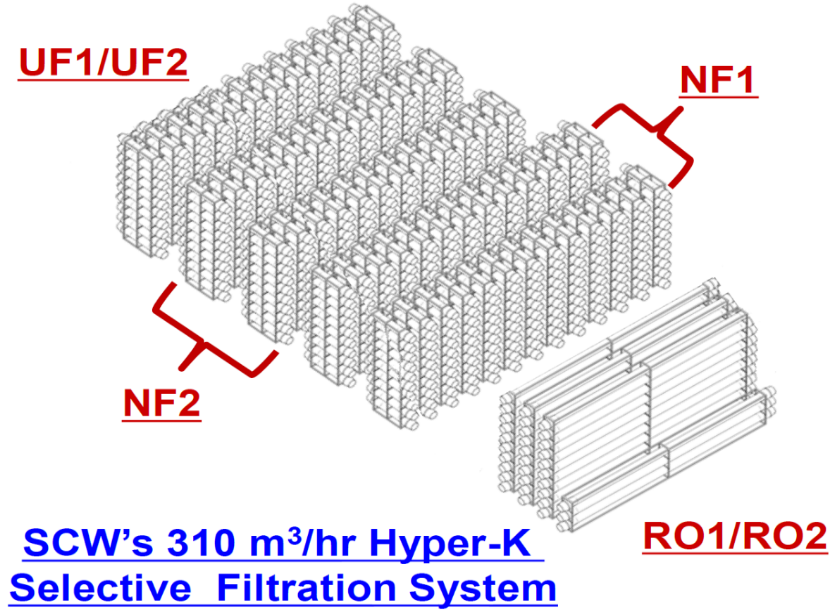

FIG. 93. South Coast Water's Gd-loaded water system for Hyper-K. Two stages each of nanofilters (NF), ultrafilters (UF), and reverse osmosis (RO) membrane racks are shown, sufficient to provide the 258kt of selectively filtered water for the Hyper-K tank.

The Gd-specific "molecular band-pass" system described here will be augmented with additional Gd-capable water handling, known as a "fast recirculation system". This will also be scaled up from a working version in EGADS.

C. Gadolinium Removal

Once the experiment is finished, or if scheduled maintenance is required, any gadolinium dissolved in Hyper-K must be removed in an efficient, safe manner. It may also be necessary to remove the gadolinium in case of an emergency. The solution employed in both EGADS and Super-K is to pass the Gd-loaded detector water through an ion exchange resin while draining, specifically a sodium form cation exchange resin called ResinTech CG8. A single pass through this resin captures at least 99.9% of the gadolinium and replaces it with sodium. The system built for the first phase of gadolinium loading of Super-K, during which 0.02% gadolinium sulphate (10t) will be added to the detector, is shown in Figure 94. A triple pass ensures that the Gd level in the outgoing water stream will be reduced by a factor of 10^9 at a flow rate of 60t/ hour. This system would be sufficient for a 0.02% loading of Hyper-K, or could be scaled up by a factor of five by adding more (or larger) tanks to the current design. The drainage rate could similarly be increased by running more of these tanks in parallel.

FIG. 94. Super-K's gadolinium removal system, capable of capturing all the Gd in 10t of gadolinium sulphate.

III.6. INNER DETECTOR DESIGN

The design of the photon detection system for the inner detector is described in this section. After the cavern excavation this is the single most expensive part of Hyper-K (≈$200M), and is the area in which most of the international contributions are expected to be made. At present we are considering a number of options based on the desired physics performance and the available funding within the collaboration.

The basic unit of the design is a 70cm square cell on the outer surface of the inner detector region with photosensors pointing inwards to detect the Cherenkov photons. This cell can either house a single 50cm (20”) diameter photosensor, or an array of smaller 8cm (3”) photomultipliers, known as a multi-PMT(mPMT) module. The design of the mPMTs is discussed in section III.8. The options for the 20” photosensors are discussed in section III.6 A, but the default choice is the high quantum efficiency Box-and-Line (B&L) PMT from Hamamatsu (R12860HQE). Table XXXIII shows the dimensions of the cells and the properties of the ID photosensors.

Property	Default	Minimum	Maximum
Cell size	$70 \times 70\text{cm}^2$		
Dead region	55cm	40cm	60cm
Height	20cm	15cm	33cm
Weight	37kg	24kg	48kg
Buoyancy	72kg	0	75kg

TABLE XXXIII. Dimensions of Inner Detector (ID) cells, depth of dead region between the Inner and Outer Detector (OD), height of the covers and/or light collection above the ID surface, and total weight and buoyancy of a 20” PMT including its covers and cables.
NOTE: These values may change.

There are 40,000 cells covering the full area of the inner detector. If these are all instrumented with the 20” B&L PMTs, we would have the maximum photo-coverage with 40% photosensitive area, within which there is a 26% detection efficiency coming from a combination of the quantum efficiency and the collection efficiency of the PMT. This give an overall photon detection efficiency of 10%. This is almost a factor of two better than the current Super-K photosensors, mainly due to the improved quantum efficiency of the new Hamamatsu PMTs.

The minimum configuration that we are considering is 20% photo-coverage by instrumenting half of the cells with the 20” PMTs. From the experience with Super-K, in particular during the period between 2004 and 2006 when Super-K ran with only half its usual photosensor coverage, we know that this reduced coverage of 20% is completely sufficient for all the high energy physics: long baseline accelerator neutrinos, atmospheric neutrinos, proton decay. For the low energy physics (supernova, solar neutrinos), we would benefit from the full 40% coverage. This is discussed in detail in the physics part V of this report. We also need sufficient photosensor coverage to detect neutron captures. This is discussed in detail in section III.5.

Between the 20% and 40% photo-coverage with 20" PMTs we are considering the option of adding ≈5,000 mPMT modules to provide higher resolution spatial and timing information. We could also add 10,000 additional 20" PMTs for 30% coverage if sufficient funds are available.

Section III.6 B describes the covers that are needed to protect the PMTs from a cascade implosion. They consist of a ultraviolet (UV) transparent acrylic cover for the front photocathode area and a stainless steel cover for the rear of the PMT. In section III.6 C the addition of a light collection system is considered as a light and cheap solution to enhance the photon detection efficiency of the 20" PMTs.

A. Inner Detector Photosensors

Table XXXIV shows the performance requirements for the ID photosensors, and Table XXXV shows the maximum amount of radioactivity allowed in the materials in the PMTs and their covers, as discussed in section III.4. The photosensors should not significantly reduce the transparency of the water. A material soak test in ultra-pure water for three months at 15°C showed that the loss of light transparency is expected to be <10% in the range of 300–600nm in Hyper-K.

1. Box-and-Line Photomultiplier Tube

For Hyper-K, a 50cm R12860-HQE PMT with a box-and-line dynode was developed with Hamamatsu Photonics (referred to as the B&L PMT). It is a substantial improvement from the R3600 PMT used for Super-K (SK PMT), with a faster time response, better charge resolution, and a higher detection efficiency with a uniform response over most of the detection area. For safe use in Hyper-K, the PMT has been designed to survive water depths of 60–80m, and this has been demonstrated by hydrostatic pressure tests. After the successful development of the B&L PMT for Hyper-K, many of them have been manufactured and are being installed in Super-K, as replacements for dead SK PMTs, and in the Jiangmen Underground Neutrino Observatory (JUNO) in

Requirements	Value	Conditions
Quantum efficiency (QE)	30%	Minimum at 400nm
Collection efficiency (CE)	85%	Minimum at 400nm
Detection efficiency	26%	QE $\times$ CE
Timing resolution	5.2ns	FWHM for 1PE
Charge resolution	50%	Maximum σ/mean for 1PE
Signal window	200ns	Contains 95% of integrated charge
Dynamic range	2 photons/cm^2	Maximum flux per unit area
Gain	10^7	Typical
Afterpulse rate	5%	Maximum for 1PE
Dark count rate	2Hz/cm^2	Typical
Rate tolerance	10MHz	1PE rate for 10% change of gain
Magnetic field tolerance	100mG	Maximum for 10% change of gain
Life time	20years	Less than 10% dead PMTs
Pressure rating	0.8MPa	Minimum static load in water

TABLE XXXIV. Requirements for the ID photosensors, where 1PE refers to a single photoelectron signal.

Source	Requirement
U-chain	$\leq$ 3Bq/PMT
Th-chain	$\leq$ 1Bq/PMT
K^{40}	$\leq$ 10Bq/PMT
Radon emanation	$\leq$ 3mBq/m^3
Total Organic Carbon	$\leq$ 10mg/m^2/day
Zinc	$\leq$ 10mg/m^2
Copper	$\leq$ 14mg/m^2
Silicon	$\leq$ 10mg/m^2

TABLE XXXV. Radioactivity and other material requirements for the ID photosensors.

China.

The specifications for a typical B&L PMT are listed in Table XXXVI. In our performance evaluations we have measured (30$\pm$3)% charge resolution, and (2.6$\pm$0.1)ns timing resolution for 1PE, where the errors include the spread over a sample of 145 PMTs. Both these resolutions are about half of the SK PMTs. The total detection efficiency of photons is almost double compared with the SK PMTs due to improvements in both quantum efficiency (QE) and the collection efficiency (CE). The peak QE of the B&L PMT is typically 30% at a wavelength of 390nm, whereas the peak QE of the SK PMT is about 22%. The B&L PMT has a high CE of 95% within a 46cm diameter, whereas the SK PMT has 73% CE within the same area. It still keeps a high efficiency of 87% over the full 50cm area, with a CE of 50% or better within a diameter of 49.2cm. The relative CE loss in a 100mG residual magnetic field is at most 2% in the worst direction. An open issue is the need to lower the dark count rate of around 8kHz to 4kHz if possible.

Shape	Hemispherical
Photocathode area	50cm diameter (20")
Bulb material	Borosilicate glass ($\sim$ 3mm)
Photocathode material	Bialkali (Sb-K-Cs)
Quantum efficiency	30% typical at $\lambda = 390$nm
Collection efficiency	95% at 10^7 gain
Dynodes	10 stage box-and-line type
Gain	10^7 at $\sim$ 2000V
Dark count rate	$\sim$ 8kHz at 10^7 gain and 13°C (after stabilization)
Transit time spread	2.7ns FWHM for 1PE
Weight	9kg (without cable)
Volume	61,000cm^3
Pressure tolerance	1.25MPa water

TABLE XXXVI. Specifications of the 50cm R12860-HQE B&L PMT by Hamamatsu.

Figure 95 shows a picture of the Hamamatsu B&L PMT and Figure 96 shows a side view. While the shape is similar to the SK PMT, the inside dynode structure is completely different from the Venetian blind structure used in the SK PMT. The glass curvature and thickness have been optimized and are well controlled in production. As a result, no damage was found in fifty B&L PMTs that were tested up to 1.25MPa in water.

The B&L PMT is operated with a positive bias voltage in the range 1500–2400V, and has a power consumption less than 1W. The single photoelectron pulse in a B&L PMT has a 6.7ns rise time (10% – 90%) and a 13.0ns FWHM without ringing. The pulse height with a large photon flux might saturate near -10V, depending on the high voltage and the PMT gain. An appropriate range for the charge integration is 200ns to cover possible pre-pulses or afterpulses, defined relative to the base voltage just before the range, if the signal has high-frequency components or a large pulse height. The base circuit (Figure 97) is put inside a waterproof case, with a 20m connector

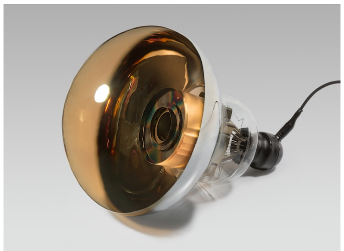

FIG. 95. Picture of the HQE 50cm B&L R12860 PMT.

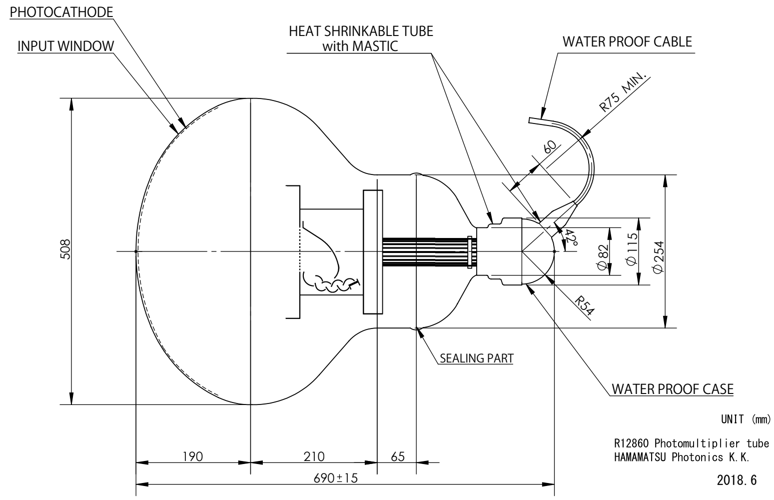

FIG. 96. Side view of the HQE 50cm B&L R12860 PMT.

containing two 9.4mm diameter coaxial cables for the high voltage (RG-174/U, 8kV DC max) and signal (RG-58C/U). The cable weight is 86.4g/m and its volume is 64.3cm^3/m. The outer sheath is made of a black polyethylene with 1mm thickness. A dedicated connector, watertight up to 100m water depth, has been developed for Hyper-K.

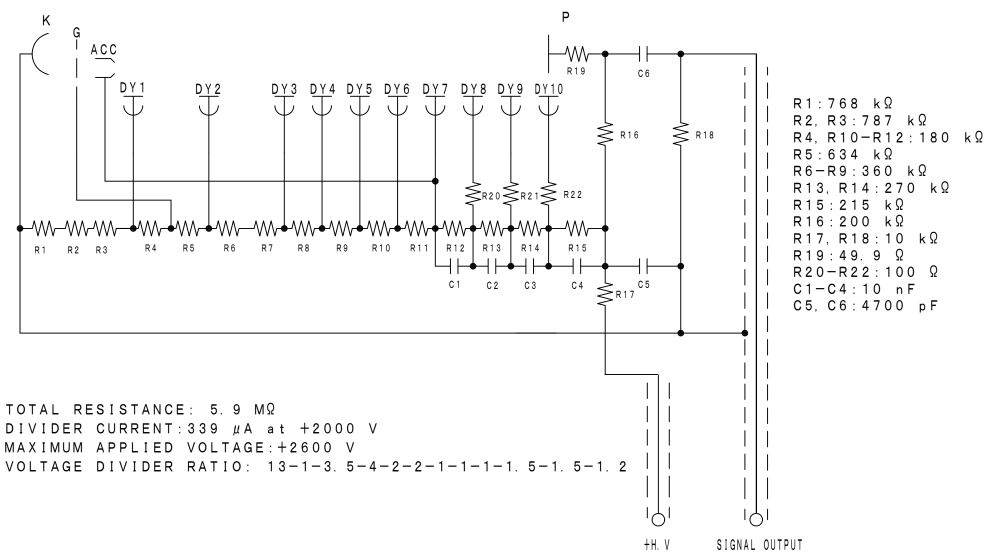

FIG. 97. PMT base circuit of the HQE B&L R12860 PMT.

The maximal production rate for the B&L PMTs in existing facilities is 3,600 PMT/year, but there is room to double this rate if required. So that a full set of 40,000 PMTs could be manufactured within the 6 year construction phase before Hyper-K starts.

2. Micro Channel Plate Photomultiplier Tube

Recently another 50cm PMT using a microchannel plate (MCP) was developed in China for the JUNO experiment, the GDB-6201 manufactured by North Night Vision Technology (NNVT). This MCP PMT has sufficient photon detection efficiency, but the timing resolution of 15ns FWHM is not yet acceptable for Hyper-K. This is mainly due to a large variation of the transit times of the photoelectrons depending on the light injection point. We have worked with NNVT to improve the timing resolution by using electrodes and a voltage divider circuit to control the photoelectron paths, and a new MCP PMT, GDB-6203, has achieved a timing resolution of 5.5ns FWHM which meets our requirements. Table 98 shows the specification of the two 50cm MCP PMTs and a 20cm MCP PMT. The QE is about 30% at peak and the CE is near to 100%, comparable with the B&L PMT. The outline of the MCP PMT (GDB-6201) for JUNO is shown in Figure 99, while the MCP PMT (GDB-6203) for Hyper-K is shown in Figure 100.

An open issue for the MCP PMT is the dark count rate of about 25kHz at 22°C. Measurements of the rate are planned in a stable underwater environment at 15°C, to see if the rate can be reduced sufficiently to meet our specifications. We also need to finalise and test a waterproof design for the MCP PMT as shown in Figure 101. The production capacity of the manufacturer is sufficient to prepare all the ID photosensors in 6 years, at a rate of 7500 PMT/year, since this rate of mass production is already being performed for JUNO.

3. The Hybrid Photodetector

A hybrid photodetector (HPD) with a 50cm diameter size, R12850-HQE by Hamamatsu, is another possible candidate for the ID photosensor. The HPD uses an avalanche diode (AD) instead of a metal dynode for the multiplication of the photoelectrons emitted from a photocathode. In order to collect photoelectrons efficiently in the small 20mm diameter area of the AD, a high voltage of 8kV is applied to accelerate and focus them. A waterproof HPD, shown in Figure 102, has operated for 20 days, and another one has been installed into a 200t water Cherenkov detector (EGADS) at Kamioka. The bulb size and photocathode are almost the same as the R12860 PMT (Figure 103). There are two options for the high voltage power. It can be generated inside the waterproof case, or it can be provided by an 8kV cable from outside the case. Both solutions have been developed for the HPD.

The HPD has the best charge resolution with a σ of 15% for 1PE. Other performance charac-

Description									
Window material	Borosilicate glass								
Photocathode	Sb-K-Cs								
Multiplier structure	Microchannel plate								
Type	**8″**			**20″**					
	GDB-6081			**GDB-6201**			**GDB-6203**		
	Min.	**Typ.**	**Max.**	**Min.**	**Typ.**	**Max.**	**Min.**	**Typ.**	**Max.**
Photocathode characteristics									
Spectral Range(nm)	300-650			300-650			300-650		
Maximum sensitivity at (nm)	380			380			380		
Sensitivity									
Luminous(μA/lm)		70			80			80	
QE at 405 nm(%)		26			30			30	
Supply Voltage(V)	1500	1900	2400	1500	1750	2000	1650	1900	2000
Gain		1×10^7			1×10^7			1×10^7	
Anode Dark Current(nA)		100	700		150	1000		100	1000
Background Noise@22℃(cps)		5 k	20 k		30 k	100 k		25 k	100 k
Single Electron Spectrum									
Energy Resolution(%)		60			35			40	
Peak to Valley Ratio		2.5		3	7	10	2.5	4.5	6
Anode Pulse									
Rise Time(ns)		1.4			1.4			1.4	
TTS (FWHM) (ns)		3			15			5.5	
Linearity @10% (P.E.)		800		800	1000	1400	800	1000	1400
After pulse ratio(%)		1			1			1	
Background radioactive									
^{238}U (Bq/kg)		2.5			2.5			2.5	
^{232}Th (Bq/kg)		0.5			0.5			0.5	
^{40}K (Bq/kg)		0.3			0.3			0.3	
Weight(kg)	~1.0			~8.0			~8.0		

FIG. 98. Specifications of the MCP PMTs by NNVT. The GDB-6201 MCP PMT was developed for JUNO, while the GDB-6203 with the improved timing resolution was developed for Hyper-K.

teristics are similar to the B&L. The current detection performance is limited by the pre-amplifier design, due to the 400pF junction capacitance of the AD, so there is a room to improve the performance further. A simple AD structure will give a good quality control in mass production, and a lower production cost than the complex of metal dynodes. On the other hand, the mass production procedure for controlling the photocathode vacuum deposition is not established yet, and there is as yet no capacity for large scale production of HPDs.

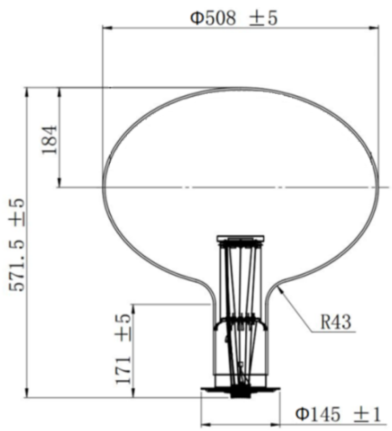

FIG. 99. The JUNO MCP GDB-6201.

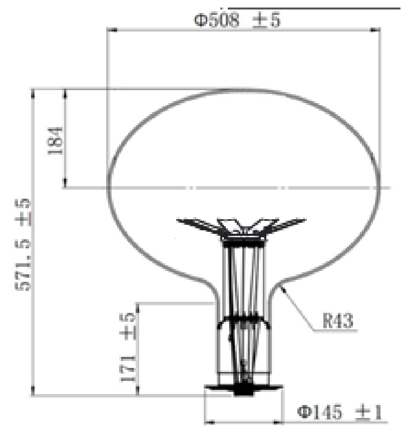

FIG. 100. The Hyper-K MCP GDB-6203.

FIG. 101. Prototype of a waterproof MCP PMT.

B. Inner Detector Covers

The 50cm photosensors are enclosed in front covers which provide a transparent window to detect Cherenkov photons and light-tight rear bodies to hold the photodetectors in place. The

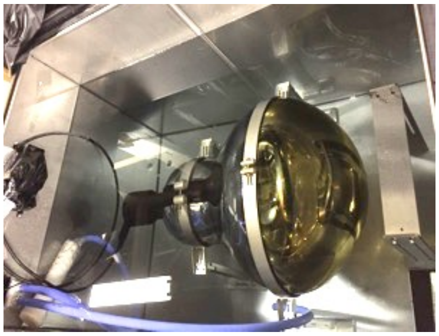

FIG. 102. The HQE 50 cm HPD (R12850) tested in water.

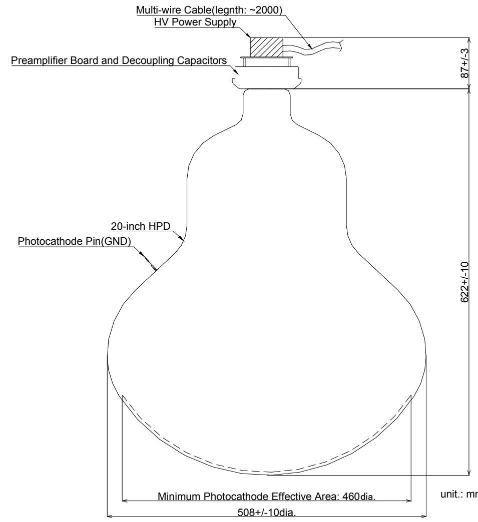

FIG. 103. Design of the HQE 50 cm HPD.

rear covers need to be water-tight, and the front windows need to provide sufficient mechanical protection to prevent a chain implosion of the photodetector bulb. The component parts of the cover are joined together and the whole structure is fixed to the photosensor support structure in the tank.

The cover should pass a hydrostatic pressure test at 60m depth equivalent pressure without being crushed. We also require that the cover should pass a set of shockwave tests in 60m water depth to demonstrate a significant reduction of the shockwave for the prevention of chain implosion. A test site was constructed to simulate the event of a photosensor implosion in a deep vertical shaft at Kami-Sunagawa town, Hokkaido (Fig. 104).

The front window is made out of ultraviolet (UV) transparent acrylic, and has a hemispherical shape with a flat 13mm thick flange. The flange has 24 holes of 9mm diameter to fix the acrylic window to the cover body. The maximum height of the window above the flange is 19cm, which is a little higher than the the comparable windows in Super-K. The minimum requirement for light transparency through the front window is 50% at 300nm and 90% between 400nm and 800nm for a photon at normal incidence to the window. The cover should also minimise the reflection of light in water at 15°C, since this effectively adds to the dark count rate of the other PMTs. The requirement here is that the dark rate increase should be much less than 0.1kHz. There are small holes in the front window to allow water to flow from outside the cover over the surface of the photosensitive area. These are designed to reduce the concentration of radon emanating from the PMT, and to prevent the formation of a biofilm on the photosensitive surface. All the material facing the water should satisfy the requirements in Table XXXV.

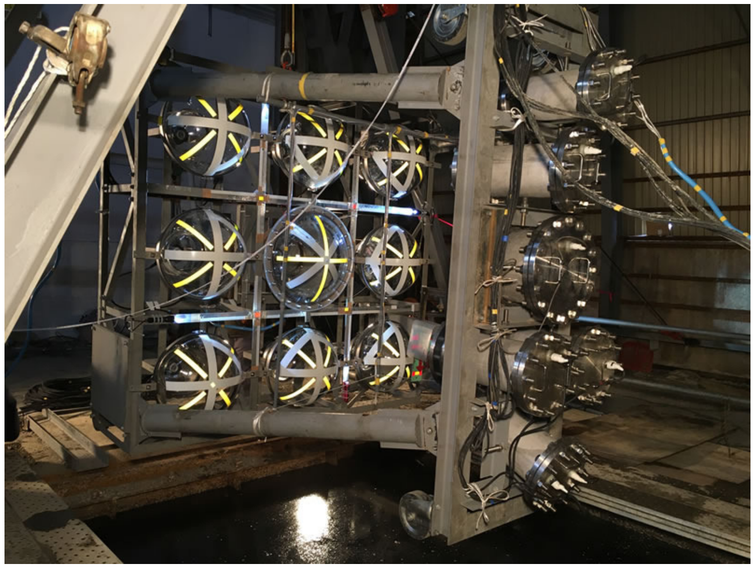

FIG. 104. The test setup for the PMT covers at Kami-Sunagawa town, Hokkaido. The effect of an artificial implosion of the centre bulb, with and without the protective covers, has been measured using pressure gauges and high-speed cameras.

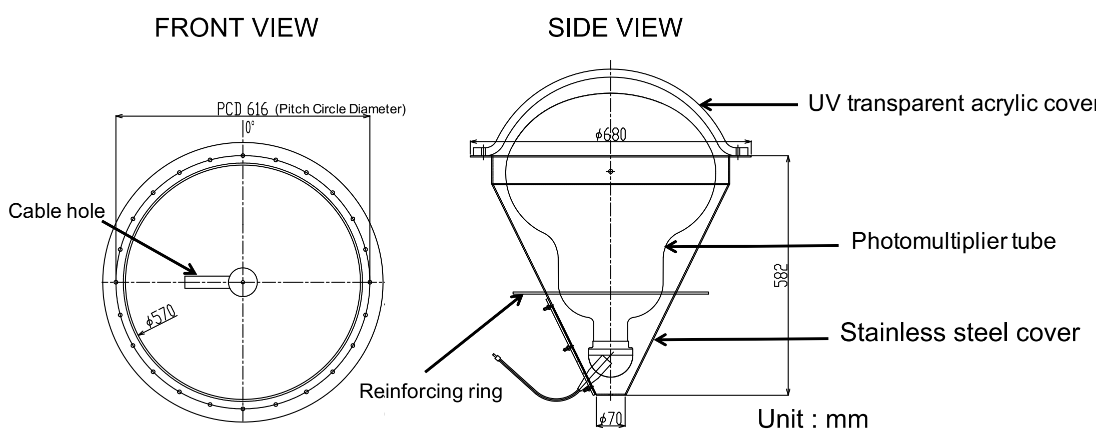

FIG. 105. A schematic view of the cover for the Hyper-K ID PMTs, composed of a stainless steel body and an acrylic UV transparent window.

The cover body has a conical shape, and needs to be mechanically connected to the front window flange, and to the PMT inside. There also needs to be a mechanical mounting for the whole PMT assembly on the photosensors support structure in the tank, which is still being designed. A stainless steel cover with 3mm thickness has been developed and tested as shown in Figure 105.

TC - We really need pictures of the alternative cover designs as well.

Alternative cover designs are being studied to reduce the weight and the production costs. A lighter cover made of 2.5mm thickness stainless steel was successfully tested in 2018. This reduces the total weight of the cover body from 22kg to 17kg. An even lighter and cheaper cover has been realised using a PPS resin material mixed with carbon fibre. Finally there is a much cheaper design of a stainless steel cover with a more cylindrical shape, but this is likely to be heavier, in the range 20–30kg. The cylindrical-shaped steel cover have been tested in 80m water depth, and the resin cover in 40m water depth. We may decide to use different covers in different parts of Hyper-K in an effort to optimise the overall weight and cost of the detector. The production of the covers is planned to take four years, with the windows and the cover bodies being delivered separately for subsequent assembly with the PMTs.

C. Inner Detector Light Collection

TC - This section has largely been rewritten.

A light collection system is being considered as an option to increase the photon detection efficiency of the 20" photosensors. The idea is to collect or focus photons that would otherwise have missed the photosensitive area. There are a number of different ways in which this can be done, of which the main ones are:

- Cone-shaped reflective mirrors.
- Photon trapping using wavelength shifting plates.
- Focusing with Fresnel lenses.

These systems are typically a cheaper way of increasing the number of photons than the addition of more photosensors. However, the amount that can be gained is limited by the available space, and by the collection efficiency of each system. In the following it is assumed that the light collection system must fit inside the unit cell of $70\times70\text{cm}^2$, and not project out more than 20cm, i.e. be the same height as the PMT covers, with the exception of the lenses which by definition have to be above the covers.

TC - The table of requirements has been suppressed here, and replaced with text and an itemised list.

In designing a light collection system the following things need to be considered:

- The angular acceptance for photons should be uniform to at least 70°, and preferably to larger angles of incidence. Loss of large angle photons leads to a degradation in the light enhancement factor as a function of distance from the centre of the detector. In the case of events near the ID wall the loss of acceptance can remove significant parts of the ring image, affecting reconstruction and particle identification.

- The reflection of photons back from the light collection system into the ID water should be kept as low as possible, since it leads to an increase in the dark count rate in the other PMTs.

- The arrival times of photons from the light collection system are typically later than the photons that directly hit the photosensor. In order not to degrade the good timing properties of the photosensors themselves, the time delay should be kept below 5ns.

- The materials in the light collection system should obey the same criteria as the photosensors and their covers. They should not increase the radioactive backgrounds, and they should not reduce the transparency of the ultra-pure water. The light collection system should be durable, losing no more than 5% of its efficiency in 10 years.

TC - The details of the parts that are being prepared for light collection system tests should be added in the descriptions of the individual systems.

1. Reflectors

A cone-shaped mirror surrounding the photosensors can concentrate photons onto the photocathode. To retain good angular acceptance for photons the mirror has to have a rather low profile with a partially elliptic curve (it is not a Winston cone!). With a 20cm high reflector of diameter 70cm, the angular acceptance extends to 72°. The optimal shape is currently being studied, with initial results suggesting that a gain in light collection of a factor $\times 1.3$ can be achieved for events in the centre of the detector, decreasing to $\times 1.1$ for events at edge of the fiducial volume, with an average gain of $\times 1.18$. A similar set of reflectors are already included in the design of the mPMT modules (section III.8), where they give a factor of $\times 1.2$ in light collection.

A mirror made out of aluminium is light and cheap, and can be coated with resin to prevent aging in the water. It should be designed to be attached to the acrylic flange of the ID photosensor cover.

TC - This needs a picture of the proposed shape.

TC - I would also add the photon angular acceptance. It would be good to report the results of the software studies of the effect of reducing the angular acceptance.

2. Wavelength Shifting Plates

This method of increasing light collection is already used in the outer detector, both in Super-K and in the design for Hyper-K (section III.7 B). The area of the unit cell that is not occupied by the photosensors is covered by a plastic wavelength-shifting plate which absorbs photons at short wavelengths (UV), and re-emits them in the visible. The incoming photons are absorbed at all angles, so there is no impact on the angular acceptance. The emitted photons have random directions, but through total internal reflection at the surface of the plate about half of them are trapped and transported across the plate. Adding reflecting foils at the edges of the plate directs photons back towards the photosensor. Simulation studies, laboratory measurements and the experience from Super-K indicate that a collection efficiency of about 10% can be achieved for photons hitting the plate. Since the area of the plate is 60% of the unit cell, the gain in light collection can be estimated to be about $\times 1.2$.

The plates themselves are light and cheap compared to the photosensors. They could even be considered as replacements or adaptations of the acrylic flange part of the PMT cover. They need to be mechanically fixed to the covers so as to made a good tight contact with the photosensor, or with its acrylic cover. Losses due to the optical coupling between the plate and the photosensors are a significant factor in the design.

The main drawbacks of the wavelength shifting plates are that 25% of the visible photons escape the plate back into the ID water, and that the photons that are trapped can have quite long propagation times in the plate before they reach the photosensor.

3. Fresnel Lenses

A a set of thin plates such as a Fresnel lens can change the light direction by refraction to concentrate photons onto the ID photodetector. For our application this system can be non-imaging, and can be designed to accept a large range of angles of incidence, with a transmission coefficient >90%. The plates can be made out of acrylic with thicknesses of a few mm.

The main drawback to a lens system is that it has to be mounted 30–50cm away from the photosensor which decreases the ID fiducial volume. The mounting structure for the lenses has to be attached to the photosensor support frame, and will inevitably block some of the photons that would have directly hit the photosensors at large angles. It is likely that the performance of the lens system will degrade significantly for events close to the edge of the fiducial volume.

4. Photon traps

Lenses or mirrors could be combined with plates to provide a more sophisticated photon trap. An example is the use of a dichroic mirror to transmit UV light and reflect visible light. This can be used to recover the visible photons that were not initially trapped in the wavelength-shifting plates by total internal reflection, potentially gaining a factor of two. Unfortunately the photons that are recovered still make large angles to the plate, and thus take a long time to reach the photosensor. Another drawback of this design is that the mirror reflects back visible Cherenkov photons into the ID. Finally the mirror has to mounted above the plate, although maybe not by very much if it only covers the plate and not the PMT itself.

D. Inner Detector Assembly

An ID photodetector production line has to be prepared with a clean environment. Here the photosensors are assembled as individual units together with their covers, light collection system (if present), and support bands. For the assembly we need to provide the necessary tools and jigs. After the transfer from the manufacturers and before the installation, a large storage area is needed for all photodetector components, which also requires environmental control. After assembly the individual units are transferred from storage to the Hyper-K cavern for installation on the photosensor support structure in the tank, as described in Section III.13 A.

1. Photodetector Support Bands

Support bands are essential to keep the photodetector fixed against 60kg of buoyancy over a period of 20 years. The photodetector bulb should be fixed with a uniformly distributed additional pressure on the overall band surface, without a local concentration of any external force from the support structure outside, including buoyancy. The bands are tightened with a torque control to hold the photodetector by a frictional force between the band and the bulb glass. A band is made of a rubber part that touches the glass glued to a thin stainless steel part that can be attached to the cover. For each photodetector there are two bands, one of which is attached to the point with the largest 50.8cm diameter, and the other to the cylindrical region at the back of the bulb with a 25.4cm diameter. The centres of the two bands are typically separated by 22.5cm along the axis of the tube as shown in Figure 106. The connection of the bands to the cover, and of the cover to the photosensor support structure in the tank, need to be flexible so that the bulb is not pressurized by a deformation of the photosensor support structure, which we assume could locally be as much as a few centimetres.

TC - Is this assumption related to earthquakes, i.e. a temporary deformation, or is it related to permanent distortions in the photosensor support structure due to buoyancy and other forces?

A structure to tighten the band has been improved upon the design used in Super-K, so as to make a more uniform distribution of the surface pressure between the band and the bulb. One of ideas that has been tested and partially introduced in Super-K, is to apply a clamp with a commercial hose band made of stainless steel. All the parts needed to connect and fix the bands to the photosensors and their covers have to be provided.

The materials in the support bands need to satisfy the same criteria as the materials in the photosensors (see Section III.6 A), i.e. they should not affect the transparency of the ultra-pure water, and they should not contribute significantly to the radioactive background. Note that the rubber and glue used in the PMT band for Super-K are not suitable to keep the water clean.
TC - How does SK manage with this problem?
A 5mm thickness of silicon rubber with the same hardness A60/S (ISO 7619) and silicon adhesives can be used in ultra pure water (Figure 107). The mechanical stability of the band after absorbing water needs to be well tested. Table XXXVII shows the requirements or typical specifications of the ID photodetector support band. All the band and related parts are delivered before the assembly starts.

FIG. 106. Picture of the support bands attached to the B&L PMT.

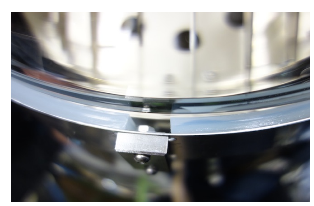

FIG. 107. Side view of the support band made of silicon rubber and adhesive between the bulb glass and the stainless steel plate, with an attachment structure at the centre of the picture.

Requirements	Value	Conditions
Maximal Weight	1kg	In total
Maximum thickness from the bulb	22mm	Maximum height at the band center
Degrease cleansing		Acid wash
Typical values	Value	Conditions
Hardness	A60/S (ISO 7619)	Touch to the glass
Band width	32mm	Larger diameter
Band width	32–40mm	Smaller diameter
Band inner diameter	508±3mm	Larger diameter
Band inner diameter	254±3mm	Smaller diameter
Temperature	13–30°C	

TABLE XXXVII. Minimum requirements (top) and typical values (bottom) of the support bands for the B&L PMT.

2. *Photodetector Storage*

A storage system to keep the components of the photodetector system is prepared near to the Hyper-K site. The size of the photodetector assembly is typically 55cm×55cm×81cm and the weight is about 10kg with the photosensor. The photodetectors should be stored with the photocathode surface looking downwards, especially during transfers, in order to avoid glass scratches, and misalignment of the dynodes due to shaking. An area of 4,000–8,000m^2 area is necessary to keep a full set of forty thousands B&L PMTs if three boxes of PMT assemblies are stacked on top of each other.

A system for the environmental control and management of the photodetector storage has to be included. Helium penetration through glass from the air can lead to a decrease in the gain and an increase in the after pulse rate. Therefore it is important to monitor the partial pressure of helium in the air, which should be less than 1Pa (10ppm), where the normal atmospheric concentration of 5.2ppm is mostly due to radioactive decays. A lower storage temperature is better as this slows down the helium penetration. The minimum temperature for storage is -10°C and the storage should be dark to avoid activating the photocathodes.

A further area of 4,000–6,000m^2 is necessary to keep a full set of forty thousand cover parts if five of these are stacked in a unit of 70cm×70cm. This area has to be shaded to avoid ultraviolet light from the sun. We assume that the parts will be sent to the storage periodically during their production, and therefore the storage areas and environmental controls need to be prepared before the production starts. We still have to determine the site for the storage areas and to construct a storage management system.

3. Assembly Line

The assembly line requires suitable tools and jigs, and a management plan with well-defined procedures. The assembly area should be clean in order to avoid any dust on the photodetector and cover, and between the bands and the photodetector. The surfaces will be cleaned after the assembly, with a check of the bulb condition by eye to minimize the risk of a small crack that might lead to implosion in the tank later. Since there is a danger that the vacuum bulb may implode during the assembly phase, a safety management plan has to be provided.

We still need to design the assembly line and identify a suitable place for it.

III.7. OUTER DETECTOR DESIGN

Neutrino interactions are characterised by a lack of incoming particles, and it is important to veto events where there is activity in the outer part of the detector. Low energy neutrino interactions produce signals that can be swamped by background from low energy (1 to 10MeV) gammas and neutrons. These backgrounds are partly due to natural radioactivity in the surrounding rock, and in the photodetectors themselves, but there is also a contribution from spallation interactions by cosmic muons. The reconstruction of events uses the expected Cherenkov cone pattern from a charged particle, and the addition of photons from these backgrounds and from the dark count rate of the photosensors, leads to mis-reconstruction and misidentification of the charged particles.

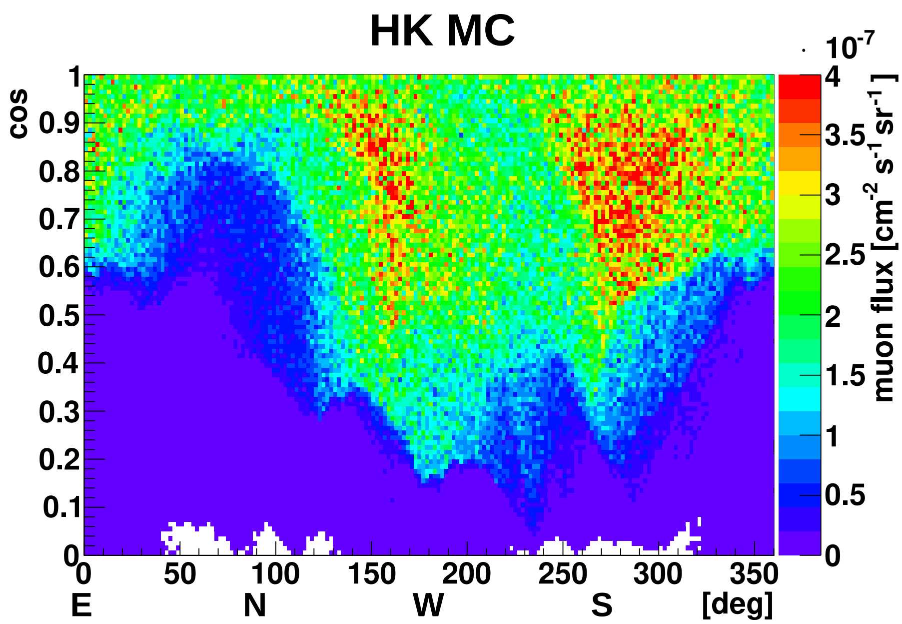

FIG. 108. Hyper-K cosmic muons flux simulated at Tochibora mine.

The second source of background is the hard component of the cosmic muon which penetrates deep inside the Earth (Fig. 108). Muons that enter the outer detector create a large number of Cherenkov photons which can be identified by the outer photosensors. A very efficient veto against incoming muons is essential for the physics programme, particularly for atmospheric neutrinos and proton decay searches.

To veto activity in the outer detector (OD) it has to be optically separated from the inner detector (ID), with photons detected by a separate array of photosensors. The current design has an outer layer thickness between 1m (barrel) and 2.5m (endcap), and a dead region of 60cm between the OD and ID photosensors, determined by the size of the ID covers. The radiation length of water is 36cm, and the typical capture distance for neutrons is ≈2m, after thermalisation in the water. From SuperK we know that this is sufficient to contain most, but not all the low energy backgrounds. We note that the 1m barrel thickness is 2x less than in SuperK, making the veto performance more challenging to deliver.

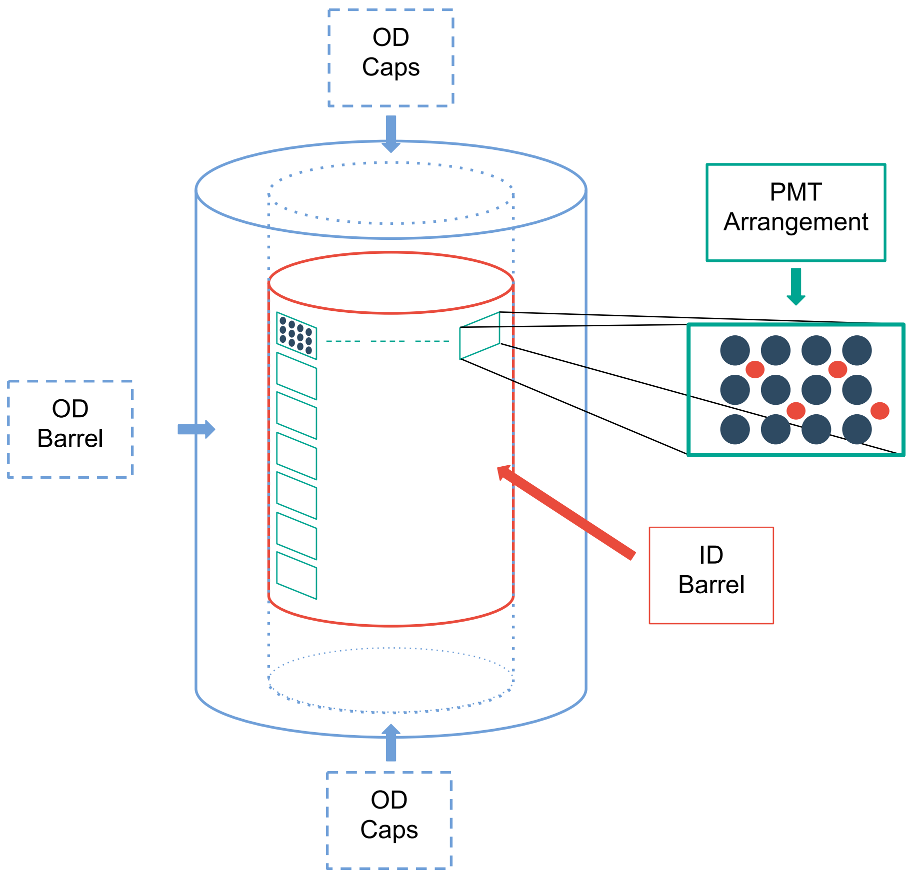

FIG. 109. A sketch of the Hyper-K detector design (not to scale). The structure holding the ID photosensors is represented in red, with the limits of the tank in blue. The area outside the ID detector is the OD volume, where we distinguish the barrel region from the top/bottom endcaps. The photosensors are arranged with respect to the green rectangle on the right side of the figure. The dark blue photosensors are the ID ones, and the red ones are the OD ones, facing outwards. The OD photosensors shown correspond to a total of 13.3k 3” PMTs.

A. Outer Detector Photosensors

The design for the Hyper-K outer detector (OD) assumes an array of between 10 and 20k 3” PMTs with a photocathode coverage between 0.21% and 0.42%. Figure 109 shows a geometry with 13.3k PMTs (0.28% coverage). The coverage will be enhanced by a factor of ×3 by light collection from wavelength shifting plates (WLS), as described in the next sub-section. For comparison Super-K has an array of 1885 8" PMTs with a photocathode coverage of about 1%, which is enhanced by a factor of ×1.6 by WLS (for Hyper-K this would translate into 6800 8" PMTs). The choice of smaller tubes for Hyper-K is motivated by the need for a finer array of detectors to veto the smaller thickness of the barrel region, and by the lower cost and dark rate of the smaller tubes. The optimum number of 3" PMTs to provide a suitable veto performance is discussed in the sub-section on design studies.

Tests of a number of 3" PMTs have been performed. The ET9302KB from Electron Tubes has been extensively tested at Queen Mary University London, and the ET9320KFLB has been studied in Edinburgh. These PMTs have a QE of 30% and a dark count rate of 400Hz, about ten times less than typical rates for 8" PMTs. The after-pulse rate of the 3" PMT is also smaller than the 8" PMT at the same gain. The estimated number of dark counts for different OD configurations, using 3" and 8" PMTs are shown in Fig. 111.

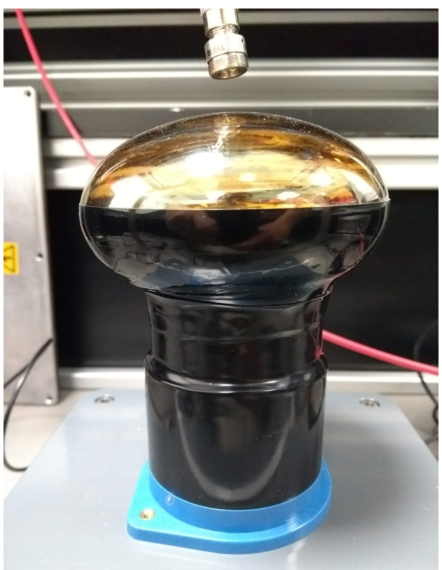

FIG. 110. ET9302KB in the black box setup at Queen Mary University London.

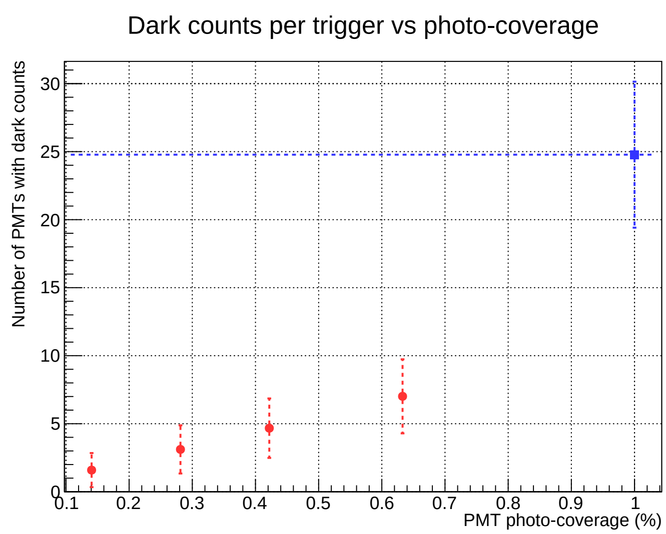

FIG. 111. Estimation of the dark count per trigger for 3" PMTs (in red) and 8" PMTs (in blue), using measured dark rates at 13°C.

The ET9302KB (ET9320KFLB) has a gain of 3×10^6 at a typical HV of 950V (800V). The measured dark rates with respect to the HV are in agreement with the quoted values of the manufacturer (Fig. 112). The dark counts are defined as signals over a 0.25pe threshold, determined separately for each value of the HV. The PMTs show excellent linearity and a peak-to-valley ratio of 2.5 for a 1pe signal. This allows for accurate reconstruction of the number of photons detected in the OD. Figure 113 shows the linearity of the photosensor, where the deviation was measured to be a few % up to 1500pe. These measurements were made by varying the amount of light emitted by an LED.

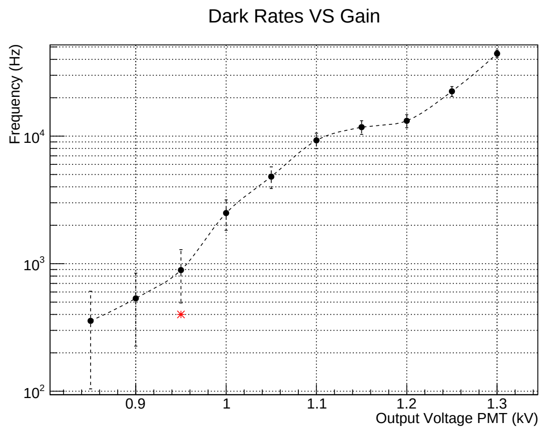

FIG. 112. Dark rates with respect to the gain for the ET9302KB measured at 20°C.

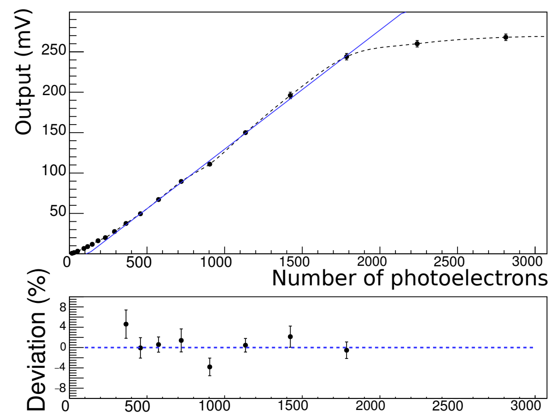

FIG. 113. Linearity for the 3" photosensor ET9302KB measured with an LED source.

The timing resolution of the ET9302KB (ET9320KFLB), with a rise time of 7.5ns (2.5ns), is not critical for our veto application. The collection time of the WLS plates is known to be longer than this. There is also a spread on the arrival times of photons reflected back from the outer wall of the tank.

B. Outer Detector Light Collection

1. Wavelength shifting plates

The 3" PMTs are chosen with hemispherical photocathode shapes, so that wavelength shifting (WLS) plates can be mounted around them with light coupling to the PMT through close contact at the sides of the photocathode. This is a straightforward way to enhance the light collection over a larger area. The WLS plates (Eljen EJ-286), absorb light in the UV region between 280 and 400nm, where most of the Cherenkov light is produced. They re-emit light in a random direction at approximately one photon per absorbed photon. The emitted light is in a narrow band between 410 and 460nm, which is well-matched to the QE of the PMTs. A plate with a standard thickness of 13mm (0.5"), absorbs all the incident UV photons.

Fig. 114 shows the principle behind the WLS plates and photosensor coupling. Photons emitted with large angles of incidence to the surface of the plate are trapped by total internal reflection,

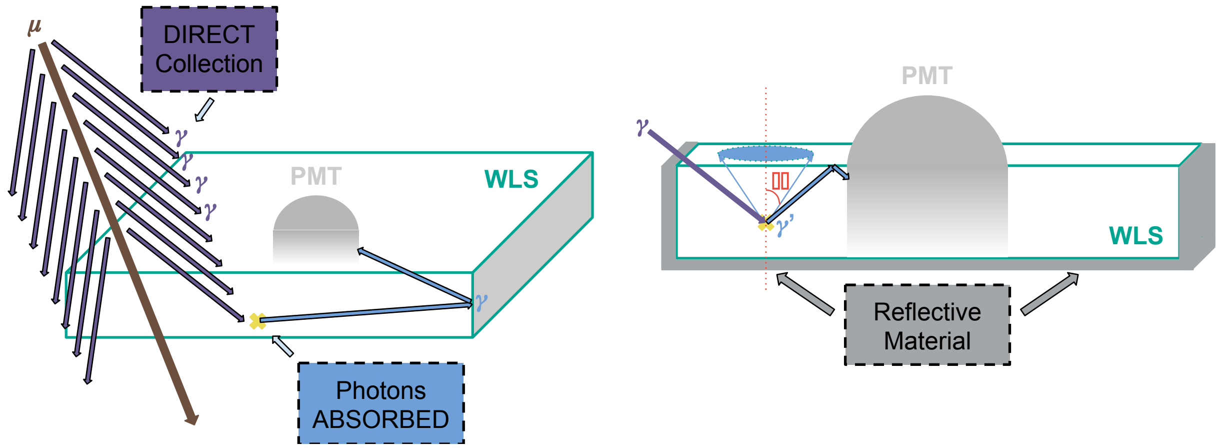

FIG. 114. Sketch of the light collection using a WLS plate. A charged muon emits light by Cherenkov radiation in the UV. This is absorbed inside the plate (yellow point), and reemitted as blue light in a random direction. By total internal reflection (right), and reflections at the edges of the plate (left), some of this light reaches the PMT indirectly, where it adds to any light that reaches the PMT directly.

and can also be reflected at the edges of the plate. The refractive index of the WLS plate is 1.58, so the critical angle for total internal reflection is 39.3° for a surface with air, and 57.3° for a surface with water. It is not really practical to create an air gap between the WLS plate and the surrounding water over the large area of the Hyper-K OD, so we assume the latter value of ≈1rad for the critical angle. The amount of light trapped in the plate is 54% (77%) for a water(air) surface. Near the PMT about half of this light travels towards the PMT, giving a maximum WLS efficiency of ≈25% (35%) at short distances. For larger distances in the plate there is a geometric dependence that goes like $1/r$ ignoring the reflections at the edges.

Laboratory tests of the WLS plates have been carried out in Edinburgh and used to develop a model of their properties. The square and rectangular plates used for the tests have dimensions of $23 \times 23 \times 1.3$ cm and $28 \times 48 \times 1.3$ cm. For the Hyper-K OD we plan to use square plates of $48 \times 48 \times 1.3$ cm. A curved circular hole is cut in the center of each of the plates, matching the shape of the sides of the photocathode, as shown in Fig. 115 (left). This allows it to be coupled to a 3" ET9320KFLB PMT with a minimal air gap. The dimensions of the hole are chosen such that the base of the plate sits close to the measured lower edge of the sensitive area of the PMT photocathode.

The studies are carried out inside a large light-tight dark box (Fig. 115(right)), and an LED with a wavelength of 370nm as a light source. The light from the LED is guided into the box using a cladded optical fibre. The LED light is attenuated such that it provides a fast pulse matching a

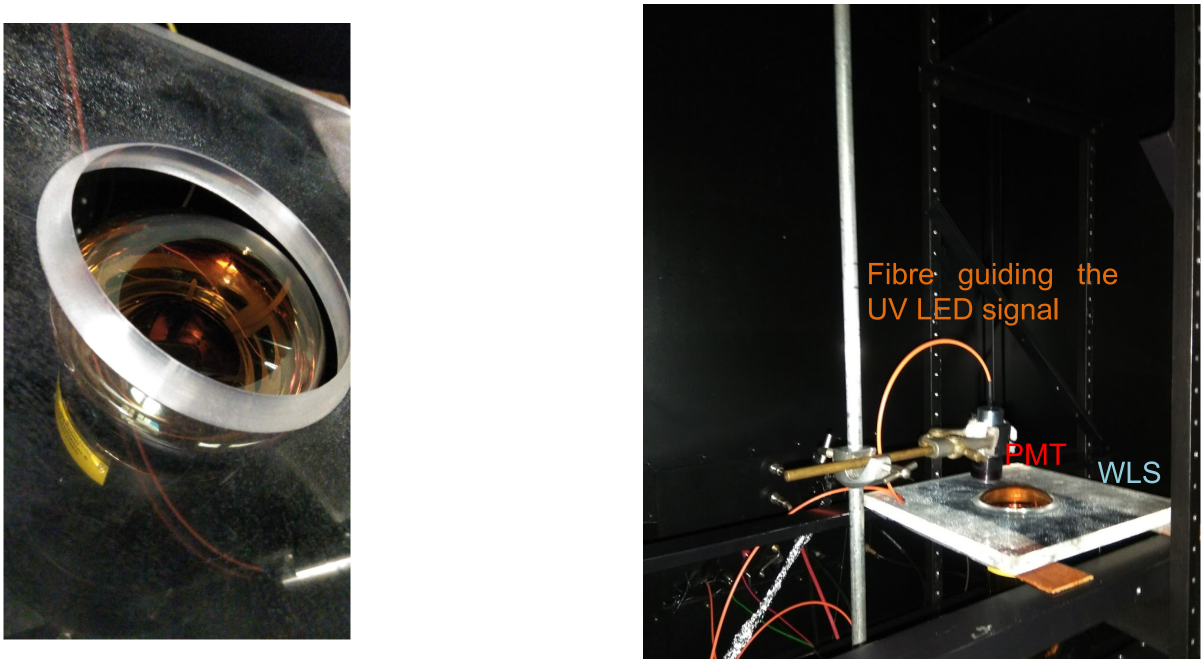

FIG. 115. Left: Mounting of the WLS plate to the PMT. Right: Setup used to measure the WLS performance.

single photon signal, and it is collimated such that the spot size is approximately 5mm in diameter. Scans of the detected photon spectra were taken by moving the LED across the surfaces of the PMT and WLS plate. Data were taken in four configurations: with the PMT and no plate; with the PMT and a bare plate; with the PMT and a plate whose side edges are wrapped in reflective mylar; and with the PMT and a plate which also has a sheet of reflective Tyvek underneath it.

The figure of merit for these studies is the efficiency relative to data taken illuminating the centre of the PMT. To calculate this for each configuration the rate of hits above threshold with the LED on is used, after correction for the dark count rate measured with the LED off. The efficiency is then

$$\eta = \frac{f^{ON} - f^{OFF}}{f^{ON}_{centre} - f^{OFF}_{centre}}$$

The accuracy of this procedure is estimated to give errors of about 10% of the values by making repeat measurements. The results are compared to a model that takes as input the known geometry of the setup and allows light in the plate to undergo up to two reflections at the plate edges. The model has the following free parameters: (i) the collection efficiency for photons produced next to the PMT and (ii) the reflectivity of the edges.

Fig. 116 summarises the results of these studies. Compared to the plate alone wrapping mylar around the edges is found to increase the efficiency of the plate by about a factor of two. In

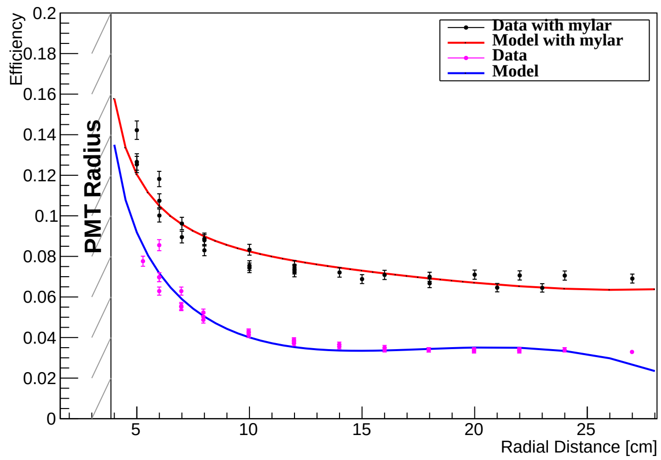

FIG. 116. The efficiency of the WLS as a function of the radial distance from the PMT centre with (black dots) and without (pink dots) mylar reflectors on the sides. The solid lines correspond to the expected results from the model.

contrast the addition of Tyvek underneath the plate made no difference at all. The data agrees reasonably well with our simple model, which gives us confidence that it can be used to predict the light collection efficiency of the larger plates proposed for use in the Outer Detector.

The performance of the wavelength shifting plate has not been fully implemented in WCSim yet, but the estimated gain in photons can be obtained by integrating the measured efficiency as a function of distance from the PMT, which goes approximately as $1/r$. The area of the integration increase like r^2, so the contribution of the WLS plate increases like the length of the side r, or faster if we believe the flatter profile when we add in the reflections at the edges. In Table XXXVIII the estimated gain in air for the 3" photosensor is consistent with the measurements performed in the University of Edinburgh, and the estimated gain in water for the 8" PMT with a 60x60cm^2 WLS plate is consistent with the Super-K measurements. For interest we also show the expected from adding a 70x70cm^2 WLS plate to a 20" ID PMT. According to this table, the addition of a 48x48cm^2 WLS plate to the 3" OD photosensors will increase the light collection efficiency by a factor of at least three in water. Thus the effective OD photocoverage becomes $\approx$1% for 15k PMTs.

TABLE XXXVIII. Estimates of the ratio of photons from the PMT+WLS relative to photons from the bare PMT, where the surface of the WLS is either air or water.

Configuration	Air	Water
3" PMT with 24x24cm^2 plate	x2.35	x1.65
3" PMT with 48x48cm^2 plate	x5.0	x3.5
8" PMT with 60x60cm^2 plate	x2.35	x1.65
20" PMT with 70x70cm^2 plate	x1.3	x1.2

2. Tyvek reflecting sheets

Although the primary purpose of the the OD is to identify incoming muons, it is also desirable to identify outgoing muons in order to separate high energy events into Fully Contained (FC) muons, Partially Contained (PC) muons, and through-going upward (UP) muons, which are also used in atmospheric neutrino analyses. The Cherenkov light from such muons mostly travels away from the OD photosensors and must be reflected back at the outer wall of the tank. As in Super-K we plan to do this by covering the outer wall in a sheet of Tyvek which has good optical reflectivity, and is a durable paper-like material for use in a pure water environment. Following Super-K we also plan to put in Tyvek sheets to vertically separate the endcap and barrel volumes of the OD. Fig. 117 (left) shows a piece of Tyvek indicating the high reflectivity and opacity of the material.

What is not so clear is whether we should put a reflective surface on the inner side of the OD. Fig. 117 (right) shows an 8" OD PMT and WLS mounted on top of a white/black Tyvek sheet in Super-K. We have shown that such a Tyvek sheet underneath the WLS plates does not add to the collection efficiency in our test setup, although it might add something if we allow for two bounces at the inner and outer sides of the OD. The same statement applies to Tyvek placed in the gaps between the WLS plates. It would take two bounces (and at least 10ns), for the light to reach the OD photosensors. Note that in any case we have to provide a black sheet somewhere between the ID and OD volumes to prevent light from crossing the dead region between them. This sheet could be made of Tyvek, or of a more rigid material.

C. Outer Detector Performance Studies

Simulations have been performed within the WCSim framework which contains the full geometry of Hyper-K including the OD. A complete and separate hits collection is available with the digitized

FIG. 117. Left: A piece of Tyvek sheet. Right: An OD phototosensor mounted inside Super-K.

information of the direct OD photosensors hits, consisting of charge and time of the signals, just as it would be with the real data. Unfortunately we not yet developed an equivalent set of information for the indirect hits from photons hitting the WLS plates, so this contribution of about $\times 3$ is not yet included in the studies reported below. Several different generators were used to study different types of events. The quantities studied so far are the total number of photons collected by the OD per event, and the number of PMTs with hits per event. We discuss how these can be used to veto activity in the OD.

The generator for downward cosmic muons is described in Fig. 118 (left). A random position is selected inside a 10 m sphere centred in the middle of Hyper-K. Then the muon energy and direction are randomly generated from this point according to the distribution shown in Fig. 108. The initial position is extrapolated to a point above Hyper-K, and the muon is tracked through the OD and ID regions. The yellow rectangles inside Hyper-K represent the areas covered by OD photosensors that detected light from the muon track indicated by the brown arrow. With an OD photosensor coverage of 0.28% (13.3k 3" PMTs), the mean number of photoelectrons is 240, with a range from 40 to 900 from a total of 1200 events. For other geometries the mean numbers of photoelectrons are 314 for 0.31% (15k 3" PMTs), 414 for 0.42% (20k 3" PMTs) and 1254 for 1% (6.8k 8" PMTs), so the mean number of photoelectrons is proportional to the photocoverage. To reach a veto efficiency of greater than 99.9% requires a threshold of about 40 photoelectrons if we just use this information. The number of PMTs with hits with respect to a number of photoelectrons observed in the OD is shown on Fig. 119 *Note - this figure is incorrect at the moment.* A two-dimensional veto on these quantities could also be used.

We generate a set of incoming "sand" muons originating from outside the tank. These are

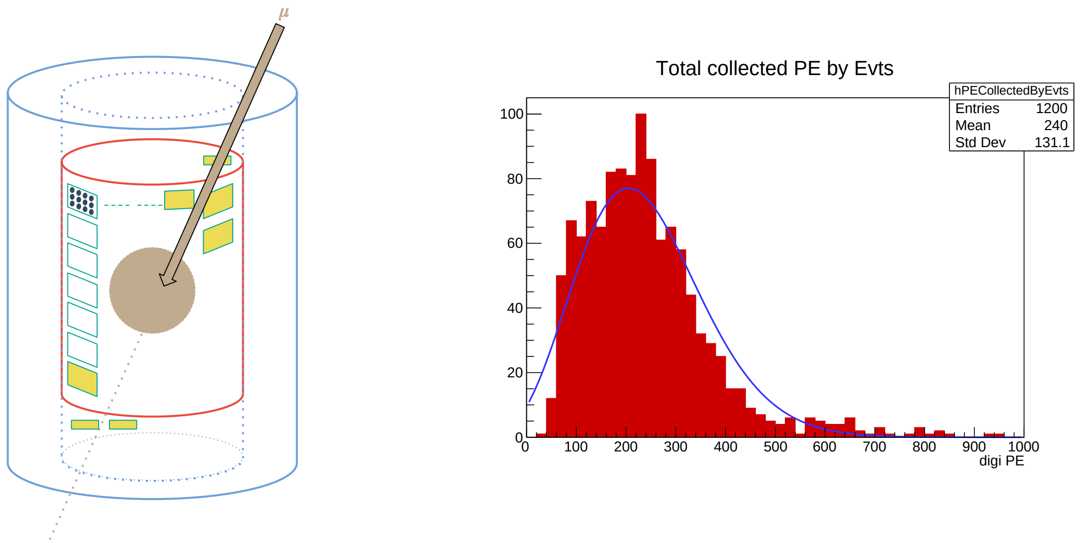

FIG. 118. Left: The generation of cosmic muons in WCSIM. The brown arrow shows a muon track entering from above and passing through the central region of Hyper-K. The yellow rectangles indicate regions where there are OD hits. Right: The number of direct photoelectrons observed with 13.3k 3" PMTs in the OD.

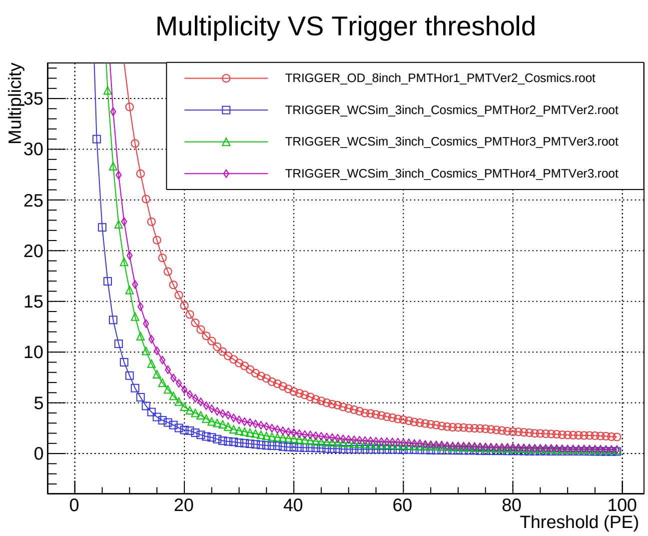

FIG. 119. Number of photosensors hits with respect to the number of photoelectrons collected in the OD with 13.3k 3" PMTs. *Please replace this figure with the one that matches this caption- SP! There is no such thing as a "trigger" threshold in the OD, and there is more information in the scatter plot of NHits vs Npe.*

due to neutrino beam interactions in the rock, and enter the tank approximately horizontally as indicated in Figure 120 (left). An initial position is selected on the incoming beam side of Hyper-K and a horizontal muon track is generated with a Gaussian distribution with a mean of 10GeV, and an rms of 1GeV *these are evidently incorrect for the JPARC beam - SP*. The mean number of photoelectrons collected in the OD for these events is shown in Fig. 121 (left). It again scales with the photocoverage, but is a factor of ×7 lower than the numbers for the cosmic muons. This is a combination of the reduction in OD width from 2.5m to 1m, and the use of normal incidence as compared to angles of incidence that allow for hits in both the barrel and the endcaps for the downward cosmic muons. We have checked that the photoelectron yield scales linearly with the thickness of the OD. To veto these events with 99.9% efficiency requires a lower threshold on the number of photoelectrons of ≈10 (*SP - Is this about the right number?*).

We also studied outgoing muons from neutrino beam interactions inside the tank. The generation of these is similar to the sand muons, except that the initial position is chosen in front of the outgoing plane of ID photosensors. The mean number of photoelectrons collected in the OD for these events is shown in Fig. 121 (right). It scales with the photocoverage for the 3" PMTs, but is a factor of ×3 lower than the numbers for the sand muons. It is lower for the 8" PMTs than expected. The reasons for these reductions are unclear, but the Cherenkov photons have to be reflected back from the Tyvek sheet on the outside wall of the tank, and this may not be correctly modelled in WCSIM. We do not need to veto these events, but we would like to identify them to separate Fully Contained and Partially Contained muons from beam interactions.

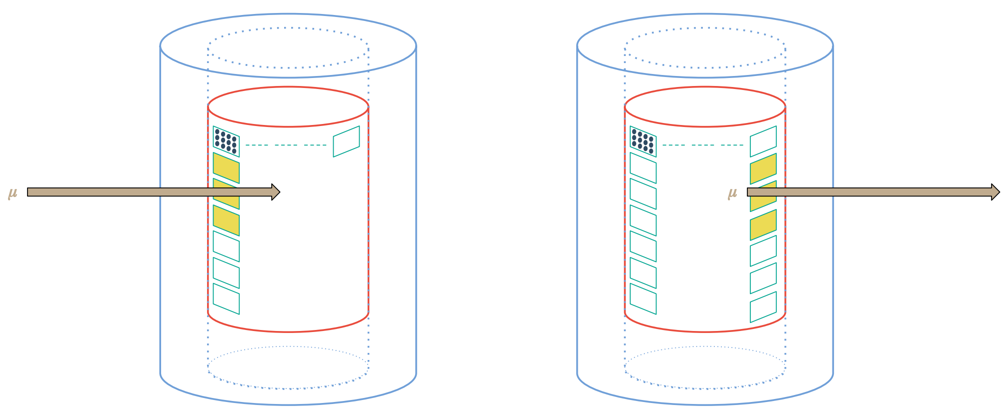

FIG. 120. Definition of the sand muon and outgoing muon event generators inside WCSim. A fixed position in front of the tank (left figure) or close to the outgoing ID photosensor plane (right figure) is generated. The muon is generated along the $+x$ axis, corresponding to the beam direction. The yellow rectangles inside Hyper-K indicate the areas covered by OD photosensors which detected light from the muons.

To study low energy background we simulated 1000 events where 10 MeV gammas enter from the side of the tank. We did not yet include the dark count rate of the PMTs in this simulation. Fig. 122 shows the total light collection for 0.28% photocoverage with 3" PMTs and 1% photocoverage with 8" PMTs. As expected, the total light collected is reduced for the 3" PMTs compared to the 8" PMTs, in this case by more than the change in photocoverage. The number of photoelectrons are well below the suggested levels for our veto thresholds. With the addition of the WLS plates we

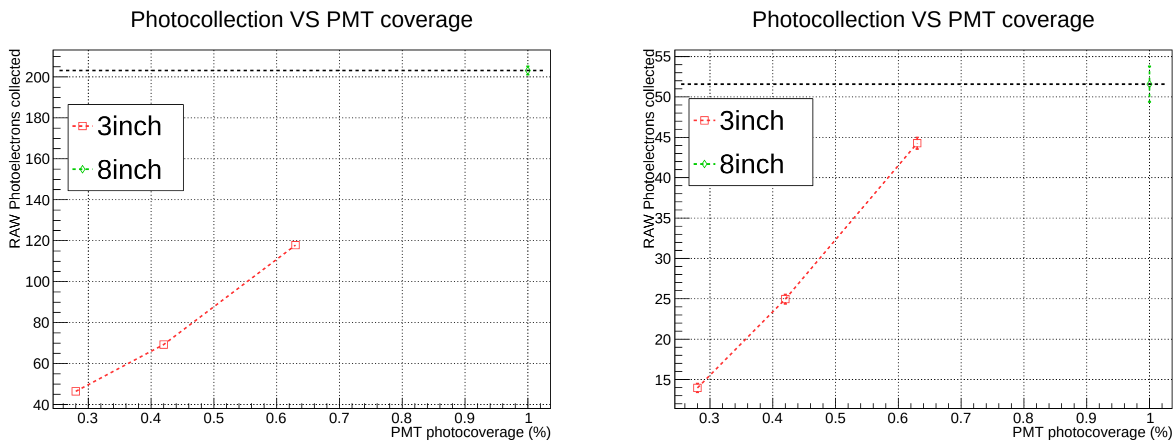

FIG. 121. The light collection with respect to the photocoverage for incoming "sand" muons (left) and outgoing muons (right) from neutrino beam interactions either in the rock or in the tank. Four different geometries are considered with 0.28% to 0.63% coverage of 3" PMTs, or 1% coverage of 8" PMTs.

would expect mean values of $\approx$ 2PE and $\approx$ 5PE for these backgrounds. We have also looked at the number of photoelectrons per PMT (Fig. 123). *Again it would be better to replace these plots with 2D plots of the Number of pe vs the Number of PMT hits - SP.*

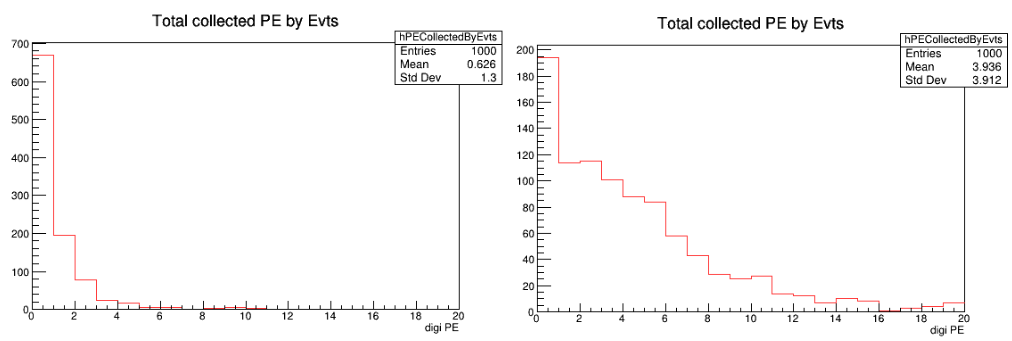

FIG. 122. The total light collection per low energy gamma for 0.28% OD photocoverage with 3" photosensors (left) and for 1% OD photocoverage with 8" photosensors (right).

D. Outer Detector Assembly

TC - This sub-section has still to be written. It is similar to the ID assembly section, but including the wavelength shifting plates and some kind of mounting structure to fix the plate to the bulb, similar to what is done in Super-K.

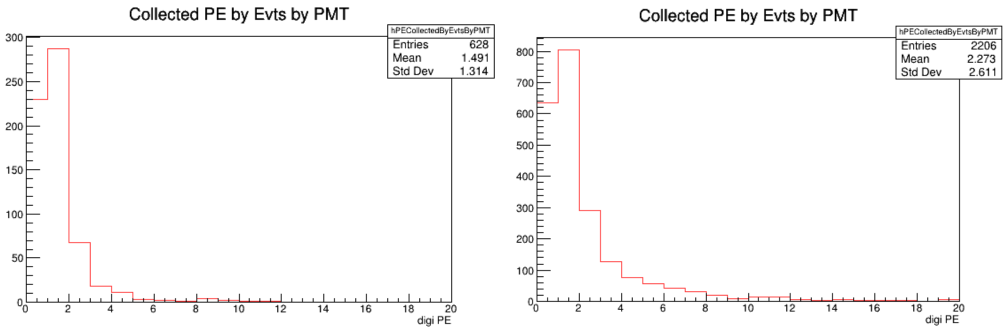

FIG. 123. The light collection per PMT per low energy gamma for 0.28% OD photocoverage with 3" photosensors (left) and for 1% OD photocoverage with 8" photosensors (right).

III.8. MULTIPLE PHOTOSENSOR MODULES

For the Hyper-K far detector there are plans to increase the photosensor coverage from the minimum 20% of 20" PMTs, by using a novel technology which combines a number of small 3" PMTs inside a multiple PMT module (mPMT). This design introduces some intrinsic directional sensitivity, improves the timing resolution, reduces the overall dark count rate and improves the reconstruction performance, particularly for events with vertices near the photosensor plane.

The mPMT is a photodetector system based on the spherical modules that have been developed for the KM3NeT experiment [Ref: S. Adrian-Martinez, et al. (KM3NeT Collaboration), Eur. Phys. J. C74 (9) (2014) 3056, Preprint arXiv:1405.0839]. The hardware functionality and physics capability of the mPMT concept have been demonstrated in-situ with the deployment and operation of KM3NeT prototypes in the Mediterranean sea. The 3" PMTs are installed in an mPMT as an array inside a mechanically safe pressure vessel with readout and calibration systems integrated inside the module. Due to the development of suitable 3" PMTs by several manufacturers, these devices can now be produced in significant numbers, with an estimated cost per mPMT that is only slightly higher than for a single 20" PMT (together with its mechanical mounting and readout).

For Hyper-K the spherical geometry of the KM3NeT mPMT has to be modified so that most or all of the 3" PMTs face inwards towards the fiducial volume of the cylindrical tank of water. We are developing two prototype designs, one with 19 inward facing PMTs, and 7 outward facing PMTs (for use as part of the OD), with these two hemispherical parts connected by a cylindrical tube containing the electronics. The other is a reduced version containing only the 19 inward facing PMTs with a shorter length of cylindrical tube containing the electronics on a flat back plate. A prototype of the first two-sided design is currently being constructed. Tests of mechanical and electrical components of the mPMTs have been performed using prototype spherical modules based on the KM3NeT design.

The details on the performance studies should probably be moved to either the Software or the Physics sections. For the moment I have left them here - SP.

The performance of the mPMTs is being studied using a two step approach:

- We have implemented an mPMT-only inner detector with 40k mPMTs, and compared it to an inner detector with 40k 20" PMTs. This does not represent a reasonable design, since the mPMTs cannot be produced in such large numbers on the timescale required. However, the geometry is simpler to implement, and provides a direct comparison between the performances of mPMTs and 20" PMTs.

- As a second step we plan to compare a hybrid far detector geometry with 20% photo-coverage of 20" PMTs and an additional 5k mPMTs, with a minimal geometry with just 20% photo-coverage of 20" PMTs. The number of additional mPMTs can eventually be adjusted between 1k and 10k depending on funding, production capacity and physics requirements.

The mPMTs have been added to WCSim successfully (Section IV.1), and both low and high energy neutrino events have been generated. The 3" PMTs has been simulated with either 200Hz or 100Hz dark count rates, as expected if we operate them with negative or positive high voltage respectively. Their transit time spread (TTS) has been conservatively assumed to be 2ns, although recent measurements at IPMU and TRIUMF have shown TTS values closer to 1.5ns for 3" Hamamatsu PMTs. The reconstruction tools for low energy (BONSAI) and high energy (fiTQun) events have to be re-tuned to optimise the performance gains from the mPMTs. Details of the software implementations can be found in Section IV, and more details of the physics studies can be found in Section V.

For low energy events there is an improvement in the vertex and direction resolution for events close to the edge of the fiducial volume (<6m), which may allow the fiducial volume to be increased. There is no significant improvement in the energy resolution compared to the 20" PMTs, even though the spatial and timing resolution of the PMTs is better, because the effective photo-coverage of an mPMT is reduced by a factor of about two compared to a 20" PMT. However, the lower dark count rate of the mPMTs with positive HV may allow the energy threshold to be reduced (see Section V.4).

These details to be moved to the physics section - SP.

- With a 200Hz dark count rate, the mPMTs reduce the vertex resolution at 4m from the wall from 54cm (20") to 51cm (mPMT), while the overall vertex resolution is increased from

60cm (20") to 63cm (mPMT). This shows that it may be possible to increase the Fiducial Volume using mPMTs. No significant improvement is observed for low energy reconstruction (E<10MeV) compared to 20" PMTs.

- With a 100Hz dark count rate, the mPMTs shows a general improvement in vertex resolution over the whole detector from 59.5 to 57cm. The vertex resolution at 4m from the wall is reduced from 54cm (20") to 48cm (mPMT). Moreover, the mPMTs are capable of reconstructing very low energy events down to 3MeV, while the 20% coverage of 20" PMTs and mPMTs with 200Hz dark rate can only go down to 5MeV. The only other way to reach a 3MeV threshold is with 40% coverage of 20" PMTs with a 4kHz dark rate (not yet achieved), which is more expensive.

- Preliminary results for high energy events also show improvements in vertex resolution, but further studies are needed to see if there are improvements in energy resolution and particle identification (muon/electron/π^0 separation).

A. mPMT Photosensors

We have assumed the Hamamatsu R12199-02 PMT as the default tube for our design studies for the mPMTs. However, several manufacturers – Hamamatsu Photonics K.K., ET Enterprises Ltd., MELZ FEU Ltd. and HZC Photonics Ltd. – have developed similar 3" PMTs. These PMTs have been characterised and tested for compliance with the Hyper-K requirements by groups at York University (Canada), the Warsaw University of Technology (Poland), the Kavli Institute for Physics and Mathematics of the Universe (Japan) and Queen Mary University of London (UK). Most efforts have focused on the Hamamatsu R14374 and the HZC XP82B20 (Fig. 124), for which transit time spread (TTS), gain, charge resolution, position dependence, dark count rate and waveform shape have been measured. Some initial measurements of ET Enterprise D793KFL were also made. Still pending are after-pulse measurements and more refined scans of position and angular dependence of the collection efficiency, which will be done using a recently assembled 5-axis measurement stand. This allows precise control of both the position and angle of incidence of the light spot (Fig. 125).

Most of the gain and TTS measurements of the new PMTs were done using a pulsed light source and a waveform digitizer – in most cases a fast oscilloscope (Fig. 126). A peak-finding algorithm was run in order to identify pulses from the PMT under test, which where then integrated and

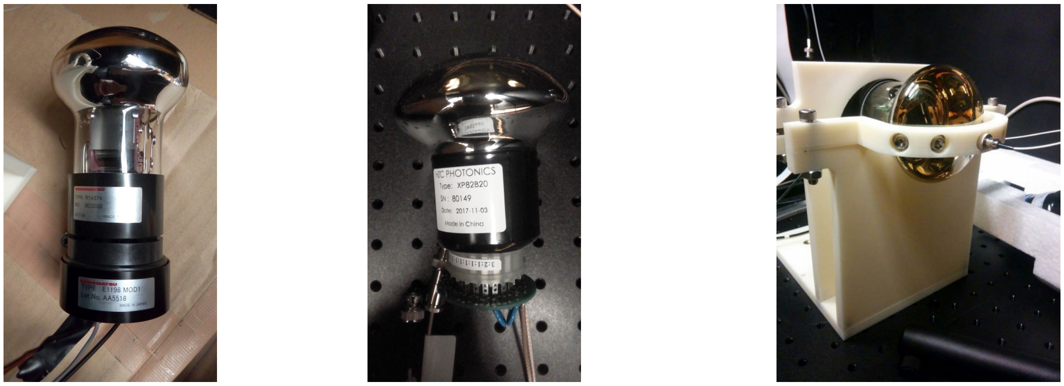

FIG. 124. Hamamatsu R14374 (left) and HZC XP82B20 (center) 3" PMTs that have been characterised. Also shown (right) is the test stand for probing various spots on the photocathode.

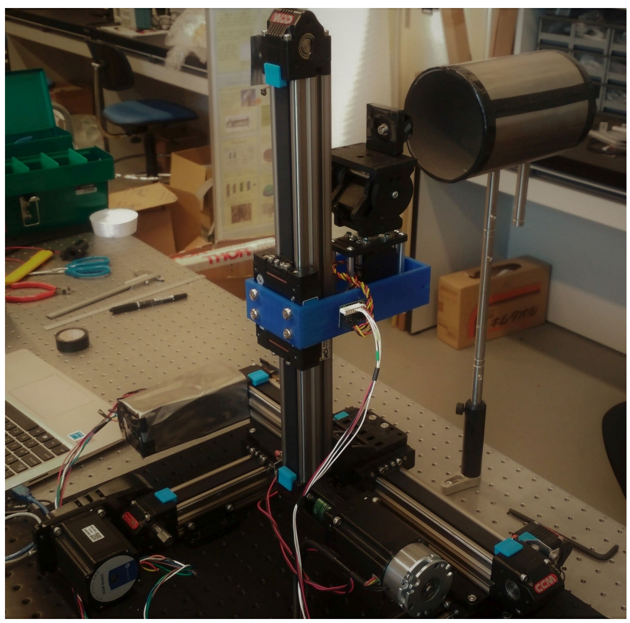

FIG. 125. Upgraded measurement setup for precise surface scans of 3" PMTs, which allows for variable angles of incidence of light over the entire photocathode.

their timing was estimated. All the measurements were performed after equalizing the gain of the PMTs to $\sim 5 \times 10^6$. The charge spectrum was fit using a formula proposed in [**?**]. The timing of the pulses was obtained by either finding the half-height point of the leading edge of the PMT response or by using a digital constant fraction algorithm. The pedestal subtraction needed for timing studies was performed using a histogram-based method. For the R14374 tube additional measurements were done at several position on the photocathode using a 3D-printed stand in order to control the position of the light spot. The results are presented in Fig. 127 and Table XXXIX. The charge resolutions of the Hamamatsu and HZC 3" PMTs are similar, but the timing resolution offered by Hamamatsu PMT is currently significantly better than that of the HZC PMT.

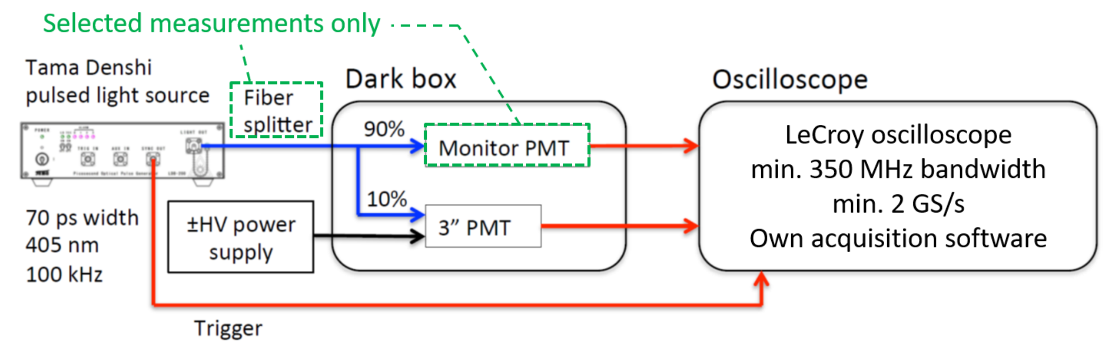

FIG. 126. Schematic of the setup used for characterisation of 3” photomultipliers.

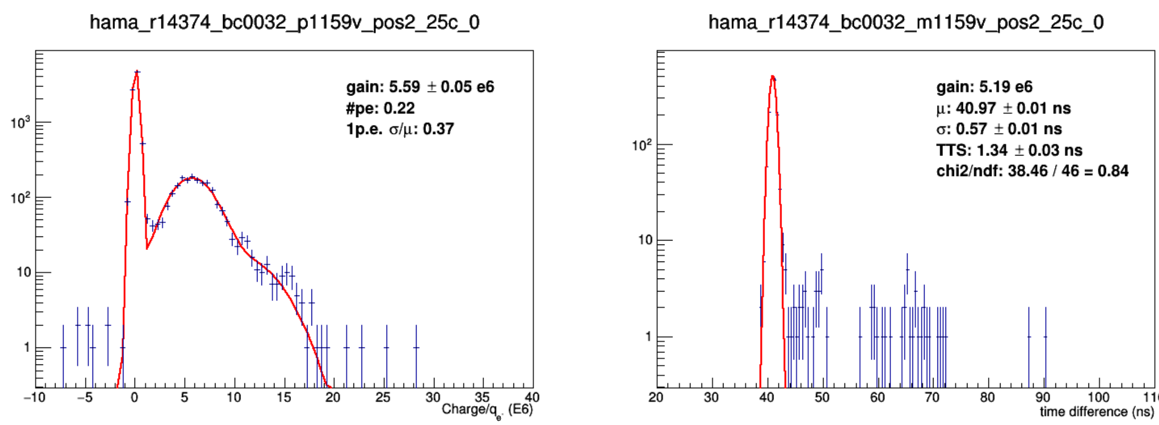

FIG. 127. Examples of charge and timing measurements for the Hamamatsu R14374 at T=25°C.

Manufacturer	PMT	HV	Gain ($\times 10^6$)	Q resolution	TTS
Hamamatsu	R14374: BC0032	-1159V	5.19 ± 0.07	0.36	1.34 ns
	R14374: BC0036	+1113V	5.12 ± 0.04	0.37	1.52 ns
HZC	XP82B20: 80148	-1324V	4.88 ± 0.04	0.33	3.62 ns
	XP82B20: 80149	+1229V	5.16 ± 0.05	0.35	3.75 ns

TABLE XXXIX. Gain, charge resolution and TTS measurements for improved versions of Hamamatsu and HZC photomultipliers. The TTS measurements were made at the centre of the photocathode.

Dark rate measurements were performed using a temperature-stabilized box with the temperature set to 9°C. The PMTs were kept in the dark for 48 hours prior to the start of a measurement to allow any activation of the photocathode to die away. The acquisition was done using an oscilloscope that had a random trigger. For each PMT, 1000 waveforms were acquired, each 100k channels in length, with a sampling rate set to 1 GS/s (total acquisition time was 0.1s). A pulse finding algorithm was run and all the pulses crossing a threshold of 1mV were identified. The results are reported in Table XL. The threshold was first converted to charge relative to the single photoelectron response, and then into single photoelectron efficiency. The latter is defined as the number of pulses crossing a particular charge threshold compared to the total number of detected pulses.

Manufacturer	PMT	Gain (HV)	Dark Rate (kHz)		
			50% eff.	85% eff.	90% eff.
Hamamatsu	R14374: BC0032	5.2E+6 (-1159V)	0.21 ± 0.03	0.34 ± 0.06	0.37 ± 0.06
		6.5E+6 (-1200V)	0.50 ± 0.05	0.70 ± 0.08	0.73 ± 0.09
	R14374: BC0036	5.1E+6 (+1113V)	0.02 ± 0.02	0.04 ± 0.03	0.05 ± 0.03
		8.6E+6 (+1200V)	0.03 ± 0.02	0.06 ± 0.03	0.07 ± 0.03
HZC	XP82B20: 80148	5.1E+6 (-1324V)	0.20 ± 0.03	0.39 ± 0.06	0.42 ± 0.06
		7.3E+6 (-1400V)	0.18 ± 0.03	0.35 ± 0.05	0.35 ± 0.06
	XP82B20: 80149	5.1E+6 (+1229V)	0.11 ± 0.02	0.14 ± 0.04	0.14 ± 0.04
		7.5E+6 (+1300V)	0.06 ± 0.02	0.09 ± 0.04	0.10 ± 0.04

TABLE XL. Dark rate measurements as a function of the efficiency for a 1PE signal for improved versions of Hamamatsu and HZC photomultipliers.

During the above tests, the PMT was operated at both positive and negative bias voltage to identify the best configuration that meets our requirements. One can observe that no significant difference exists in the gain, charge resolution and timing measurements, but that the polarity of the HV supply does have a profound impact on the level of dark rate, with the positive HV resulting in a lower dark rate by $\times 10$ for the Hamamatsu PMT, and by $\times 3$ for the HZC PMT. We believe that this is a consequence of the high electric field near the photocathode and glass envelope area. This can be particularly problematic when objects at ground potential are placed close to the window or, more generally, near the glass envelope of the PMT. In such circumstances micro-discharges can occur. With the photocathode grounded this effect does not exist, as there is no potential difference between the PMT and the outside structures. The drawback to positive HV is that the readout requires capacitive coupling. Moreover, we currently have active base designs for negative HV voltage, which are refinements of the KM3NeT designs, but using positive HV would require additional R&D effort.

One way of improving the dark rate with a negative HV supply is to apply a metallic layer around the PMT, which is then covered by a dielectric layer [?]. The metallic layer is kept at the photocathode potential. Still another method, which proved very successful, is the conformal coating adopted by the KM3NeT experiment [**?**]. We plan to conduct a series of experiments to decide on the treatment of the outside of the PMT and the preferred HV polarity.

The last part of our studies has been the analysis of the waveform shape of the PMT response, which is of particular interest for the FADC digitization option (see section III.8 B). The measurements revealed that the bandwidth of the single photoelectron response of the R14374 tube is around 350MHz. The rise time and FWHM depend on the number of photoelectrons, and for 1PE are of the order of 2ns and 2.8ns respectively (Fig. 128). There is some dependence on the location of the light spot on the photocathode surface which we plan to study further.

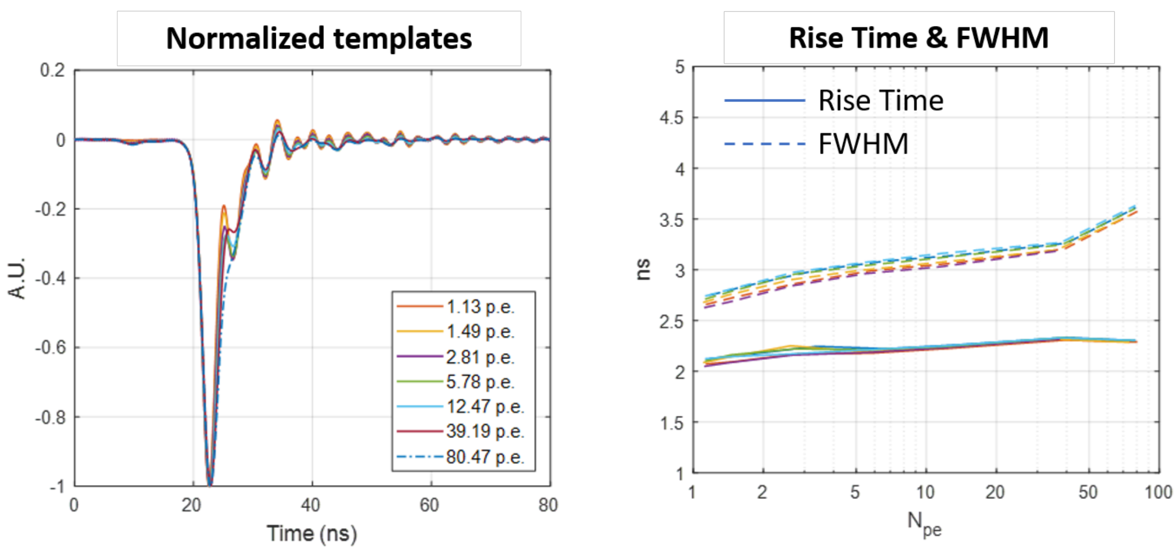

FIG. 128. Examples of waveform responses from the Hamamatsu R14374.

1. *Reflectors*

TC - This text taken from presentations at the recent Collaboration Meeting. Need to add some details of dimensions, and a picture.

Each 3” PMT in the module is surrounded by a small conical optical reflector that increases the light collection efficiency by a factor of ×1.2. The reflectors are made by water jet cutting the metal to shape using a technique developed for KM3NeT which works reasonably well and only takes a few minutes per reflector.

2. Optical coupling

TC - This text taken from presentations at the recent Collaboration Meeting. Details of the transparency tests need to be added. Also need to add a picture.

An optical gel is used as a coupling between the PMTs and the acrylic window on the front of the module. This gel can either be poured into the module filling all the space between the PMTs and the window, or can be prepared separately using a moulded former, as a tapered cylinder that matches the gap between each PMT and the window.

In the current prototype modules the gel Wacker 612 is being used by default, but it is very sticky. We are using a thin layer of plastic wrap to allow the acrylic window to be lowered onto the gel without sticking. We are investigating the batch-to-batch variability of the gel, and the best method to prepare it. The baseline method is a 60:40 mix of the two components, which is then de-gassed in a vacuum chamber, and cured at ≈20°C. The quality of the mix is important, and the hardness of the gel appears to depend on the age of the components.

B. mPMT Electronics

TC - This contains quite a full description of the electronics that is integrated into the mPMT modules, and thus contains some overlaps with the separate section on the electronics design for the read out of the 20" PMTs. There are some significant differences, particularly with regard to the digitisation that is proposed.

The Hyper-K mPMT electronics shall conform to the following performance requirements:

- The timing resolution should be better than the 3"?? PMT transit time spread of 1.5ns. We assume an electronics timing resolution of <300ps for 1PE and <200ps for larger signals.

- The electronics charge resolution should be ∼0.05PE and linear up to 25PE. Note that we do not expect the 3" PMTs to see the very large signals ≈1000PE that are expected in the 20" PMTs, due to the much smaller photocathode area.

- The power consumption should be <4W/mPMT. This is driven by the water circulation requirements.

- The cost of the electronics should be low enough so that it does not drive the overall cost of the mPMT module.

- For the Intermediate Water Cherenkov Detector (IWCD), there are additional requirements for the hit dead-time and for handling event pile-up. These are explained in Section II.3.

To match these requirements, two different designs for the mPMT digitization are currently under development. One is a Q/T digitization based on discrete components, and the other is based on an FADC digitization, with on-board signal processing. More details on these two designs can be found in Section III.9 A, where they are discussed in the context of the readout of the 20" Inner Detector PMTs.

TC - There is not yet very much more detail in the electronics section referenced here. In particular the FADC option is not really discussed. We need to decide where to put the details for both digitiser designs.

Ideally the same readout design would be used for the 20" PMTs and the mPMTs if both are used in the far detector. In particular it should be a goal to use the same clock and data transfer scheme, as described in Sections III.9 B and III.9 F. In the following sub-sections we discuss some of the differences between the electronics for the 20" PMTs and the mPMTs.

It is also desirable to use the same electronics for the mPMTs in the far detector and in the IWCD, but there is a much higher event rate in the IWCD, which may lead to some different design choices. The requirements on the clock and data transfer could also be different for the IWCD since it is at a separate site. These potential differences are discussed in Section II.3.

1. Q/T digitization based on discrete components

TC - This sub-section needs to make clear where the design is in common with the 20" readout, and where it differs. At the moment it is hard to tell. This is partly due to the different level of detail here compared to the digitisation part of the electronics section.

The mPMTs electronics can be divided into two parts: a set of single channel Front End boards (FEB) which are mechanically connected to HV boards that are placed very close to the individual PMTs; and a Main board (MB), mounted on the electronics support structure as described in section III.8 C 4. The outputs of the single channels merge into the main board through individual flat cables. A very low power MCU is embedded on the Front End to control both the HV board and the FEB itself, and only one connector for both boards is needed.

The time measurement circuit consists of a fast high gain amplifier and a discriminator. The output of the amplifier is compared with a threshold set by the DAC and the output of the discriminator is sent to the main board using a differential signal. There it is used by an FPGA to produce a time stamp and generate a hold signal for the ADC. For the charge measurement the input signal is shaped with a three stage integrator and acquired with a 2Msps 12-bit ADC. An energy resolution of 0.1% FWHM and a time resolution of 100ps have been measured for this digitization system, with a power consumption of 40.5 mW per channel.

The main board provides the power supply to each channel and collects, processes and transfers the data acquired by the FEBs. The power supply contains a non-Ethernet module, DC-DC converters and a single channel switch. The FPGA on the main board acquires the data and generates an output of 12 Byte/event which is transferred to the Single Board Computer, where the data are collected and transmitted out of the mPMT with a single Ethernet cable. This cable also provides the module power supply, the clock, control signals and the trigger. The total power consumption for an mPMT with 19 PMTs, including the contribution from the HV, FEB and main board is about 4.1W.

TC - The description here differs from Figure 147 in the electronics section, which describes the front-end electronics in terms of 7 blocks, one of which is the signal digitizer, and another the HV system. It is not clear what the equivalent of the main board is. Is it the combination of the other 5 blocks in Fig.147? It would be good to show a block diagram of the Q/T digitization option described here, similar to Figure 127 for the FADC digitization option.

2. FADC digitization

Figure 129 shows a block diagram of the FADC digitization option for the mPMT. There would be an analog shaping circuit and HV generation on the PMT base. The shaped PMT signal and a trigger signal, together with HV control signals and the power supply for the PMT would all be on the same cable between the PMT base and the main board. The shaped signals travel as differential signals to the main board, where they would be digitized by an ≈100Msps 12-bit FADC. Options for the FADC are the TI ADC 3424 and the AD LTC-2260-12. The FADC data will be transferred to the FPGA, where digital signal processing (DSP) techniques will be used to find hits and calculate the charge and time for the hits. A summary of the information on each hit will be sent from the front-end electronics in the mPMT to the readout system via an ethernet cable.

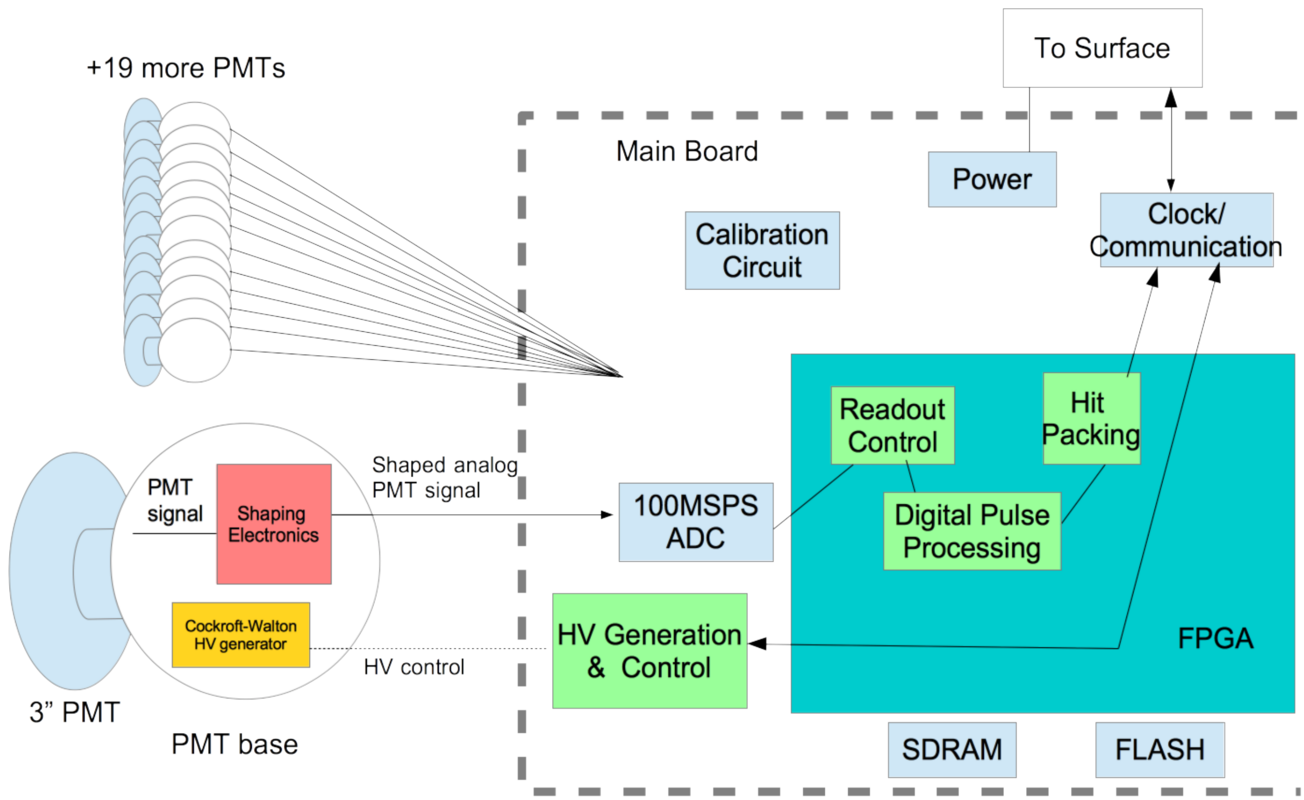

FIG. 129. Block diagram of the mPMT mainboard for the FADC digitization option.

3. The HV board

Each PMT needs an appropriate voltage supply to collect the primary photoelectric emission of the photocathode and the secondary multiplication of the dynodes. To produce a signal, the anode of the PMT has to be at a higher voltage with respect to the cathode. One can put the cathode to ground and set the anode to a positive high voltage, or one can put the anode to ground and set the cathode to a negative high voltage. These two choices have advantages and disadvantages. The positive voltage supply has a lower dark count rate, and the cathode of the PMT is connected to ground, so there is no possibility of glass discharges. On the other hand the pedestal shifts with the event rate, and it is not possible to use voltage multipliers to generate the power supply. To read out the anode signal at high voltage it is necessary to have a decoupling capacitor with a very high insulation tension. The negative voltage supply has a higher dark count rate and the glass of the PMT is connected to the high voltage supply, but the pedestal does no??t shift with the event rate and the anode signal is read out relative to the ground.

The layout of the HV system is shown in Figure 130. To cope with the limited budget for power consumption, we cannot simply use a standard HV supply and a resistive voltage divider. Instead we have developed an active power supply based on the Cockcroft-Walton voltage multiplier, similar to the solution adopted in the KM3NeT PMT base design. The HV board has a single 5V supply and needs one analogue input, namely a reference voltage in the range 0 –2V, and one digital on/off bit. The outputs of the boards are the high voltages for the PMTs and two analogue values in the range 0–3.3V corresponding to the anode voltage and the current. Two HV board prototypes have

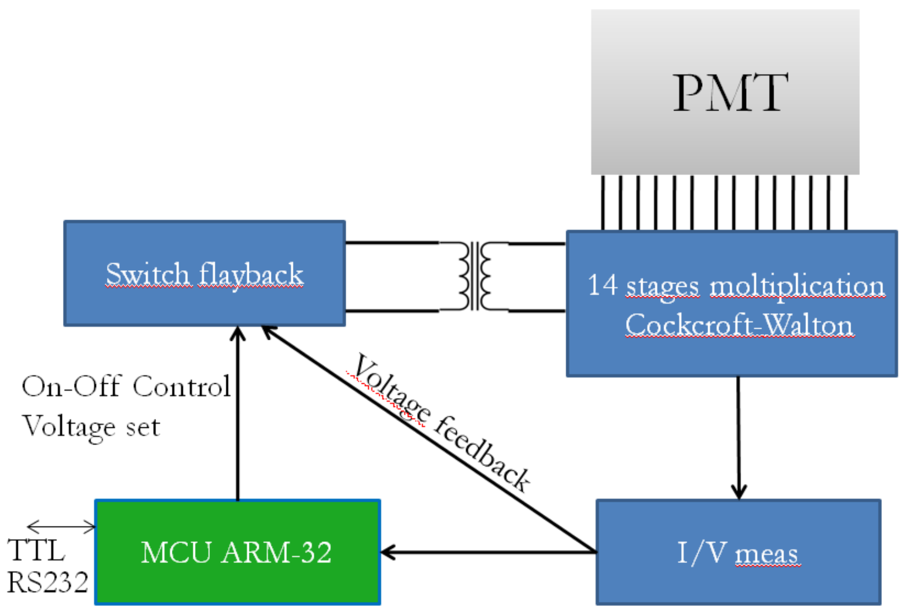

FIG. 130. Block diagram of the HV circuit: in blue the components on the HV board, and in green the component off the board.

been built and tested. Figure 131 shows the measured power consumption of the two prototypes compared with the expectation. A power consumption of 12.5 mW per channel has been achieved, corresponding to a 237.5 mW power consumption for the HV board for a full mPMT.

The base shape is defined by space conditions in the current mPMT vessel design. It features a central hole for the glass process at the rear surface of the PMTs, allowing the mounting of the base closer to the tube in order to gain space. The most recent layout together with a first prototype of the dedicated mPMT HV base is presented in figure XXX.

TC - This figure appears to be missing. It would be nice to have a picture of the actual prototype board.

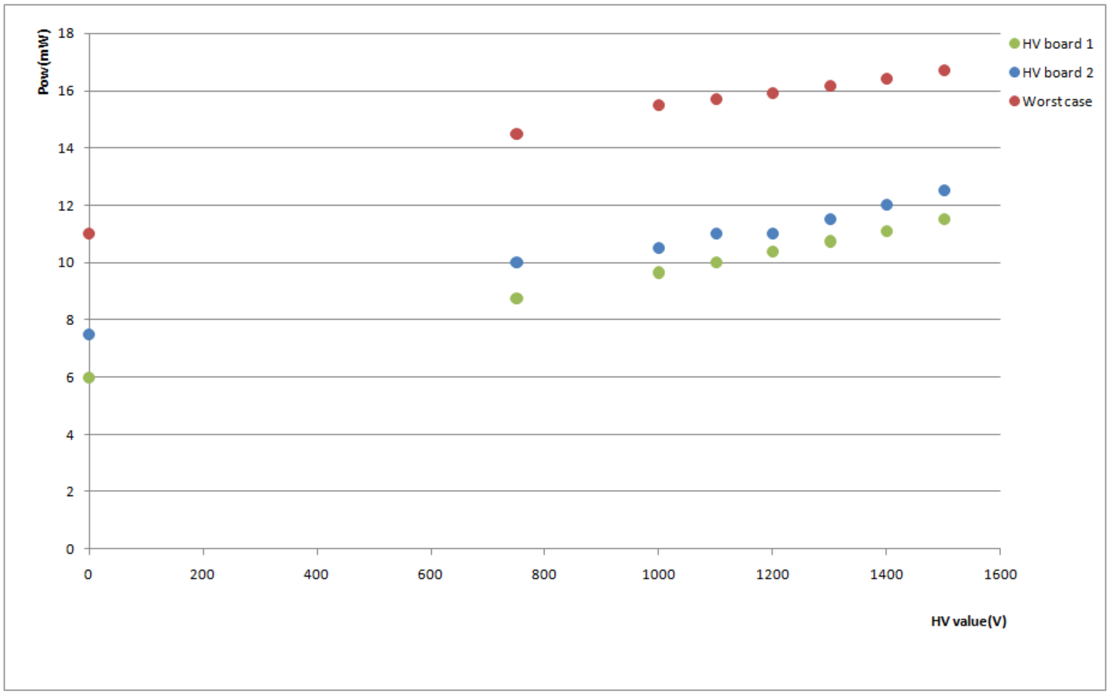

FIG. 131. Power consumption in mW/channel of the two HV board prototypes at different cathode voltages: in red the evaluated (worst case) power consumption, in green the measured one for the first prototype, in blue for the second prototype.

C. mPMT Module Design

TC - This section is far more detailed than anything else in this report. For the moment a lot of this detail has been suppressed. We need to decide if we want a 300 page report with less detail, or a 500 page with more detail. It may be better to document the mPMT details in a separate internal note.

The mPMT module is designed to occupy the same $70{\times}70\text{cm}^2$ footprint as the 20" PMT to aid integration within the Hyper-K photosensor support structure. An initial design, shown in Figure 132, has 3" PMTs facing into both the inner and outer detectors. This is subsequently referred to as the "two-sided" design. After an mPMT workshop in July 2018 it was decided to update the design to only include the inner detector PMTs, with separate PMTs outside the module providing an outer detector veto. This "one-sided" design has no effect on the physics performance of the mPMTs, since the inner detector PMTs are unchanged. It does however reduce the mass of the modules, making production and installation easier. It also reduces the cost of each module, makes cable feedthroughs simpler and allows us to reduce the dead space between the inner and outer detectors in the intermediate water Cherenkov detector. The one-sided design is currently under development at TRIUMF, and this section will be updated once that design has been completed. For this draft both designs will be discussed, with necessary changes for the one-sided module highlighted.

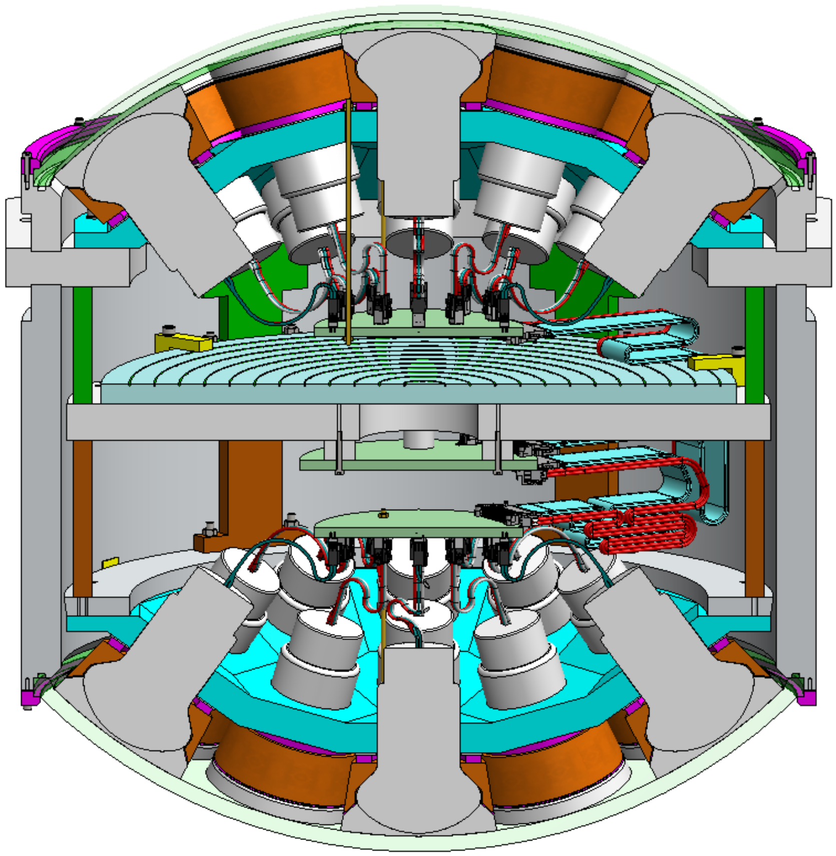

FIG. 132. Initial design for the two-sided mPMT

The mPMT pressure vessel consists of an acrylic dome, which acts as a window for the PMTs to view the detector volume, and a cylindrical section that houses the PMT support structure, electronics and potentially a scintillator veto. For the two-sided design the acrylic dome and PMT support structure is copied on each side of the cylindrical section, whereas for the one-sided design the cylinder will be blanked off by a stainless steel plate.

1. Acrylic Window

We have made comparisons of acrylic samples to identify the best material for the mPMT windows. These are based on the experience gained with PMT covers both in Super-K and in the R&D for the Hyper-K 20" PMTs, and on contact with experts in plastic materials at the Polymer Science Unit of Politecnico di Bari. An initial selection of acrylic samples was made using the nominal characteristics provided by the manufacturers, and samples by Poly One Corporation, Evonik Industries, and CLAX Italia have been selected for further testing.

TC - Need to turn footnotes into standardised references.

TC - A detailed list of the acrylic samples has been suppressed.

The transmittance and reflectance in air have been measured. Figure 133 shows the reflectance measurements. Transmittance measurements of acrylic samples from Evonik and Polycast have been made in pure water both with and without a 5mm layer of the optical gel (Figure 134). Studies to identify a gel with very good UV transparency are described in III.8 A 2.

TC - The description of these studies is missing.

After these tests the Plexiglas GS UVT by Evonik has been selected as the acrylic with the best optical properties for the mPMTs.

TC - First figure of transmittances suppressed It is mostly redundant with the later one.

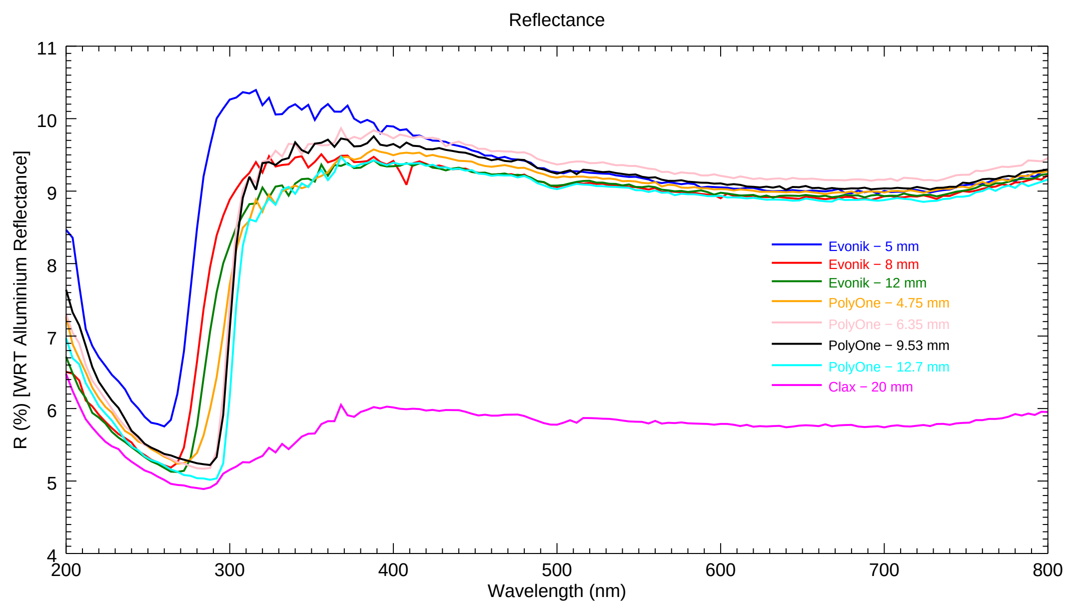

FIG. 133. Reflectance of acrylic samples

Mechanical tests have been performed in order to accurately predict the final performance of the acrylic cover in the mPMT. These include compression tests of the basic deformation mechanisms under uniaxial loads, as well as the behaviour of the samples under static conditions and under cyclic loads. Finite element (FE) models were used to identify the material parameters and to model the final design of the mPMT cover. Figure 135 reports the calibration curves obtained from the numerical simulation and the compression test results in terms of the radius expansion

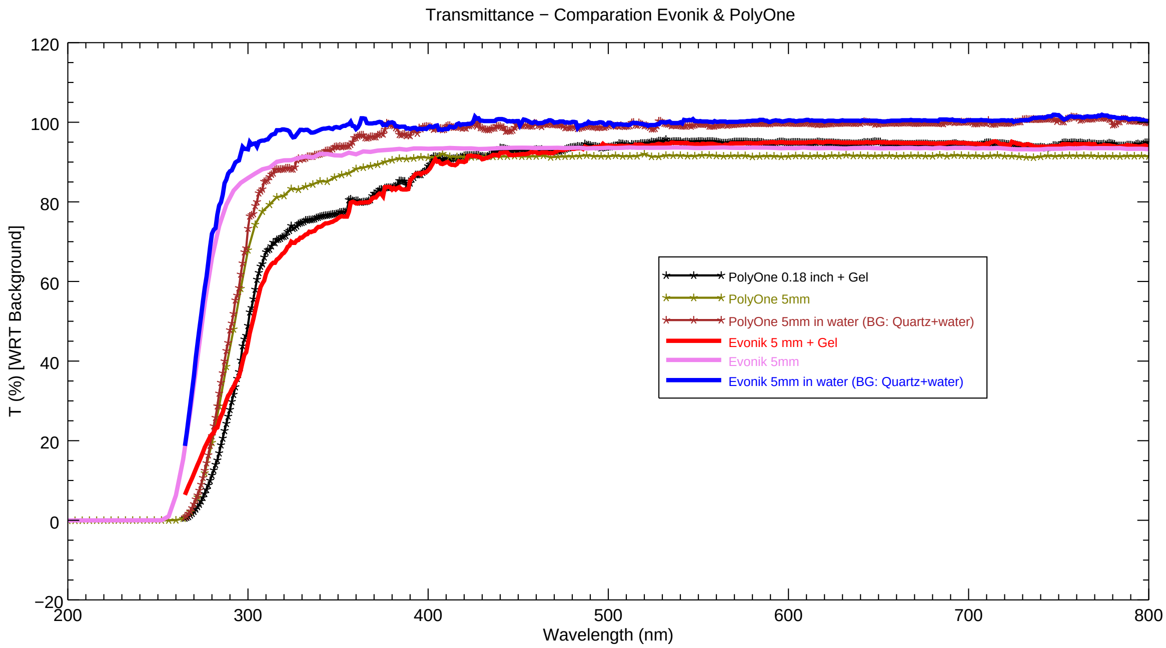

FIG. 134. Transmittance of acrylic samples in air, water and coupled with optical gel.

and height reduction, showing a very good agreement between experimental results and numerical computations. Once the material model had been validated for the sample, a full 3D FE model of the mPMT cover was made for the prototype window. This showed that a 15mm thick acrylic window can withstand a pressure of 1.5MPa with a maximum displacement lower than 0.5mm along the radial direction.

TC - Figure of FEA analysis of dome suppressed. It is too detailed and can't be read at normal magnification.

Two pressure tests were carried out for the mPMT prototype module design. An 15mm thick window has undergone a maximum external hydrostatic pressure of 1.84MPa in a test lasting more than 4 hours, where the Hyper-K requirement is 1.25MPa. Figure 136 shows the pressure curve supported by the vessel. A crash test was carried out on a 20mm thick window, where breakdown happened at 8.6MPa, demonstrating that an acrylic pressure vessel is very resistant to external pressure. After these tests a thinner thickness can be considered for the final design.

TC - Figure of crash test suppressed. The 15mm test is sufficient information.

We also need to verify the background emissions from the acrylic. A preliminary test has been performed in Naples to investigate contaminations of ^{238}U, ^{232}Th, ^{210}Pb and ^{40}K, giving upper limits of 1.3×10^{-3} Bq/g for Evonik samples and 9.5×10^{-2} Bq/g for Poly One samples.

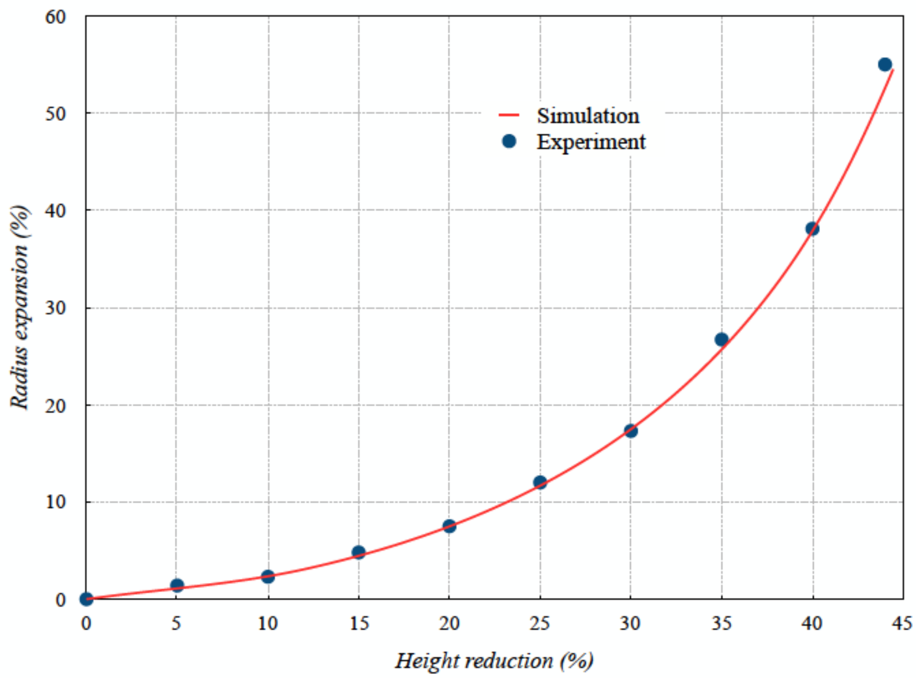

FIG. 135. Comparison between radius and height variations of the acrylic samples under compression tests, showing a good agreement between numerical computations and experimental test results.

TC - for which of the four nuclei listed above?

More sensitive measurements were then performed with a Germanium detector in the underground laboratory at Gran Sasso (LNGS), and results are shown in table XLI.

Isotope	Activity	Contamination
	^{232}Th: Thorium series	
Ra-228	< 0.11 mBq/kg	< 0.027 ppb
Th-228	< 93 μBq/kg	< 0.023 ppb
	^{238}U: Uranium series	
Ra-226	< 65 μBq/kg	< 0.0052 ppb
Th-234	< 4.6 mBq/kg	< 0.38 ppb
Pa-234m	< 2.5 mBq/kg	< 0.20 ppb
U-235	(0.15 ± 0.07) mBq/kg	$(3 \pm 1)\cdot 10^{-1}$ ppb
K-40	< 0.69 mBq/kg	< 0.022 ppm
Cs-137	< 25 μBq/kg	-

TABLE XLI. Measurement of nuclear contamination of Evonik acrylic samples.

For the mPMT prototypes the acrylic dome fits into a circular ledge cut into the cylinder wall.

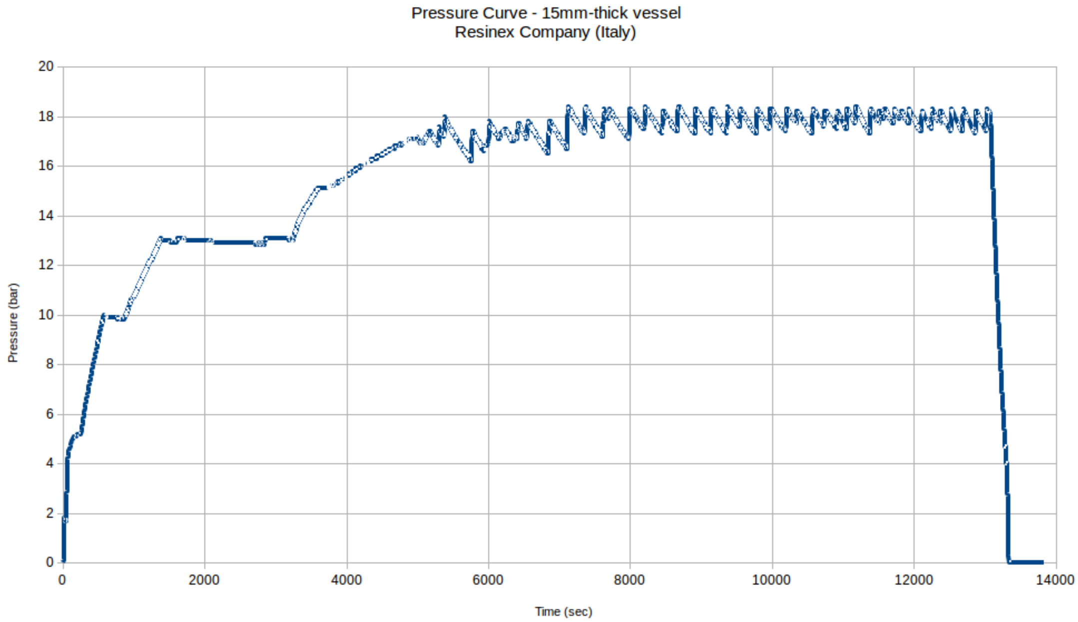

FIG. 136. Pressure curve inside the 30 bar tank (on the 15mm thick vessel) at Resinex Company. The curve returned to 0 bar after the test.

The ledge has an O-ring seal between the acrylic and the cylinder to keep the detector watertight, and a clamping ring that applies 4bar of pressure to the dome, keeping the acrylic in place. The clamping ring does not drastically change the stress on the dome, and increasing the clamping pressure by a factor of four actually reduces the maximum stress for the dome, since this stiffens the clamping area. From an FE analysis of the stress with the ring a 10mm thick acrylic dome should be more than adequate for the mPMTs in Hyper-K.

TC - Figures of FE analysis of dome + clamping ring suppressed.

Prototype acrylic domes have been produced by Liras using thermal forming from sheets of the Evonik acrylic described earlier. The dome diameter was measured at three points around the dome circumference to test the uniformity of the prototypes.

TC - Table of dome dimensions suppressed

2. Cylindrical Section of Module

Two prototype mPMT modules are being built at TRIUMF using aluminium for the cylindrical section. The first, shown in Fig. 137, will test the pressure tolerance of the acrylic dome, clamp ring and penetrators. Fig. 138 shows the second prototype, which will test the optical coupling and cross-talk between the PMTs and the acrylic, as well as providing preliminary measurements of the PMT noise. These tests are expected to take place in late 2018 or early 2019. The prototypes will also be used to develop and improve the assembly procedure for the mPMT modules.

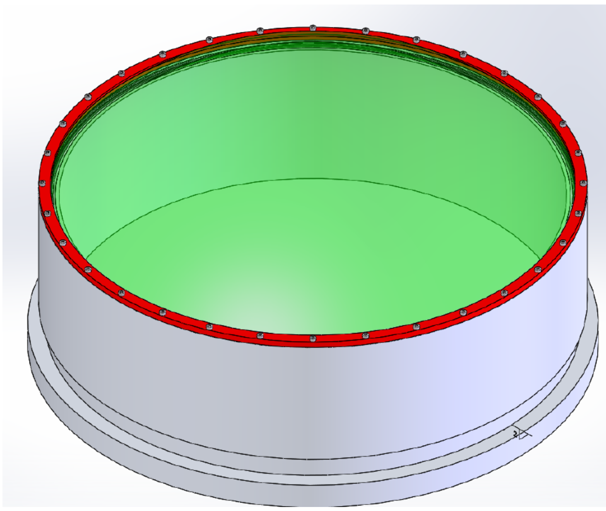

FIG. 137. Pressure test prototype

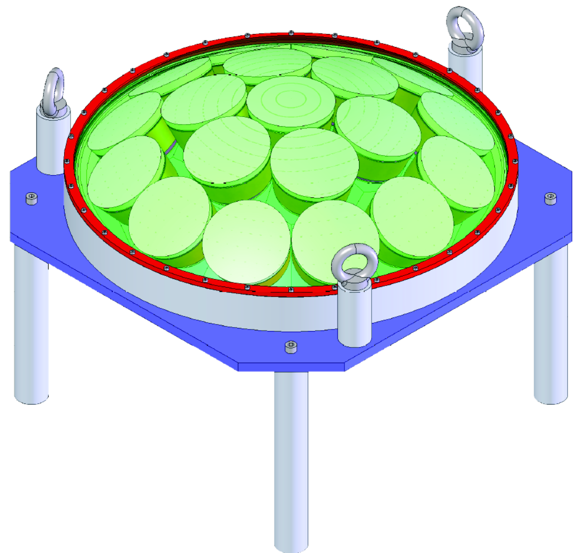

FIG. 138. Optical testing prototype

For the cylinder the main considerations are the strength required to withstand the Hyper-K water pressure, the contribution to the module mass, and the ability to radiate away the heat from the electronics. Aluminium provides the necessary strength, low mass and heat conduction, but may not be compatible with the ultra-pure water. A stainless steel cylinder, whilst compatible with ultra-pure water and a good conductor of heat, would be significantly more massive than the aluminium design, making the mPMT mounting difficult, although this may be less of a problem with the one-sided design. Another option is Poly-phenylene sulfide (PPS), a high-performance thermoplastic that is being investigated as a material for the 20" PMT covers. It has a low radioactive contamination and, when mixed with carbon fibre, achieves a good enough strength to withstand the hydrostatic pressure. It can be injection moulded, making mass production of the modules faster and cheaper.

Engineers at TRIUMF are currently working on a new design for a one-sided mPMT using PPS as the cylinder material. The PPS cylinder would be terminated at the back using a stainless steel plate, allowing heat transfer from the electronics and providing a better surface for cable penetrators. A prototype one-sided module is expected to be built in 2019, and the one-sided design using PPS for the support structure will be the nominal mPMT design for both the IWCD and the Hyper-K far detector.

3. PMT Support inside the mPMT

A 3D mounting structure is used to hold the 3" PMTs in the correct positions, ensuring a good contact between the PMT, the optical gel and the acrylic window. This support structure is currently 3D-printed in a single piece using black ABS plastic. The structure does not come into contact with the ultra-pure water, so compatibility is not an issue.

TC - You still need to worry about radioactive emissions from all the materials inside the mPMT.

A prototype mounting structure, produced by AON3D, is shown in Fig. 139. 3D-printing of the support takes approximately two days, which is sufficient for small-scale production. The support design is fairly simple, so injection moulding will be investigated for large-scale production.

TC - The detailed diagram of the support structure design has been suppressed. The photo is better, and the dimensions can be estimated from the 3" holes for the PMTs.

FIG. 139. Prototype for the PMT support structure within the mPMT.

4. Electronics Support & Connectors

TC - There is significant overlap between this sub-section and the equivalent sub-section on watertight connectors in the Electronics section.

For the two-sided mPMT design the electronics are supported internally by an aluminium plate. This hangs from the mPMT mounting plate, held by the green and red support pieces shown in

Fig. 132. These support pieces conduct heat from the electronics into the mPMT cylinder, which is then cooled by the surrounding water. For the one-sided design the electronics will be mounted directly onto the back plate, which will be in contact with the water in the dead region of the tank. A grounding shield may be needed. *TC - in both designs, or just in the one-sided case?*

One of the main goals of the mPMT vessel is to preserve the PMTs and their electronics in a sealed environment, but there need to be penetrators and connections to the outside. These have been used successfully developed by the KM3NeT, IceCube and JUNO collaborations in conditions much harsher than those in Hyper-K. *TC - why is JUNO harsher than Hyper-K?*.
For the connection between the onboard mPMT electronics and the outside, a penetrator with an underwater Ethernet cable (about 30m long) could be the cheapest solution. The cable and penetrator will be fixed by a washer, O-rings and nuts, during the mPMT assembly. A custom penetrator in plastic material (e.g. PEEK) could be considered, instead of metal, to avoid chemical reactions with Gadolinium and pure water. However, further studies are needed to identify the best solution. Examples of some penetrators are shown in Figure 140. An alternative option to a penetrator might be a connector + bulkhead system, but this is very expensive, although very handy for assembly and final installation.

The Ethernet cable to the outside has to be a guaranteed underwater cable, because water must not enter into the cable to preserve the electronics onboard the pressure vessel. Once the mPMT with its cable has been assembled, it can be connected to an external cable with a watertight Ethernet connector of the type under study by the electronics group (Section III.9). A standard cable was suggested by the CRE company (England), and other commercial solutions could be interesting for this project. We plan to test the water resistance and penetration of all the components used for the mPMT using the CIRCE laboratories in Italy.

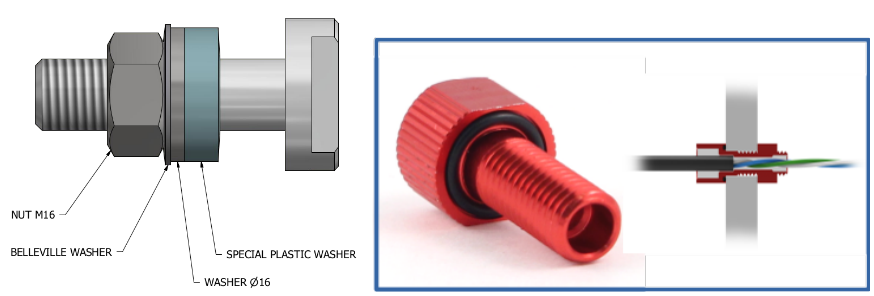

FIG. 140. On the left, a sketch of the dummy penetrator used for the hydrostatic pressure test at Resinex (Italy). On the right, a commercial penetrator. A glue could fix the Ethernet cable with the penetrator.

5. Mounting Structure for the mPMT

The two-sided mPMT design has a plate located close to the acrylic dome that provides both a feedthrough for cabling as well as a mounting point for the mPMT. For the one-sided design the back plate provides an alternative way to mount the mPMT to the photosensor support structure. In both cases the mounting structure will be designed to be compatible with the 20” PMT support structure, so that 20” PMTs or mPMTs could eventually be mounted in any of the unit cells. The mass of the one-sided mPMT module is ≈40kg, which is comparable to the 20” PMT including its cover, so the design of the photosensor support structure should not depend significantly on the relative fractions of 20” PMTs and mPMTs.

D. mPMT Assembly

The assembly procedure for the mPMT modules is based on the experience from KM3NeT, with adaptations specific to the one-sided Hyper-K mPMT module design. The procedure for assembly and testing can be broken into six major steps:

- Preparation of parts.
- Pre-testing of components before mPMT assembly.
- Assembly of the PMTs in the PMT holder, with the reflectors and optical gel.
- Optical testing of the PMT sub-units.
- Assembly of the mPMT module parts.
- Operational testing of the mPMT module.

TC - Pre-calibration has been moved to the calibration section.

1. Preparation of parts

The acrylic dome for the mPMT will be injection moulded and delivered ready for use. Sanding of the part of the dome that makes contact with the O-ring may be necessary to ensure a watertight contact. The PPS cylindrical vessel will also be injection moulded but will require machining at each end for the grooves and screw holes where the acrylic dome and backplate will be installed.

The stainless steel backplate will be machined with screw holes for connecting to the cylinder and with a hole where the cable penetrator will be installed. The internal structures to support the electronics main board and the PMTs with either be produced by an external company or by our own university/laboratory workshops.

For the initial mPMT production, an industrial 3-D printer will be used to print the PMT support matrix and the individual PMT holders. The print time for the support matrix is ∼2 days and the print time for 19 PMT holders is ∼1 day, so one printer operating for 1 year can produce parts for ∼100 modules. For the production of mPMT modules for the IWC it may be possible to produce these parts using a few 3-D printers. For the large scale production of mPMT modules for Hyper-K an injection moulding method will be needed for these parts.

2. Pre-testing of components

The PMTs themselves will have been tested by Hamamatsu (or an alternative company) before shipment. Since we expect a low rate of bad PMTs from the suppliers, we will only perform detailed testing of individual PMTs for optical and electrical performance at a later stage after the assembly of the PMTs into a sub-unit with their holders, reflectors and optical gel (see Section **??**). We perform an initial test of the high voltage and the electronics after the high voltage bases have be soldered onto the PMTs, and the PMTs have been connected to the electronics main board. For this we use a light source equivalent to 1PE.

The acrylic dome, PPS cylinder, stainless steel backplate, PMT support matrix and internal mechanical parts will be visually inspected for any defects. Jigs will be constructed to test that the shapes of these parts are within the tolerances allowed for the mPMT module assembly. The individual PMT holders and reflectors will also be tested for correct shape with a jig. The reflectors will also receive a visual inspection. At this stage, all parts will be given a QR code, which will be stored in a database along with the status from the pre-testing.

3. Assembly of the holder and optical gel

After the bases has been soldered to the PMT and the pre-testing is complete, the individual PMT sub-units can be assembled. These sub-units include the PMT and its holder, the reflector and the optical gel. The PMT holders are 3-D printed parts and include a removable spout for the pouring of the optical gel. As a the first step the reflectors are glued into the PMT holder. Next

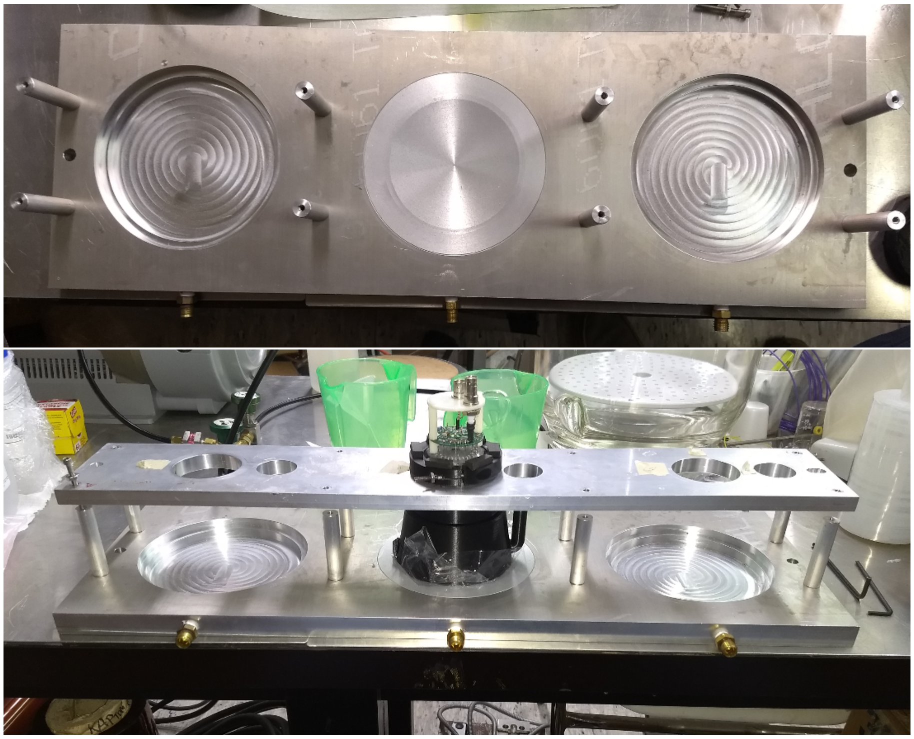

FIG. 141. Top: The 3×1 prototype bottom plate for gel pouring at TRIUMF. The porous aluminium bottom part of the mould is installed in the middle slot. Bottom: The 3×1 prototype gel pouring station at TRIUMF with a PMT installed in the centre. The top aluminium plate holds the PMT in place and pushes it against the bottom plate to form the mould. The gel is poured through the spout on the right side of the PMT holder.

the PMT is installed in the holder, and a clamp is placed on the back side of holder to hold the PMT in place until the optical gel is poured and set. This part of the assembly will be done for sets of 25 PMTs, with one batch of optical gel being poured for all 25 PMTs in a 5×5 grid. The PMTs and holders are placed upside down on aluminium pieces that are shaped to match the curvature of the acrylic window. A polyurethane foam ring is placed on the back side of each PMT holder to allow for compression. An aluminium plate with 25 holes of 53mm diameter is lowered onto the back side of the holders with the PMT bases fitting through the holes, and the plate is screwed in place to hold the PMT holders against the aluminium pieces to form the mould for the optical gel. Finally a second clamp is added on the other side of the aluminium plate so that the PMTs are held in the aluminium plate. Prototypes of the components to form the optical gel moulds are shown in Fig. 141.

The optical gel is prepared by mixing two components, taking about 5 minutes. The mixed gel is then placed in a vacuum chamber, which is pumped down to remove air from the gel, taking another 5 minutes. After the air is removed from the gel, it can be poured into the mould for each PMT. The setting time is approximately 2 hours, depending on the gel type and room temperature. After the gel is set, the aluminium plate holding the PMTs is removed and flipped over, and the parts that form the top of the mould and the spout are removed. The PMTs are now ready for optical testing.

4. Optical testing of PMTs

The PMTs are kept in the 5×5 aluminium plate described in the previous section, and moved to an optical test stand. This stand will contain two light sources that can scan over the PMT array using a 2-dimensional motorised stage. The first light source, which provides uniform illumination of each PMT and the reflector, will be used to test the PMT response integrated over the photosensitive surface. The second light source provides collimated light with a spot size of $\sim$ 2mm. This will be used to test the PMT response at selected points on the photocathode. The system may be set up with a single pair of light sources that scans over all 25 PMTs, or with 25 pairs of light sources that scan over all the PMTs simultaneously. After optical testing the PMTs will be kept in a temperature controlled dark box, where the dark count rate will be measured. At this stage any PMTs that do not have the required optical performance or dark count rate will be removed.

5. Assembly of the module

With the one-sided module design, it is expected that the internal parts of the mPMT module will first be assembled onto the backplate of the module, before installing the PPS cylinder and the acrylic dome. We first install the penetrator into the backplate along with the internal cables. Then we install the PMTs into the support matrix and connect their bases to the HV daughter boards. The next step is to install an internal support onto the backplate, attach the electronics main board to it, and connect up the cables from the penetrator to the main board. We can then install the support matrix with the PMTs onto the internal support and connect the HV boards to the main board. The last two steps are to connect the PPS cylinder to the backplate with an O-ring seal, and then to connect the acrylic dome to the PPS cylinder with another O-ring seal. This plan for the module assembly procedure may need to be modified following our prototype test.

6. Operational testing of the module

A procedure for testing the water tightness of the mPMT module will need to be developed. After the water tightness has been confirmed, the mPMT module will be placed in a dark box and illuminated at the 1PE level. This is the last part of the assembly and testing before the pre-calibration that is described in section III.12 C.

TODO: Add summary of assembly steps with time estimate.

TC - Summary of steps is not needed, but the time estimate is important.

III.9. ELECTRONICS

The basic requirements of the front-end electronics are to provide and monitor HV for each photo sensor, to collect all the hit data without loss, to transfer data to the readout system and to keep the collected data until they are read out. All the front-end electronics have to be synchronized and there should be no large phase shift at a level of a few hundreds of ps or larger even after a power recycling. Further details are described in each sub-section.

In designing the electronics and the DAQ system, it is necessary to estimate the amount to be processed. At this moment, all the signals from PMT above the 1/3 p.e. including the dark noises are considered to be recorded by the electronics and transfereed to the DAQ readout. The DAQ system reduces unnecessary noise the data by applying software triggers. One of the most important role of the front-end electronics and the DAQ system is not to lost information even if nearby supernova burst occurs. Therefore, we evaluated the amount of data using the some assumptions, which have been discussed with the other working groups.

The first assumption is the dark rate from a 20inch PMT. At this moment, the requirement is 4kHz but we set 10kHz considering the existence of high dark rate PMTs as observed in SK. The data size per one PMT hit is set to 8 bytes. The nominal data rate from 40,000 ID pmts and 6,700 OD pmts becomes 3.8GBytes/sec. When the supernova occurs in 500 light years, 75M events are expected in the first 1 second and 105M events are expected in the following 9 seconds. In total, 180 Mevents are expected in 10 seconds. The expected amounts of data from the front-end electronics becomes 125Gbytes in the first 1 second and 202Gbyts in the following 9 seconds. As a result, 327 GBytes of data are expected to be produced from the front-end electronics in 10 seconds when there is a nearby supernova.

At this moment, there seems to be no technical reason to differentiate the inner and outer detector electronics and DAQ system. However, if there are groups that would like to provide only ID or OD system components, we would ask the group to develop components which satisfy the requirements documented here and are compatible (if applicable) with the other relevant components. It is not clear how to integrate the detailed description of the mPMT electronics into this section, so it has been included as a separate sub-section III.8 B within the section describing the mPMT modules.

Some of the work packages have several technical options. We need to fix the procedure for the technology selection, and simultaneously assign the responsibility for securing the budget to provide the component or system.

The main component of the electronics system is the front-end electronics module, which is expected to be mounted on the PMT support structure. The block diagram of the module is shown in Fig.142. This module consists of several blocks which provide the signal digitizer, the data handling, the system control, the network interface, the clock and counter, the slow control, the HV supply and the LV power converter. The function of the LV block is to provide a regulated voltage for each of the other blocks, but the design of the LV block is rather simple and is not described in this document. All the blocks are enclosed in a watertight pressure-tolerant case. It is necessary to use water resistant connectors to the case for the optical communication fibres and the metal power supply cables. It is also necessary to design water resistant connectors for the signal and HV cables at the PMTs. Since the front-end electronics module is located under the water and the surrounding water is degasified, the air inside the case, which encloses the electronics blocks, may escape from the case and the pressure in the case may decrease.

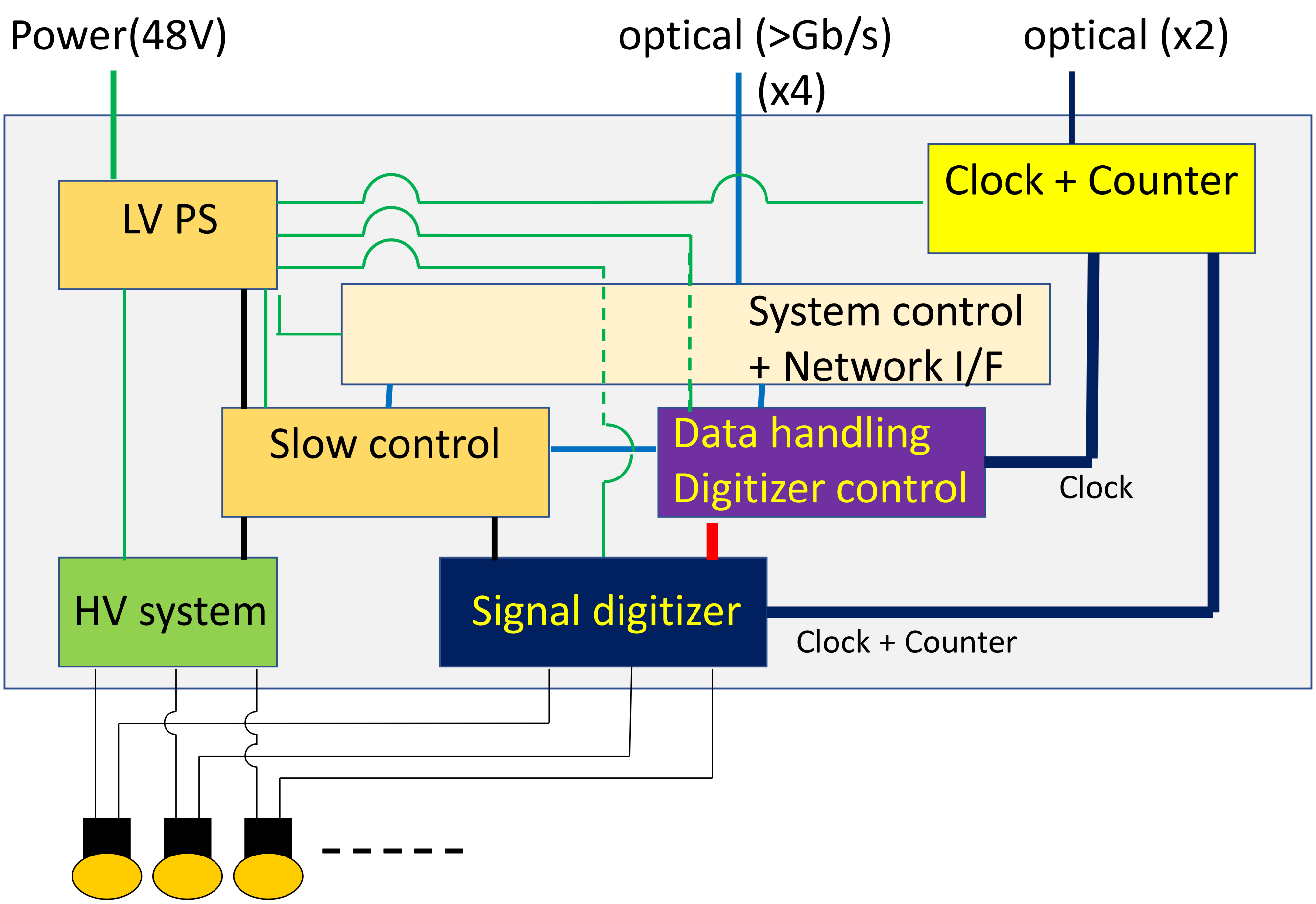

FIG. 142. Block diagram of the front-end electronics module.

Item	Requirements
Trigger	self triggering for each channel
PMT impedance	50Ω
Signal reflection	<0.1%
Discriminator threshold	<0.25 p.e. (well below 1 p.e.)
Processing speed/hit (channel dead time)	<1 μs
Maximum hit rate	>1 MHz for each channel
Charge dynamic range	0.1 to 1250 p.e. (0.2 to 2500 pC)
Charge resolution	RMS$\sim$ 0.05 p.e. (below 25 p.e.)
Timing LSB	<0.5ns
Timing resolution	RMS <0.3ns at 1 p.e. RMS <0.2ns above 5 p.e.
Power consumption	<1W per channel

TABLE XLII. Basic requirements for the performance of the signal digitizer.

A. Photosensor Digitization

The signal digitizer block accepts 24 PMT inputs and outputs the timing and charge values for each input signal. The requirements that the digitizer module has to satisfy are summarized in Table XLII. The digitized data have to be transferred to the data transmission block without any loss even when all the PMTs are producing hits at the maximum rate of ∼1MHz. The input power supply voltage is 48V and the digitizer board has appropriate voltage regulators (converters) on board. The power consumption is expected to be below 24W for 24 channels.

1. Digitizer interfaces

The interfaces of the signal digitizer with the other components are shown in Fig.143. The TDC are synchronised to a reference clock provided at 62.5MHz. There is another clock signal provided at 61kHz (every 1024 times the 62.5MHz clock). The 61kHz signal is used to reset the TDC counter. There is a 32 bit counter attached to the data, which is incremented when the 61kHz counter increments. Assuming one count of the TDC corresponds to 0.25ns, the maximum value of the TDC counter will be 65535. The digitizer is expected to return a signal indicating its status, together with the total number of hits in one TDC reset cycle (16384 ns). This information will be transmitted to the clock distribution module and used for independent system monitoring.

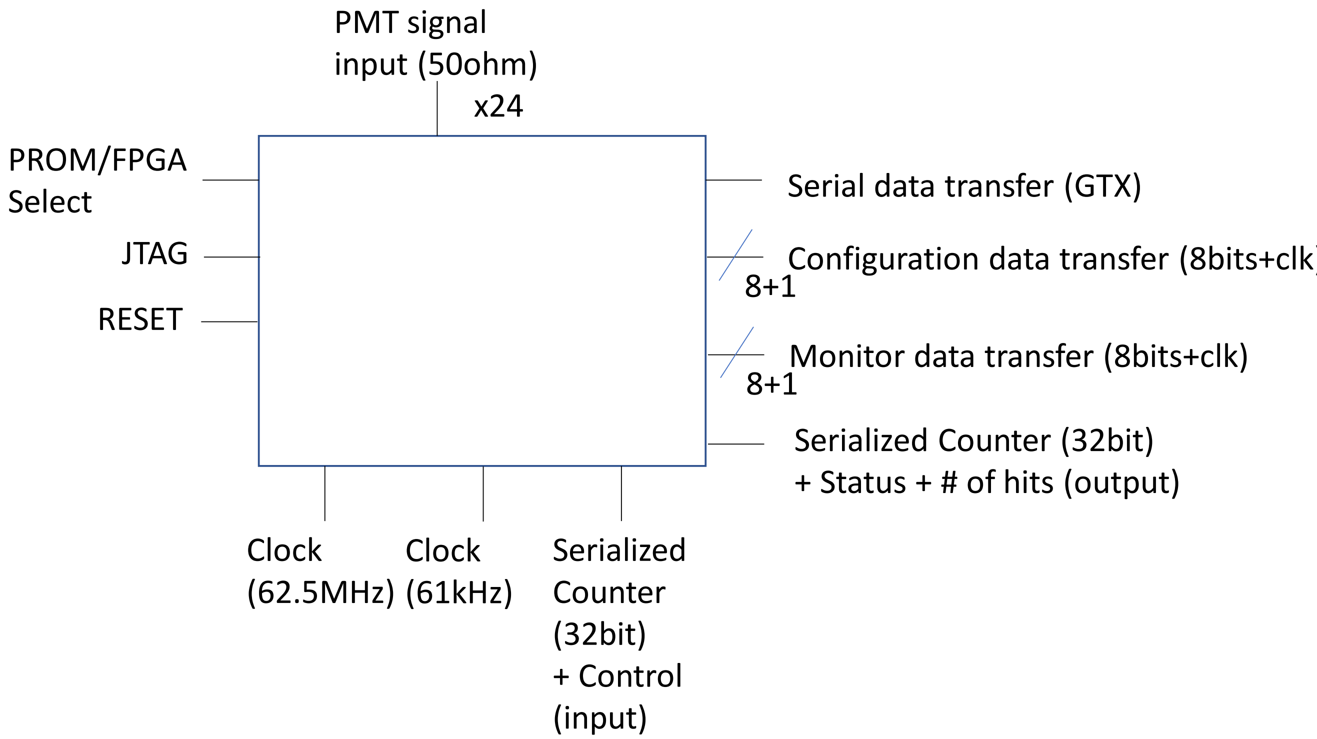

FIG. 143. I/O interfaces of the digitizer block

The data are expected to be transmitted through fast serial data transceivers. There are also control signals that are used to tell the digitizer to take pedestal or calibration events, or to apply a veto on the digitization. These signals could come with the counter information, but it may be better to have special independent inputs to process those requests, in which case the output from the clock receiver module could be used, and appropriate I/O pins would have to be defined in this document.

The digitizer block has to have a functionality to change all the configurable parameters in the digitizer and to read back these parameters. It is necessary to have a digital signal input to reset all the components of the digitizer module. The protocol or interface signal lines for the control or the monitor lines (8bit + 1bit) could be modified in the actual implementation. This block is required to let the other blocks know the status of the FIFO, such as empty, half full, almost full or full. It is better to have independent output I/O pins assigned for each of them.

2. Treatment of the data

The output digitized data have to be associated with the information of enabled and disabled channels. Also, it is necessary to have the length and the checksum of the data. There should be some amount of FIFO buffer to keep the data to be read out by the system and network block. It is necessary to insert a special flag when the FIFO is filled (FIFO FULL begin) and cannot keep the hit information from the digitizer. This is recorded together with the 32-bit counter. When there is a sufficient amount of FIFO to resume the data recording, another special flag (FIFO FULL end) has to be inserted with the 32-bit counter, before the hit data is stored, to let the later processing know exactly which part of the data has been lost. If there are troubles in the received pulse from the digitizer, error data blocks have to be sent.

The firmware of the EEPROM needs to be accessible from the other components via a JTAG interface. It is better to have a functionality to download the firmware through this interface to test new firmware without storing the firmware on the EEPROM.

There may be more than one charge range for each channel. Therefore, the digitizer module is expected to provide the value from the appropriate range. It is necessary to provide for special modes to return both the leading and trailing edges of the timing, or T and Q for all three charge ranges. The latter of these is necessary for the pedestal or calibration data taking.

3. Digitizer technologies

There are two kinds of technologies that have been proposed. The first approach is to use a charge to time converter chip together with the TDC. The charge to time converter chip integrates the charge in a pre-defined gate time when the signal pulse height exceeds the threshold. Then, a single square shape pulse is output, whose rising edge indicates the signal timing and whose width is proportional to the input charge. Because of these characteristics of the output pulse, there will be a dead time during the signal pulse output but this dead time can be smaller than 1 μs, which satisfies our requirements.

The second approach is to use a waveform digitizer, of which there are several types. One possibility is to use an FADC with a sampling rate around 100 to 250 MHz. An alternative would be a capacitor array (analog memory cell), where the sampling rate could be extremely fast, up to a few GHz if necessary. Currently, Japanese and US groups are collaborating to design the digitizer using a QTC chip + an FPGA based TDC. Canadian and Polish groups are collaborating to study the feasibility of using an FADC, and a Swiss group is studying the use of an analog memory cell (DRS) system.

The QTC chip was developed for the Super-Kamiokande detector and has been used since 2008, so it is known that the QTC satisfies our requirements. The production line for this ASIC is still available (as of April 2018) and it is possible to produce the same chip. The QTC chip has to be associated with a TDC that has sufficient performance, and this will be implemented in an FPGA. The development of the signal input circuits that are needed to protect the QTC chip from unexpectedly large signals from the PMTs has been started and seems to be feasible.

4. Amount of data from various sources

Actually, the expected number of neutrino events from sun and atmosphere is almost negligible because there much less than a few hundreds per day. The actual data, which are expected to be stored are mostly from cosmic-ray muons and the low energy activities from various radioisotopes. The rate of the cosmic ray muon is exepcted to be 45Hz. If the gate width of an event is set to be 60μs, amount of the data will be $\sim$30MBytes/sec. It is not easy to estimate the low energy activities but if we assume the rate is 7 times higher than the SK for events with energy larger than 6MeV, trigger rate will be 350Hz and this amount of the data will be $\sim$80MBytes/sec for 60μs gate width. The trigger rate for lower energy could be determined by the speed to access the storage and its capacity. If we set the trigger rate to 10kHz, which is almost same as current SK, the expected data rate will be 80μBytes/s for 1.5μs gate window events. In addion to the dark noise, one of the source of the data to be handled is the pedestal and the QTC calibration data. The trigger rate is rather low and it is 1Hz but there are 46,700 channels and each channel have two hits for three ranges. In total 2MBytes/sec of data will be produced. Even if we use the other digitier solution, almost same amount of data will be produced for this kind of information.

B. System Clock and Counter

The clock and counter system consists of five components: the master clock generator, the signal distributors, the clock and counter receiver blocks, a commercial atomic clock and the GPS receivers. (Fig. 144)

The reference clocks and relevant signals are generated by the master clock generator. The signals from the master clock generator are decoded and fed to the other components in the front-

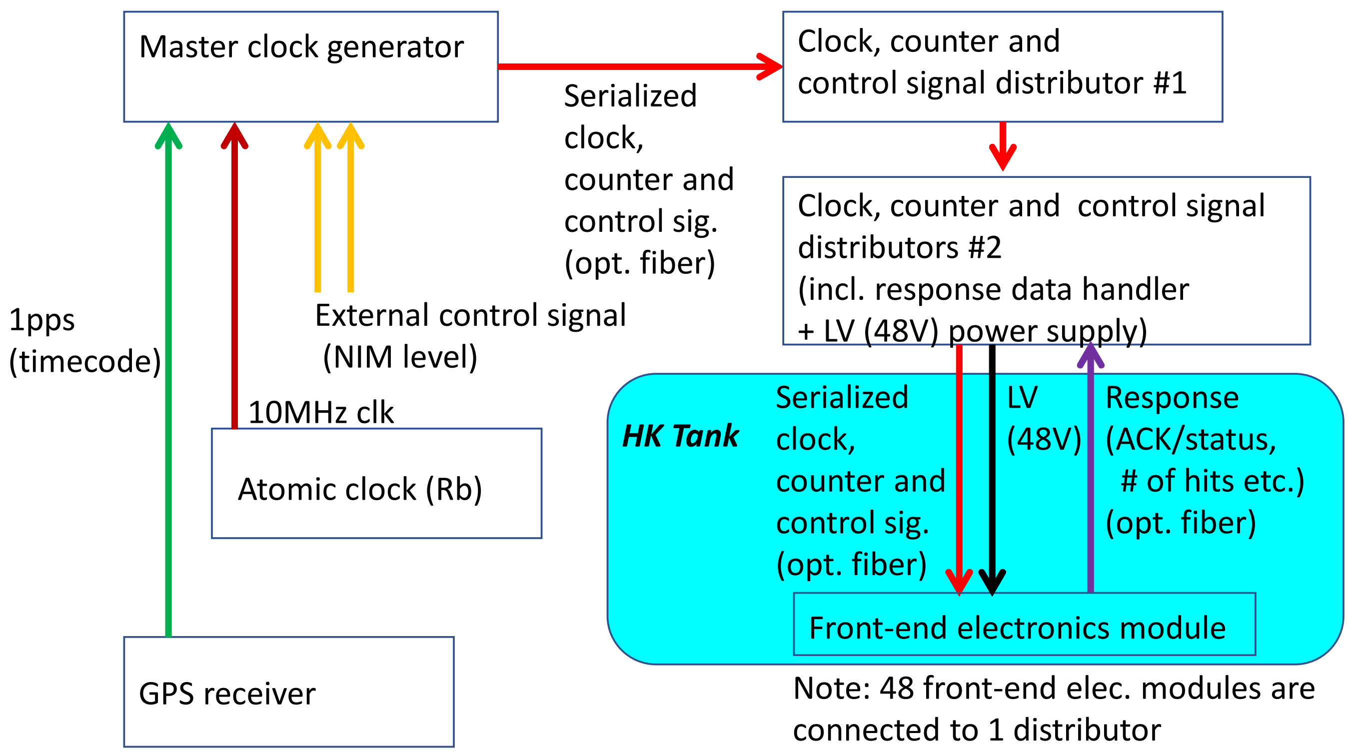

FIG. 144. Components of the clock and the counter system. All the components are outside the HK tank, except for the fibres and receiver blocks which are in the blue box.

end electronics box in the water by the clock and counter receiver block. There are distributors between the master clock and the clock receivers. The distributors are cascaded to reduce the number of outputs from one distributor.

The long term stability of the clocks provided by this system has to be better than 2×10^{-11}. This is achieved using an external atomic clock as a reference, and compensating it by GPS as necessary. The jitter on the clock signal has to be less than 100ps. The relative timing (phase) difference between the signal from the clock and the counter generator and the output of the receiver module has to be stable, and the change of the phase after a reset or the power cycling of any part of this system should also be less than 100ps.

The timing signal is distributed through OM3 optical fibres. The interface to the optical transceivers could be either SFP or 1x9pin (Appointech TR78R85M3) but it is possible to use other interfaces if they have better performance or durability. A 1.25 Gbps baseline optical module is commercially available. Each of the counter receiver blocks has to have two optical interfaces to realize an active backup fault-tolerant system. The backup transceiver is not turned on until the primary one stops working. The module fault identification system has to be running independently and switch over if a problem is detected. Therefore, there have to be two interfaces prepared for each clock receiver block in the distributor module.

1. Master clock generator

The master clock generator provides a 62.5MHz clock, a 61kHz clock, a 32-bit counter, a GPS based timestamp and additional bits to control the blocks in the front-end electronics (Fig. 145).

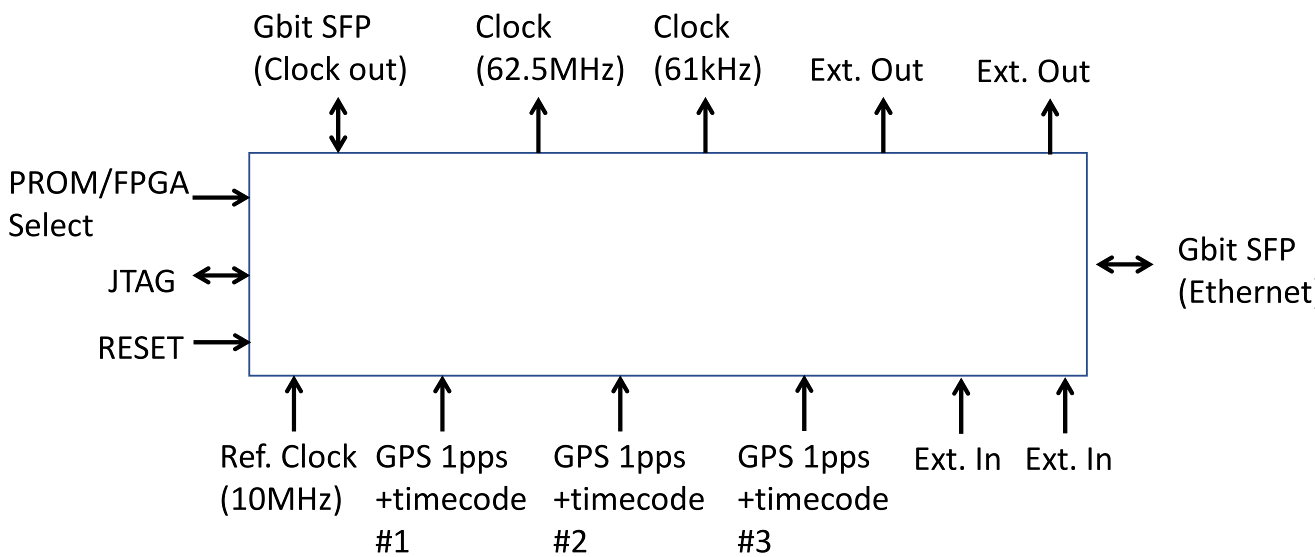

FIG. 145. Inputs and outputs of the master clock generator.

The 62.5MHz clock is generated using external inputs from an atomic clock. The frequency of the most of the atomic clocks is set to 10MHz which we assume is fine, but we may need to be capable of accepting other frequencies. The 61kHz clock is generated every 1024 counts of the 62.5MHz clock. It is used to increment the 32-bit counter, which is distributed to the front-end electronics. Both the 62.5MHz and the 61kHz clocks need to be accessible from an external output by configuration.

The generator module has to have at least 4 external signal inputs, which are transmitted with the 32-bit counter to control the front-end electronics module. It has to accept three independent GPS 1pps inputs, which are associated with a serialized timecode. There are various timecode protocols available, so the module has to be configurable to accept them. The relative time differences between the latest 61kHz clock and the most recent GPS 1pps pulse has to be recorded with the data for each GPS. For this it is necessary to have at least one ethernet port to send out the information. The same information is also embedded within the 32-bit counter and sent to each of the front-end modules.

The data transmission speed of the optical transceiver to send the clock, the counter and the other information is required to be faster than 1.25Gbits/s. Even if the maximum data rate is 1.25Gbits/s, 20 bits are available in one cycle of the 62.5MHz clock. Therefore, one optical fibre could carry two clocks (62.5MHz and 61kHz) and the additional information. The detailed format of the bit stream has to be determined with careful consideration of maximising the accuracy and minimising the jitter. It is also acceptable not to send the clocks directly through the fibres but to send the reference timing at certain periods to compensate the clock signal in each clock receiver. However, it is necessary to have the functionality to send the counter and the additional information, which have to be synchronized to the clocks.

2. Clock, counter and control signal distributor

The distributor receives the clock and the counter signals from the master clock generator and distributes the signals to the receivers in the front-end electronics. The maximum number of receiver modules that can be connected to a distributor is 48. The distributor module has two optical transceivers for each receiver module and these interfaces act as an active-standby configuration. If one of the module interfaces fails, the clock distribution has to be transfer over to the other one automatically. SFP is used as the optical transceiver interface.

The distributor receives the information from each receiver, which sends back the counter, the status and the number of hits in one 61kHz clock cycle. This information has to be summarised and transferred to a dedicated readout computer through the ethernet interface. The returned signal is also used to compensate the clock timing distribution by adjusting for timing differences (<25ns), between the modules due to the different lengths of the fibres. The distributor module also provides the 48V DC power to each of the front-end modules. The specification for this is described in the LV supply section.

3. Clock and counter receiver block

Within the front-end electronics module the clock and counter receiver block decodes the clock and counter signals, and other information from the master clock, and distributes them to the other blocks in the front-end electronics. It receives the status and the number of hits information from the digitiser, and encodes and returns them to the distributor module. The information which is sent back to the distributor has to be received within 25μs. (Fig. 146)

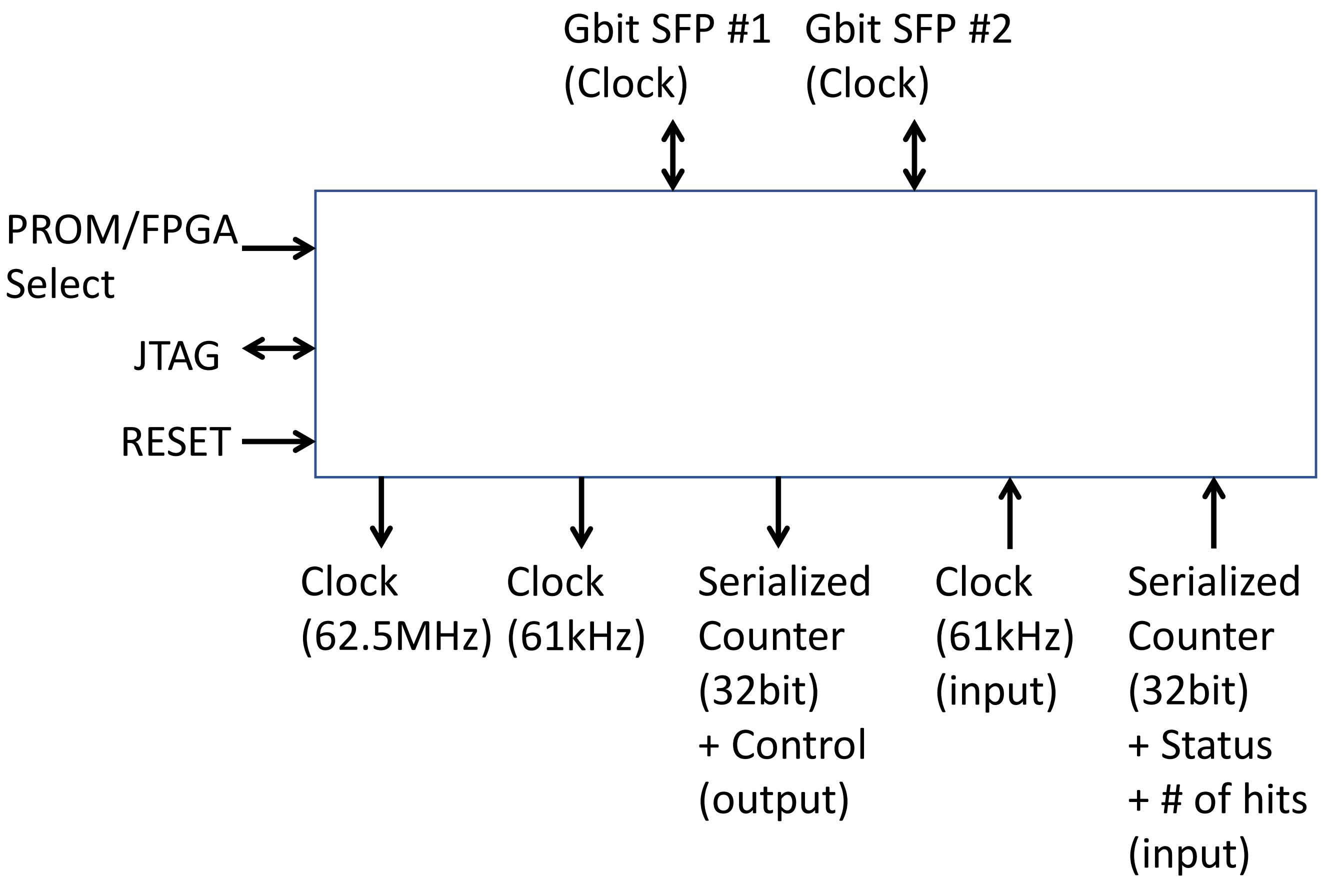

FIG. 146. Inputs and outputs of the receiver module.

C. Digitizer Control System

The digitizer control system receives commands from the readout system through the network block and the digitizer block. It also receives the data from the digitizers, buffers them and sends them to the readout system. The data transfer speed from the digitizer has to be faster than the maximum speed of the data processing in the digitizer. This system controls the pedestal data taking and other necessary calibration data taking, as configured by commands from the readout system. It also checks the data from the digitizer module and detect errors. If there are errors, all the received data from the digitizer block have to be transferred to the readout block with special tags for fault diagnosis.

This block has to have at least 8 GB of dedicated buffer to keep all the hits for more than 2400 seconds. If the system uses CPU, the memory area for the CPU has to be separately prepared. The information provided by the slow control monitor system has to be combined and transferred to the readout system together with the data from the digitizer. The data transfer speed to the readout computer system has to be faster than 1Gbps, so the system has to be capable of sending out the data faster than the speed of the network. For future extendability, it is preferred to have the capability to send data at more than a few Gbps.

It is also possible to have the data compression functionality in this block. This will reduce the amount of the memory to be used to keep the data during the burst. However, it is necessary to keep all the information including various flags, which comes with the data.

This system could be integrated with the system control and network interfaces (Fig.142). It receives the commands to control the other blocks, including the HV or the slow control system. These requests have to be processed in this block and transferred to the relevant blocks.

D. High Voltage Power Supplies

This block is expected to provide a stable and low noise (ripple) high voltage power to each of the 24 PMTs associated with a front-end electronics module. It needs to have the capability to turn on and off individual channels, to monitor the voltage and the current of each channel and to cut the power supply of each channel if the current or the voltage are different from the expected values. The basic requirements are summarized in Table XLIII.

The HV block is enclosed in the same underwater chassis as the front-end electronics. Therefore, the HV system is shielded and the electronic noise through the ground and power supply lines has to be minimized. It is possible to provide 48V as the input power source but this could be lowered to 24 or 12V. Within the chassis the HV module might be moulded to avoid trouble from a possible water leak. If the module is not moulded, the environment could be anything between a vacuum and 100% humidity, and it is necessary to test it under such environments. For the 20” B&L PMTs (and the 20” MCP PMTs) it is fine to have an adjustable voltage range between 1500 and 2500V for the 24 channels. If the same front-end electronics modules are used for the 3” Outer Detector PMTs, the voltage range needs to be reduced to 600 to 1100V. For the 20” HPD option a higher voltage of 8kV needs to be supplied.

The interface to control or monitor the HV could be either SPI or Ethernet. The configuration

Item	Requirements
Output voltage	0 to 2500 V
Accuracy	< 0.2% (1500 to 2500 V) < 3V (0 to 1500V)
Output current	> 0.5mA/channel
Output stability	< 0.2% / year
Accuracy of voltage monitor	< 0.2%
Accuracy of current monitor	< 0.5%
Ramp up/down speed	Tunable from 100 to 500 V/s
Ripple noise level	< 10mV p-p at 10kHz
Temperature dependence	50ppm/K
Failure rate (per channel)	< 1% / 10 years
Power consumption	< 1W/channel

TABLE XLIII. Basic requirements of the HV power supply for the 20” B&L PMTs.

of the HV system could be either via a primary HV with a distributor or via individual HV supplies for each channel. For the first option there should be more than one primary HV to allow for a switch to a backup primary HV to realize a fault-tolerant system.

E. Slow Control and Monitoring

This block receives the commands from the digitizer control system and controls the HV power supplies. The HV system has a preset voltage for each channel, limits on the allowed current or voltage, and a ramp up or ramp down speed. These parameters have to be both read and write accessible. The block also monitors the voltages and currents of the LV and HV, and the temperature and humidity of the front-end electronics. The monitored values are read out by the digitizer control system and sent back to the main control module via a serial interface. The required accuracy on the monitored quantities is:

- Temperature to better than 0.5 degrees.
- Humidity to better than 10%.
- Low Voltage to better than 0.1V and 10mA.
- High Voltage to better than 0.2% for the voltage and 0.5% for the current.

F. System Control and Network Interface

This block has to communicate with the other blocks in the front-end electronics module, including the digitizer control system and the slow control and monitoring. The interfaces to those blocks have to be compatible with the requirements described in the other sub-sections. We expect there to be at least two optical network interfaces which have to have data transfer rates faster than 1Gbps.

The preferred data transport protocol is TCP/IP, which is required to transmit data faster than 95% of the bandwidth of the optical transceivers. These have to use GTX or a similar serial transceiver to realize sufficiently fast data transmission if this block is separated from the digitizer control system. It may be better to combine this block with the digitizer control system to minimize the necessary resources. The data transmission line has to have error detection and preferably correction capabilities.

The preferred protocol for the control commands and monitor responses is UDP/IP. Detailed formats for the control commands have to be defined based on the descriptions in the digitizer control and slow control sub-sections.

G. Optical Interfaces

The optical interface is one of the most critical components in the front-end electronics module, because most optical transceivers are known to have a limited lifetime. Therefore, it is necessary to identify the most durable products, since the front-end module is expected to be in use continuously for more than 10 years.

The optical fibres are multi-mode (OM3), and need to have a length longer than 200m to go to the outside of the tank. The data transmission speed has to be faster than 1Gbps, and preferably 2.5Gbps or 5Gbps but this is not mandatory. The optical transceivers for the front-end electronics modules do not necessarily need to be small form-factor pluggable (SFP), but it is better if they are for easier maintenance. The operating temperature inside the tank is expected to be lower than 30°C, but it could be higher inside the module if it is moulded. The pressure inside the module may be lowered in case of a small leak of the gas. Therefore, it is necessary to test the optical interfaces under these environments.

The transceiver has to have the capability to monitor the light level. There are two optical connections per module, providing an active-backup configuration if one of the connections has trouble. It is useful to have information of the failure rate of the optical interfaces both with and without operation. The optical interfaces used in the distributor modules outside the tank have to be compatible with the ones in the front-end electronics modules. However, the transceivers used in the distributor modules are replaceable, so it is not necessary to satisfy some of the requirements, including the lifetime and the need for operation at non-standard temperatures and pressures.

The timing system is required to have small jitter, better than 100ps. Therefore, the optical transceiver for the clock system has to have a sufficiently fast timing characteristic to satisfy the requirements. The timing system may send longer pulses or special duty cycle pulses. The optical transceivers have to be capable of sending the special pulses required by the timing system. Note that most of the optical transceivers for Ethernet are not capable of sending or receiving slower frequencies, or working at something different from a 50% duty cycle.

H. Watertight Case

A watertight case encloses the front-end electronics and the HV power supplies. The case has to protect the electronics from the water and the pressure, and has to be built with materials which do not harm the quality of the water. This means that the case is likely to be built with stainless steel and/or some resin. The water pressure should not to be propagated through to the components enclosed in the case, and the heat generated by the components in the case has to be removed from the surface of the case by the surrounding water. At least some of the surface should be covered with metal to have a better heat exchange capability. It is possible to fill the case with some resin, in a similar way to the 20" PMT base. However, it is essential to have appropriate heat deposition methods for the components whose power consumption is largest. If the case is not filled by the resin, it is necessary to confirm that the gas inside the case does not leak out into the water, as a lower pressure inside the case would make heat removal more difficult.

There will be 24 cable connections from the case to the PMTs, which provide the HV and return the signals. There will also be an optical fibre connecting the module to the outside of the tank, which provides a combination of data readout, control signals and the LV power supply. A spare optical fibre is foreseen to make the system robust against failure. These cables and fibres need to go through feed-throughs, which have to withstand at least 10 atmospheres.

The dimension of the case depends on the size of the components of the front-end electronics and the HV system. We estimate the size to be roughly 50cm $\times$ 40cm with a thickness is 8 cm. The case has to be mounted on the PMT support structure, either in a slot that is not occupied

Item	Requirements
Water tightness	10 atm ($\sim$1MPa)
Maximum high voltage and current	+3000V, 1mA (DC) Need to operate in a vacuum environment
Impedance of the coaxial signal cable	50Ω
Cable diameter (outer sheath)	8.4mm
Signal cable	RG58C/U
High voltage cable	RG74/U
Material	Stainless steel (SUS304) or resin
Durability	>20 years

TABLE XLIV. Requirements for the underwater connector for the signal and HV cable at the PMT.

by a 20" PMT (or an mPMT), or to the side of the PMT if all 40k slots are populated with the 20" PMTs. A module reads out an array of 6×8 slots (4.5m × 6m) with 20k PMTs, or an array of 4×6 slots (3m × 4.5m) with 40k PMTs.

I. Watertight Connectors

The connections between the front-end electronics modules and the PMTs are located under water. For the connections at the PMT in Super-Kamiokande there is a BNC connector for the signal and a cramping connector for the HV pins. These connectors are covered with special heat shrink tubes. The cable connecting procedure is complicated and it takes a fair amount of time and careful treatment on site to connect the PMTs. This could be avoided if we could prepare an appropriate watertight connector that carries both the HV and the signals, and can be quickly connected to the PMT during the construction phase. The connectors have to stand up to 10 atmospheres of water pressure, be stable for more than 20 years, and be usable in a vacuum environment because the gaps around the connectors may be degasified by the surrounding water. If it is not feasible to create efficient combined connectors at the PMTs, we will use the established method to connect the HV and the signal cables with the existing BNC and HV connectors, and protect them from the water using heat shrink tubes. The requirements of the watertight connector are summarized in Table XLIV.

The materials used for the connectors have to be compatible with not disturbing the water quality for both pure water and Gd_2SO_4 doped water. For example, it is not allowed to use an oil seal. The outer shell of the connector is preferably made from an appropriate resin or from stainless steel (SUS304). The schematic of a combined PMT signal and HV cable is shown in Fig. 147 (top). This connector has to be compatible with the cable which comes with the PMT. A company in Japan has already designed a set of underwater connectors for HPDs and performed basic functionality tests in water. Based on this experience, they re-designed a new connector for PMTs, which is smaller than the one for an HPD and they have made a prototype connector (Fig. 147 middle). These connectors are composed of an outer shell and inner connectors.

The connections between the readout system and clock distributor outside the tank, and the front-end modules, also need underwater connectors at the module end. There are two wires supplying the Low Voltage power (see next sub-section). Optical fibres are used to transmit the timing signal, the control information and the data. A candidate for these is the OM3 multi-mode fibre. There is a connector called MPO, which can house up to 24 fibres in a small connector head. It is possible to design underwater Ethernet connectors which house special RJ45 connectors without a latch as shown in Fig. 147 (bottom). Unfortunately the Japanese company do not have experience of the MPO fibre connectors, so they cannot design the optical fibre connectors.

J. Low Voltage Power Supplies

The LV power supplies provide 48V DC power to the front-end electronics modules. The maximum current for each module is 3A. For this we need a pair of wires with an area larger than 1.25mm^2 in order to minimise the voltage drop. The voltage and current are monitored, and the power supply to each module can be turned on and off independently, particularly of the monitored values are outside the acceptable range. This is done using commands sent through the ethernet interface.

K. GPS system

The GPS system uses commercially available GPS antennas and receivers to transmit precise 1pps information with the time code to the system clock and the counter system. The timing accuracy is better than 10ns. Most of these GPS receivers and antennas are not assumed to be used in the mine, so it is necessary to transmit the 1pps pulse from the antenna to the detector using an optical fibre. The distance from the entrance of the mine, where the GPS antenna could be located, to the detector, is not well defined at the moment, but it could be several km, similar to the distance from the Mozumi mine entrance to Super-Kamiokande.

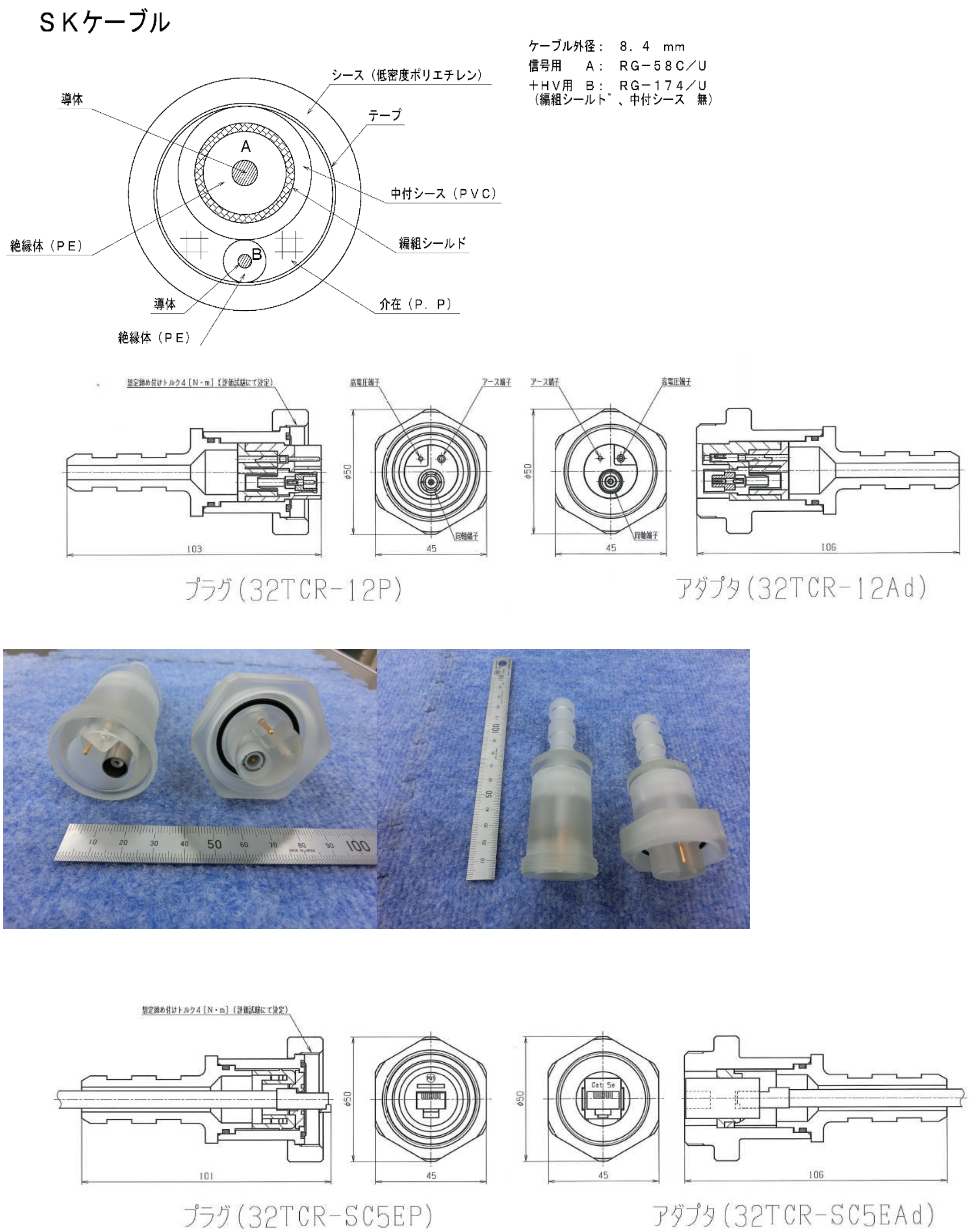

FIG. 147. Schematic diagrams of the underwater cables. Top: PMT connector designs, Middle (Photos): Prototype PMT connector, Bottom: Ethernet connector design.

The GPS system is required to come with the Rb clock to provide faster frequency if necessary. The jitter of the clocks provided by this system at the clock and the timing module has to be better than 100ps. It has to be verified that it is possible to transmit the 1pps pulse over the distance from the mine entrance to the detector, without creating too much jitter.

There should be at least 2 different GPS receivers to realize an active-active system, and there has to be one common-view receiver, which is capable of providing the time difference between JST and the 1pps pulse from one of the GPS receivers. This system has to continuously monitor the status of the GPS receivers including the number of used satellites, the signal levels from each satellite, the time differences between the 1pps signals from different receivers, and the differences from JST for both receivers using the common-view system. There are several new satellites available in Japan and is is better to have the capability of using them in addition to the traditional ones.

III.10. DATA ACQUISITION

The data acquisition system for the far detector will be built using the open source ToolDAQ framework, with commercial computing hardware. The system consists of four main components: Readout Buffer Units (RBUs) which read out the signals and store the data for future usage in short term buffers, Trigger Processor Units (TPUs) which analyse short data windows with multiple algorithms to determine if the data is useful, Event Builder Units (EBUs) which construct the events in the positively triggered data windows and write them to disk, and the Brokers which are responsible for distributing jobs to the TPUs and EBUs and organising the whole system. The monitoring and control interfaces for the system will be web-based and taken care of by a separate web server.

A. Readout Buffer Units

The detector signals will be read out from the Front End Electronics (FEE) modules by the Readout Buffer Units (RBUs). There will be roughly 70 RBUs built from commercial computer server hardware. Each RBU will read out ≈30 FEE boards via a gigabit network switch, which allows for rerouting of the data if an RBU failure occurs. The RBUs will run a version of the ToolDAQ framework and will undertake many operations and functions within the DAQ. The software will be multithreaded to allow data from the FEEs to be recorded directly into memory without incurring any dead time. From here the data will be catalogued and organised based on the time of recording. Once the ≈100 seconds of active memory is filled data catalogues are archived onto drive storage for periods of ≈1 hour, where eventually they will be removed. The management of these buffers and archives will be controlled seamlessly by the software, so no user intervention is required. This forms the major component of the RBUs task of reading out and buffering the data from the FEEs.

The other roles of the RBUs are to send a reduced version of the data to the Trigger Possessing Units (TPUs) for making trigger decisions, and to distribute the data to the Event Builder Units (EBUs) following a trigger decision. These activities occur upon direct requests for data by the TPUs and EBUs. Data is requested by giving a range of interested timestamps, and will then be sent to the TPUs or EBUs using standard TCP/IP packets through a separate network via a gigabit connection. A number of internal buffers, connection checks, acknowledgements and time outs are used to ensure data is sent successfully or that systems are triggered to resend or recover from data loss or connection issues. To recover from an RBU failure the data which is pushed to disk storage should be retrievable on restart of the process. Extra FEEs can be assigned to an RBU by the brokers, to pick up the slack of lost nodes.

The final job of the RBUs is to handle the data stream from a close supernova. A thread on the RBU process will be waiting continuously for a supernova trigger signal to put it into a supernova read out mode. When this signal arrives the RBU will stop the more processor intensive tasks of reducing the data for trigger decisions, and will simply stream all data coming in to storage as fast as the data connections to the EBUs will allow. The specific EBUs to stream data to will be assigned by the brokers when a supernova event occurs.

B. Simple Majority Trigger

All PMT hits above a threshold of 0.25 pe will be delivered to the data readout and processing systems. A sliding time window is applied to the incoming data, and if the number of PMT hits in the window exceeds a given threshold, the event will be read out. To identify interactions that result from the beam spill neutrinos, the trigger system will receive a GPS timestamp from the accelerator at JPARC. Each of these timestamps will be used to define an additional software trigger that will record all hits in a 1 ms window around the beam arrival time. The trigger system will also require a separate external input for use with calibration devices.

A simple trigger with a low enough threshold on the number of hits to be sensitive to low energy ($<$ 15 MeV) events, is not viable. Reading out all the hit information in such events would be difficult as the dark noise from the PMTs would lead to a data rate of 5 GB/s. Events that fail a higher threshold requirement on the number of hits will be passed to a second “intelligent” trigger. This will perform real-time processing of the hits in the detector to determine whether a low energy event has taken place. This is discussed in section III.10 C.

Finally incoming events will be monitored to check for supernova bursts. A set of monitoring criteria will be defined and implemented in the trigger framework. The buffer size of the DAQ machines will be determined by the requirements for recording local supernovae. The supernova trigger is discussed further in section III.10 E.

C. Vertex Reconstruction Trigger

A neutrino interaction leads to final state particles that produce Cherenkov light which can be associated back to a common space-time vertex where the original interaction occurred. Events where the hits arise from dark noise in the PMTs will not have a common vertex. For each event below the simple majority threshold, but above a lower threshold on the number of hits, we need to ascertain whether there is a common vertex for the hits. This allows us to discriminate between noise and low energy physics events. It is not feasible to process the events in real time using the full reconstruction chain as this would require significant computing power and processing time. It may also result in a trigger that has significant systematic uncertainties associated with it. Therefore a fast, reliable method is required to estimate the event vertex for use in triggering low energy events.

The vertex of an event can be estimated using a uniformly spaced 3D grid of test vertices in the detector volume. This type of algorithm is well suited for online triggering as it can be implemented as a simple operation on the data repeated many times, which could be performed in parallel be several processors. The arrival time of detected Cherenkov photons from an interaction point depends on how far the photons have travelled from the vertex. For each PMT hit and test vertex pair, a time of flight correction is made using a look up table. Following the corrections, the number of hits that arrive from each vertex within 20ns is calculated. The test vertex that maximises the number of hits within the 20ns interval is chosen as the candidate vertex and the number of hits in that interval is stored. The event is kept if the number of associated hits in the 20ns window exceeds a given threshold. Noise events would fail the number of hits cut, whereas low energy neutrino interactions should pass.

Despite the use of a test grid, this method is computationally intensive. The processing time can be reduced significantly by implementing the algorithm on a GPU. Extensive testing has confirmed that the code, when run on a GPU, reproduces exactly the results that it gives on an ordinary CPU machine, but runs 5 times more quickly. Further studies have shown that the test vertex trigger lowers the energy threshold by 2 MeV compared with the simple majority trigger for a comparable data rate.

D. Event Building Units

The Event Building Units (EBUs) receive messages from a broker which distributes to them the time stamps of data windows which have been positively triggered on. As such there is no direct communication between the TPUs and EBUs, and instead the broker is tasked with the distribution of information. On receiving a time stamp from a broker an EBU requests data in that region from the RBUs via 10 Gb/s connections, and identifies hits within the time window that can be associated with an event. The events are then written to disk and passed to a local disk server for archiving. Failure to build events will be picked up by the broker and the job redistributed to another EBU node for event building.

We need to define the requirements for performance, buffer size and disk storage. Also the data interfaces from the software vertex trigger.

E. Supernova Data Handling

A separate supernova trigger will monitor incoming data and in the event of a supernova burst, it will instruct the RBUs to transfer all of their data to the EBUs. All detector hits for a period of ±30 seconds either side of the burst period would be read out via a buffer and written to disk. Each EBU will be assigned a subset of RBUs which will stream data directly to them for saving. This data will be buffered both sides of the connection to ensure no data loss. GPS timestamps for the start and end of the burst would also be written to disk. It is likely that Hyper-Kamiokande will form part of a world-wide supernova monitoring effort (SNEWS). If this is the case, an alert would need to be sent to such a network.

Need to define the requirements for performance, buffer size and disk storage (for which the demands are significant). Not clear what is meant by a separate supernova software trigger.

III.11. CALIBRATION SYSTEMS

The Hyper-K detector consists of an Inner and an Outer Detector, and both parts need to be calibrated for operational monitoring, and specifically to meet the systematic goals of the Hyper-K experimental programme. The Super-K detector has been successfully operated for about two decades and has established several techniques to calibrate a large water Cherenkov detector [**?**]. The proposed Hyper-K calibration systems are based on extensions of the Super-K calibrations. This section describes the calibration hardware required for the successful operation of the Hyper-K detector. The overall calibration strategy will exploit data from these dedicated systems, particularly for the low energy calibration. For the high energy calibration there are additional sources of information available in the data, including cosmic muons, stopping muons, Michel electrons and π^0 events. A summary of the energy scale calibration obtained from these sources in SK-IV is shown in figure 148.

A. LINAC system

A Linac has been used to deliver a low energy electron beam to Super-K at periodical intervals. It is used for calibrating the low energy scale. For the physics requirements of Hyper-K, given the statistical uncertainties, an uncertainty of 0.2–0.3% in the low energy scale and of 2% in the energy resolution are desirable, but we note that for the solar neutrino day-night analysis a larger uncertainty of 0.5% in the energy scale would be sufficient. It is important to understand the energy scale at this level across the whole fiducial volume, in all directions and across the whole energy range of interest. In Super-K the Linac calibration was required to achieve these targets.

An analysis of data from the other low energy calibration sources available to Super-K has been conducted, and we have concluded that it is not possible to achieve our calibration targets without using a Linac in Hyper-K. This applies to both the direct measurement of the energy scale and to the measurement of angular resolution for which no replacement source has currently been proposed. For these reasons we include a LINAC in the Hyper-K design. It needs to provide a beam of single electrons with a tuneable momentum from 4 to 20 MeV/c.

To install a LINAC for Hyper-K we have adapted the installation plan of the Super-K LINAC, while noting that a more detailed design will be required, which needs to be taken on by a new group with responsibility for the LINAC. The design can be broken down into the follow areas: the LINAC room, the LINAC itself, the beam transport, control and measurement, and the deployment

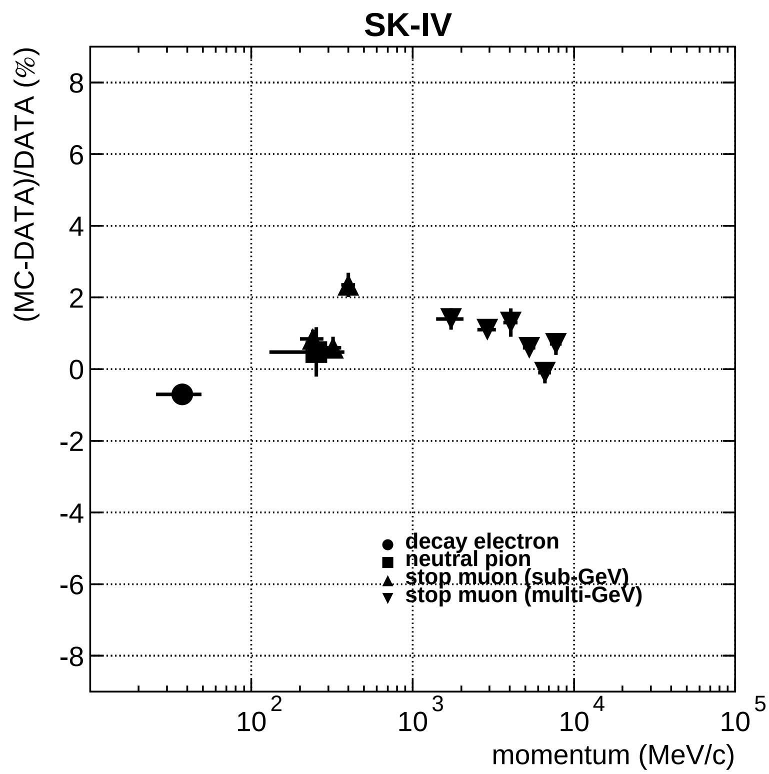

FIG. 148. Measurement of the absolute energy scale in SK-IV with various high energy sources.

system in the tank.

The LINAC room should be about the same size as the current Super-K room (4mx4mx15m). It is located at a position outside the main cavern, ≈5m higher than the top of the tank and at least 10m away, to allow for a shallow slope for the beam transport system. The room will require shielding of at least 50cm of concrete between it and the corridor to which it is connected, and to any other rooms.

We plan to use a commercial LINAC, although a particular model has not yet been identified. However, we do not expect it to be larger than the current Super-K LINAC, so the room for it should be more than adequate. The beam from the LINAC will need to be attenuated to achieve a beam power that provides a single electron per event window inside Hyper-K.

A beam transport system will be installed with a pipe through the concrete or rock to connect the LINAC to the main cavern. There it will be connected to a deployment system which enters the Hyper-K tank for the period of the calibration. The beam uses dipole and quadrupole magnets to select the desired beam energy. The energy will be measured using a Ge detector to provide a precise control of the electrons entering the detector. The deployment system uses a guide tube that will allow the electrons to be injected into the detector at multiple depths. We will explore the use of a further magnet system at the end of this system to provide control of the electron direction. This would allow us to probe the energy scale in multiple directions during the calibration which addresses one of the largest areas of uncertainty in the current Super-K calibration. To insert this system into the Hyper-K tank a minimum clearance of 10m is needed above any calibration port, with 20m being recommended.

B. Light Injection system

Hyper-K will include an integrated light injection system for calibration of both the inner and outer detector. This will be used to measure the optical properties of the water, including the absorption and the scattering as a function of position. It will also be used to measure the timing, gain and multi-photon response of the PMTs. Finally it provides monitoring of the correct operation of the PMTs and the front-end electronics.

The system will consist of a number of light injection points connected via optical fibres to light pulsers in the electronics hut on top of the tank. Light pulses of ≈1ns can be produced using LEDs, laser diodes, or similar solid state optical devices that can be produced inexpensively. The LEDs (or equivalent) are coupled to a set of optical fibres which are routed into the tank through ports in the top plate. For the inner detector the fibres are connected to optical injector points on the photosensor support structure. For the outer detector the injector points are on the tank wall. The optical injector is used to shape the light inside the detector, with different designs providing calibration pulses for different needs.

In order to maintain fast light pulses over the ≈100m distance of the optical fibres needed for Hyper-K, a graded index fibre is required. The small active core of these fibres complicates the design of the light injection system. The key challenges of this system are the coupling of the LEDs to the optical fibres, minimising the dispersion within the fibres to maintain short optical pulses, and achieving the required dynamic range without compromising the fast optical pulses. Research and development is currently underway in the UK to solve these problems.

For the light injectors there are three approaches that can be taken. The first is to use a bare optical fibre which will provide a cone of light in the detector of approximately 12°, depending of the numerical aperture of the fibre. The second approach is to use a diffuser ball to produce a wide-angle beam to illuminate as many PMTs as possible. The final approach is to use a collimator to produce a narrow-angle beam to illuminate only a few PMTs directly. Each approach has different strengths and in combination these can provide the widest possible calibration scheme for the ID. In the OD a simple diffuser with a very wide-angle beam meets the calibration requirements with the smallest number of injection points. A system consisting of a collimator, diffuser and bare fibre has been deployed in the Super-K ID during 2018. This will allow calibration procedures to be developed and tested with detector data. The light injector plate deployed in Super-K with the three systems is shown in Figure 149.

The design of the light injection pulsing system is undergoing continued development to improve the performance of the timing, dynamic range and optical coupling. The current design utilises a mother board and daughter board design. The mother board contains the FPGA control systems and is responsible for communication with the DAQ and trigger systems. The daughter boards contain the LED drivers themselves. The interface between these two is designed to be independent of the detailed design of the driver system on the daughter board, allowing the boards to be developed simultaneously, and for multiple driver systems to be used in the same electronics scheme. The most vulnerable components will be placed on the daughter boards, allowing for a more straightforward replacement to be carried out during operation. In the current design each mother board can control up to 8 daughter boards. The electronics is shown in figure 150.

For some calibrations it will be essential to monitor the light injected into the detector. One option is to couple multiple fibres to the LED, or there are commercially available fibre splitters that can be used to redirect a fraction of the light for monitoring purposes. The monitoring light can be measured via optical sensors, which are typically PMTs. The monitoring PMTs will themselves be calibrated and monitored by a dedicated channel where the main pulse is not injected into the detector, but is instead delivered to a well calibrated optical power meter. This cross calibration will allow the absolute optical signal of the monitoring system to be determined. This allows a comparison of the light injected pulse by pulse and across the running time of Hyper-K. By deploying a three way split of the light from the source, the third path being read out via an optical diode, a safety cut-off can be added to the system to ensure that DC light emission into the detector does not occur.

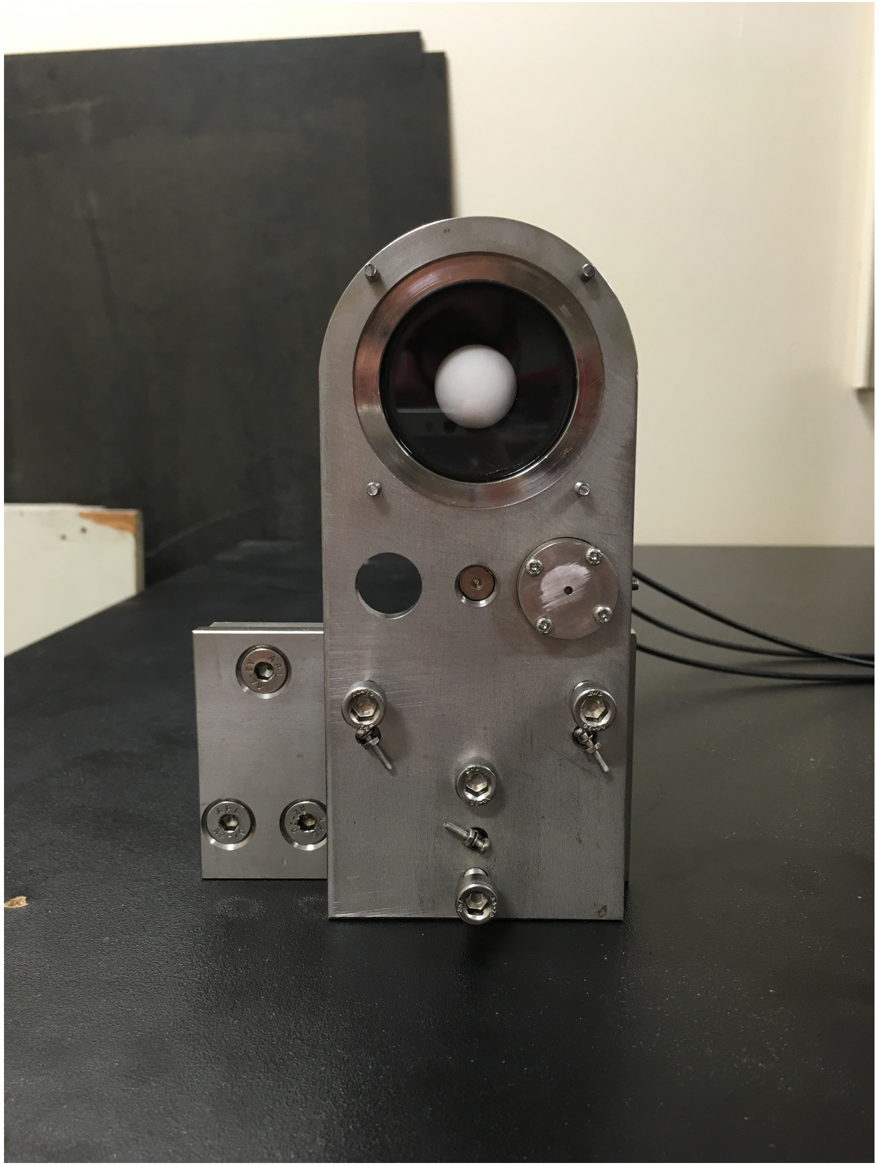

FIG. 149. Photograph of the light injector deployed in Super-K in 2018. The system contains a bare fibre (centre), diffuser (top) and collimator (right).

This system allows PMT and optical calibration data to be taken without the manpower intensive deployment of calibration sources that have been used previously in water Cherenkov detectors. The data from the light injection system can be collected either in dedicated high rate calibration runs, or can be interspersed during normal data taking. This allows calibration to be conducted during extended periods of running, where deployment of calibration sources would otherwise result in detector downtime. Given the systematic error budget of Hyper-K this system will mean we do not have to compromise between efficiency and the collection of sufficient calibration data. Calibration sources would still be used during short intensive periods, but these would occur out-

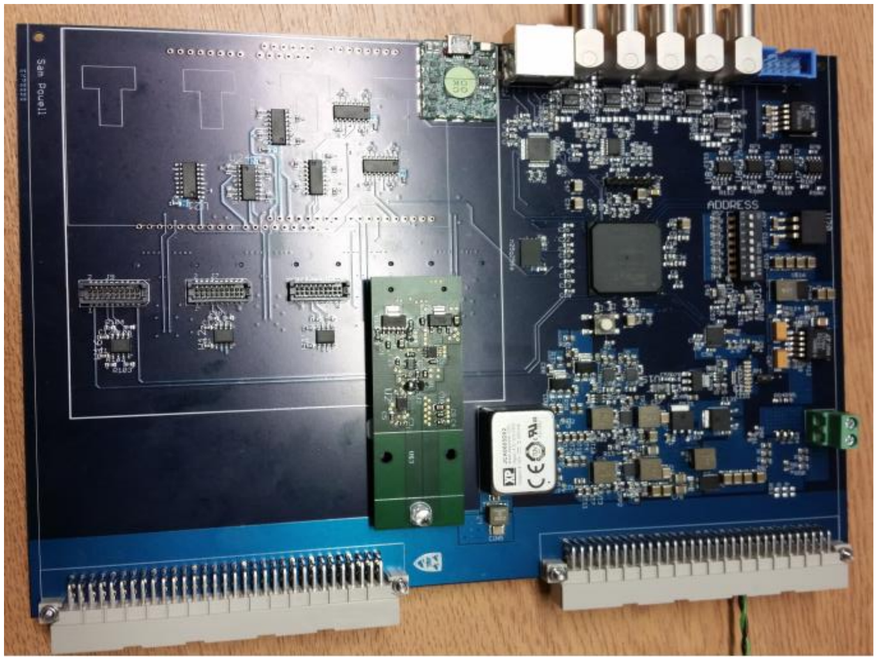

FIG. 150. Photograph of the LED driver system with mother board and daughter board that was deployed in Super-K in 2018.

side of neutrino beam running periods.

TC - They still have an impact on non-accelerator data. Is there a strategy for aborting a calibration in the event of a supernova, or are we just screwed if we are unlucky?

The calibration of the PMT timing requires a short duration light pulse of known origin and time. The integrated light injection system, from any given fibre, provides this but clearly cannot illuminate the entire PMT array at once. To minimise the number of fibres the optical diffuser is required to provide a wide opening angle to illuminate ≈1000 PMTs on the far side of the ID. The diffuser is designed to ensure that there is no time dependence as a function of angle. To achieve the overall calibration of the global time offset of the array, the PMTs must be illuminated by at least two fibres to allow the fibre times to be cross calibrated. In the ID we aim for a six-fold degeneracy of the PMT calibration fibre points to allow for improved cross calibration, and to provide redundancy against single point failures in the fibre system. This system will allow for the calibration of PMT timing, the dependence of time on charge and the PMT charge response.

The light injection system can also be used to measure optical absorption and scattering. While the basic elements of the system are the same as that used for PMT calibration, a number of changes are required, meaning that the fibres and diffusers used for these calibrations are different. These properties are required as a function of wavelength, so several LEDs will be used to provide light at six different wavelengths between 320nm and 500nm. To measure scattering the narrow beam from the collimator is required, and the scattering length is measured by monitoring the light detected by PMTs outside the narrow beam as a function of the path length. Optical absorption is measured by monitoring the light levels on given PMTs inside the optical beams. This uses the directly illuminated PMTs in the collimated beam and the bare fibre, as well as the wide-angle beams. This provides a variety of path lengths.

The light injectors must be constructed at multiple positions in the detector to allow for any variation of optical properties. For the ID we will require both horizontal and vertical injection positions, with horizontal positions at multiple levels to measure and monitor water properties as a function of depth. Light should be injected from multiple sides to provide redundancy of measurement and to test for detector variations. This distribution should also ensure that the 6-fold degeneracy of illumination required for the timing calibration is met. Each injection position will have a diffuser, collimator and bare fibre injector. The pulse by pulse monitoring of the calibration system is essential for this calibration as the light level at given PMTs is the key measurement of the system. The measured light level is a combination of absorption and PMT response as a function of angle, so several light paths and angles are required to decouple these, requiring a variety of diffuser points to be deployed.

Compared to the ID system, the OD has various disadvantages for the light injection system. Many light injection points are necessary to illuminate all the photosensors in the OD to an intensity level of a few 100PE, and it is difficult to build in any redundancy for cross-calibration and non-functional channels. There are photosensor support structures which can hinder the delivery of calibration light, particularly in the top and bottom endcaps. However, compared to the ID there is no need for multiple light injection types, with a diffuser being sufficient for all calibrations. Extrapolating from the Super-K OD calibration system, we think that $\approx$80 fibres will be required to achieve the same density of coverage on the cylindrical tank wall of Hyper-K, and $\approx$60 fibres each for the top and bottom endcaps. For the bottom endcap the fibres need to be $\approx$200m long, while for the other regions they can be $\approx$100m.

To calibrate the timing between the ID and OD a further fibre system is required. This makes use of two fibres of the same length connected to the same light source to inject light with the same timing properties into the ID and the OD. It is envisioned that this system would also use diffusers to inject light into both regions. Only a single injection system is required here as the OD calibration system will establish the overall OD timing calibration. We envisage the installation of three such systems to ensure degeneracy and failure tolerance.

C. D-T Generator

The ^{16}N nucleus decays via a $\beta\gamma$ process producing an electron with a β spectrum end point of 4.3MeV and a photon of 6.1MeV in the dominant decay branch. The overall decay spectrum across all branches is well understood and the half-life of ^{16}N is 7.13s. This makes the decay of ^{16}N an excellent candidate for a calibration source.

A commercial D-T generator produces 14.2MeV neutrons. These are energetic enough to produce ^{16}N by an (n,p) reaction on the ^{16}O in the water, for which the threshold is $\approx$ 11MeV. There are also (n,α) and (n,d) reactions on ^{16}O, but these result in the creation of stable isotopes, while the creation of ^{15}O by the (n,2n) reaction is energetically forbidden. The (n,p) reactions on ^{17}O and ^{18}O are suppressed by their low isotopic abundance and smaller reaction cross sections, with yields of ^{17}N and ^{18}N that are $< 10^{-4}$ of ^{16}N.

The deployment of the D-T generator will occur by lowering it into the water, and creating a triggered pulse of $\approx 3 \times 10^6$ neutrons. The source is then raised away from the cloud of ^{16}N that has been produced. The ^{16}N is then allowed to decay and the data recorded before the cycle is repeated with the generator moved to a different position. The process is summarised in figure 151. It allows sufficient ^{16}N to be collected at enough points across the detector for calibration of the detector energy scale as a function of position and direction. If there is no LINAC in the Hyper-K calibration system, then the ^{16}N from the D-T source will also be used to tune the PMT collection efficiency and fix the absolute energy scale.

D. Xenon Lamp

Hyper-K will use a commercial Auto Xeon lamp to provide a light source for some elements of the detector calibration. These will include the initial detector high voltage settings, and the measurement of detector asymmetries. Light pulses from the Xenon lamp are injected into the detector via an optical fibre which is connected to a scintillating ball in the centre of the detector. Additional fibres are used to monitor the intensity of the pulses using photodiodes.

The scintillator ball is a 5cm diameter acrylic ball containing 15ppm of POPOP as a wavelength shifter and 2000ppm of MgO as a diffuser to make the light emission from the ball as uniform as possible. The Super-K diffuser ball was measured to have an azimuthal asymmetry of less than 1% [?]. By mounting the fibre in either a horizontal or vertical direction the azimuthal symmetry of the ball can be used to first tune the PMT voltage settings and equalise the detector response during

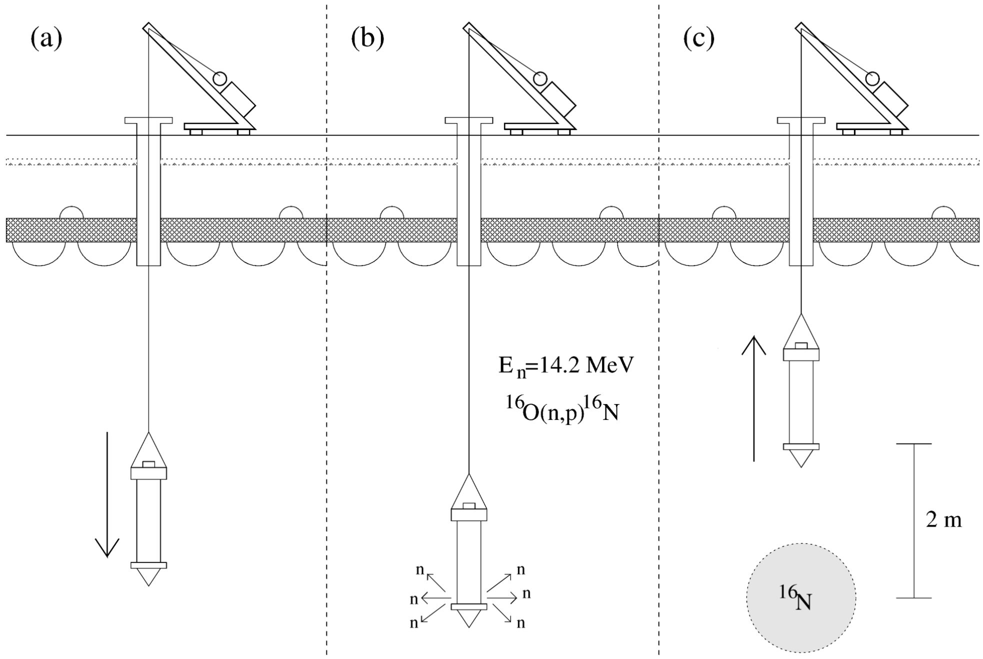

FIG. 151. An overview of D-T data-taking in Super-K. The D-T source is lowered into position, the neutron generator is fired, and then the source is raised 2m to remove it from the ^{16}N decay region. [**?**].

the detector commissioning phase. Later on this system can be used to monitor the uniformity of the response of the photosensor array.

E. Radioactive Sources

1. Californium/Nickel Source

A Cf/Ni source is used to produce 9 MeV of energy in the form of gammas. An average of 3.76 neutrons are produced by the spontaneous fission of ^{252}Cf with a half life of 2.56 years. The few MeV neutrons are thermalised and captured by an (n,γ) reaction on ^{58}Ni nuclei contained in a 6.5kg polyethylene ball. The decay of the excited ^{59}Ni occurs through 37 separate branches with the emission of 1 to 4 γ-rays with a total energy of $\approx$9 MeV. The fission products of the embedded ^{252}Cf can also penetrate the source and contribute to the Cherenkov light production. The additional contribution of these processes combined with the uncertainty in the knowledge of the Ni decay make the Cf/Ni source unsuitable for the calibration of the absolute energy scale. However, the Cf/Ni source provides a uniform, stable source of Cherenkov light at an intensity where all the hits are single photoelectrons. It can be used to calibrate the PMT gains, and to measure the 1PE charge distribution.

2. Americium/Beryllium Source

An Am/Be source is used as a neutron source to measure the neutron detection efficiency of Hyper-K. The Am/Be source will be encapsulated in acrylic for deployment into the tank. The neutron is produced by an (α,n) reaction on ^{9}Be following the decay of ^{241}Am. It is produced in association with a 4.44MeV photon due to the production of an excited state of ^{12}C in the reaction. This acts as a tag for the neutron, and can also be used to improve the energy calibration. The neutrons are produced with an energy up to 10MeV and thermalise in the water of Hyper-K. The capture of these neutrons on hydrogen creates a 2.2MeV photon that can be measured to determine the neutron detection efficiency. If Gadolinium is added to the water, at least half the captures will occur on Gd with the release of several photons with $\approx$8MeV total energy. The neutron detection efficiency becomes a combination of the Gd and H capture rates and the detector response. This needs to be calibrated by a tagged neutron source such as Am/Be.

F. Calibration Infrastructure

The preceding sections of this document have described a series of calibration sources, all of which must be deployed inside the Hyper-K detector for calibration. This requires deployment ports, a source deployment system and in some cases the source must interface with the electronics, DAQ and slow control systems.

Rather than construct a 3D deployment system Hyper-K will use a vertical deployment system that can be moved between calibration ports on the upper endcap. This allows full deployment of sources throughout the fiducial volume in a straightforward and well-defined way, due to the cylindrical nature of the detector. Multiple calibration ports will be distributed with a 3m spacing across two perpendicular axes of the endcap. At the edge of the fiducial volume it is important to increase the sampling so additional calibration ports are required every 50cm from the edge of the ID volume to 3m inside the photosensor array. This arrangement means that wherever we define the fiducial volume edge to be, it will be no more than 25cm from a given source deployment, allowing systematic uncertainties to be reduced.

The calibration ports must fit in the gaps between the upper endcap photosensors. This limits the size of the port, and thus the size of the calibration sources. In Super-K these ports are 22cm inner diameter and a similar size will be required in HyperK. The ports will be closed when not in use with a removable light-tight cover. The ports require sufficient connection points to allow the source deployment system to be attached, and must remain light-tight during the source deployment. To facilitate the deployment of larger devices a port of at least 75cm will be required in one location near the centre of the detector. This will require the removal of one PMT if all the 40,000 unit cells have been instrumented with 20" PMTs (or mPMTs).

The source deployment system will lower the calibration sources into the detector on a stainless steel attachment cord and accurately place them in the required position. The source deployment has several requirements:

- It must lower the source to a known location in the HK tank, taking into account the effect of the weight of the source on the stainless steel attachment cord.
- It must ensure that no slippage can occur in the deployment.
- It must ensure that the source cannot become disconnected from the attachment cord during deployment and lost in the detector.
- It must be able to deploy any wires, fibre optics or umbilical cords that the source requires.
- It must allow the safe retrieval of the source in the case of a breakdown, power cut or other emergency.
- It must attach to the deployment plate and provide a light-tight seal to the detector.
- It must be free of oil and other lubricants to ensure the cleanliness of the detector.

The prototype deployment system for Hyper-K is the auto-deployment system that was installed in Super-K during 2018. A picture of this system is shown in figure 152.

Any source deployed into the detector produces a signal that must be able to be read out by the Hyper-K electronics, and included in an event for later analysis. The slow control must also be designed to control the deployment system and any calibration source settings that are required.

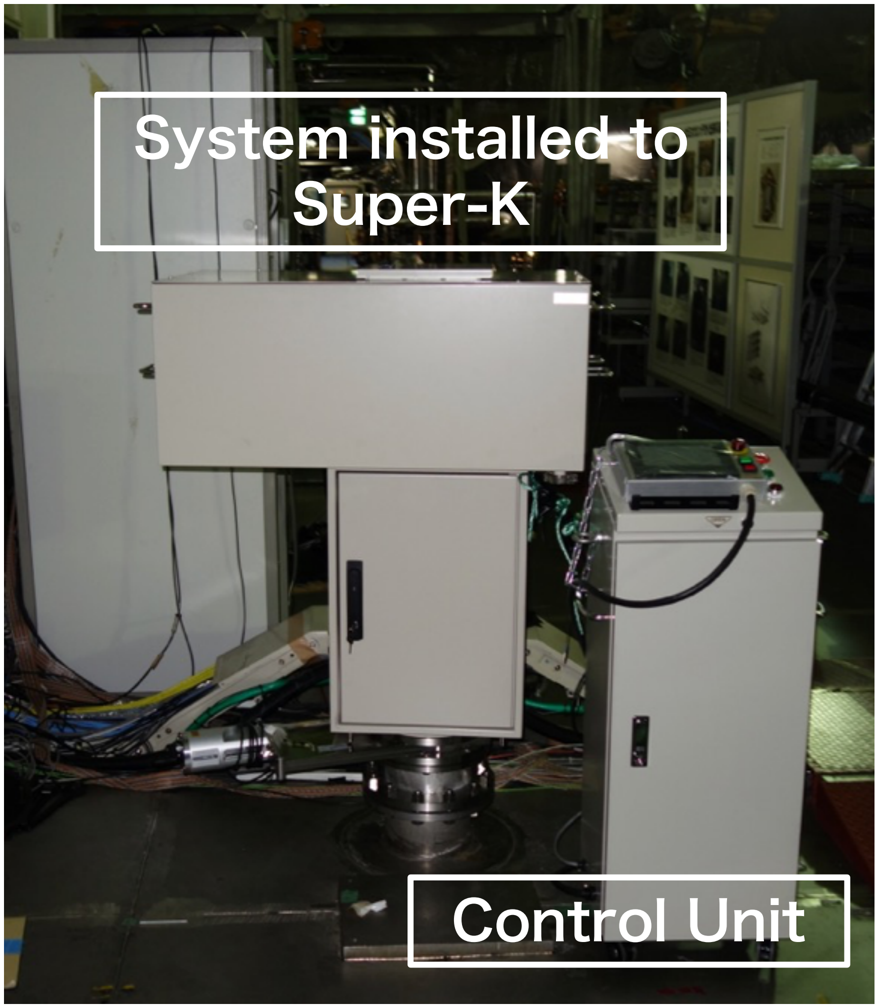

FIG. 152. Photograph of the auto-deployment system installed in SuperK in 2018.

III.12. PRE-CALIBRATION OF PHOTOSENSORS

A. Pre-calibration of ID photosensors

Before the installation of the 20" ID PMTs into the Hyper-K tank an extensive programme of pre-calibration is required. This starts with a basic set of tests that are applied to every PMT to ensure that they operate correctly. The signal shape, gain and dark rate are checked quickly by an automated program that confirms the signal is there, and determines the high voltage to get the typical gain. For the signal check, a dark box for a single photodetector is sufficient with a high voltage power supply, readout electronics, and a pulsed point light source.

For approximately 2% of the PMTs we will measure the quantum efficiency and characterise the PMT gain as a function of high voltage. To perform these measurements, a dark room with geomagnetic compensation is required to store about 16 photodetectors. We will need some Hyper-K readout electronics and an automated data acquisition system. A pulsed light source with <0.2ns pulse width is uniformly diffused over the whole photodetector surface. A database is prepared containing the results of the pre-calibration and evaluation, as well as the data sheet from the manufacturer. A significant shift load is expected to be needed to run this pre-calibration system.

During installation this 2% subset of pre-calibrated PMTs are distributed uniformly inside the detector, and used as references to tune the individual HV settings of all the other PMTs during the initial turn on of Hyper-K to ensure that they are operating with the same gain. The pre-calibrated PMTs are also used to more generally understand the detector response.

For a smaller subset of approximately 0.5% of the PMTs we will measure the gain, the timing performance and the quantum efficiency as a function of the location and angle of the light incident on the PMT front face, and as a function of the residual magnetic field. The 20" PMTs that are used in Hyper-K are known to exhibit large changes in performance as a function of these parameters. This impacts on the detector reconstruction and must be understood. The effect of the PMT covers and light collection system, if present, will also be measured as part of this pre-calibration.

The measurement setup in laboratory B of the Kamioka mine allows to measure the properties of a PMT as a function of the magnetic field and hit position of the photon on the PMT. It is composed of a dark room located inside a system of coils, which allows control of the magnetic field along three perpendicular directions. In the current system, the field can take any value between −500mG and +500mG on each axis. The PMT is installed inside the dark room, and 24 fibres are attached to its surface to inject light from a diode at different positions. The difference of transmission through the fibres has been measured and is corrected for in the analysis. A 1" PMT is used to monitor the variation of the intensity of the LED light. The system is shown in figure 153.

TC - This reads as if the plan to use this laboratory in the Mozumi mine for Hyper-K. Presumably we need to build the equivalent facility inside the Tochibora mine.

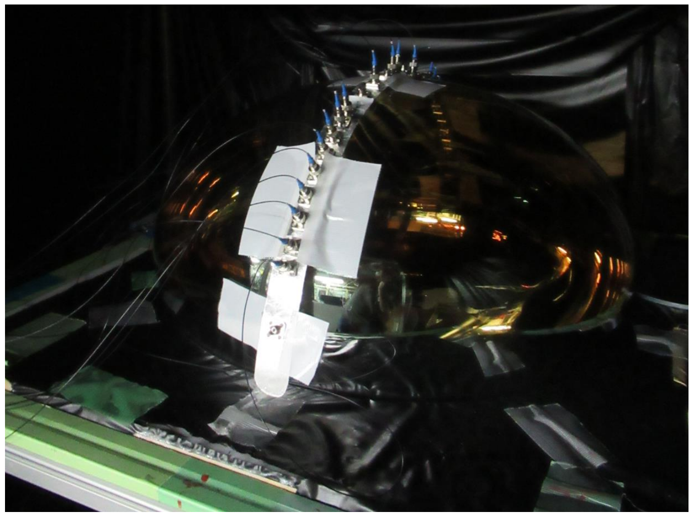

FIG. 153. Photograph of the PMT testing system in Kamioka.

This setup has been used to characterize the properties of the 20" candidate PMTs for Hyper-K, including the Hamamatsu R12860 B&L PMT and several different versions of the MCP PMT. The variation of the gain as a function of the photon hit position in the absence of a magnetic field for the MCP PMT PC1804-2205 is shown in Figure 154.

A prototype of the automated calibration system was constructed in 2018 and used for the 140 B&L PMTs that have now been installed in Super-K. The dark room can store 6 PMTs at once, and it took one day for one cycle of measurements including the waiting time for stabilization. Apart from an initial screening of PMTs based on information provided by the manufacturer, the selection criteria from the pre-calibration are summarized in Table XLV.

A PMT test facility (PTF) has also been constructed at TRIUMF to characterises the PMTs that will be used in Hyper-K. Figure 156 shows a photograph and schematic diagram of the PTF. It has two manipulator arms (gantries) which are motorized and move independently in the x-, y-, z-direction, and rotate or tilt. Each gantry is equipped with an optical box that contains a light source with a chosen wavelength, a monitor PMT to measure the intensity of the injected light and a receiver PMT which is used for measurement of reflectivity. The response of the PMT,

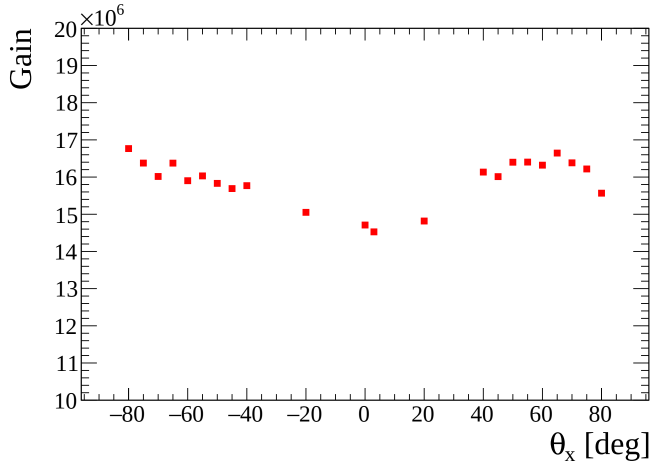

FIG. 154. Measurement of the MCP PMT gain as a function of position made with the system in Kamioka.

Requirements	Unit	Min.	Max.	Conditions
Bias voltage	V	1,500	2,350	Gain at 10^7
Dark rate	kHz	2	30	After stabilization at room temperature
Transit time spread	nsec	1	4	FWHM around 1/4–1/6 PE
Single photon resolution	%	20	70	σ/1PE
Afterpulse rate	%	–	10	Multi-hits 0.5–40μs after main pulse
Maximum output	V	3	12	With 20m cable

TABLE XLV. Selection criteria for the pre-calibration of 140 B&L PMTs for Super-K in 2018.

and any additional light collection device, can be measured across the full 2-dimensional surface. The PTF is equipped with a water purification system which generates ultra-pure water, and can measure PMT responses underwater. Magnetic shielding and Helmholtz coils are used to cancel the Earth's magnetic field, and the residual field is monitored throughout the PTF volume, so the PMT performance as a function of magnetic field can also be measured.

Figure 155 shows the gain of an SK PMT from the first series of measurements at the PTF. Upgrades to ensure optimal performance of the PTF are ongoing prior to the start of the characterisation of HyperK PMTs in 2022.

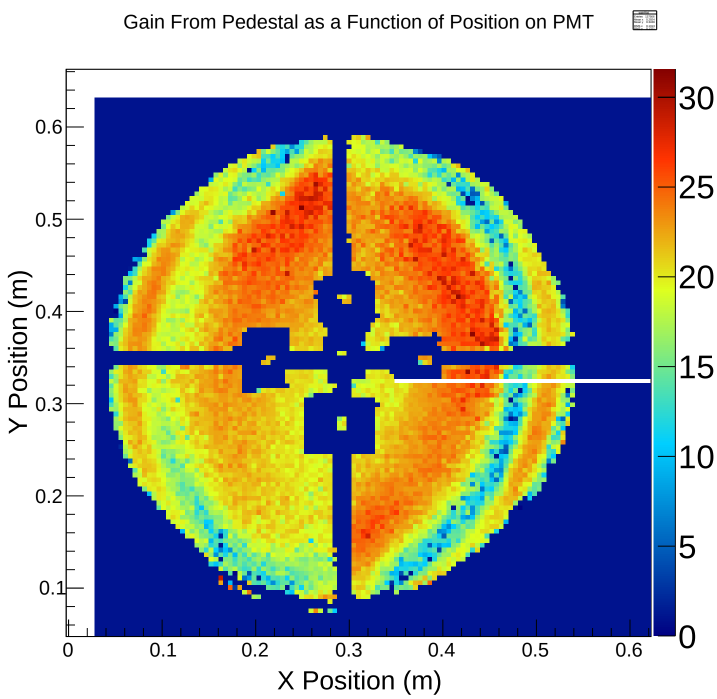

FIG. 155. SK-PMT gain distribution under fully compensated field. The low gain valley comes from the photoelectrons escaping the first stage of the venetian blind dynode. Also visible in the figure is the effect of adhesive tape applied to the PMT to allow precise determination of position and orientation of the system.

B. Pre-calibration of OD photosensors

The 3" PMTs in the OD must also be pre-calibrated, but here the performance requirements are less strict, since timing and charge resolution are not as important in a veto system where the Cherenkov rings are not reconstructed. The 3" PMTs are much less sensitive to magnetic fields, so no geomagnetic compensation coils are needed during pre-calibration.

The first stage is once again an operational test of every PMT, in which the signal is established at the nominal gain, and the dark count rate is measured after stabilization. We also need to check that signals are seen from all the wavelength shifting plates after they have been mechanically attached to the PMTs. For this purpose we need a quick scan of a few points on the plate surface with a collimated light source (UV LED).

The second stage of more detailed characterisation will only be applied to a small subset of the PMTs, approximately 0.1%. The gain and dark count rate as a function of high voltage will be measured, together with the charge and timing resolution. There will also be a full scan of both the PMT and the plate with a light source that can be varied in both position and angle. Ideally this would be done underwater.

C. Pre-calibration of mPMTs

There needs to be a pre-calibration of the mPMTs both for the IWCD, and for the Hyper-K far detector, if mPMTs are installed in it. This will take place after the individual PMTs have been tested, and the modules have been assembled. For the IWCD a full mapping of the response of each mPMT module will be made starting in 2020, since we would like to have a very good understanding of the detector performance in order to reduce systematic errors. Measurements to be made include the gain as a function of high voltage, dark count rate, quantum efficiency, timing and charge resolution. We will also do a full scan over the whole upper surface of the module to measure the photon detection efficiency, including the light collectors, and the reflectivity of all the materials. These measurements will use the PTF facility at TRIUMF (Figure 156), where improvements will continue to be made during the early stages of the mPMT pre-calibration.

For the modules to be used in Hyper-K itself it is not feasible to do such detailed testing of all the modules, so we will limit the full scan to a sample of 1–2% of the modules. This part of the pre-calibration will be done at both TRIUMF and Kamioka, and perhaps at other production sites as well.

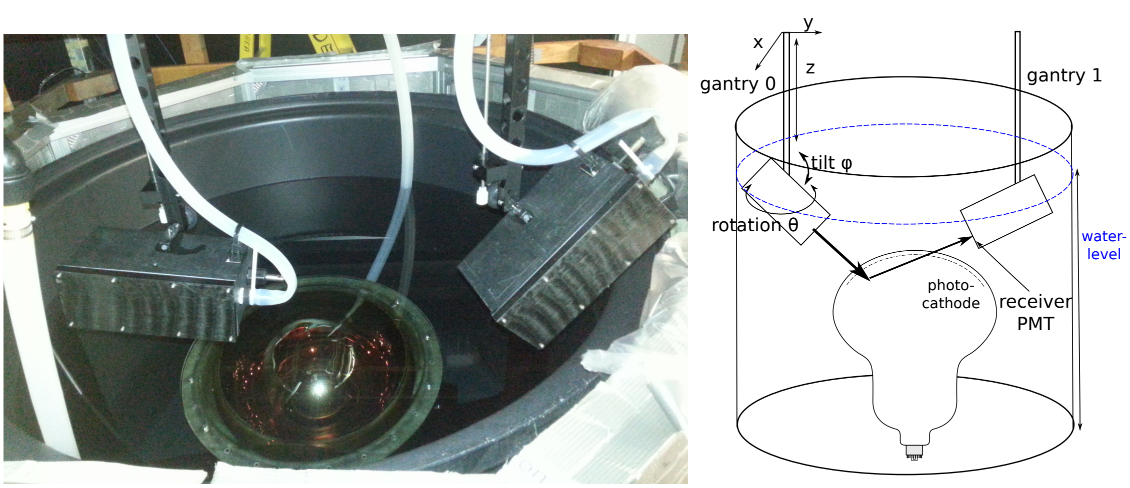

FIG. 156. Photograph (left) and schematic diagram (right) of the photosensor test facility at TRIUMF.

III.13. INSTALLATION WORK IN TANK

Add a general overview of the installation work in the tank.

A. Installation of ID photosensors

The full inner detector system is constructed by installing individual photosensors into the support structure after they have been assembled with their covers and light collection system (if present). Transfer and mounting jigs need to be provided so that two people can transport the heavy PMT and photosensor with a maximum load of 20kg/person. Care needs to be taken to avoid dropping or damaging the PMT at this stage. The procedure for installing mPMT modules, if present, will be similar. Both the PMTs and mPMTS will be installed individually following the pre-callibration described in the previous section.

The installation procedure for mounting the photosensors into the support structure has still to be worked out. There need to be different procedures for the top endcap, the barrel, and the bottom endcap.

TC - I think the installation of the PMTs has to take place either in the bottom of the tank or on top of the tank, with sections of the support structure + PMTs subsequently raised or lowered into position with a crane. In SK the sections of the assembly were $4(\phi)\times 3(z)$ *unit cells, and entire barrel columns were assembled at the bottom of the tank and raised into position. Depending on the final HK cavern dimensions it may not be possible to assemble a complete column at the bottom of the tank. In any case we should consider larger assembly sections for HK, matched to the electronic readout modularity of 24 channels, so either* $8(\phi)\times 6(z)$ *for 20k PMTs, or* $6(\phi)\times 4(z)$ *for 40k PMTs.*

It is estimated that a mounting speed of 200PMTs/day could be achieved with double shift operations, i.e. that 20k(40k) PMTs could be installed within 4(8)months, but the feasibility of this rate has yet to be demonstrated.

B. Separation of Inner and Outer Detectors

TC - significantly rewritten to clarify requirements and current design

A separation on the inner detector (ID) wall and perhaps on the outer detector (OD) wall is required for the following reasons:

- The ID wall should suppress reflections back into the ID water as much as possible.

- Optical separation is needed to prevent photons from the ID being seen by the OD and used as a veto. An initial estimate is that we require < 2 hits of the OD photosensors within five meters of an ID photosensor if it detects 1,000 photoelectrons. This "crosstalk" requirement is currently under study in Super-K.

- It is desirable, but not essential, to prevent photons from the OD being seen by the ID photosensors, where they would simply add to the background. The optical separation described above should do this anyway.

- The OD wall should enhance reflections, to allow for photons that miss the PMTs and wavelength shifting plates to do multiple reflections across the OD volume. Since the detection efficiency and timing of these multiply reflected photons is not very good this is not a strong requirement.

- The water flow system is designed to provide separate inputs and outputs for the ID and OD volumes. The flow in the outer volume is used to remove radon and other backgrounds before they reach the ID. It is desirable to avoid mixing these flows as much as possible. Whether the separation needs to be completely "hermetic" is still under discussion.

- If gadolinium is added to the water it may be desirable to add it just to the ID, and to prevent it entering the OD as much as possible.

If there are "hermetic" boundaries at both the ID and OD walls a separate water flow would be need for the dead space between them to cool the electronics. This is an argument against making two hermetic seals, i.e. leaving the OD side partly open so the OD flow also covers the dead region. If there is a hermetic separation at the ID (or OD) wall then the pressure differential across the wall must be $<$0.5kPa.

1. Inner Detector Wall

The parts of the detector wall not occupied by the photosensors are covered with black sheets. These would either be matched to the individual unit cells, to make installation easier, or they could be designed as corner pieces covering four quadrants of neighbouring unit cells. In either case 40k such sheets are required, and there need to be connectors between the sheets, and connectors between the sheets and the covers of the PMTs. There also need to be stoppers to hold the black sheet on the edges of the acrylic window. Additional black sheets will be needed in the corners of the tank, and around the various holes for water, cables and calibration systems. To make the ID wall "hermetic" the connections between the sheets and between the sheets and the covers would need to be filled with a sealant.

Figure 157 illustrates one black sheet set at the corners of four photodetector covers, and the required connectors and stoppers. The photodetector cover has an extension to support the black sheet on a flat surface, and each black sheet will be connected to its neighbour without gaps using the connectors. Differences in the distances between the four covers can be adjusted by little long black sheets overlapped with the main sheet and some extra connectors.

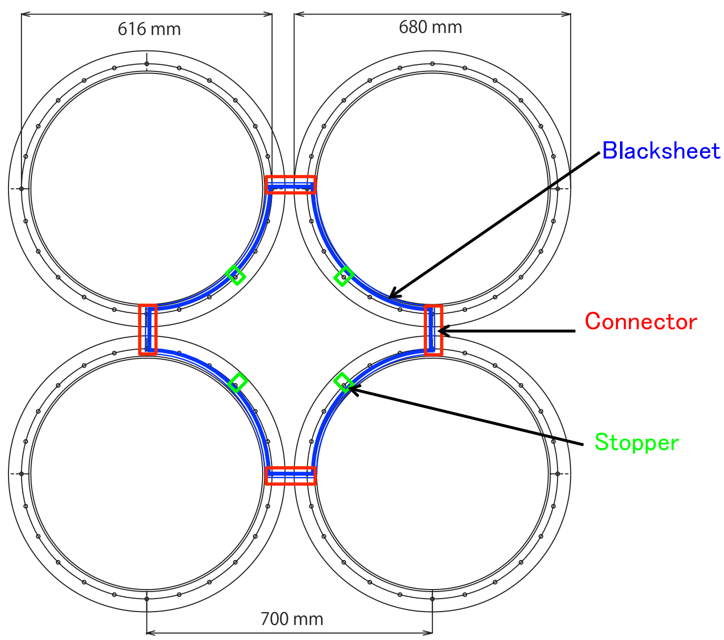

FIG. 157. A single black sheet on flanges of the photodetector covers (black circles) viewed from the photodetection side. The four edges of the sheet are connected to other sheets using the connectors. The stoppers are for fixing the spacing between the sheet and the flange of the photodetector cover.

In Super-K these black sheets were simply made of Tyvek. A more robust solution proposed for Hyper-K is to us a PET (polyethyleneterephthalate) plastic with a thickness around 100μm and a black colour, e.g. Toray lumirror X30 #100. The material should be tested before use to make sure it satisfies the requirements for radioactive backgrounds and compatibility with ultra-pure water (see Sections III.4 and III.6 A).

2. Outer Detector Wall

In Super-K the outer wall is covered in two-sided white/black Tyvek, providing a further optical barrier to ID photons and reflecting back OD photons. In our tests we have shown that placing a reflector behind the wavelength shifting plates does not significantly enhance the performance, since photons that hit the plate have already been absorbed. It may be useful to put a reflective surface over the 80% of the wall that is not covered by the plates, but this has to be studied further. As with the ID wall we are considering more robust plastic materials for these sheets. For any such sheets a black inner side adds a further barrier against ID photons entering the OD.

As mentioned in the requirements, we will deliberately not make the OD wall hermetic, but allow for significant gaps between the plates and the sheets. This is to facilitate water flow between the OD and the dead region.

C. Outer Detector Installation

The OD photosensor and its wavelength shifting plate are treated as a single mechanical assembly for installation purposes. As with the ID we need to prepare jigs for handling these and to develop mounting procedures, although in this case the weight of the assembly is much less and could be managed by one person. The OD photosensors will be mounted towards the corners of their unit cells to avoid the covers of the ID photosensors. We need to design an attachment between the OD assembly and the photosensor support structure. The plates will occupy space on the outside of the OD wall in four quadrants of neighbouring unit cells.

As mentioned in the previous section we may add reflective sheets between the plates which would also need to be attached to the photosensor support structure, or to the plates. The final part of the OD installation is the addition of reflective sheets (Tyvek?) on the outer tank wall, and of vertical reflective sheets at the top and bottom of the barrel to separate the OD volume into barrel and endcap parts. This separation was found to be helpful in understanding corner muon events in Super-K.

D. Cabling: Photosensors to Frontend Electronics

Determine how to run the cable from each PMT to the front-end electronics module. Define the type of cable and its weight. Devise mounting methods for the cables and connectors.

E. Cabling: Frontend Electronics to Outside of Tank

Determine the way to run the cable from each front-end electronics module to the outside of the tank. Define the type of cable and its weight. Devise mounting methods for the cables and connectors.

Part IV

Software and Computing

The Hyper-K software system is designed around the following principles:

- Adaptable. The Hyper-K experiment is expected to run for more than a decade. This period typically spans more than one generation of software and infrastructure. The Hyper-K offline system is being designed to be flexible enough to accommodate changes in tools or infrastructures.
- Reliable. Each component needs to demonstrate it's reliability by exhibiting well defined behaviour on control samples.
- Understandable. Documentation on what the component does, what it's dependencies are as well as test samples and outputs are essential in being able to use it successfully.
- Low overhead. The management and maintenance should be as automated as possible to free collaborators to focus on the challenge of extracting the high-quality physics measurements.

The software consists of a collection of loosely-coupled packages, some of which are open-source and some of which are specific to Hyper-K. The distributed code management system Git [?] is used to manage the software. Each package is hosted on a third-party central repository (`https://github.com/`) that provides distributed access to the packages. The distributed nature of the code management allows researchers the possibility to develop the software independently without impacting other researchers. The loose-coupling between packages allows those that reach their end of life to be replaced by better alternatives with minimal impact on the rest of the system. Where possible standard particle physics software libraries are used to reduce the burden of support of experiment-specific code. The working language for the Hyper-K software packages is C++, with the output files being written in ROOT [?] format.

The flow for the simulation is as follows: The event topologies are generated by a neutrino interaction package(GENIE [?] and NEUT [?], for example), and modeled by a Monte Carlo detector response code called WCSim [?]. The event information is reconstructed using either BONSAI [?] (for low energy events) or fiTQun (for high energy events) [?]. This is shown schematically in Figure 158. These packages will be described in more detail in the next Sections.

An online workbook is also maintained to provide higher-level documentation on overall procedures and information for new users of the software and developers. An overall software control package allows for the fully automated download, compilation and running of the software, based on user requests.

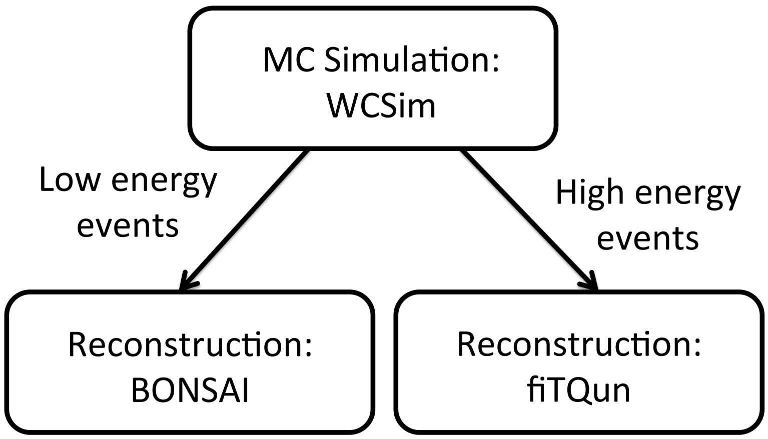

FIG. 158. Flowchart of the simulation process.

IV.1. SIMULATION

A. Simulation Software

The Water Cherenkov Simulation (WCSim) package is a flexible, Geant4-based code that is designed to simulate the geometry and physics response of user-defined water Cherenkov detector configurations. WCSim is an open-source code and is available for download at `https://github.com/WCSim/WCSim`. A more detailed description of the software, as well as specific cases of how to use it can be found on the wiki page `https://github.com/WCSim/WCSim/wiki`.

The final performance of the Hyper-Kamiokande detector depends on the detector geometry, the type of photodetectors, and the photocoverage that will be used. WCSim takes these variables as inputs and simulates the detector response, which can then be used to determine the physics potential. WCSim users specify the type of photodetectors, the number of photodetectors, the detector diameter and radius, and whether the water should be doped with gadolinium. The general work flow of the code is shown in Figure 159.

For this report, the relevant photodetectors in WCSim are the R3600 20" diameter PMTs, the R12850 20" and 12" diameter box and line photodetectors, and the multi-PMTs, which consist of

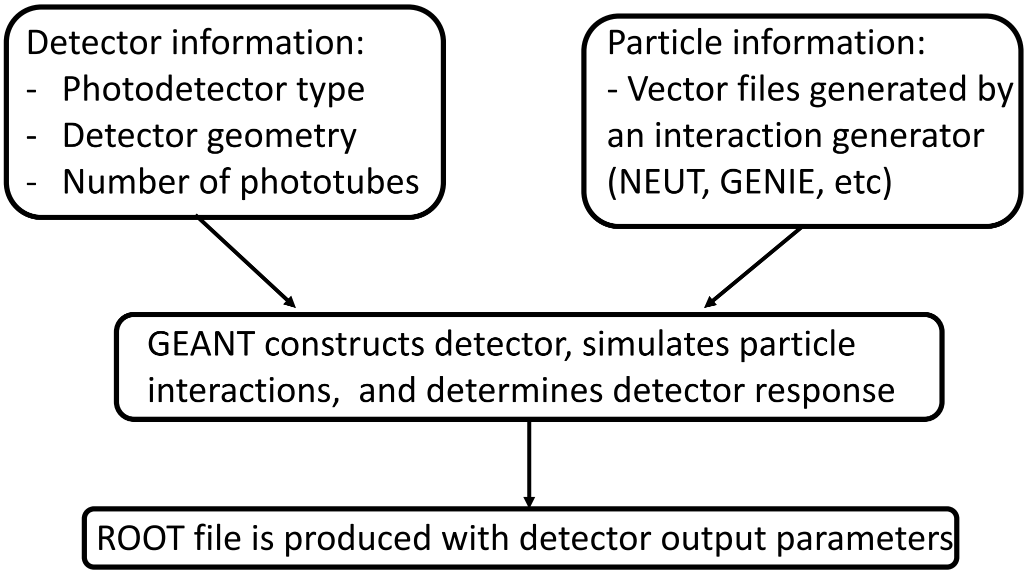

FIG. 159. A high-level schematic of the work flow of WCSim.

nineteen 3-inch R12199-02 PMTs clustered together (see Section III.8 for further details). Photodetector parameters in the simulation include the timing resolution, dark noise rate, and the overall efficiency for a photon to register a charge (including the quantum efficiency, collection efficiency, and hit efficiency. For the R3600 PMTs, the parameters were taken from the Super-Kamiokande simulation code SKDETSIM *[ref?]*. The parameters for the R12850 are taken from measurements. Some higher-level photodetector effects such as after-pulsing are not currently simulated in WCSim, though this is a planned upgrade for a future releases.

The detailed work flow from particle creation through to the recording of event information is shown in Figure 160. Geant4 [**?**] is used to track the particles as they pass through the detector and compute the final deposited energy. Particles that reach the photodetector glass and pass the quantum efficiency and collection efficiency cuts are registered as a hit. The hits are then digitized based on the SK-I electronics scheme, though the code has the flexibility for users to include their own custom electronics configurations.

The output for the WCSim code includes both the raw hit and the digitized information. The

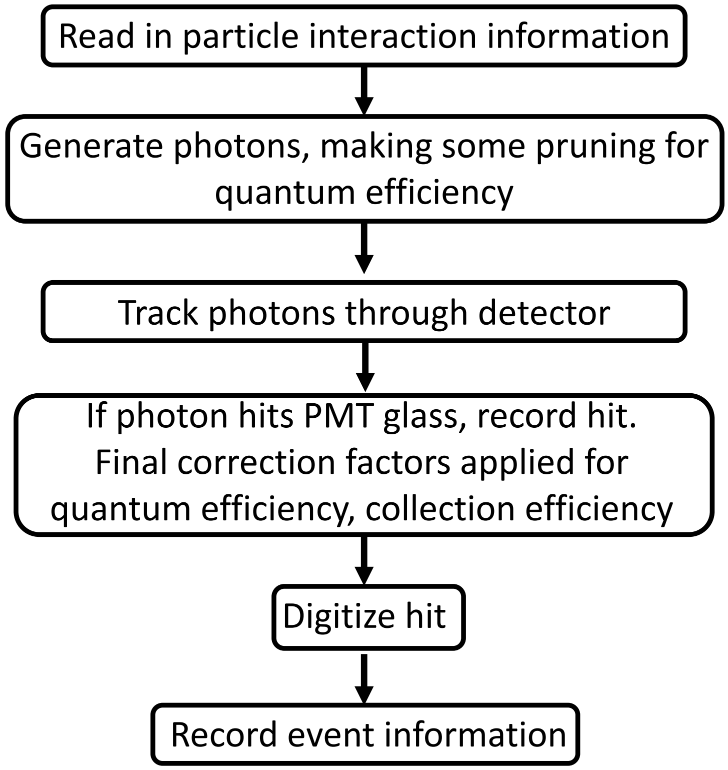

FIG. 160. The work flow of particle creation, propagation, and recording in WCSim.

raw hit information includes which tubes were hit and how many times each tube was hit. The digitized information includes the number of hits in a trigger window, as well as the charge and time of the hit tubes. WCSim output files can be used for event reconstruction by fiTQun or BONSAI, which are described in the following subsections. Geant4 visualization tools can be used to display the detector geometry and particle tracks. Figure 161 is a rendering of one of the proposed Hyper-K tanks. Figure 162 shows an example of an event display for an electron and for a muon, each with 1 GeV kinetic energy.

B. Far Detector Simulation Studies

Figure 163 shows how the flexibility of WCSim can be used to explore different detector configurations. Here, the total charge distribution for electrons and muons at several momenta in the Hyper-Kamiokande detector with two different photocoverage options are shown. RMS divided by mean charge is plotted in Figure 164 indicating better resolution with 40% photocoverage than with

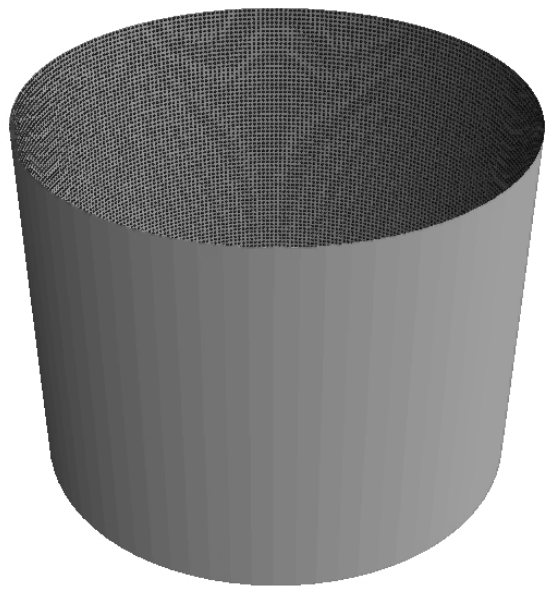

FIG. 161. Geant4 visualization of the Hyper-Kamiokande detector configuration. The top cap of the detector has been removed for visualization purposes. Phototubes are shown in black, while the walls of the detector are shown in grey.

14% photocoverage. For lower energy particles, the resolution can be approximated using nhits (the number of phototubes that register a hit). The nhit distribution for both 14% photocoverage and 40% photocoverage are shown in Figure 165.

C. Near Detector Simulation Studies

This part should focus onthe WCSimulation for E61. The ND280 simulation should not be discussed in this section, but in the introduction a reference to the ND280 should be cited. Describes detector simulation studies for the near detectors. In particular this is a place to put studies relevant to technical decisions about the IWCD design.

It is assumed that simulation of the ND detectors has already been done for T2K2. Do we need to report any further work on this in this document?

Note that physics studies are described in a separate part of this document.

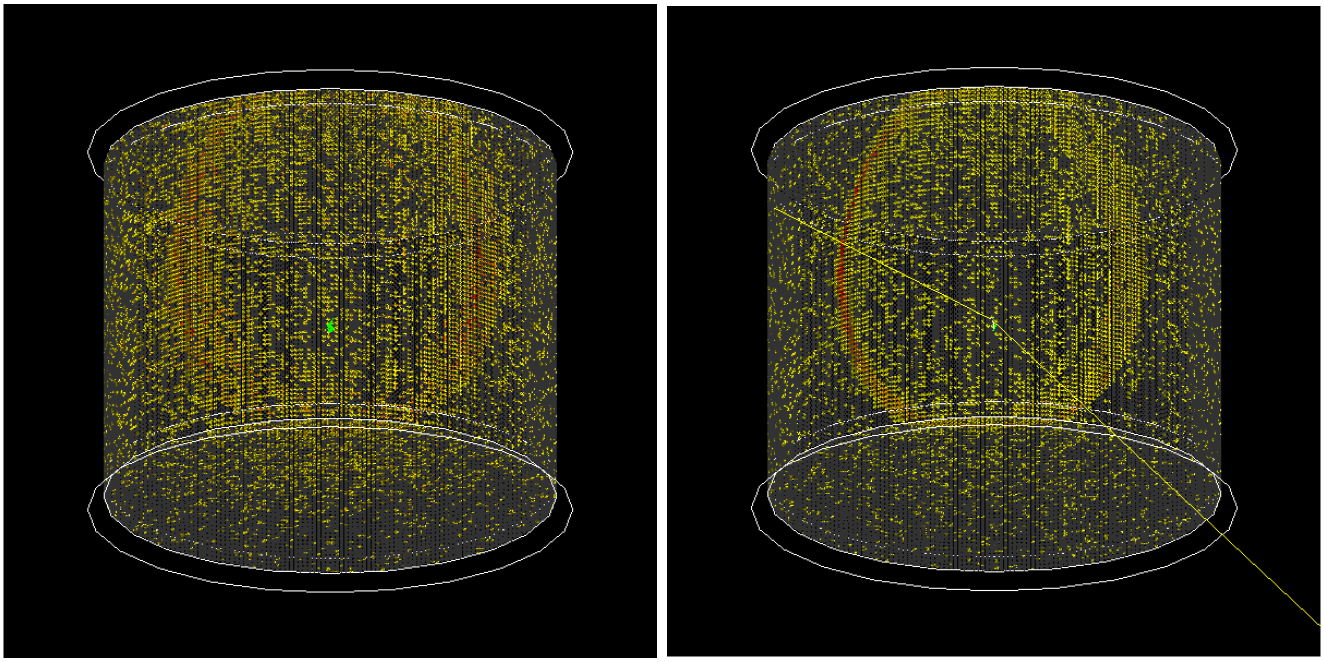

FIG. 162. Event displays in the HK detector for a 1 GeV electron (left) and a 1 GeV muon (right).

IV.2. RECONSTRUCTION

A. High Energy Reconstruction

The FiTQun algorithm will be used for reconstruction of events above a few tens of MeV in both the far detector and the IWCD. This algorithm is based on a maximum likelihood estimation approach, where for a given event hypothesis hit probabilities as well as total charges and hit times are predicted for each photosensor in the detector. Probability distribution functions capturing the time and charge response of the photosensors are then used to calculate the likelihood for each event hypothesis. The algorithm is based on the MiniBooNE reconstruction described in detail in [?].

Event hypotheses range from single rings above Cherenkov threshold, such as a single elecron or a single muon, to complex hypotheses comprising several rings arising for example, from neutral pion decays, hadronically scattered charged pions, or neutrino interactions with several mesons in

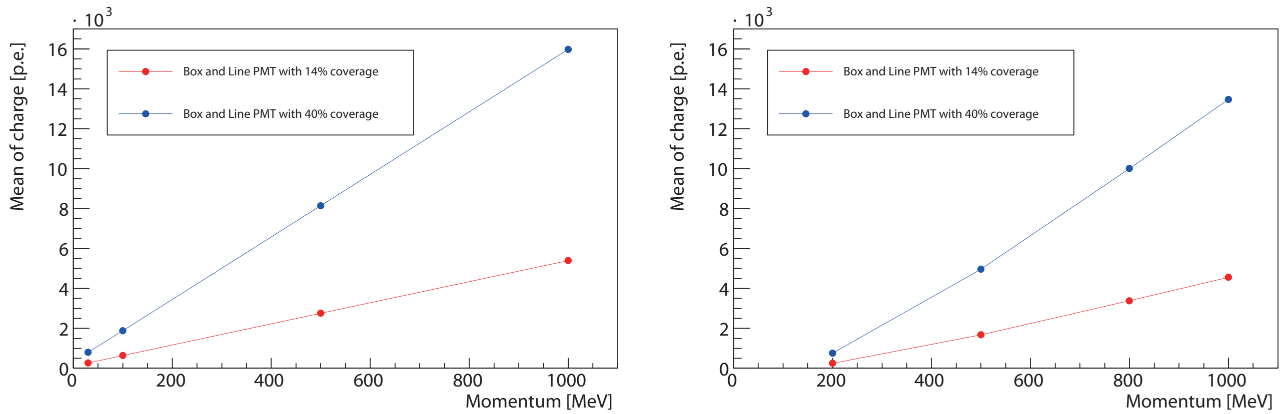

FIG. 163. Total charge distributions for electrons (left) and muons (right) with several momenta in the Hyper-K detector. The red line corresponds to 14% photocoverage, while the blue line corresponds to 40% photocoverage.

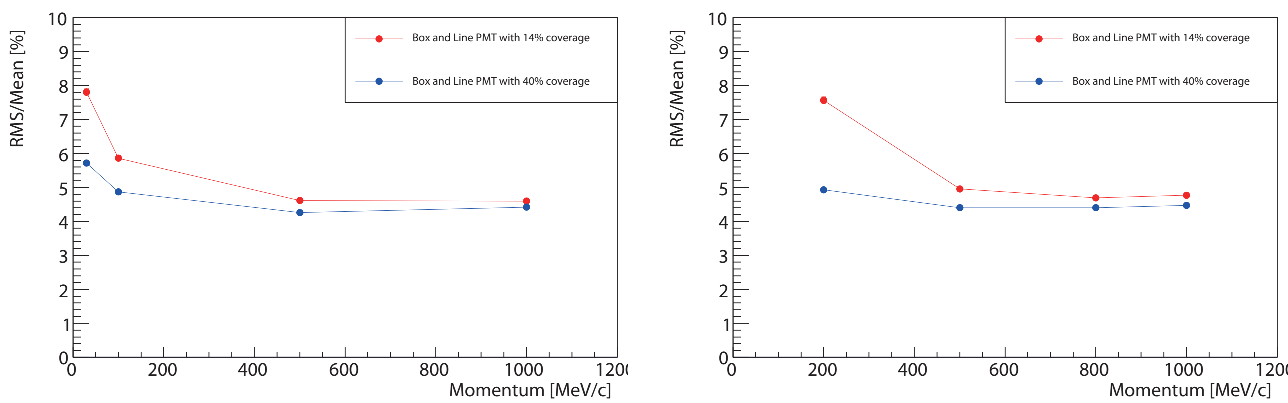

FIG. 164. RMS/Total charge distributions for electrons (left) and muons (right) with several momenta. The red line corresponds to the configuration with 14% photocoverage, while the blue line corresponds to the configuration with 40% photocoverage.

the final state. A generic multiple-ring algorithm exists where rings are sequentially added to the best-fit hypothesis with the sequence terminating when no improvement is achieved by adding a further ring or when the maximum of six rings is reached.

To discriminate between event hypotheses, likelihood ratios are formed between them and a cut point is chosen that optimally separates event categories. Auxilliary variables are often used in addition to the likelihood ratio, such as the reconstructed momentum of the rings or the recon-

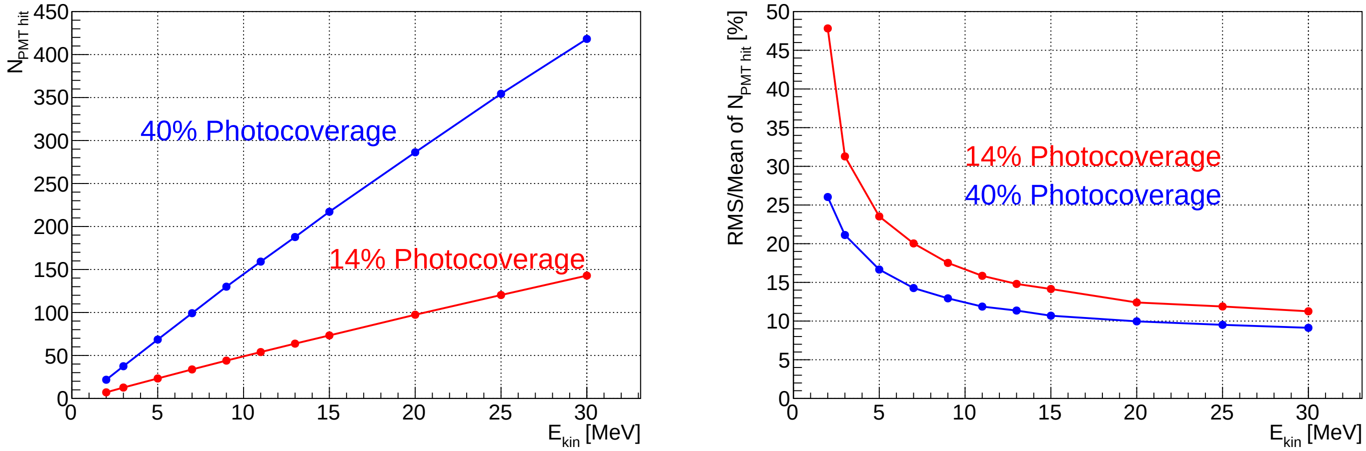

FIG. 165. Expected number of PMT hits ($N_{PMThits}$) and the RMS of the N_{PMThit} distributions. WCsim is used for simulating the injection of electrons with several values of kinetic energy (E_{kin}). The initial position is uniformly distributed inside the fiducial volume (>2 m from inner detector wall). The red line corresponds to the 14% photocoverage configuration, while the blue line corresponds to the configuration with 40% photocoverage.

structed neutral pion mass.

The most recent neutrino oscillation results from T2K[] use FiTQun for event selection and reconstruction. Studies are ongoing for FiTQun-based Super-K atmospheric neutrino oscillation analyses, where the improved reconstruction might allow for relaxing the fiducial volume criterion leading to a significant increase in statistics. The use of FiTQun is also being studied for proton decay searches. In particular, the efficiency for detecting $p \to K^+\bar{\nu}$ events is expected to significantly improve.

B. Low Energy Reconstruction

For event reconstruction at low energy, i.e. few MeV - few tens MeV, a reconstruction algorithm BONSAI (Branch Optimization Navigating Successive Annealing Iterations) is supplied for Hyper-Kamiokande. BONSAI was originally developed for Super-Kamiokande [**?**] and written in C++. It has been used for the low energy physics analysis of SK-I to SK-IV. In the low energy region, most of the photosensor signals are single photon hits. BONSAI uses this relative hit time information to reconstruct the position of the Cherenkov light source, i.e. the position of low energy event. For Hyper-K analysis, a wrapper library (libWCsimBonsai) is supplied for ROOT environment.

1. Vertex reconstruction

For the vertex reconstruction, BONSAI performs a maximum likelihood fit using the photosensor hit timing residuals. This likelihood fit is done for the Cherenkov signal as well as the dark noise background for each vertex hypothesis. The likelihood of the selected hypothesis is compared to the likelihood of a hypothesis in an area nearby. Highly ranked hypotheses and new points in the likelihood will survive this step. Finally, after several iterations, the hypothesis with the largest likelihood is chosen as the reconstructed vertex.

The vertex goodness criterion testing the time residual distribution is defined as follows:

$$g(\vec{v}) = \sum_{i=1}^{N} w_i \exp -0.5(t_i - |\vec{x_i} - \vec{v}|/c_{wat})/\sigma)^2 \tag{1}$$

where t_i are the measured PMT hit times, $\vec{x_i}$ the photosensor locations, $\vec{v}$ is reconstructed event vertex, σ is the effective timing resolution expected for Cherenkov events (total of photosensor and DAQ resolution). c_{wat} is the group speed of light in the water, i.e. c/n with the speed of light in vacuum c and refractive index n. ω_i are Gaussian hit weights also based on the hit time residuals, but with a much wider effective time resolution. The weights reduces the dark noise contamination of the Cherenkov light. A result of vertex reconstruction performance study with BONSAI and WCSim can be found in the figure 166. More Cherenkov photons could be detected with new photosensors for Hyper-K and it improves the reconstruction results, comparing to those of Super-K Though, at same time, the random photosensor signals caused by their dark pulse can spoil the merit. So reducing dark pulse is a crucial factor to improve the low energy event detection. Many efforts for the dark pulse reduction (**??**) and improvements of the softwares are being continued.

2. Energy and direction reconstruction

BONSAI and its related subroutines also determine the energy and the event direction reconstruction. Because most of the photosensor signals consist of single photon hits at low energy below few tens MeV, the total number of photosensor hits is the leading parameter for reconstructing the energy of events. First, time-of-flight values are subtracted from each of the hit timing values based on the position of each photosensor and the result of the BONSAI vertex reconstruction. Next, the number of photosensor hits around the expected event timing is calculated, considering its cross-section and the local photocoverage with neighboring photosensors. Finally, the number

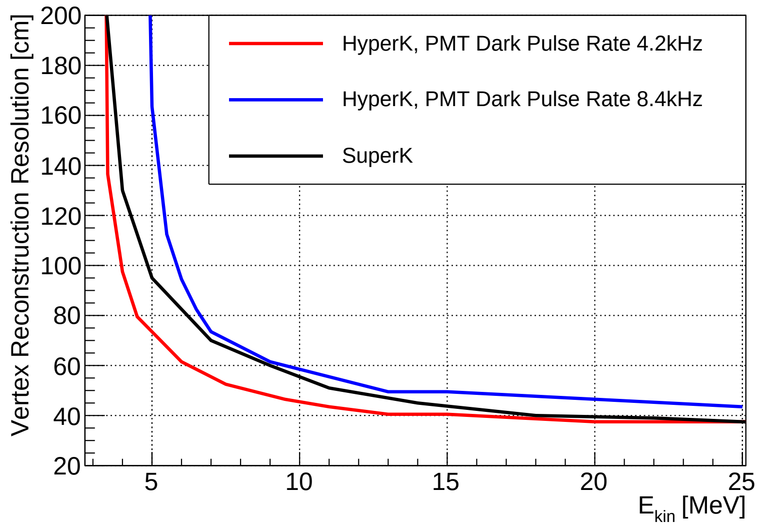

FIG. 166. Vertex reconstruction resolution for electrons with BONSAI for Hyper-K and Super-K detectors. Here, WCSim is used for Hyper-K detector simulation. Red line shows the resolution with the PMT dark pulse rate of 8.4 kHz, as seen in **??**. Blue is for the case of PMT dark pulse rate of 4.2 kHz, which is same as the rate of Super-K photosensors. Black line shows the performance with Super-K detector, simulated with SKDETSIM.

of hits are scaled to energy using the information from detector simulations and calibrations. The direction reconstruction is also performed on the photosensor hit patterns using a circular KS test that checks the azimuthal symmetry around the Cherenkov cone. As the result, the vertex position, direction and energy of low-energy events are available after BONSAI reconstruction.

Several likelihoods to test mis-reconstruction are also available during the reconstruction. Likelihoods calculated using photosensor hit patterns are also used in particle identification, e.g. to differentiate between electron and gamma events.

C. Far Detector Event Reconstruction

Reconstruction performance for high energy events at Hyper-K tends meet or exceed that of Super-K. This can be understood in terms of the combination of two effects: higher light collection by the high quantum efficiency photosensors; and an increased effective granularity from the larger number of photosensors, with Cherenkov rings being sampled by more photosensors in Hyper-K, on average.

Momentum resolution for electrons spans from 2% at around 1 GeV/c to 9% at 50 MeV/c.

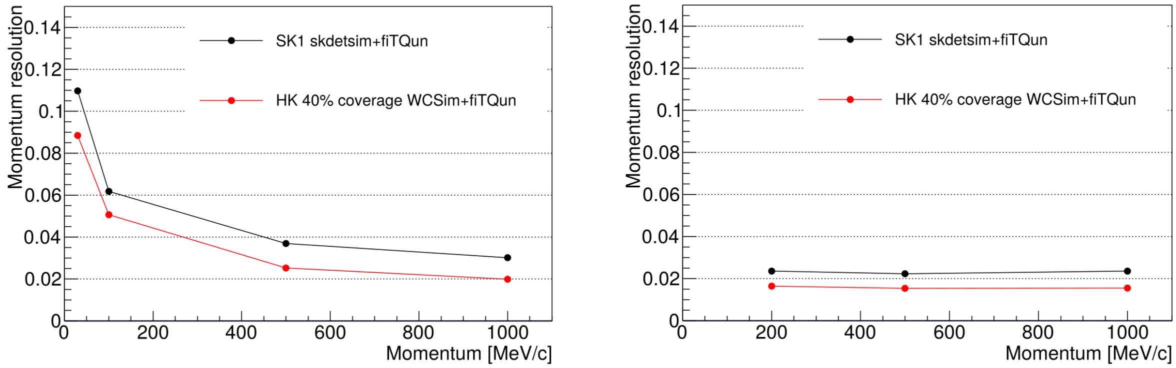

FIG. 167. Momentum resolution for electrons (left) and muons (right). The Hyper-K resolutions are shown in red and compared to the equivalent Super-K resolutions in black.

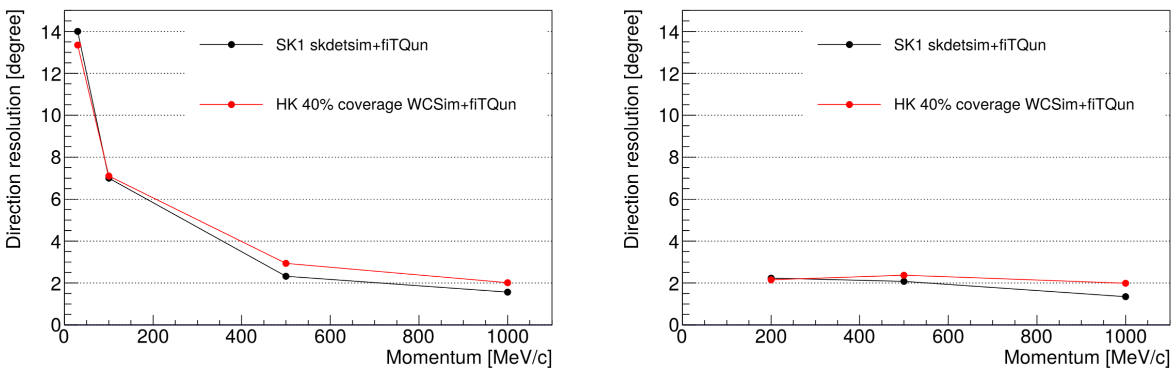

FIG. 168. Direction resolution for electrons (left) and muons (right). The Hyper-K resolutions are shown in red and compared to the equivalent Super-K resolutions in black.

Compared to Super-K, this represents an improvement of 30% to 50%. Muon momentum resolution is roughly constant with energy at around 1.5%. In this case, the improvement compared to Super-K is around 50%. Momentum resolutions for both electrons and muons are shown as a function of particle momentum in Figure 167.

Direction and position resolutions for muons and electrons are comparable to those of Super-K, as shown in Figures 168 and 169.

Significant improvements relative to Super-K are also seen in particle identification of neutral pion events events. Distributions of electron and neutral pion particle gun events are shown in Figure 170 as a function of the likelihood ratio of the neutral pion to electron hypotheses and the

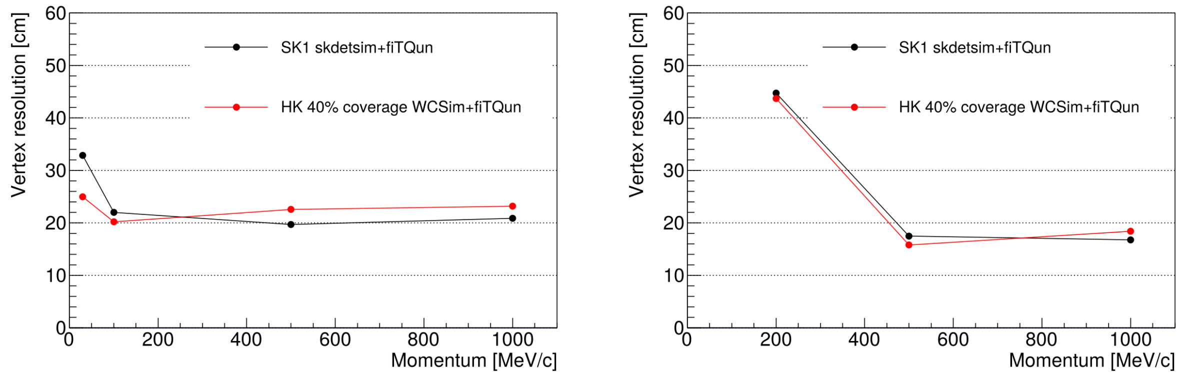

FIG. 169. Position resolution for electrons (left) and muons (right). The Hyper-K resolutions are shown in red and compared to the equivalent Super-K resolutions in black.

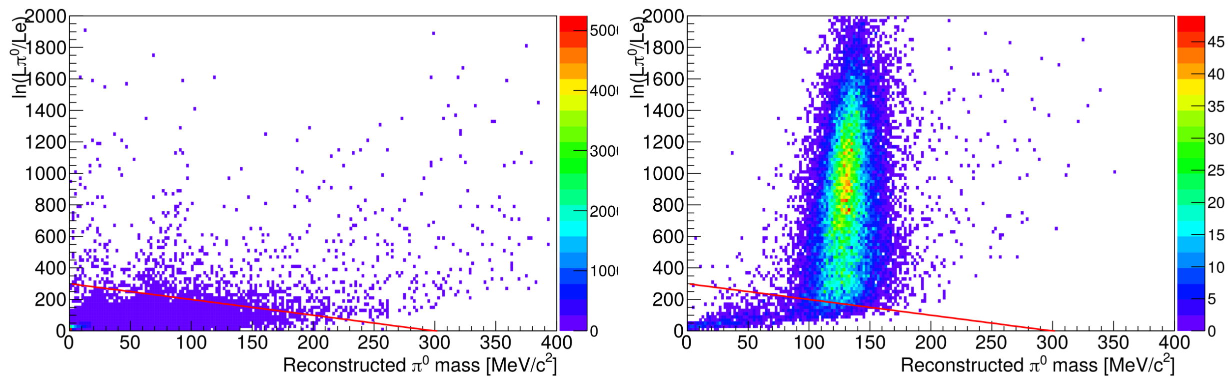

FIG. 170. Separation between electron and neutral pion events in the likelihood ratio *vs* neutral pion reconstructed mass space. Electrons are shown on the left and neutral pions on the right with the cut separating the two populations shown as a red line in both plots.

reconstructed neutral pion mass. Neutral pion events tend to have higher values of the likelihood ratio and cluster at the known neutral pion mass while electron events have lower likelihood ratios and tend to have a low reconstructed mass. The true positive rate, defined as the ratio of correctly identified events to total events of that type, obtained using the cut line shown in Figure 170 is shown in Figure 173. While neutral pion identification at Hyper-K is comparable to Super-K at lower energies, it is significantly improved at higher energies, where boosted neutral pions result in overlapping rings, benefitting from the increased effective granularity.

In Figure 172, distributions of electron and muon particle gun events are shown in the two-dimensional plane of the likelihood ratio between the electron-like and muon-like hypotheses and the electron-like reconstructed momentum. Since, in this case, higher energy events are more easily

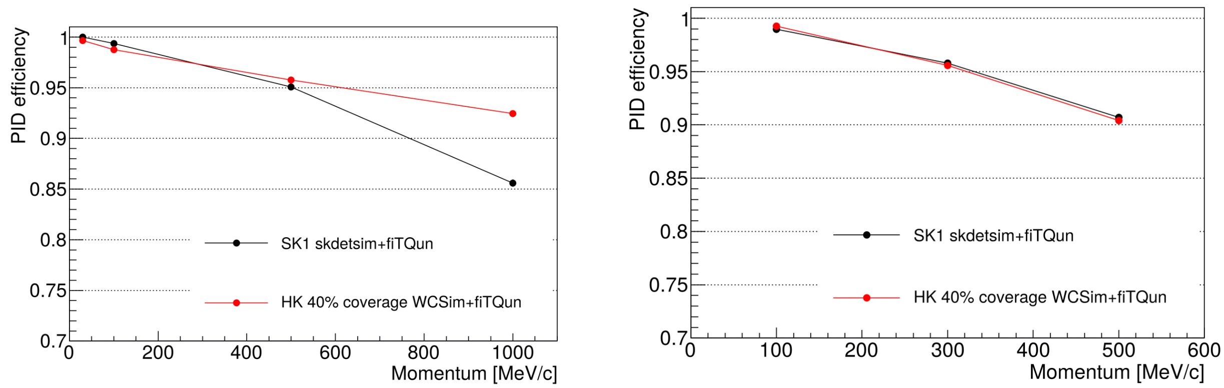

FIG. 171. True positive rate for electron *vs* neutral pion classification shown for electrons on the left and neutral pions on the right, both as a function of true momentum. The Hyper-K rates are shown in red and compared to the equivalent Super-K rates in black.

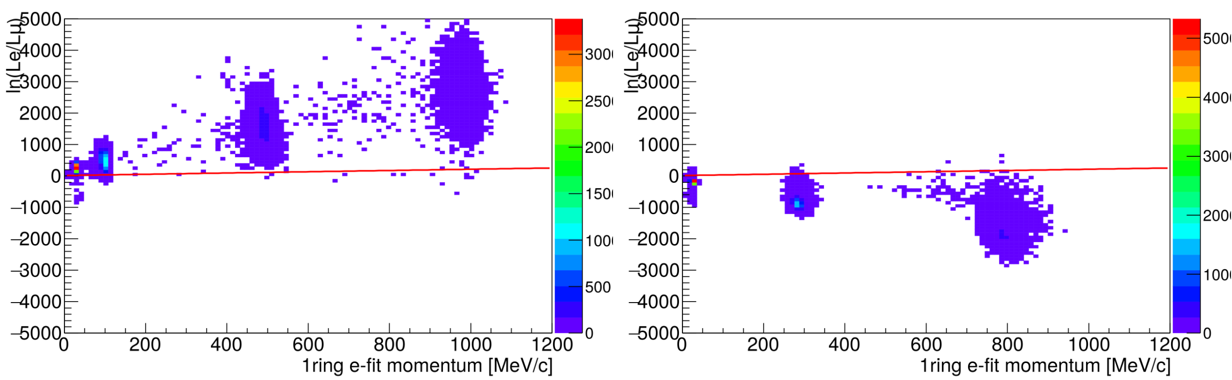

FIG. 172. Separation between electron and muon events in the likelihood ratio *vs* electron-like reconstructed momentum space. Electrons are shown on the left and muons on the right with the cut separating the two populations shown as a red line in both plots.

separable, it is useful for the particle identification criterion to be a function of these two variables. The true positive rate for both electrons and muons is shown in Figure 173, where comparable performance to Super-K is seen.

D. Near Detector Event Reconstruction

For the smaller dimensions of the IWCD tank, improved timing resolution and photosensor granularity are required in order for far detector reconstruction performance to be matched. The closer proximity of event vertices to the detector walls also requires more detailed modeling of the

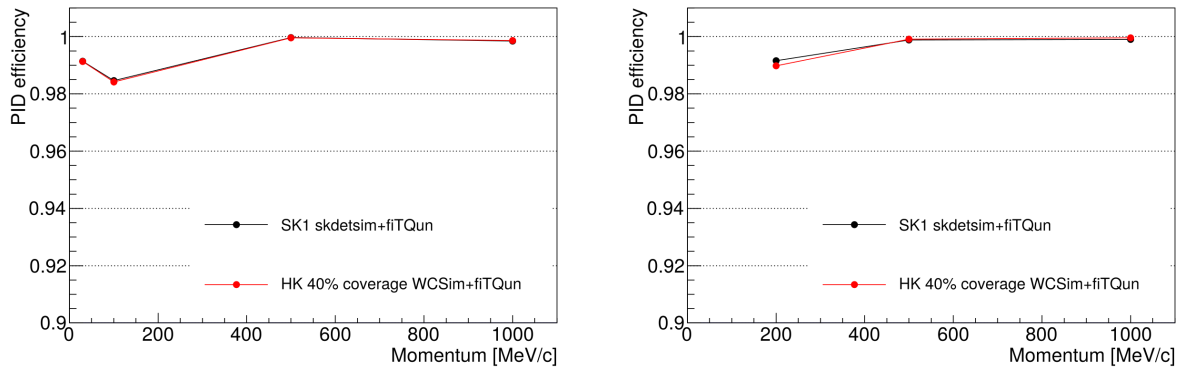

FIG. 173. True positive rate for electron *vs* muon classification shown for electrons on the left and muons on the right, both as a function of true momentum. The Hyper-K rates are shown in red and compared to the equivalent Super-K rates in black.

photosensor response to be used in FiTQun reconstruction.

The reconstruction software development efforts have been focused on adding detail to the FiTQun hit time and charge predictions by increasing the dimensionality of several aspects of the detector modeling such as the photosensor angular response function or the look-up table used to characterize scattered and reflected light. These efforts are currently ongoing and it is expected that IWCD reconstruction performance will improve, particularly for geometries populated with multi-PMT modules.

Initial studies of IWCD high energy event reconstruction have demonstrated that momentum resolution comparable to that of the far detector can be obtained, provided photosensors 8” in diameter or smaller are used. Momentum resolution for a small tank populated with multi-PMT modules with a photocathode coverage fraction of 28% is at least as good as the one obtained for 8” photosensors at a coverage fraction of 40%. Momentum resolution for electrons and muons as a function of true momentum are shown in Figure 174 for both photosensor configurations. In addition, a poorly performing configuration with 20% photosensors is shown for reference.

Position reconstruction benefits from the better timing resolution of the smaller photosensors as well as the smaller tank dimensions. With 8” photosensors, the small tank slightly outperforms the far detector vertex resolution, while the multi-PMT module configuration shows clear improvements (Figure 175).

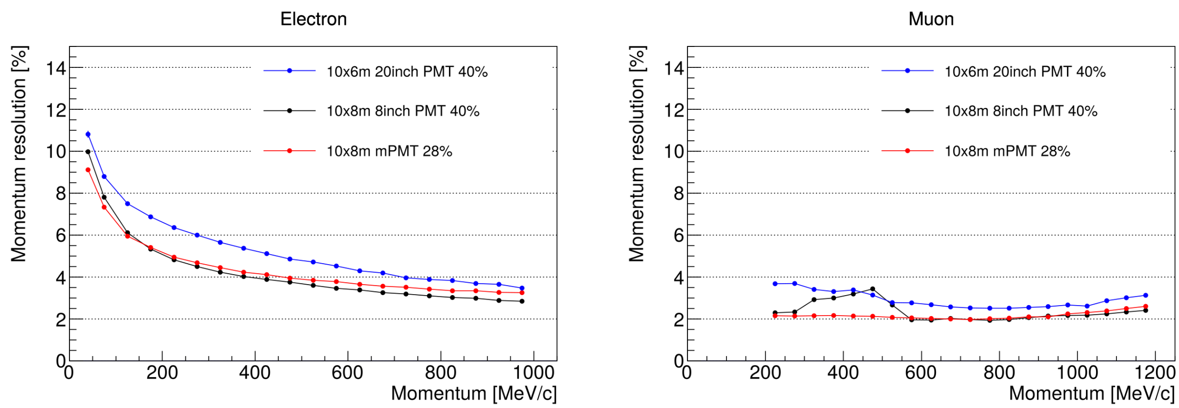

FIG. 174. Momentum resolution for electrons (left) and muons (right) as a function of true momentum for IWCD configurations with 8" photosensors and multi-PMTs. A configuration with 20" photosensors is shown for reference.

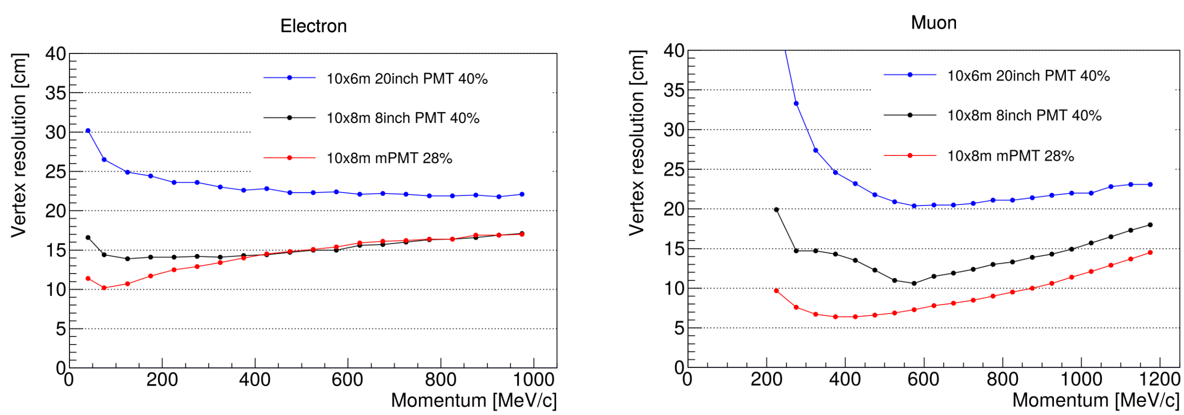

FIG. 175. Position resolution for electrons (left) and muons (right) as a function of true momentum for IWCD configurations with 8" photosensors and multi-PMTs. A configuration with 20" photosensors is shown for reference.

The ability to distinguish electrons from muons (and other particle identification) is strongly related to the effective granularity of the detector. In the small tank geometries, with particles typically closer to the detector walls, electron muon separation comparable to the far detector is obtained with multi-PMT modules but not with 8" photosensors, where performance is degraded at lower moemnta. Efficiency for selecting electrons for a constant 0.5% muon mis-identification rate is shown as a function of true momentum in Figure 176.

Neutral pion identification capabilities of the IWCD are under study, with 8" photosensor performance being worse than that of the far detector and multi-PMT reconstruction still under

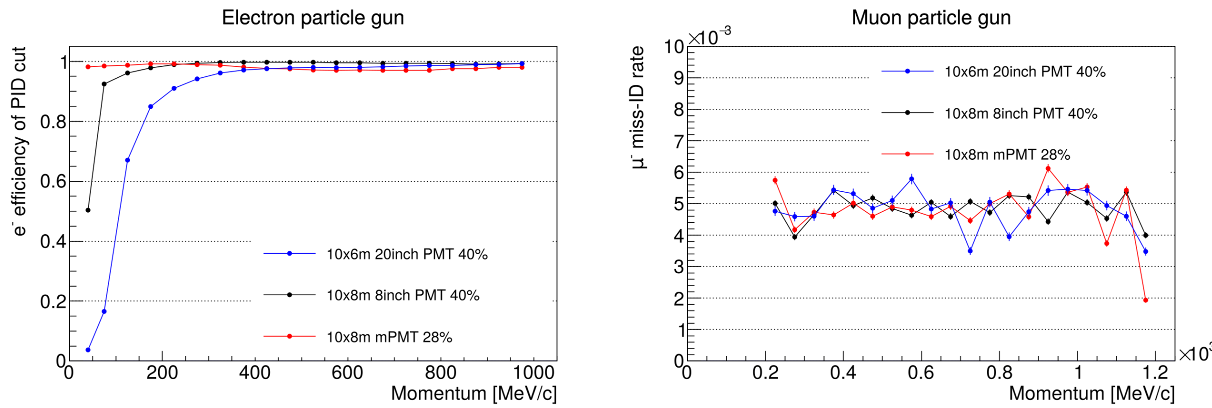

FIG. 176. Efficiency for selecting electrons (left) for a constant muon mis-identification rate of 0.5% (right) as a function of true momentum for IWCD configurations with 8" photosensors and multi-PMTs. A configuration with 20" photosensors is shown for reference.

development.

IV.3. DATA REDUCTION AND STORAGE

A. Data Handling for the Far Detector

Describes the selection of data events in the far detector following the completion of the data acquisition. It also describes the format in which the events are stored for further analysis.

B. Data Handling for the Near Detectors

Describes the selection of data events in the near detectors following the completion of the data acquisition. It also describes the format in which the events are stored for further analysis.

Here it is necessary to describe both the ND detectors and the IWCD.

IV.4. COMPUTING REQUIREMENTS

This section outlines the computing model for the Hyper-K experiment. Existing computing resources at participating institutions are utlised in combination with increased CPU and storage at the KEK and Kamioka sites. These are organised into a tiered system and connected through The Worldwide LHC Computing GRID (WLCG), which hereafter we refer to simply as the GRID.

The Tier0 (T0) sites consist of KEK-T0 and Kamioka-T0. While KEK is already a T0 site, there are plans for Kamioka to purchase increased storage and CPU (which is estimated in the following section) and to maintain a GRID storage element (SE) to bring it up to T0 standards. Raw data from the far detectors is archived at Kamioka; it also undergoes reduction and some basic reconstruction before it is copied to T1 sites from the GRID SE. Similarly, data from the intermediate detectors is archived in the KEK-T0 HPSS storage, and then temporarily copied to the KEKCC SE while it is synced with the T1 sites.

Possible T1 sites for HK are RAL (UK), INFN (Italy), IN2P3 (France) and TRIUMF (Canada). This is where all data is stored, replicated across multiple T1 SEs for backup purposes. Some MC simulation and calibration processing is performed at these sites, where the associated file are then stored.

The T2 sites typically constitute collaborating universities. MC and calibration jobs also run on T2 sites, which generally contain a subset of the MC for ease of access. It is likely the MC stored at these locations will change according to what is in high demand at any given time.

At present HK has 20TB on the Queen Mary University of London (QM) SEs to begin mini productions and develop our custom computing scripts. The predicted numbers in this section of the report will be used to outline the short and long term computing requirements of HK such that we can take this to GridPP (The UK branch of the GRID) and the GRID sites of collaborating institutions in Europe and Canada. This will be done before the end of 2018 with the aim to request resources for the next 5 years (2019-2024) as well as forecasting our longer term needs, including predictions for when data taking commences.

A. Far Site Computing Resources

The CPU and most of the storage at Kamioka is not required until HK starts taking data, though prior to the detector being switched on MC simulation can potentially be stored there. Once data taking commences, the expected rate of raw data is 4TB/day, which amounts to about 1.5 PB/year.

The raw data from HK is to be put through data reduction and reconstruction, as well as supernova detection software, on site at Kamioka. HK must be quick to respond to a supernova, so the supernova analysis is performed in real time, independent of other algorithms. High- and low-energy neutrinos go through different reconstruction algorithms; furthermore, timing and directional information in conjunction with these energy regions allows data to be put into different samples for analysis. The low energy region is used for the study of solar neutrinos, while the high-energy neutrinos are used in atmospheric or nucleon decay studies. Selecting downward going muon tracks forms a control sample for the background study of solar neutrinos. Beam events are distinguished according to timing coincidence. It is estimated that the CPU required to run the data through the various software at Kamioka is around 3000 Xenon processor cores. The storage requirement for raw data, reduction and reconstruction and some allocation for MC simulation, is around 1.5 PB/year. Only raw data will be backed up onto tape storage, as part of the T0 duties of the Kamioka computing site.

The forecasted cost of upgrading the Kamioka computing resources is estimated to be around 18 Oku yen for 3000 Xenon cores, and up to 12 Oku yen for 15 PB of storage, which would be sufficient for 5 years of data taking. Note that these numbers do not include SK requirements

B. Near Site Computing Resources

Raw data from the near and intermediate detectors is transferred to KEK where it is archived permanently; this is done using the Archiver Programmes which copy data written from the DAQ to the Semi-Offline system and to the HPSS cluster at KEK via an ssh connection. This software is also responsible for removing data from the DAQ disks, checking first the data transferred successfully, to ensure there is always a sufficient amount of free storage. This data is also copied onto the KEKCC SE to enable files to be transferred to the T1 sites. Once registered at the T1 sites, the data is wiped from the KEKCC SE.

The current data rates for ND280 and INGRID are 53 GB/day and 23 GB/day respectively. Plans to introduce two HTPCs and a new FGD have a significant impact on the rate of data. Taking a conservative estimate concerning the different options for the FGD design, the data rate is expected to increase by a factor of up to four[3]. Though it should be noted that these numbers are based on the upcoming (2019/2010) ND280 upgrade; it is likely that further upgrades will take place prior to the HK era. The IWCD is estimated to have a data rate around 2.5 GB/s, which amounts to 216 TB/day.

If we assume that the near/intermediate detectors operate for 150 days a year (2017-2018 had 131 days of neutrino flux with 100 days of physics run), then 5 years of data taking from IWCD, INGRID and the upgraded ND280 requires about 35 PB of storage, which is completely dominated by the IWCD data.

[3] This assumes that the loss in data rate from taking out the P0D will be made up by the upstream ECal and new time of flight system. It also assumes that the HTPCs will have a laser calibration system. The MMs and backend electrons for new FGD/TPCs are assumed to be the same as those currently used.

C. Remote Computing Resources

As previously mentioned, the GRID provides a convenient framework in which to transfer data from the near- and far-sites for the purpose of creating backup copies and distributing to HK members across the world. File transfer services (FTS) are an efficient and reliable way to transfer large amounts of data between SEs. An example is the RAL FTS, which interacts with SEs that have a storage resource manager (SRM) interface such as those on the GRID.

The workload management system (WMS) used by HK, i.e. middleware that interfaces users with the GRID computing resources they wish to access, is provided by the DIRAC (Distributed Infrastructure with Remote Agent Control) project. DIRAC adopts a pilot based system, which means that pilot jobs are sent to the various computing resources to check the running conditions and report back to the central WMS server. The pilot jobs act to reserve the resources and are subsequently assigned a job. This enables the WMS to delay the decision of job allocations and thereby optimise it based on the information received, avoiding unforeseen problems or delays that may have arisen from pushing jobs to resources without this intermediate step. When a user submits jobs, they submit through their VO (Virtual Organization); the Hyper-K VO, hyperk.org, is configured with DIRAC and the process of job submission and retrieval is running smoothly.

Strict bookkeeping via a file catalogue is vital when dealing with large amounts of data spread across multiple locations, and again the DIRAC project provides a solution for this: the DIRAC File Catalogue (DFC). Initial tests show that the hyperk.org catalogue is working as expected.

DIRAC software is versatile; the user can execute operations via the command line, or make use of the DIRAC API inside custom python scripts. The DFC has an additional method of interacting via the DFC command line interface (CLI). This enables uses to look around the file catalogue in a manner similar to browsing a local disk, which provides a very user-friendly way to search, upload and download files for non-experienced users. Custom Hyper-K scripts will be developed during the first batch of mini productions; these will be python scripts that utilise the DIRAC API to write JDL (job description language) files, access the DFC, and check the status and output of jobs. This software will ensure strict bookkeeping is upheld for MC production.

The Cern Virtual Machine File System (CVMFS) is a read-only file system optimised for software distribution. The advantage is that compiled software can be run locally both by individual users, and by jobs executed on the GRID, without the need of a local install. The hyper-K mount point is /cvmfs/hyperk.egi.eu and the repository is hosted by RAL. WCSim, fiTQun and BONSAI (and their requirements) have recent versions installed on the Hyper-K CVMFS repository. As

Hyper-K moves forward, the plans is to keep putting each hyper-k software release onto CVMFS, such that users always have access to the latest official releases.

The current status at the time of writing is that test jobs submitted through DIRAC by the hyperk.org VO are successfully able to run software installed on the hyperk.org CVMFS repository. Test files have been successfully uploaded to GRID SEs and registered in the DFC. The first physics jobs are being prepared; a very small scale mini supernova production is in preparation. Following this the aim is to begin larger scale mini productions for other analyses by the end of the year. The predicted computing requirements for the next 5 years, which assumes two productions that includes ND280, E61 and HK, is estimated to be 300TB and 8k CPU core years of GRID resources.

Part V

Physics Performance

V.1. LONG BASELINE ACCELERATOR NEUTRINOS

Hyper-K will perform a precise study of CP asymmetry in the lepton sector by a long baseline neutrino oscillation experiment using the J-PARC neutrino beam described in Sec. II.1. A direct comparison of the oscillation probabilities for neutrinos and anti-neutrinos is required for a direct and model-independent measurement of leptonic CP asymmetry. This measurement is significant since the existence of leptonic CP violation may be a necessary condition to explain the matter-antimatter asymmetry of the Universe.

It will also be possible to check the consistency of the PMNS mixing framework by comparing the accelerator (ν_μ to ν_e appearance of GeV neutrino over 295 km) and reactor ($\overline{\nu}_e$ disappearance of MeV neutrino over $\sim$1 km) θ_{13} measurements, which may have different contributions from new physics.

The Hyper-K long-baseline program will also be able to make precise measurements of the oscillation parameters $|\Delta m^2_{32}|$ and $\sin^2\theta_{23}$.

The standard PMNS flavor mixing scenario is assumed in the following as a baseline study, although it is possible that new physics is involved in neutrino oscillations and will be revealed by Hyper-K. The analysis presented in this report is based on that described in [**?**], but with an updated treatment of systematic uncertainties.

1. *Oscillation probabilities and measurement channels*

The long-baseline oscillation analysis is performed by combined fits of the ν_e appearance and ν_μ disappearance channels using the full PMNS oscillation probability formula.

a. $\nu_\mu \to \nu_e$ appearance channel The $\nu_\mu \to \nu_e$ oscillation channel is most sensitive to the oscillation parameters $\sin^2\theta_{13}$ and δ_{CP}, although other parameters also contribute to the oscillation probability. Figure 177 shows the $\nu_\mu \to \nu_e$ and $\overline{\nu}_\mu \to \overline{\nu}_e$ oscillation probabilities as a function of the true neutrino energy for a baseline of 295 km for various true values of δ_{CP} and the mass hierarchy (the Earth matter density is assumed to be $2.6\,g/\mathrm{cm}^3$).

Similar oscillation probabilities can be observed for different combinations of the mass hierarchy and values of δ_{CP}, resulting in a potential degeneracy if the mass hierarchy is unknown. By combining information from experiments currently ongoing [**? ? ? ? ?**] and/or planned in the near future [**? ? ? ? ?**], it is expected that the mass hierarchy will be determined by the time Hyper-K starts to take data. If not, Hyper-K itself has a sensitivity to the mass hierarchy by

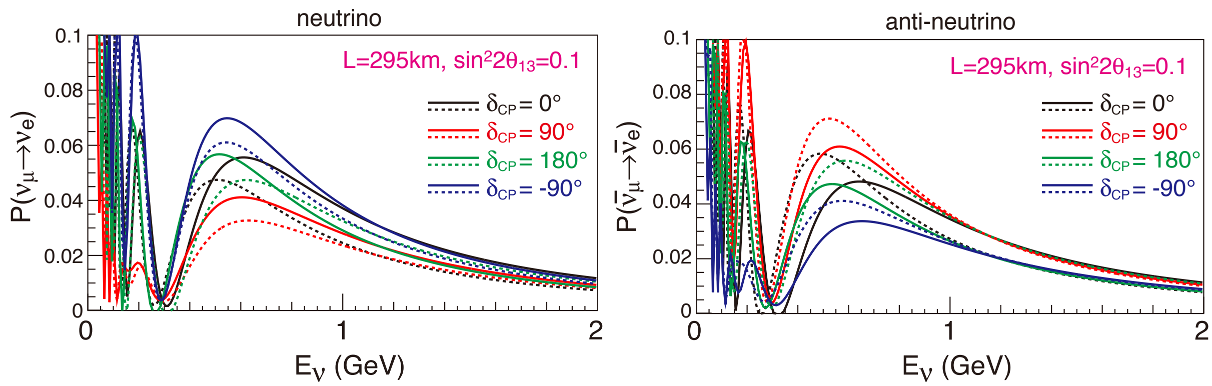

FIG. 177. Oscillation probabilities as a function of the neutrino energy for $\nu_\mu \to \nu_e$ (left) and $\overline{\nu}_\mu \to \overline{\nu}_e$ (right) transitions with baseline L=295 km and $\sin^2 2\theta_{13} = 0.1$. Black, red, green, and blue lines correspond to $\delta_{CP} = 0°$, 90°, 180° and −90°, respectively. Solid (dashed) line represents the case for a normal (inverted) mass hierarchy.

atmospheric neutrino measurements as described in Sec. **??**. Thus, the mass hierarchy is assumed to be known here, unless otherwise stated.

b. ν_μ disappearance channel The currently measured value of θ_{23} is consistent with maximal mixing, $\theta_{23} \approx \pi/4$ [**? ? ?**], while the NOvA collaboration recently reported a possible hint of non-maximal mixing [**?**]. It is of great interest to determine if $\sin^2\theta_{23}$ is maximal or not, and if not, whether θ_{23} is less or greater than $\pi/4$, as it could constrain models of neutrino mass generation and quark-lepton unification [**? ? ? ? ? ?**]. The ν_μ survival probability $P(\nu_\mu \to \nu_\mu)$ is proportional to $\sin^2 2\theta_{23}$ to first order,

$$P(\nu_\mu \to \nu_\mu) \simeq 1 - (\cos^4\theta_{13}\sin^2 2\theta_{23} + \sin^2\theta_{23}\sin^2 2\theta_{13})\sin^2(\Delta m^2_{32}L/4E_\nu), \tag{2}$$

where L is the baseline and E_ν is the neutrino energy. However, there is an octant ambiguity to first order, since for each value of $\theta_{23} \leq 45°$ (in the first octant), there is a value in the second octant ($\theta_{23} > 45°$) that gives rise to the same oscillation probability. A ν_e appearance measurement can determine $\sin^2\theta_{23}\sin^2 2\theta_{13}$, and reactor experiments also provide an almost pure measurement of $\sin^2 2\theta_{13}$. Thus, the combination of complementary measurements will be able to resolve this degeneracy if θ_{23} is sufficiently away from $\frac{\pi}{4}$ [**? ? ?**].

A measurement of $\overline{\nu}_e$ disappearance by reactor neutrino experiments provides a constraint on the combination of mass-squared differences

$$\Delta m^2_{ee} = \cos^2\theta_{12}\Delta m^2_{31} + \sin^2\theta_{12}\Delta m^2_{32}, \tag{3}$$

TABLE XLVI. Oscillation parameters used for the sensitivity analysis and treatment in the fitting. The *nominal* values are used for figures and numbers in this section, unless otherwise stated.

Parameter	$\sin^2 2\theta_{13}$	δ_{CP}	$\sin^2\theta_{23}$	Δm^2_{32}	mass hierarchy	$\sin^2 2\theta_{12}$	Δm^2_{21}
Nominal	0.10	0	0.50	2.4×10^{-3} eV^2	Normal	0.8704	7.6×10^{-5} eV^2
Treatment	Fitted	Fitted	Fitted	Fitted	Fixed	Fixed	Fixed

while a ν_μ disappearance measurement with Hyper-K provides a different combination [**?** **?**]

$$\Delta m^2_{\mu\mu} = \sin^2\theta_{12}\Delta m^2_{31} + \cos^2\theta_{12}\Delta m^2_{32} + \cos\delta_{CP}\sin\theta_{13}\sin 2\theta_{12}\tan\theta_{23}\Delta m^2_{21}. \quad (4)$$

Because the mass squared difference measurements by Hyper-K and reactor experiments give independent information, the comparison can be used to check the consistency of the PMNS mixing matrix framework. In order to have sensitivity to the mass hierarchy, the uncertainties of both measurements must be <1%. Future medium baseline reactor experiments, JUNO [**?**] and RENO-50 [**?**], plan to measure Δm^2_{ee} with precision better than 1%, and a precision measurement of Δm^2 by Hyper-K will also be required.

2. Analysis overview

The analysis used in this report is based on a framework developed for the sensitivity study by T2K presented in [**?**]. A binned likelihood analysis using the reconstructed neutrino energy distributions is performed by fitting four samples (ν_e and $\overline{\nu}_e$ appearance and ν_μ and $\overline{\nu}_\mu$ disappearance) simultaneously. Table XLVI shows the nominal oscillation parameters used in the study presented in this report, and the treatment of each parameter during fitting – the parameters $\sin^2\theta_{13}$, $\sin^2\theta_{23}$, Δm^2_{32} and δ_{CP} are fit.

An integrated beam power of 13 MW$\times10^7$ sec is assumed in this study, corresponding to 2.7×10^{22} protons on target with 30 GeV J-PARC beam (∼10 Snowmass years at 1.3 MW). Various neutrino mode and anti-neutrino mode beam running time ratio scenarios have been studied, but there is no significant change in the CP sensitivity between ν:$\overline{\nu}$=1:1 to 1:5; the ν:$\overline{\nu}$ ratio is set to be 1:3 in this document.

Interactions of neutrinos in the Hyper-K detector are simulated with the NEUT program library [**?** **?** **?**], which is used in both Super-K and T2K. The response of the detector is simulated using the Super-K (SK-IV) full Monte Carlo simulation based on the GEANT3 package [**?**]. Events are reconstructed with the Super-K reconstruction software, which gives a realistic estimate of the Hyper-K performance.

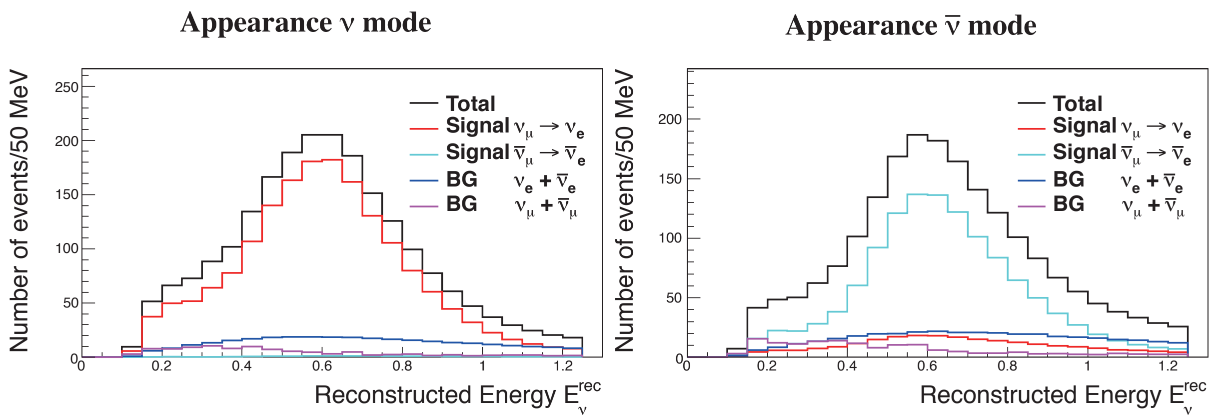

FIG. 178. Reconstructed neutrino energy distribution of the ν_e candidate events in neutrino beam mode (left) and anti-neutrino beam mode (right). The appearance signal, $\nu_\mu \rightarrow \nu_e$ and $\overline{\nu}_\mu \rightarrow \overline{\nu}_e$, and background events originating from $(\nu_\mu + \overline{\nu}_\mu)$ and $(\nu_e + \overline{\nu}_e)$ are shown separately.

Results shown here assume ten years of running with a 187 kton fiducial volume single tank detector.

3. Expected observables at the far detector

The criteria to select ν_e and ν_μ candidate events are based on those developed for and established with the Super-K and T2K experiments[]. Fully contained (FC) events with a reconstructed vertex inside the fiducial volume (FV), which is defined as the region more than 1.5 m away from the inner detector wall, and visible energy (E_{vis}) greater than 30 MeV are selected as FCFV neutrino event candidates. In order to enhance charged current quasielastic (CCQE, $\nu_l + n \rightarrow l^- + p$ or $\overline{\nu}_l + p \rightarrow l^+ + n$) interactions, a single Cherenkov ring is required.

The neutrino energy (E_ν^{rec}) is reconstructed from the energy of the final state charged lepton and the angle between the neutrino beam and the charged lepton direction assuming a CCQE interaction. It has been shown in T2K analyses that the sensitivity can be slightly improved by using two-dimensional momentum and angle information (p_ℓ, θ) in the oscillation fit – Hyper-K fits using (p_ℓ, θ) will be performed in the future.

Then, to select $\nu_e/\overline{\nu}_e$ candidate events the following criteria are applied: the reconstructed ring is identified as electron-like (e-like), E_{vis} is greater than 100 MeV, there is no decay electron associated to the event, and E_ν^{rec} is less than 1.25 GeV. Finally, in order to reduce the background from mis-reconstructed π^0 events, additional criteria using the reconstructed π^0 mass and the ratio of the best-fit likelihoods of the π^0 and electron fits [**?**] are applied. Figure 178 shows

TABLE XLVII. The expected number of $\nu_e/\overline{\nu}_e$ candidate events and efficiencies with respect to FCFV events. Background is categorized by the flavor before oscillation.

		signal		BG						Total
		$\nu_\mu \to \nu_e$	$\overline{\nu}_\mu \to \overline{\nu}_e$	ν_μ CC	$\overline{\nu}_\mu$ CC	ν_e CC	$\overline{\nu}_e$ CC	NC	BG Total	
ν mode	Events	1643	15	7	0	248	11	134	400	2058
	Eff.(%)	63.6	47.3	0.1	0.0	24.5	12.6	1.4	1.6	—
$\bar{\nu}$ mode	Events	206	1183	2	2	101	216	196	517	1906
	Eff. (%)	45.0	70.8	0.03	0.02	13.5	30.8	1.6	1.6	—

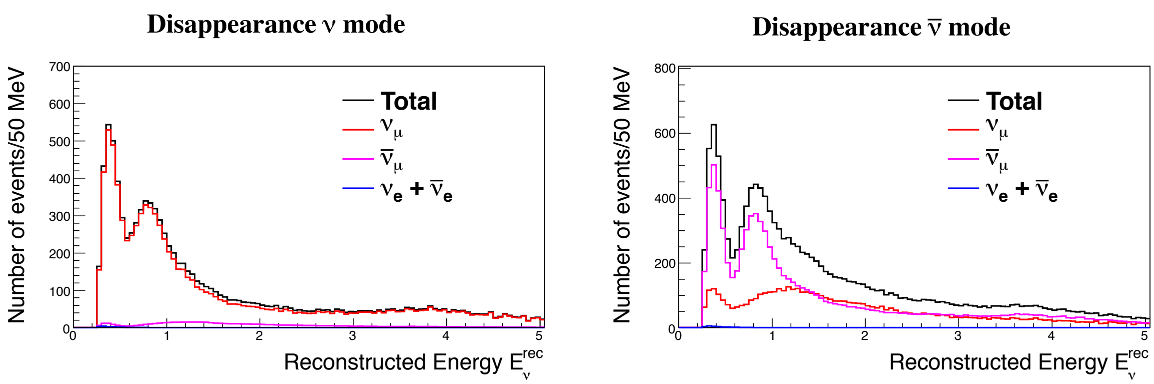

FIG. 179. Reconstructed neutrino energy distribution of the $\nu_\mu/\overline{\nu}_\mu$ candidate events after oscillation in neutrino beam mode (left) and anti-neutrino beam mode (right).

the reconstructed neutrino energy distributions of ν_e and $\overline{\nu}_e$ appearance candidate events after all selections. The expected number of ν_e and $\overline{\nu}_e$ candidate events and selection efficiencies are shown in Table XLVII.

For the $\nu_\mu/\overline{\nu}_\mu$ candidate events the following criteria are applied: the reconstructed ring is

TABLE XLVIII. The expected number of $\nu_\mu/\overline{\nu}_\mu$ candidate events and efficiencies (with respect to FCFV events) for each flavor and interaction type.

		ν_μCCQE	ν_μCC non-QE	$\overline{\nu}_\mu$CCQE	$\overline{\nu}_\mu$CC non-QE	$\nu_e + \overline{\nu}_e$ CC	NC	$\nu_\mu \to \nu_e$	total
ν mode	Events	6043	2981	348	194	6	480	29	10080
	Eff. (%)	91.0	20.7	95.6	53.5	0.5	8.8	1.1	—
$\bar{\nu}$ mode	Events	2699	2354	6099	1961	7	603	4	13726
	Eff. (%)	88.0	20.1	95.4	54.8	0.4	8.8	0.7	—

identified as muon-like (μ-like), the reconstructed muon momentum is greater than 200 MeV/c, and there is at most one decay electron associated with the event. Figure 179 shows the reconstructed neutrino energy distributions of the selected ν_μ and $\overline{\nu}_\mu$ candidate events. Table XLVIII shows the number of ν_μ and $\overline{\nu}_\mu$ candidate events and selection efficiencies.

4. Additional studies with dedicated Hyper-K simulation package

Studies shown here use the SK-IV Monte Carlo simulation and reconstruction (with 40% photocoverage), however dedicated studies using a simulation package developed for Hyper-K are also planned. Although, based on comparisons between SK-III and SK-II, the reconstruction performance for beam neutrino events at $\sim$1 GeV does not degrade with a reduction of photocathode coverage from 40% to 20% (with R3600), future Hyper-K studies will include further checks to understand the dependence of the physics sensitivity on the Hyper-K PMT photocoverage and PMT type (ie baseline 40% Hyper-K PMT coverage vs 20% Hyper-K PMT + 5% mPMT coverage, etc). Studies including neutron tagging with different photocoverage will also be performed, but neutron tagging is not taken into account in the current study.

5. Systematic uncertainties

Uncertainties have been estimated based the T2K 2013 official errors with significant reductions in the cross section and far detector uncertainties[]. The uncertainties for anti-neutrino beam mode are approximately equal to those for neutrino beam mode. The flux and cross section uncertainties are assumed to be uncorrelated between the neutrino and anti-neutrino data, except for the uncertainty of the ν_e/ν_μ cross section ratio, which is conservatively treated as anti-correlated considering the theoretical uncertainties studied in [**?**]. The far detector uncertainty is treated as fully correlated between the neutrino and anti-neutrino data.

The systematic uncertainties on the number of expected events at the far detector are summarized in Table XLIX for the analysis shown here. Studies with various updated systematic errors will be performed.

6. Measurement of CP asymmetry

Figure 180 shows examples of the 90% CL allowed regions on the $\sin^2 2\theta_{13}$–δ_{CP} plane resulting from the true values of $\delta_{CP} = (-90°, 0, 90°, 180°)$. Also shown are the allowed regions when we

TABLE XLIX. Uncertainties on the expected number of events at Hyper-K for the study shown here.

		Flux & ND-constrained cross section	ND-independent cross section	Far detector	Total
ν mode	Appearance	3.0%	0.5%	0.7%	3.2%
	Disappearance	3.3%	0.9%	1.0%	3.6%
$\overline{\nu}$ mode	Appearance	3.2%	1.5%	1.5%	3.9%
	Disappearance	3.3%	0.9%	1.1%	3.6%

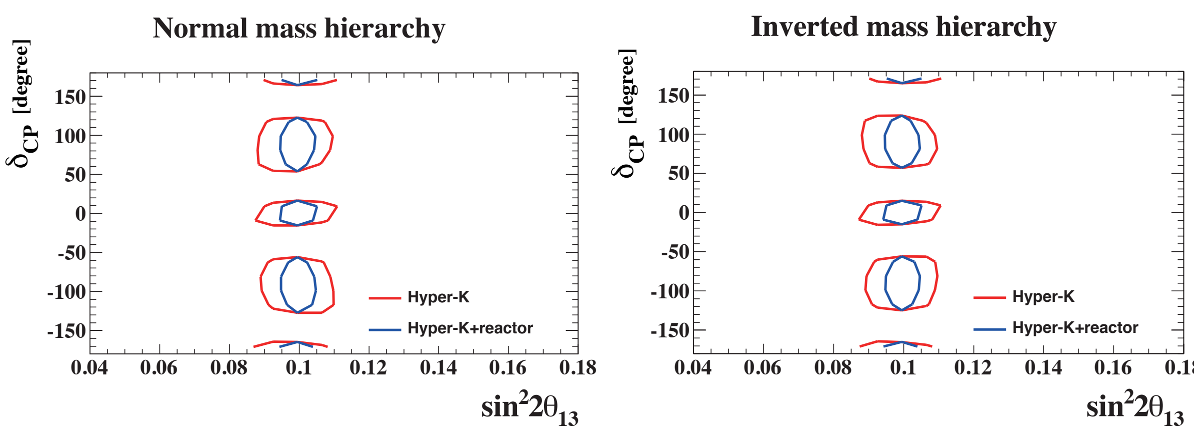

FIG. 180. The expected 90% CL allowed regions in the $\sin^2 2\theta_{13}$-δ_{CP} plane for true normal (left) and inverted (right) mass hierarchy. The results for the true values of $\delta_{CP} = (-90°, 0, 90°, 180°)$ are shown. Red (blue) lines show the result with Hyper-K only (with $\sin^2 2\theta_{13}$ constraint from reactor experiments).

include a constraint from the reactor experiments of $\sin^2 2\theta_{13} = 0.100 \pm 0.005$.

Figure 181 shows the expected significance to exclude $\sin\delta_{CP} = 0$ (the CP conserved case). The significance is calculated as $\sqrt{\Delta\chi^2}$, where $\Delta\chi^2$ is the difference of χ^2 for the *trial* value of δ_{CP} and for $\delta_{CP} = 0°$ or $180°$ (whichever is lower). Figure 181 also shows the fraction of δ_{CP} for which $\sin\delta_{CP} = 0$ is excluded with more than $3\,\sigma$ and $5\,\sigma$ significance as a function of the running time. CP violation in the lepton sector can be observed with more than $3(5)\,\sigma$ significance for 76(57)% of the possible true values of δ_{CP}. The value of δ_{CP} can be determined with an uncertainty of 7.2° for $\delta_{CP} = 0°$ or 180°, and 23° for $\delta_{CP} = \pm 90°$.

Plots are shown for Hyper-K alone, but the result changes only slightly when a reactor constraint is included in the fit. Although sensitivities to δ_{CP} depend on the true value of θ_{23}, results shown here assume the true value of $\sin^2\theta_{23} = 0.5$.

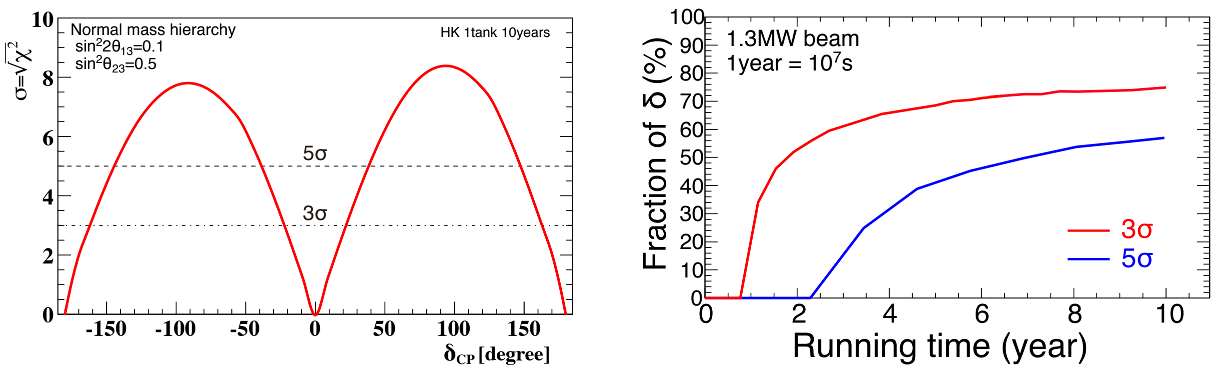

FIG. 181. Left : expected significance to exclude $\sin\delta_{CP} = 0$ plotted as a function of true δ_{CP}. Right : fraction of δ_{CP} for which $\sin\delta_{CP} = 0$ can be excluded with more than $3\,\sigma$ (red) and $5\,\sigma$ (blue) significance as a function of the running time.

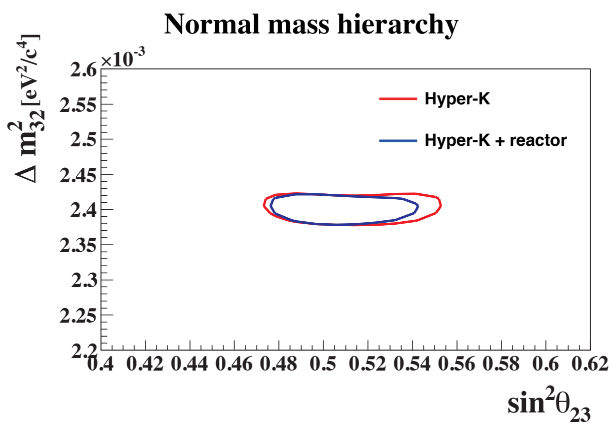

FIG. 182. The 90% CL allowed regions in the $\sin^2\theta_{23}$–Δm^2_{32} plane assuming $\sin^2\theta_{23} = 0.5$. The red (blue) line corresponds to the result with Hyper-K alone (with a reactor constraint on $\sin^2 2\theta_{13}$).

7. *Precise measurements of* Δm^2_{32} *and* $\sin^2\theta_{23}$

A joint fit of the ν_μ and ν_e samples enables us to also precisely measure $\sin^2\theta_{23}$ and Δm^2_{32}. Figures 182 and 183 show 90% CL allowed regions on the $\sin^2\theta_{23}$–Δm^2_{32} plane assuming different true values of $\sin^2\theta_{23}$. The expected measurement precision for Δm^2_{32} and $\sin^2\theta_{23}$ is summarized in Table L. Figure 184 shows the expected significance ($\sigma \equiv \sqrt{\Delta\chi^2}$) for wrong octant rejection as a function of true value of $\sin^2\theta_{23}$.

As discussed above, a precision measurement of Δm^2_{32}, compared with reactor measurements of Δm^2_{ee}, will enable a consistency check of the PMNS mixing framework. The uncertainty on Δm^2_{32} by Hyper-K measurements is expected to reach 0.6%, which will allow for a significant check.

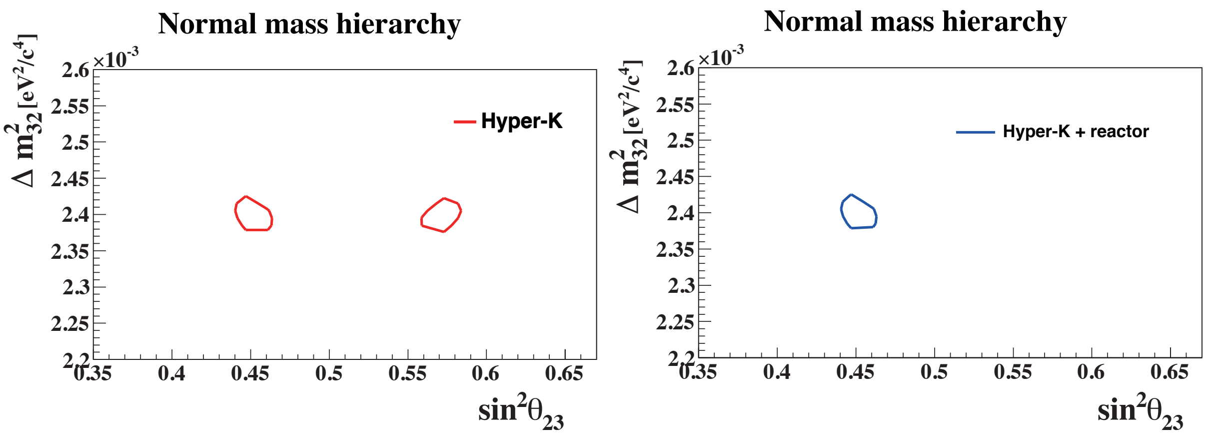

FIG. 183. 90% CL allowed regions in the $\sin^2\theta_{23}$–Δm^2_{32} plane assuming $\sin^2\theta_{23} = 0.45$ for Hyper-K only (left) and with a reactor constraint (right).

TABLE L. Expected 1σ uncertainty of Δm^2_{32} and $\sin^2\theta_{23}$ for true $\sin^2\theta_{23} = 0.45, 0.50, 0.55$. A reactor constraint on $\sin^2 2\theta_{13} = 0.1 \pm 0.005$ is imposed.

True $\sin^2\theta_{23}$	0.45		0.50		0.55	
Parameter	Δm^2_{32} (eV^2)	$\sin^2\theta_{23}$	Δm^2_{32} (eV^2)	$\sin^2\theta_{23}$	Δm^2_{32} (eV^2)	$\sin^2\theta_{23}$
NH	1.4×10^{-5}	0.006	1.4×10^{-5}	0.017	1.5×10^{-5}	0.009
IH	1.5×10^{-5}	0.006	1.4×10^{-5}	0.017	1.5×10^{-5}	0.009

8. *Neutrino cross section measurements*

With the set of highly capable neutrino detectors envisioned for the Hyper-K project, a variety of neutrino interaction cross section measurements will become possible. The near detector suite offers a range of capabilities to probe different theoretical models for neutrino interactions across different momenta ranges and a range of lepton emission angles. In table LI, we estimate the sensitivity of each proposed near detector for key selections based on a flux of 10^{21} POT.

9. *Searches for new physics*

In addition to the study of standard neutrino oscillations, the combination of an intense accelerator-generated neutrino beam and high performance detectors enables us to search for new physics in various ways. Examples of possible searches for new physics include searches for sterile neutrinos in both the disappearance and appearance channels in near and intermediate detectors,

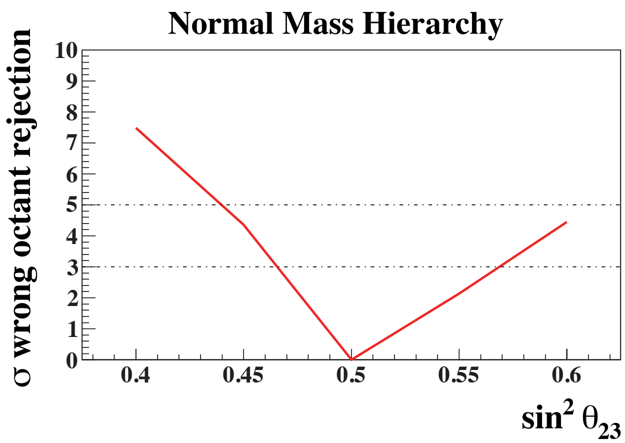

FIG. 184. The expected significance ($\sigma \equiv \sqrt{\Delta\chi^2}$) for wrong θ_{23} octant rejection, by a beam neutrino measurement with a reactor constraint, as a function of true $\sin^2\theta_{23}$ assuming true normal hierarchy.

as well as in neutral current measurements at the far detector. Tests of Lorentz and CPT invariance have been performed by various experiments, including T2K, and the sensitivity of these measurements can be improved with the Hyper-K larger statistics and improved detectors. The feasibility of a search for heavy neutral leptons (heavy neutrinos) using an accelerator neutrino experiment, in particular T2K, is studied in [?]. The sensitivity of a heavy neutrino search would be improved by Hyper-K-era measurements, as well as by implementing large gas detectors at the near detector site.

Detector	Selection	Nevents	Selection Characteristics
ND280 detector, 280m	ν_μCC0π	20k	FGD1 (1–3 GeV), $P \approx$72% [?]
ND280 detector, 280m	ν_μCC1π	6k	FGD1 (1–3 GeV), $P \approx$50% [?]
ND280 detector, 280m	ν_μCC inclusive	40k	FGD1 (1–3 GeV), $P \approx$90%[?]
INGRID	ν_μCC inclusive	17.6×10^6	$\epsilon >$70% (1–3 GeV), P = 97% [?]
HPTPC, 8 m^3, 10 bar Ne (CF_4)	ν_μCC inclusive	4.2k (18.4k)	$\epsilon \approx$70%, protons > 5 MeV detected
HPTPC, 8 m^3, 10 bar Ne (CF_4)	ν_eCC inclusive	80 (450)	$\epsilon \approx$70%, protons > 5 MeV detected
WAGASCI	ν_μCC0π	63k	P=75%, proton reconstruction: $\epsilon \approx$ 15% at p=500 MeV/c, water in; $\epsilon \approx$ 27% at p=250 MeV/c, water out (15% @ 150MeV/c)
WAGASCI	ν_μCC1π	10k	P=50% (protons as above)
WAGASCI	ν_μCC inclusive	75k	P=96% (protons as above)
200kg Water target emulsion off-axis, 280m	ν_μ CC+NC inclusive	10k-20k	4π automated readout proton > 10-30 MeV detected
200kg Water target emulsion off-axis, 280m	ν_e CC inclusive	1k	4π automated readout proton > 10-30 MeV detected
1kton WC 1 km	ν_μCC0π (1-2°,2-3°,3-4°)	1682k,1060k,519k	$P \approx$92%,95%,95%
1kton WC 1 km	$\bar{\nu}_\mu$CC0π (1-2°,2-3°,3-4°)	519k,331k,186k	$P \approx$74%,77%,76%
1kton WC 1 km	ν_μCC1π (1-2°,2-3°,3-4°)	208k,65k,27k	$P \approx$46%,44%,31%
1kton WC 1 km	ν_eCC0π (1-2°,2-3°,3-4°)	11.2k,6.9k,4.6k	$P \approx$54%,71%,80%
1kton WC 1 km	νNCπ^0 (1-2°,2-3°,3-4°)	300k,111k,45k	$P \approx$58%,63%,60%

TABLE LI. Some of the primary cross section measurements accessible with different elements of the Near Detector Suite (see Sec. **??** for details). The predicted number of events or measurement precision have been evaluated for 10^{21} POT. ϵ = efficiency = number of selected / total events for the given topology, P = purity = number for the given topology / total events selected. For the ND280 measurements only events for a single fine grained detector (FGD1) are projected, the second FGD and other detector components as targets increase the statistical significance. Numbers are obtained either from independent Monte Carlo studies, or extrapolated from the cited references.

V.2. ATMOSPHERIC NEUTRINOS

Cosmic ray interactions with air nuclei provide a continuous flux of both electron and muon neutrinos (and their antiparticles) through the decays of mesons emerging from those interactions. In addition to being produced isotropically about the Earth and therefore yielding neutrinos of pathlengths ranging from $O(10)$ to more than 10,000 km, the neutrino spectrum spans many orders of magnitude. Unlike the beam measurement there is no a priori knowledge of the direction and energy of these neutrinos, so they must be inferred by reconstruction of the particles produced in their interactions. Despite these limitations the large size of Hyper-Kamiokande coupled with its precise reconstruction capabilities makes its atmospheric neutrino sample a useful probe of many types of oscillation physics. In combination with the accelerator neutrino sample, the Hyper-K data have improved sensitivity to many of the open questions in the PMNS oscillation formalism. The following sections describe that sensitivity, first with atmospheric neutrinos alone and then with the combined data set. Sensitivity to the appearance of oscillation-induced ν_τ as well as various types of exotic oscillations are presented elsewhere [**?**].

A. Oscillation Sensitivity with Atmospheric Neutrinos

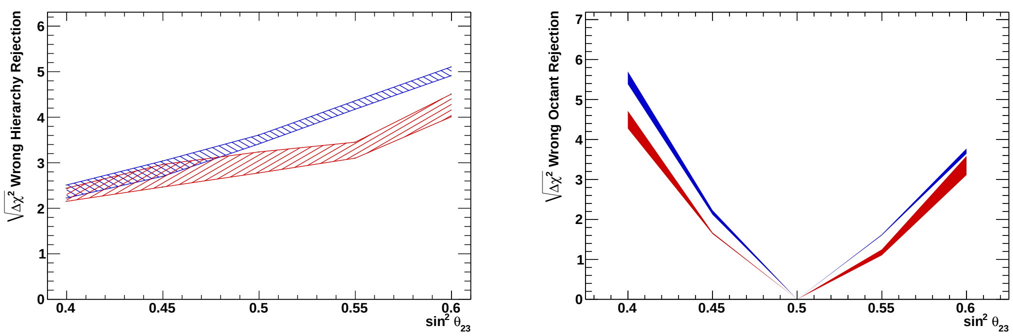

FIG. 185. Neutrino mass hierarchy sensitivity (left) and octant sensitivity (right) as a function of the true value of $\sin^2\theta_{23}$ for a single detector after 10 years. (a 1.9 Mton·year exposure). In both figures the blue (red) band denotes the normal (inverted) hierarchy and the uncertainty from δ_{CP} is shown by the width of the band.

Though the dominant oscillation mode of atmospheric neutrinos is $\nu_\mu \to \nu_\tau$, with the ν_τ going largely undetected, oscillation of the form $\nu_\mu \to \nu_e$ provide sensitivity to the mass hierarchy, δ_{CP}, and additional sensitivity to the octant of θ_{23}. The expected electron neutrino flux at Hyper-K relative to an unoscillated flux can be written approximately as

$$\begin{aligned}\frac{\Psi(\nu_e)}{\Psi_0(\nu_e)} - 1 \approx\ & P_2 \cdot (r \cdot \cos^2\theta_{23} - 1) \\ & -r \cdot \sin\tilde{\theta}_{13} \cdot \cos^2\tilde{\theta}_{13} \cdot \sin 2\theta_{23} \cdot (\cos\delta_{CP} \cdot R_2 - \sin\delta_{CP} \cdot I_2) \\ & +2\sin^2\tilde{\theta}_{13} \cdot (r \cdot \sin^2\theta_{23} - 1),\end{aligned} \tag{5}$$

where $\tilde{\theta}_{13}$ is the effective value of θ_{13} in matter, $\tilde{\theta}_{13} \approx \theta_{13}(1 \pm EV/\Delta m^2_{31}$, where V is the matter potential and $+$ $(-)$ is for neutrinos (antineutrinos). Here R_2 and I_2 are amplitudes and P_2 denotes two-flavor oscillations of $\nu_e \to \nu_x$ driven by the solar mixing parameters. The parameter r is the ratio of the ν_μ to ν_e fluxes prior to oscillations, which decreases from ~ 3 at 10 GeV to ~ 2 at 1 GeV where it stabilizes.

For neutrinos traveling through the Earth, and in particular though its core, matter effects induce resonantly enhanced oscillations of neutrinos while suppressing those of antineutrinos if the mass hierarchy is normal via $\tilde{\theta}_{13}$. On the other hand if nature uses an inverted hierarchy, the roles of neutrinos and antineutrinos are reversed. In practice then the mass hierarchy can be determined by measuring the rate of upward-going electron neutrinos and that sensitivity improves with improved separation between neutrinos and antineutrinos with energies between $2 < E < 10$ GeV. The rate further depends on $\sin^2\theta_{23}$ and to a lesser extent δ_{CP}. At lower energies the impact of larger such that the sub-GeV electron neutrino sample at Hyper-K can be utilized to constrain them. Though not presented in detail here it should be noted that the muon neutrino samples also have sensitivity to these parameters, especially the θ_{23} octant via the same matter effects discussed above.

The Hyper-K atmospheric neutrino analysis follows that of Super-Kamiokande closely and uses 19 analysis samples separated into electron-like and muon-like interactions, which are further divided based on the event topology and energy. Though improvements in the world's understanding of the atmospheric neutrino flux and neutrino interaction modeling are expected in the future no such improvements are assumed in the relevant systematic errors of the present analysis. Figure 185 shows the expected sensitivity to the mass hierarchy and octant after a 1.9 Mton·year exposure. After 10 years with a single Hyper-K detector the hierarchy sensitivity is more than 2σ for all presently allowed values of θ_{23}. Similarly the octant of θ_{23} can be determined at more than 2σ provided $|\theta_{23} - 45°| > 4°|$. Sensitivity to δ_{CP} is largely complimentary to that of the beam sample and is presented below in Figure 187.

B. Combination of Beam and Atmospheric Neutrinos

Hyper-K's sensitivity to oscillations improves markedly when the beam and atmospheric neutrino samples (c.f. Section 5) are combined. Due to the relatively short baseline of the accelerator neutrinos, compared to atmospheric neutrinos they experience weaker matter effects while providing exquisite sensitivity to the atmospheric mixing parameters and δ_{CP}. At the same time it is the uncertainty in these parameters that weaken the atmospheric sample's hierarchy sensitivity. It is possible in principle for normal hierarchy and second octant of θ_{23} to appear as an inverted hierarchy with the first octant of θ_{23} due to the different rates of neutrinos and antineutrinos in the atmospheric neutrino sample and the limited ability of Hyper-K to distinguish between them. Figure 186 shows the sensitivity to the mass hierarchy as a function of running time for the currently allowed values of $\sin^2\theta_{23}$ for the combined beam and atmospheric neutrino data. Unlike the case of atmospheric neutrinos alone, the sensitivity exceeds 3σ for all cases after 10 years. The situation is similar for the octant determination, whose sensitivity is summarized in Table V.2 B.

Metric		1TankHD	
	$\sin^2(\theta_{23})$	Atmospheric ν	Atm + Beam
Hierarchy	0.40	2.2 σ	3.8 σ
Hierarchy	0.60	4.9 σ	6.2 σ
Octant	0.45	2.2 σ	6.2 σ
Octant	0.55	1.6 σ	3.6 σ

TABLE LII. Summary of Hyper-K's sensitivity in various metrics with atmospheric neutrinos only (Atmospheric) and with the combination of atmospheric neutrino and beam data (Atm + Beam) for the staged 1TankHDdesign. These numbers assume a normal hierarchy, $\Delta m^2_{23} = 2.5 \times 10^{-3}\text{eV}^2$, $\sin^2\theta_{13} = 0.0219$, and the value of δ_{CP} that minimizes the sensitivity. Entries in the table are in units of $\sqrt{\Delta\chi^2}$. See text for details.

On the other hand, the beam sample has comparatively little sensitivity to the mass hierarchy, which leads to parameter degeneracies with δ_{CP} when the hierarchy is unknown. Atmospheric neutrinos can resolve these degeneracies via their sensitivity to the hierarchy and at the same time provide complimentary sensitivity to δ_{CP}. This scenario is depicted in the constraint on δ_{CP} as shown in Figure 187. In particular, when the true value of the parameter is 0° the beam-only constraint suffers from erroneous allowed regions near 180° due to parameter degeneracies. Though the atmospheric neutrino sensitivity is weaker it has sufficient power to reject the degenerate solutions, thereby improving the total constraint on δ_{CP}.

Similarly Figure 188 shows the fraction of the δ_{CP} parameter space for which the combined atmospheric and beam neutrino data set can observed CP violation at 3σ significance. For the range of allowed values of θ_{23} and both hierarchies more than 66% of the phase space is covered by Hyper-K.

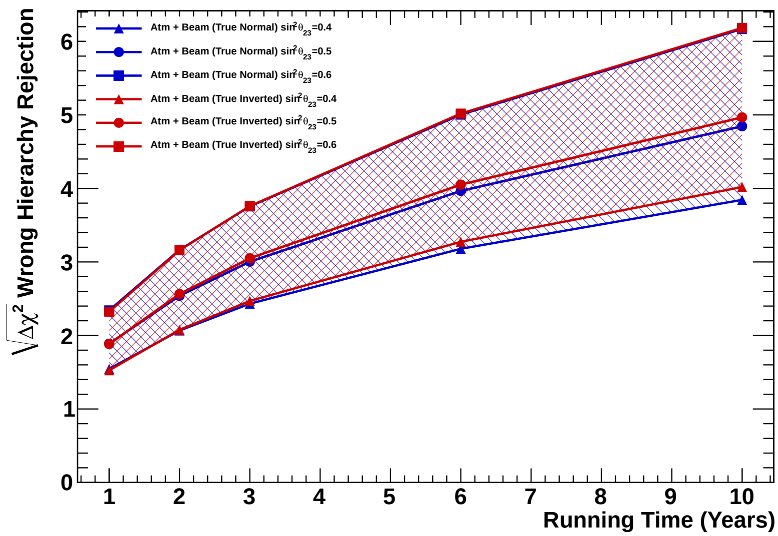

FIG. 186. Expected sensitivity to the mass hierarchy as a function of time assuming $\sin^2\theta_{23} = 0.4$ (triangle), 0.5 (circle), and 0.6 (square) from a combined analysis of atmospheric and accelerator neutrinos data at Hyper-K. Blue (red) colors denote the normal (inverted) hierarchy.

V.3. PROTON DECAYS

Though baryon number is explicitly conserved in the Standard Model Lagrangian its violation is thought to have a critical role in the evolution of the early universe and is expected to be a key ingredient to understanding the matter-antimatter asymmetric universe observed today. One of the hallmarks of Grand Unified Theories (GUT) is their predictions of proton and bound nucleon decays, both of which are processes that violate baryon number. Such theories can additionally provide explanations for the observed pattern of quark and lepton charges, often have mechanisms for generating neutrino masses, and introduce new force carries at energy scales around 10^{16} GeV, well beyond the reach of present accelerator technologies. Accordingly, the search for proton decay at Hyper-Kamiokande is an important port of its physics program, not only for the purpose of studies these theories but for understanding the development of the early universe.

In general GUTs provide interactions that can induce transitions between quarks and leptons and thereby predict a variety of potential nucleon decay modes. The following sections provide descriptions of Hyper-K's sensitivity to $p \to e^+\pi^0$ and $p \to \bar{\nu} K^+$, favored decay modes from two dominant classes of GUT models, the experiment is expected to have world-leading sensitivity to several other channels. Interested readers may refer to Ref. [**?**] for more details.

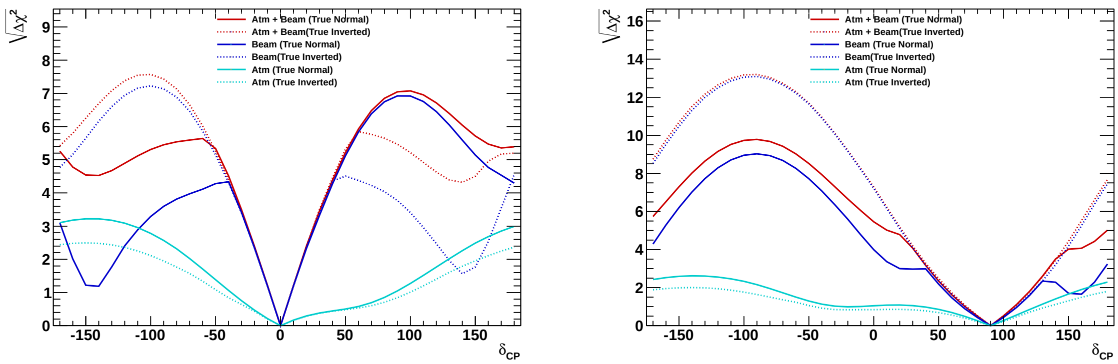

FIG. 187. Constraints on δ_{CP} after a 10 year exposure of Hyper-K assuming the normal mass hierarchy. Cyan and blue lines show the constraint from the atmospheric neutrino sample and beam neutrino sample individually, whereas the constraint from their combination appears in the red line. The left (right) figure assumes the true value of δ_{CP} is 0° (90°). Solid and dashed lines denote the normal and inverted hierarchies, respectively.

A. Search for $p \rightarrow e^+\pi^0$

Proton decay into a positron and a neutral pion is two body process which creates a back-to-back topology of three electromagnetic showers within Hyper-K: two showers from the pion decay appear opposite that from the positron. In the absence of intra- or extra-nuclear hadronic scatters, there are no invisible particles in the final state, making it possible to fully reconstruct the mass and momentum of the initial proton. The focus of the analysis is searching events that are reconstructed near the proton mass $800 < m_{inv} < 1050$ GeV/c and with a low total momentum from the sum of all visible particles. As Hyper-K's target material water contains both eight protons bound in the oxygen nucleus and two free protons from its hydrogen atoms separate total momentum cuts are applied to enrich the signal sample. Free protons are expected to decay nearly at rest and as a result the total momentum is required to be $p_{tot} < 100$ MeV/c, whereas bound protons may have non-zero momenta due the Fermi motion and correlated nucleon effects so the threshold is $100 < p_{tot} < 250$ MeV/c.

The primary background to this and all nucleon decay searches is atmospheric neutrinos. Indeed, charged current single-pion production processes such as $\nu_e + n \rightarrow e^- + \pi 0 + p$, where the proton is below Cerenkov threshold, can in principle have the same event topology as the signal. The problem is confounded by the presence of nuclear effects which can produce pions from the recoiling nucleon in a quasi-elastic scatter and thereby mimic a proton decay event. Neutron tagging at Hyper-K

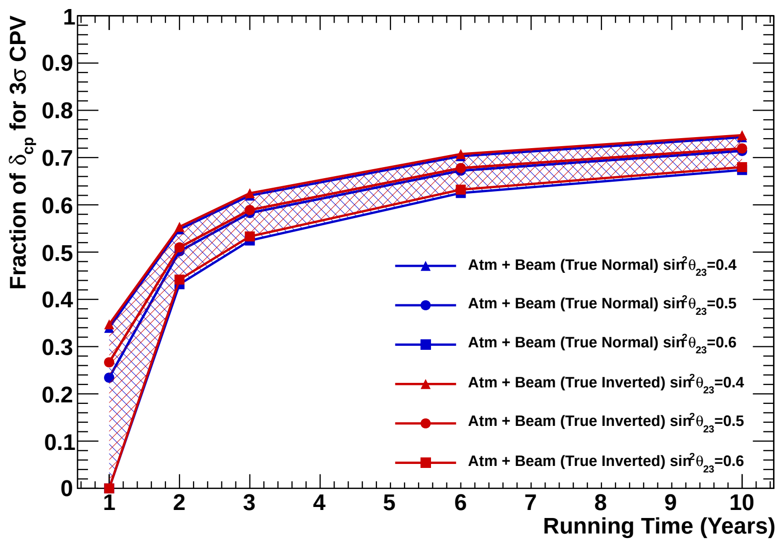

FIG. 188. Fraction of δ_{CP} phase space at which a 3σ observation of CP violation can be made as a function of time assuming $\sin^2\theta_{23} = 0.4$ (triangle) , 0.5 (circle) , and 0.6 (square) from a combined analysis of atmospheric and accelerator neutrinos data at Hyper-K. Blue (red) colors denote the normal (inverted) hierarchy.

is expected to be 70% efficient and therefore a powerful tool for reducing atmospheric neutrino backgrounds. Since proton decays are only rarely expected to produce a neutron in the final state (via the de-excitation of the parent oxygen nucleus) requiring signal candidates have no tagged neutrons reduces the background contamination by 75% without affecting the signal efficiency. Table LIII shows the expected signal efficiency and background rates for the $p \to e^+\pi^0$ search together with their systematic uncertainties.

$0 < p_{tot} < 100$ MeV/c		$100 < p_{tot} < 250$ MeV/c	
ϵ_{sig} [%]	Bkg [/Mton·yr]	ϵ_{sig} [%]	Bkg [/Mton·yr]
18.7 ± 1.2	0.06 ± 0.02	19.4 ± 2.9	0.62 ± 0.20

TABLE LIII. Signal efficiency and background rates as well as estimated systematic uncertainties for the $p \to e^+\pi^0$ analysis at Hyper-K.

Figure 189 shows the one-sided 3σ discovery potential for observing a $p \to e^+\pi^0$ signal based on these estimates. Projections from other experiments including DUNE and Super-K as well as the expectation for two Hyper-K tanks, one starting six years after the first, are shown for comparison.

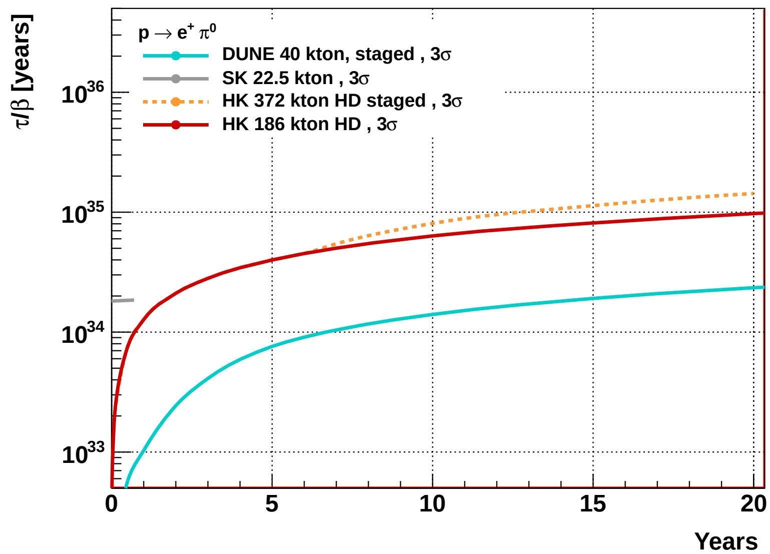

FIG. 189. Comparison of the 3 σ $p \to e^+\pi^0$ discovery potential as a function of year Hyper-K (red solid) assuming a single tank as well as that of the 40 kton liquid argon detector DUNE (cyan solid) following [**?**]. In the orange dashed line an additional Hyper-K tank is assumed to come online six years after the start of the experiment. Super-K's discovery potential in 2026 assuming 23 years of data is also shown.

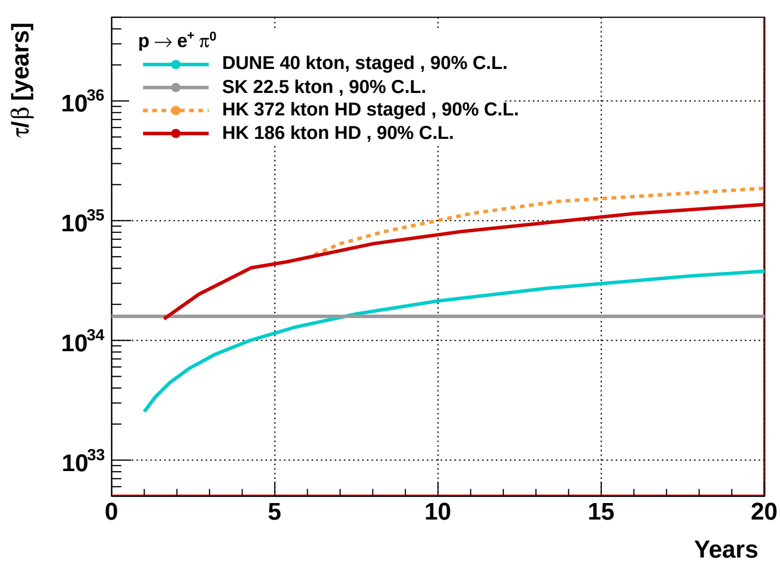

FIG. 190. Hyper-K's sensitivity to the $p \to e^+\pi^0$ decay mode at 90% C.L. as a function of run time appears in red assuming one detector in comparison with other experiments (see caption of Figure 189). Super-K's current limit is shown by a horizontal line.

With only one Hyper-K tank a proton decay signal can be observed at 3σ if the proton lifetime is less than 10^{35} years with a 20 year exposure. In the event that a signal is not observed, Hyper-K is expected to produce limits as shown in Figure 190. After a 15 year exposure the lifetime limit on decay into this mode will exceed 10^{35} years. It should be noted that Hyper-K leads other experiments by nearly an order of magnitude in both metrics.

B. Search for $p \to \overline{\nu} K^+$ decays

Often supersymmetric GUT models predict proton decay into a neutrino and a charged kaon. Unlike the search for $e^+\pi^0$ events it is not possible to fully reconstruct the initial proton kinematics since the neutrino is essentially invisible to Hyper-K. Further, the Kaon is emitted with momentum of 340 MeV/c, which is well below its Cerenkov threshold in water. Searching for this decay mode is Hyper-K is done based on identifying a monochromatic kaon with the appropriate momentum by reconstructing its decay particles.

The search proceeds in three parts with each focused on a different aspect of the K^+ decay. Two of these use the $K^+ \to \nu + \mu^+$ decay mode (64% branching fraction) and search for a single 236 MeV/c muon. Muon candidates are required to have momenta in the range $215 < p_\mu < 260$ MeV/c, there is a considerable background from atmospheric neutrinos. While one search mode attempts to fit a proton decay signal excess above this background, the other further isolates the signal using the decay time of the kaon. For proton decays inside oxygen the de-excitation of the resulting ^{15}N nucleus will produce a prompt 6.3 MeV γ ray that should proceed the kaon decay. Accordingly, the search for this process seeks to identify a low energy photon occurring prior to and separated in time from the kaon's monochromatic muon $t_\mu - t_\gamma < 75$ ns ($\sim 6\tau_K$). The improved timing resolution of the Hyper-K is expected to provide a higher signal efficiency than achieved in previous experiments.

Kaon decay into a charged and neutral pion, $K \to \pi^+\pi^0$, is the target of the third search. Though the photons from the π^0 are easily visible in Hyper-K, the 205 MeV/c momentum of the π^+ is not sufficiently above its Cerenkov threshold to produce enough light to fully reconstruct a ring. The analysis proceeds by identifying photons which reconstruct to an invariant mass consistent with a neutral pion, $85 < m_{\gamma\gamma} < 195\text{MeV/c}^2$ and searching for 7 to 17 MeV of visible energy deposited more than 140 degrees behind the direction of the π^0 candidate. A likelihood method is employed to determine whether or not this energy deposition is consistent with the expectation of a low momentum π^+.

Strangeness-conserving kaon production processes such as, $\nu + p \rightarrow \nu K^+ \Lambda (\Lambda \rightarrow p\pi^-)$, and quasi-elastic scattering from muon neutrinos accompanying by prompt γ emission from the recoiling nucleus for the dominant atmospheric neutrino backgrounds. In both cases the final state topologies are identical to the signal since protons in such reactions are produced below the Cerenkov threshold. As in the search for proton decay into $e^+\pi^0$ neutron tagging reduces the expected background by more than 50%. Signal efficiencies and background estimates are presented with their estimated uncertainties in Table [**?**].

Prompt γ		$\pi^+\pi^0$		p_μ Spectrum		
ϵ_{sig} [%]	Bkg [/Mton·yr]	ϵ_{sig} [%]	Bkg [/Mton·yr]	ϵ_{sig} [%]	Bkg [/Mton·yr]	σ_{fit} [%]
12.7 ± 2.4	0.9 ± 0.2	10.8 ± 1.1	0.7 ± 0.2	31.0	1916.0	8.0

TABLE LIV. Signal efficiency and background rates as well as estimated systematic uncertainties for the $p \rightarrow \bar{\nu} K^+$ analysis at Hyper-K.

Figures 191 and 192 show the 3σ discovery potential and 90% C.L. sensitivity as a function of running time for the $p \rightarrow \bar{nu} K^+$ search. Both figures compare Hyper-K with other future experiments. Though Hyper-K has a larger total volume its relatively low signal efficiency places its sensitivity between that of the DUNE and JUNO experiments. If the proton lifetime is near the current Super-K limit of $\sim 7 \times 10^{34}$ years Hyper-K would expect to see a signal at 3σ significance in its first three years of running. After a 10 year exposure a signal would be observed if the lifetime is less than three times longer than the present limit. Assuming no signal is observed, Hyper-K will improve on the existing limit by a factor of four or five in the same time period.

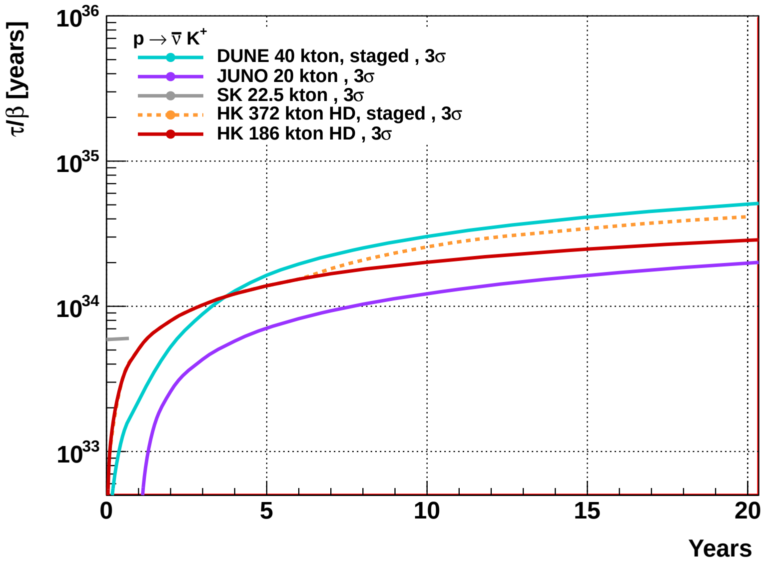

FIG. 191. Comparison of the 3 σ $p \to \bar{\nu}K^+$ discovery potential as a function of year for the Hyper-K as well as that of the 40 kton DUNE detector (cyan solid) based on [**?**] and the 20 kton JUNO detector based on [**?**]. The red line denotes a single Hyper-K tank, while the orange line shows the expectation when a second tank comes online after six years. The expected discovery potential for Super-K by 2026 assuming 23 years of data is also shown.

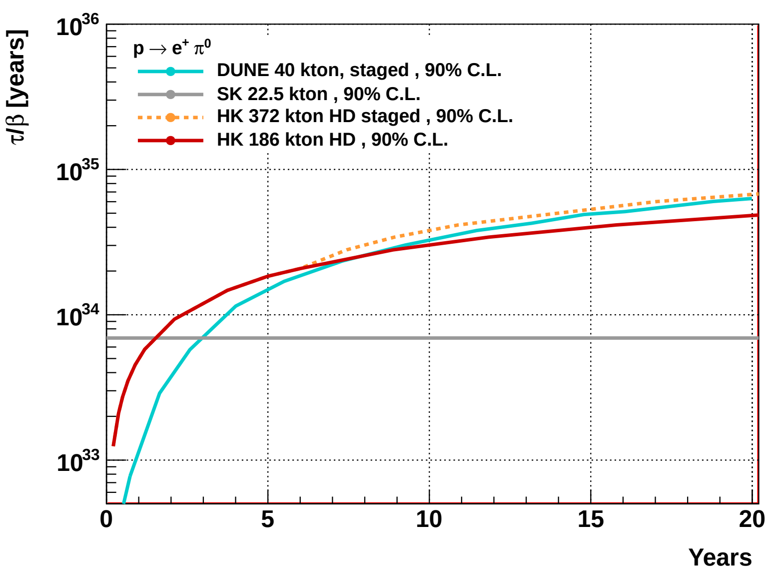

FIG. 192. Hyper-K's sensitivity to the $p \to \bar{\nu}K^+$ decay mode at 90% C.L. as a function of run time is shown in red against other experiments (see caption of Figure 191). Super-K's current limit is also shown.

V.4. SOLAR NEUTRINOS

Solar neutrinos are generated as nuclear fusion products in the Sun, and their measurements have contributed much to the development of neutrino physics and astrophysics. The neutrino oscillation parameters between mass eigenstate ν_1 and ν_2 are determined based on the solar neutrino data and the reactor anti-neutrino data in KamLAND assuming CPT invariance, as illustrated in Fig. 193 [**?**]. The mixing angle θ_{12} is consistent between solar and reactor data, however, about 2σ tension exists in Δm^2_{21}. Owing to the MSW matter oscillation in the Sun and the Earth, the solar data is sensitive to Δm^2_{21} in spite of the long flight distance. The constraint on Δm^2_{21} comes mainly from the Super-K data observing the zenith angle and energy dependent neutrino fluxes. The observed day-night flux asymmetry is $\sim$4%, which is higher than the expectation from the reactor data, and contributes to the 2σ tension. Hyper-K will have a better sensitivity on the day-night asymmetry, and clarify the new problem in the neutrino oscillations which might be a key to the discovery of new physics. In addition, if the energy threshold is lowered, the observation of the upturn in the solar neutrino survival probability might be possible. The precise spectrum shape measured in Hyper-K will distinguish the standard neutrino oscillation from several exotic models,

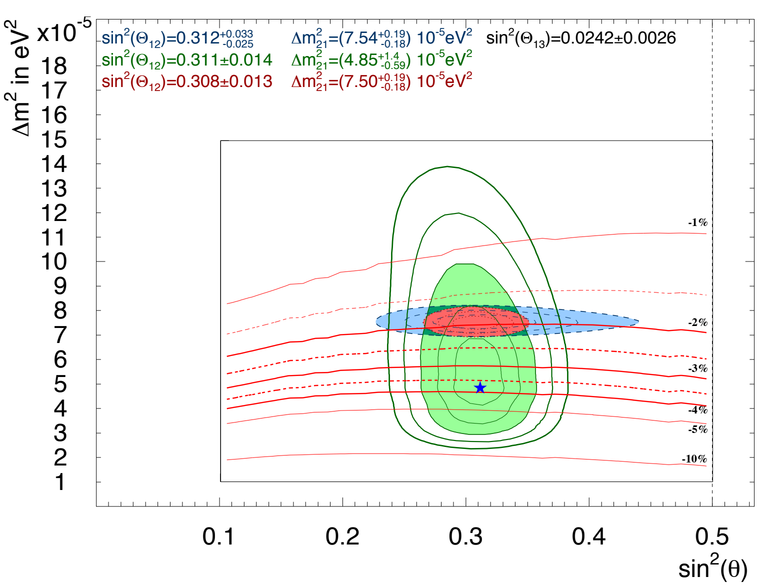

FIG. 193. Allowed neutrino oscillation parameter region from all the solar neutrino experiments (green), reactor neutrino from KamLAND (blue) and combined (red) from one to five sigma lines and three sigma filled area. The star shows the best fit parameter from the solar neutrinos. The contour of the expected day-night asymmetry with 6.5 MeV (in kinetic energy) energy threshold is overlaid.

such as non-standard interaction [?], MaVaN [?], and sterile neutrino [?]. In solar physics, the solar neutrinos are an important probe to investigate ongoing fusion conditions in the core region of the Sun. Hyper-K, with its unprecedented statistical power, will measure the short-period flux variations, realizing a real-time monitor of the Sun's core temperature in the solar core. Hyper-K could also achieve the first measurement of hep solar neutrinos, providing new information on solar physics.

1. Background estimation

The major background sources for the ^{8}B solar neutrino measurements are the radioactive spallation products created by cosmic-ray muons [?] and the radioactive daughter isotopes of ^{222}Rn in water. The muon flux is about five times higher in Hyper-K compared to Super-K because of its shallow depth. Assuming the naive scaling by the increase in the muon flux and the detector size, the muon trigger rate in Hyper-K is ∼45 Hz, which corresponds to ∼15 times of the Super-K rate (∼3 Hz). The muon spallation background rate in Hyper-K will be 2.7 times of Super-K considering the energy dependence in the spallation reaction and the future improvement in the spallation cut method. As the radioactive daughter isotopes, ^{222}Rn is an important background source for the spectrum upturn measurement. First of all, the water purification system must achieve ^{222}Rn levels similar to Super-K. Furthermore, this background level must be achieved across the full fiducial volume, unlike at Super-K, where only a limited volume can be used for events with less than 5 MeV. It is a challenging task but we believe that this should be possible by design improvements over the next several years. Therefore, the same ^{222}Rn background level as Super-K in full fiducial volume is assumed in the following calculation.

2. Oscillation studies

For the day-night asymmetry study in Hyper-K, we assume the analysis energy threshold of 6.5 MeV in kinetic energy. In this energy region, the dominant background comes from muon spallation products. The spallation backgrounds in Super-K phase IV (40% photo-coverage) has been reduced by a factor three comparing to Super-K phase II (20% photo-coverage), owing to the better energy and vertex resolutions in Super-K phase IV. From this experience, the spallation background in Hyper-K will be reduced by a factor three from Super-K phase IV considering the higher photon detection efficiency. Figure 194 (Left) shows the sensitivity on the day-night

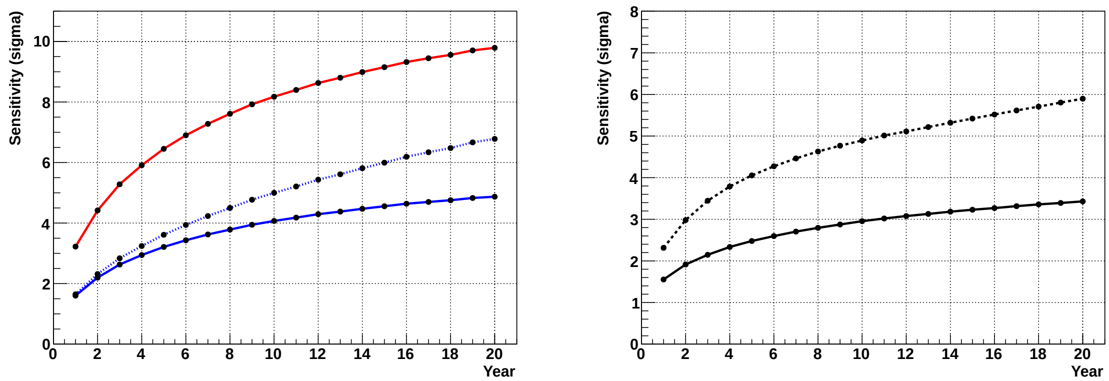

FIG. 194. (Left) Day-night asymmetry observation sensitivity as a function of observation time. The red line shows the sensitivity from the no asymmetry, while the blue line shows from the asymmetry expected by the reactor neutrino oscillation. The solid line shows that the systematic uncertainty which comes from the remaining background direction is 0.3%, while the dotted line shows the 0.1% case. (Right) Spectrum upturn discovery sensitivity as a function of observation time. The solid line shows that the energy threshold is 4.5 MeV, while the dotted line shows the 3.5 MeV.

asymmetry as a function of the observation time. The Δm^2_{21} separation ability between solar neutrino (Hyper-K) and reactor anti-neutrino (KamLAND) is expected to reach $4{-}5\sigma$ level in ten year observation.

For the observation of the spectrum upturn, the critical background source is ^{222}Rn producing the resolution tail of ^{214}Bi decays (3.27 MeV end-point energy). In Hyper-K, such backgrounds can be significantly reduced owing to the better energy resolution. In addition to that, we need to plan precise calibrations to control systematic uncertainties. In this sensitivity study, we assume Hyper-K have the same ^{222}Rn rate and the same calibrations with Super-K. Figure 194 (Right) shows the sensitivity of the spectrum upturn discovery as a function of the observation time. It is about 3σ level in ten years observation with 4.5 MeV energy threshold.

3. Hep solar neutrino

Hep solar neutrino produced by the ^{3}He + p fusion reaction has the highest energy in solar neutrinos. But, most of the hep energy spectrum is overlapped with ^{8}B solar neutrinos, whose expected flux is more than 100 times larger than hep's. The better energy resolution in Hyper-K is advantageous for the hep solar neutrino detection, because the resolution tail of ^{8}B solar neutrino events is mitigated. Assuming the spallation background rejection efficiency in SK-IV solar analysis, the expected uncertainty of the hep neutrino flux measurement will be $\sim$60% ($\sim$40%), and the non-zero significance will be 1.8σ (2.3σ) in ten (twenty) years observation in Hyper-K.

TABLE LV. Expected number of neutrino events from Galactic supernova (10 kpc) in Hyper-K with the detection threshold of 3 MeV. Our references for each neutrino cross-section are also shown.

Neutrino source	Single Tank (220 kt Full Volume)	2 Tanks (440 kt Full Volume)	Ref.
$\bar{\nu}_e + p$	50,000 - 75,000 events	100,000 - 150,000 events	[?]
$\nu + e^-$	3,400 - 3,600 events	6,800 - 7,200 events	[?]
$\nu_e +^{16}$ O CC	80 - 7,900 events	160 - 11,000 events	[?]
$\bar{\nu}_e +^{16}$ O CC	660 - 5,900 events	1,300 - 12,000 events	[?]
$\nu + e^-$ (Neutronization)	9 - 55 events	17 - 110 events	[?]
Total	54,000 - 90,000 events	109,000 - 180,000 events	

V.5. SUPERNOVA NEUTRINOS

In the gravitational collapse of massive stars ($> 8\mathrm{M}_\odot$) which will go on to form either a neutron star or a black hole, almost 99% of the released energy is carried out by neutrinos. So the detection of supernova neutrinos gives direct information of energy flow during the explosion. The observation of supernova neutrinos from SN1987A proved that the basic scenario of the supernova explosion was correct, however, more than three decades later the detailed mechanism of explosions is still unknown. Among the current or planned experiments, Hyper-K has several advantages: the high statistics of neutrino events owing to the large volume, the low detection threshold of 3 MeV, and the event-by-event directional sensitivity. It will allow the comprehensive study of supernova neutrinos. The expected number of supernova neutrino events in Hyper-K is summarized in Table LV. This high statistics data will provide key information on the supernova explosion mechanism and neutrino oscillations.

1. *Expected observation in Hyper-Kamiokande*

Expected time profiles for various interactions in Hyper-K, inverse beta decay ($\bar{\nu}_e + p \to e^+ + n$), νe-scattering ($\nu + e^- \to \nu + e^-$), ν_e+^{16}O CC ($\nu_e + ^{16}\mathrm{O} \to e^- + ^{16}\mathrm{F}^{(*)}$), and $\bar{\nu}_e$+^{16}O CC ($\bar{\nu}_e + ^{16}\mathrm{O} \to e^+ + ^{16}\mathrm{N}^{(*)}$), for a supernova at a distance of 10 kpc are shown in Fig. 195. The burst time period is about 10 s and the peak event rate of inverse beta decay events reaches about 50 kHz at 10 kpc. The DAQ and its buffering system of Hyper-K will be designed to accept the broad range of rates, for a galactic supernova closer than 10 kpc. A sharp timing spike is expected for νe-scattering events at the time of neutronization. The Hyper-K can observe about 50,000 to 75,000 inverse beta decay events, 3,400 to 3,600 νe-scattering events, 80 to 7,900 ν_e+^{16}O CC events, and 660 to

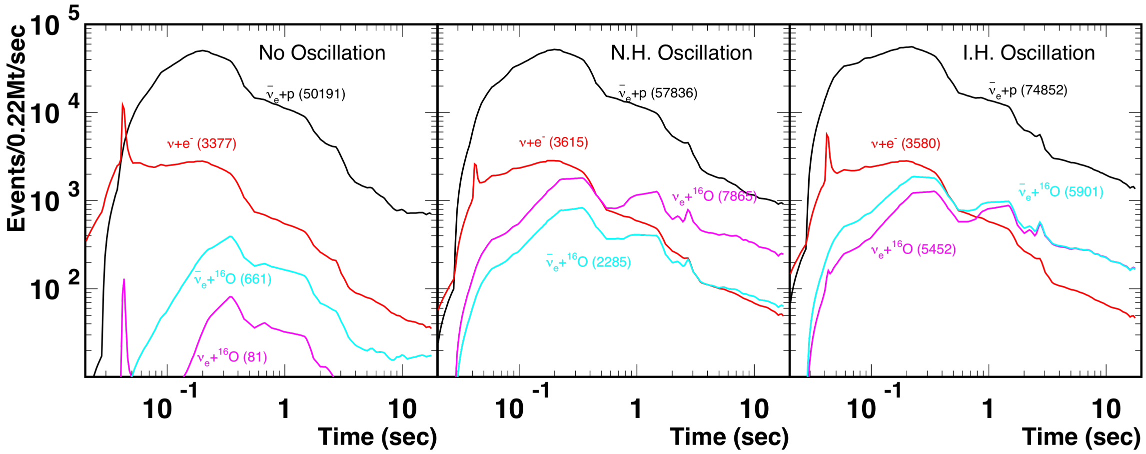

FIG. 195. Expected time profile of a supernova at 10 kpc. Left, center, and right figures show profiles for no oscillation, normal hierarchy, and inverted hierarchy, respectively. The numbers in parentheses are integrated number of events over the burst. The fluxes and energy spectra are from the Livermore simulation [**?**].

TABLE LVI. Expected total number of neutrino events from supernovae at 10 kpc (galactic center) and 200 pc (Betelgeuse) in Hyper-K.

time window	10 kpc (galactic center)	200 pc (Betelgeuse)
0−1 sec	24,000 - 30,000 events	60,000,000 - 75,000,000 events
0−10 sec	47,000 - 72,000 events	117,500,000 - 180,000,000 events

5,900 $\bar{\nu}_e$ + ^{16}O CC events, in total 54,000 to 90,000 events, for a 10 kpc supernova. The range of each of these numbers covers possible variations due to the neutrino oscillation scenario (no oscillation, normal hierarchy, and inverted hierarchy). Even for a supernova at M31 (Andromeda Galaxy), about 10 to 16 events are expected at Hyper-K. In the case of the Large Magellanic Cloud (LMC) where SN1987A was located, about 2,200 to 3,600 events are expected. The expected total number of neutrino events from supernovae at 10 kpc (galactic center) and 200 pc (Betelgeuse) for each time window after the onset of the burst are shown in Table LVI, which gives estimates on the temporal trigger rate.

2. Physics impacts

The shape of the rising time of supernova neutrino flux and energy strongly depends on the model. Figure 196 shows inverse beta decay event rates and mean $\bar{\nu}_e$ energy distributions predicted by various models [**? ? ? ? ? ? ?**] for the first 0.3 s after the onset of a burst. The statistical error

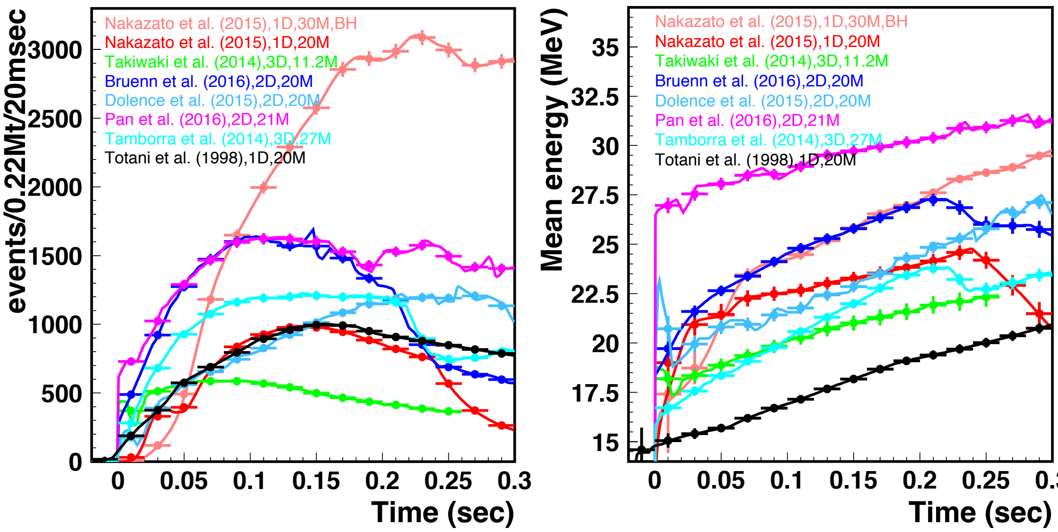

FIG. 196. Time profiles of the observed inverse beta decay event rate (left) and mean energy of these events (right), predicted by supernova simulations [? ? ? ? ? ? ?] for the first 0.3 s after the onset of a 10 kpc distant burst.

is much smaller than the difference between the models, so Hyper-K should give crucial data for comparing model predictions. Our measurement will also provide an opportunity to observe black hole formation directly, as a sharp drop of the neutrino flux [?]. In addition, recent computer simulation studies predict new characteristic modulations of the supernova neutrino flux due to the dynamic motions in the supernovae. The stall of shock wave after core bounce has been an issue in supernova computer simulations, which was not able to achieve successful explosions. These dynamic motions enable the inner materials to be heated more efficiently by the neutrinos from collapsed core, and realize the shock wave revival. One source of such modulation is the Standing Accretion Shock Instability (SASI) [? ? ?]. Under the assumption of a 3% flux modulation which depends on progenitor mass or equation of states [?], we will have chances to prove SASI effects for ∼90% of galactic supernovae with Hyper-K, compared with only ∼15% with Super-K.

Neutrino oscillations in high density matter could be studied using supernova neutrino events [? ? ? ? ? ? ?]. While it requires complicated calculations for collective and MSW effects [? ? ? ? ?], the supernova neutrino measurement could determine the neutrino mass hierarchy. The first chance is the neutronization burst, because pure ν_e from the proto-neutron star have no collective effect through $\nu_e\bar{\nu}_e \to \nu_x\bar{\nu}_x$. The flux is well predicted and hardly affected by the physics modeling of the EOS or the progenitor mass [? ?]. In Hyper-K, the expected number of event is about 50% larger in the inverted hierarchy case comparing to the normal hierarchy, after 20 ms from the core bounce. In the succeeding accretion phase, we will have another chance by observing the

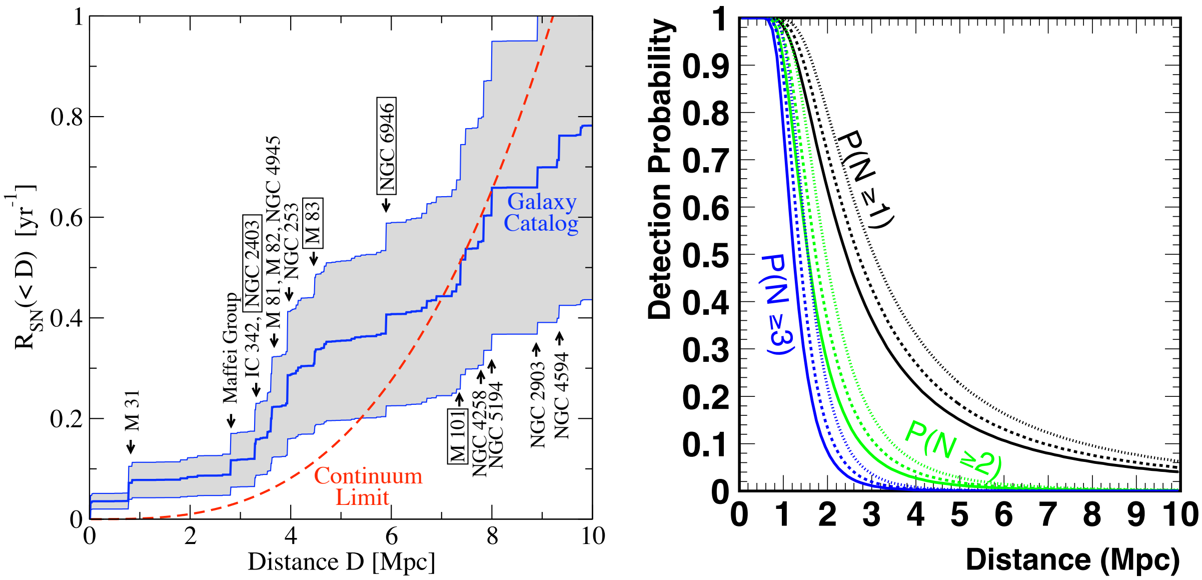

FIG. 197. (Left) Cumulative calculated supernova rate versus distance for supernovae in nearby galaxies. The dashed line is core-collapse supernova rate expectation, using the $z = 0$ limit of star formation rate measured by GALLEX. The figure is reproduced from ref. [**?**]. (Right) Detection probability of supernova neutrinos versus distance at Hyper-K assuming a 187 kton fiducial volume and 10 MeV threshold for this analysis. Black, green, and blue curves show the detection efficiency resulting in requiring more than or equal to one, two, and three events per burst, respectively. Solid, dotted, and dashed curves are for neutrino oscillation scenarios of no oscillation, normal hierarchy, and inverted hierarchy, respectively.

rise-time of neutrino event rate. The mixing of $\bar{\nu}_x$ to $\bar{\nu}_e$, will result in a 100 ms faster rise time for the inverted hierarchy compared to the normal hierarchy case [**?**].

3. Supernovae in nearby galaxies

In Hyper-K, it could be possible to detect burst neutrinos from supernovae in nearby galaxies. The supernovae rate in nearby galaxies was discussed in [**?**] and a figure from the paper is shown in Fig. 197 (Left). It shows the cumulative supernova rate versus distance and indicates that if Hyper-K can see signals out to 4 Mpc then we could expect a supernova about every three years. It should be noted that recent astronomical observations indicate about 3 times higher nearby supernova rate [**?**], compared to the conservative calculation. It is also valuable to mention that two strange supernovae have been found at $\sim$2 Mpc distance in the past 11 years observation, which are called dim supernovae [**?**]. The detections of supernova neutrinos from these dim supernovae will prove their explosion mechanism is core-collapse. Figure 197 (Right) shows detection probability versus distance in Hyper-K. Requiring the number of neutrino events to be more than or equal to two (one), the detection probability is 27% to 48% (64% to 80%), for a supernova at 2 Mpc. The probability will be 3% to 6% (22% to 33%) for the supernovae at 4 Mpc. If we can use a tight timing coincidence with other types of supernova sensors (*e.g.* future gravitational wave detectors), we should be able to identify even single supernova neutrinos.

4. High-energy neutrinos from supernovae with interactions with circumstellar material

Core-collapse supernovae are promising sources of high-energy ($\gtrsim$ GeV) neutrinos as well as multi-MeV neutrinos. If the supernova shock becomes collisionless after a shock breakout, the conventional cosmic-ray (CR) acceleration starts to be effective [**?** **?**]. In the early phase just after the breakout, the matter density is still high, so that accelerated CRs are efficiently used for neutrino production via inelastic *pp* scatterings. For type II supernovae, the released energy of high-energy neutrinos is typically $\mathcal{E}_\nu \sim 10^{47}$ erg [**?**]. One to two events of GeV neutrinos are expected in a timescale of hours after the core-collapse for a Galactic supernova at 10kpc in Hyper-K 1 tank. About 10% of core-collapse supernovae show strong interactions with ambient circumstellar material. If the circumstellar material mass is $\sim$ 0.1-1 $M_\odot$, the released high-energy neutrino energy reaches $\mathcal{E}_\nu \sim 10^{49}$-$10^{50}$ erg [**?**]. High-energy neutrinos from supernovae are detectable hours to months after the core-collapse, and detecting the signals will give us new insights into supernova physics.

5. Supernova relic neutrinos

The neutrinos produced by all of the supernova explosions since the beginning of the universe are called supernova relic neutrinos (SRN) or diffuse supernova neutrino background (DSNB). Figure 198 shows the SRN spectra predicted by various models. The expected inverse beta ($\bar{\nu}_e + p \to e^+ + n$) event rate at Super-Kamiokande (SK) is 0.8-5 events/year above 10 MeV, but no evidence of SRN signals has yet been obtained because of the small flux of SRN and large background events in SK.

In order to reduce background, lower the energy threshold, individually identify true inverse beta events by tagging their neutrons, and thereby positively detect SRN signals at SK, a project to add 0.1% gadolinium (Gd) to SK detector (the SK-Gd project, called GADZOOKS! [**?**] previously) is ongoing. As a first step of the SK-Gd project, a refurbishment work of the current SK detector was started in June 2018.

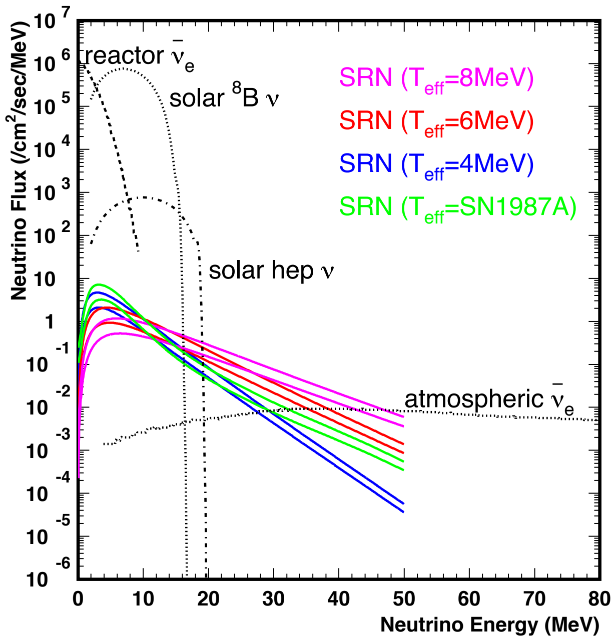

FIG. 198. Predictions of the supernova relic neutrino (SRN) spectrum. Fluxes of reactor neutrinos and atmospheric neutrinos are also shown [?].

The first observation of the SRN could be made by the SK-Gd project. However, a megaton-scale detector is still desired to measure the spectrum of the SRN and to investigate the history of the universe because of its huge statistics as shown in Fig. 199. Furthermore, Hyper-K could

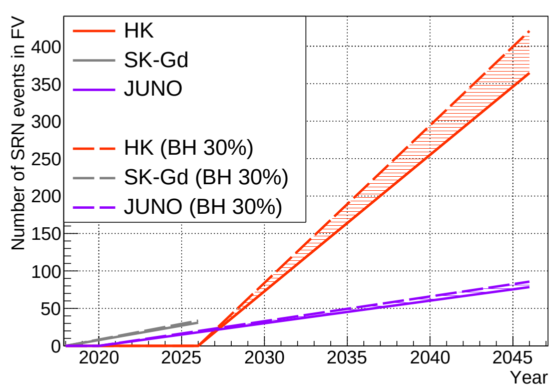

FIG. 199. Expected number of inverse beta decay reactions due to supernova relic neutrinos in several experiments as a function of year. Red, gray and purple line shows Hyper-Kamiokande, SK-Gd, and JUNO, respectively. The sizes of their fiducial volume and analysis energy thresholds were considered. The neutrino temperature is assumed to be 6MeV. Solid line corresponds to the case, in which all the core-collapse supernovae emits neutrinos with the particular energy. Dashed line corresponds to the case, in which 30% of the supernovae form black hole and emits higher energy neutrinos corresponding to the neutrino temperature of 8 MeV.

measure the SRN neutrinos at E = 16-30 MeV, while the SK-Gd project concentrates on the energy of 10-20 MeV. These observation at a different energy region can measure the contribution of extraordinary supernova bursts on the SRN, e.g. black hole formation [**?** **?**].

Considering the event selection efficiency after spallation product background reduction, the expected number of SRN events in E = 16 to 30 MeV is about 70 after 10 years observation with Hyper-K 1 tank. The statistical error will be 17 events, corresponding to an observation of SRN in the energy range 16 to 30 MeV with 4.2 σ significance. Here, we assumed the flux prediction described in ref. [**?**] and neutron tagging using $n+p \rightarrow d+\gamma$ (2.2 MeV) with the tagging efficiency of 70%.

It is still important to measure the SRN spectrum down to $\sim$ 10 MeV in order to explore the history of supernova bursts back to the epoch of red shift (z) $\sim$1. Therefore, adding 0.1% Gd to Hyper-K, we assume that an analysis with a lower energy threshold of $\sim$ 10MeV is possible with gadolinium neutron tagging. The expected number of SRN events in the energy range of 10-30 MeV is about 280 with 10 years of live time with Gd-loaded Hyper-K 1 tank.

V.6. OTHER ASTROPHYSICAL NEUTRINOS

A. WIMP dark matter searches

It is thought that the self-interaction or decay of WIMP-type dark matter particles bound in strong gravitational potentials, such as the milky way galaxy or our sun, may produce standard model particles. In particular, neutrinos may be produced either through direct annihilation or decay of dark matter particles or through the decays of heavier particles produced in these processes, and can be observed at Hyper-K.

In the analyses below WIMP dark matter is assumed to produce standard model particles such as $\chi\chi \to W^+W^-$, $\tau^+\tau^-$, $b\bar{b}$, $\mu^+\mu^-$, and $\nu\bar{\nu}$ each with 100% branching fraction. In this estimation, the DarkSUSY package [**?**] is used. Then, the angular distributions to the sources (galactic center, the sun, or the Earth) are studied to extract the dark matter signal from the atmospheric neutrino sample described in Section V.2. Hyper-K is expected to have superior sensitivity to lower mass (below 100 GeV/c^2) WIMPs.

Figure 200 shows typical angular distributions of the atmospheric neutrino background and WIMP signal samples. The WIMP signal samples show peaks in the source direction.

Figure 201 left shows the expected sensitivity of Hyper-K to WIMP annihilations at the galactic center. This search method can place the limits on the velocity averaged self-annihilation cross section, $< \sigma \times v >$, where v is the assumed velocity distribution of WIMPs in the halo. Since Hyper-K can reconstruct down to $O(100)$ MeV neutrino interactions, Hyper-K has better sensitivities to WIMPs with masses less than $\sim$ 100 GeV/c^2.

For WIMPs trapped gravitationally within the Earth (or sun), if these pair annihilate and produce neutrinos, they will escape the core of the Earth (or sun) and be detectable at Hyper-K. Since the Earth is composed of heavy nuclei (relative to hydrogen) it is further possible to study WIMP interactions that are not coupled to the nuclear spin (spin independent, SI). In this analysis, the WIMPSIM package [**?**], which accounts for the passage of particles through terrestrial matter, is used. Limits on the WIMP-induced neutrino flux are translated into limits on the WIMP-nucleon SI cross sections using the DarkSUSY simulation.

Figure 201 right shows the sensitivity to the WIMP-nucleon SI cross section for masses $m_\chi >$ 4GeV/c^2. These limits have been produced assuming WIMPs have only SI interactions and have been estimated for $\chi\chi \to W^+W^-, b\bar{b}$, and $\tau^+\tau^-$. Hyper-K's is expected to produce limits a factor of 3 $\sim$ 4 times stringent than Super-K if no WIMP signal is seen.

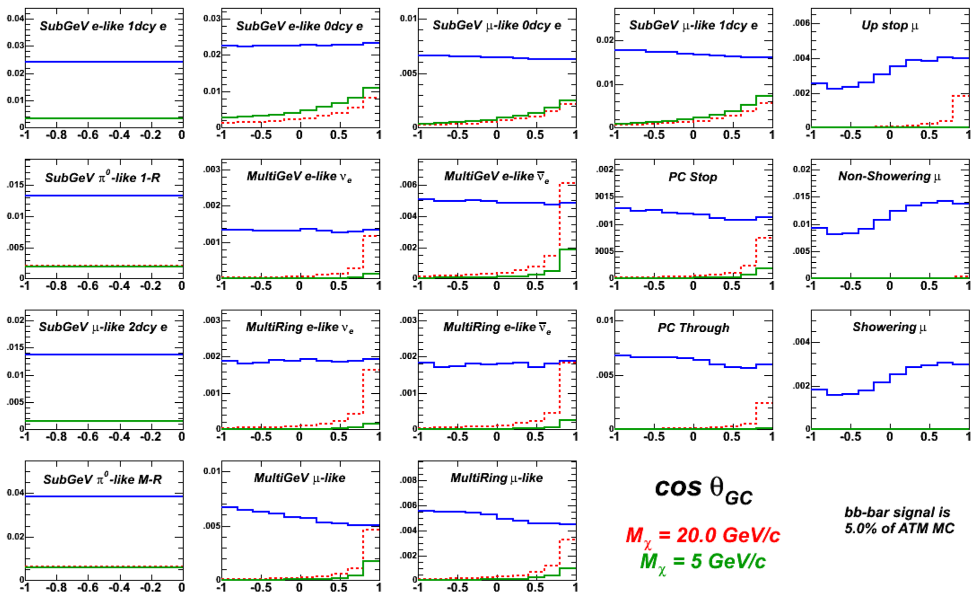

FIG. 200. Signal and background (blue) distributions used in the Hyper-K sensitivity study of dark matter annihilating via $\chi\chi \to b\bar{b}$ at the galactic center. Analysis samples are binned in cosθ_{gc}, the direction to the galactic center. Two WIMP hypotheses are shown: $m_\chi = 5\text{GeV/c}^2$ in green and $m_\chi = 20\text{GeV/c}^2$ in red. All distributions have been area normalized with the WIMP normalization taken to 5% of the background MC.

B. Solar flare

Solar flares are the most energetic bursts which occur in the solar surface. In a large flare, an energy of 10^{33} ergs is emitted over 10's of minutes, and the accelerated protons can reach energies greater than 10 GeV. It is likely that neutrinos are also emitted by the decay of mesons following interactions of accelerated particles. Detection of neutrinos from a solar flare was first discussed in 1970's by R. Davis [**?** **?**], but no significant signal has yet been found [**?** **?**]. There have been some estimates of the number of neutrinos which could be observed by large water Cherenkov detectors [**?** **?**]. According to [**?**], about 6-7 neutrinos will be observed at Hyper-K during a solar flare as large as the one in 20 January 2005, although the expected numbers have large uncertainties. Therefore, regarding solar flares our first astrophysics goal is to discover solar flare neutrinos with Hyper-K. This will give us important information about the mechanism of the particle acceleration at work in solar flares.

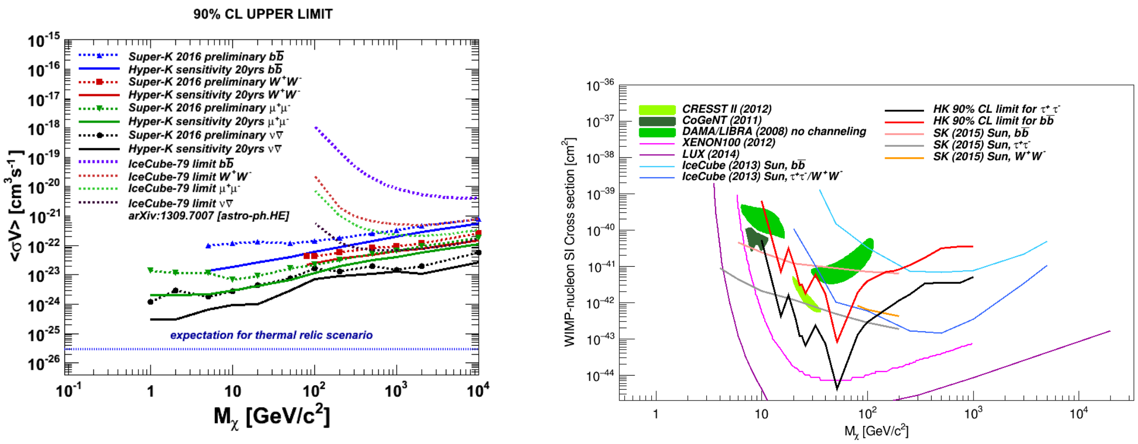

FIG. 201. The 90% C.L. upper limits as a function of the dark matter mass. (left) Limits on the WIMP velocity averaged annihilation cross section based on a search from WIMP-induced neutrinos coming from the galactic center. The exposure of Hyper-K is 20 years (3.8 Mton·year). (right) Limits on the spin-independent WIMP-nucleon scattering cross section based on a search from WIMP-induced neutrinos coming from the center of the Earth. The exposure of Hyper-K is 10 years (1.9 Mton·year). Limits and allowed regions are shown as lines and hatched regions, respectively. Results from Super-K assuming annihilations in the sun are taken from [?].

C. Gamma-Ray Burst Jets and Newborn Pulsar Winds

Gamma-ray bursts (GRBs) are the most luminous astrophysical phenomena with the isotropically-equivalent gamma-ray luminosity, $L_\gamma \sim 10^{52}$ erg s^{-1}, which typically occur at cosmological distance. Energy dissipation may be caused by inelastic nucleon-neutron collisions [? ? ?]. Then, quasi-thermal GeV-TeV neutrino emission is an inevitable consequence of such inelastic nucleon-neutron collisions [?]. Hyper-K will enable us to search these quasi-thermal GeV-TeV neutrinos from GRB jets, and it also has an advantage over IceCube (that is suitable for higher-energy $>$ 10-100 GeV neutrinos).

Note that it is critical to have large volume detectors for the purpose of detecting GeV-TeV neutrinos. The present Super-K and liquid scintillator detectors such as JUNO and RENO-50 are too small to detect high-energy signals from astrophysical objects especially if extragalactic, and much bigger detectors such as Hyper-K is necessary to have a good chance to hunt high-energy neutrinos from GRBs and energetic supernovae.

D. Neutrinos from gravitational-wave sources

Gravitational waves (GWs) have been detected by advanced-LIGO in 2015 [**?**]. This has allowed us to conduct multi-messenger observations of astrophysical objects via multiple signals, i.e., electromagnetic waves, neutrinos and GWs. Hyper-K has the potential to detect thermal neutrinos from nearby ($\lesssim$ 10Mpc) neutron star merger events. The central engine of gamma-ray bursts are also candidates of strong emitters of neutrinos and GWs. The mechanism that generates the jet is still unclear. If this jet is driven by neutrino annihilation, which is one of the promising scenarios, concurrent observations of neutrinos and GWs will be important probe of the very central part of the violent cosmic explosions at Hyper-K era [**?**].

V.7. NEUTRINO GEOPHYSICS

The chemical composition of the Earth's core is one of the most important properties of the planet's interior, because it is deeply connected to not only the formation and evolution of the Earth [**?**] itself but also to the origin of the geomagnetic field [**?**]. While paleomagnetic evidence suggests that the geomagnetic field has existed for roughly three billion years, it is known that a core composed of iron alone could not sustain this magnetic field for more than 20,000 years. Explaining the continued generation of the geomagnetic field as well as its other properties requires knowledge of composition of the core matter.

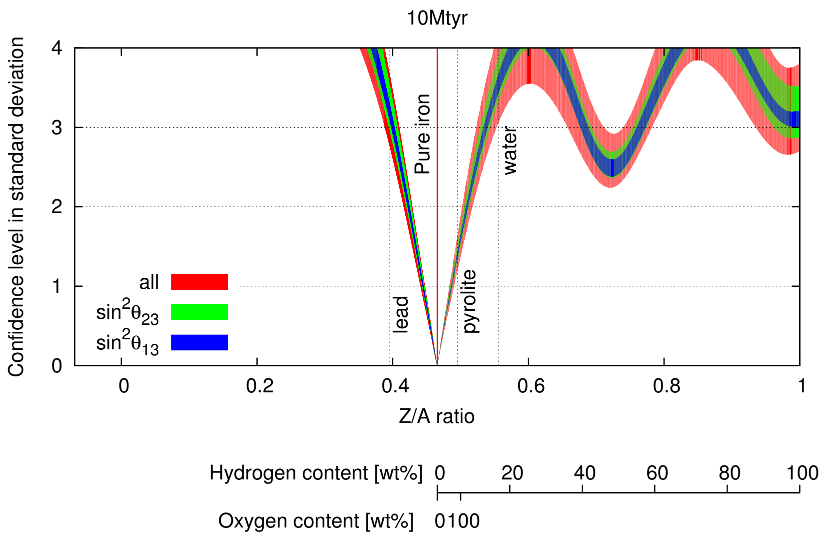

FIG. 202. Constraints on the proton to nucleon ratio of the Earth's outer core for a 10 Mton year exposure of Hyper-K to atmospheric neutrinos. Colored bands indicate the effect of present uncertainties in the neutrino mixing parameters.

The oscillation probability of atmospheric neutrinos depends on the electron density of the media they traverse. This property makes atmospheric neutrinos an ideal probe for measuring the electron density distribution of the Earth. Hyper-K's sensitivity has been studied in the context of atmospheric neutrino spectrum's dependence upon the ratio of the proton to nucleon ratio (Z/A) of material in the outer core. Assuming that the inner core and mantle layers of the Earth are the pure iron (Z/A = 0.467) and pyrolite (Z/A = 0.496), the expected constraint on the Z/A of the outer core is shown in Figure 202. While geophysics models will ultimately require even greater precision in such measurements, Hyper-K has the potential to make the spectroscopic measurements of the Earth's core.

Part VI

Organization

VI.1. ORGANIZATION

VI.2. INTERNATIONAL RESPONSIBILITIES

Part VII

Appendices

Appendix A: Construction Timeline

1. Electronics deliverables

III.9A Signal digitizer:

- Block diagram of the system.
- Specification of the input and output signals.
- Timing characteristics of the input and output signals.
- Schematics of the system.
- Circuit diagram of the system.
- Specification of the necessary power supplies.
- Electrical test results in laboratory environment.
- Electrical test results in a vacuum.
- Estimation of the power consumption.
- Estimation of the durability.
- Estimation of the cost.

III.9B System clock and counter:

- Block diagram of the system.
- Specification of the input and the output signals.
- Timing char of the input and the output signals.
- Schematics of the system.
- Circuit diagram of the system.

- Specification of the necessary power supplies.
- Electrical test results in the room environment.
- Electrical test results in vacuum.
- Estimation of the power consumption.
- Estimation of the durability.
- Estimation of the cost.

III.9C Digitizer control system:

- Block diagram of the system.
- Specification of the input and the output signals.
- Timing char of the input and the output signals.
- Schematics of the system.
- Circuit diagram of the system.
- Specification of the necessary power supplies.
- Estimation of the power consumption.
- Estimation of the durability.
- Estimation of the cost.

III.9D High voltage power supplies:

- Block diagram of the system.
- Specifications of the HV control protocol.
- Specifications of the HV monitoring protocol.
- Electrical test results in the room environment.
- Electrical test results in vacuum.

- Electrical test results with 100% humidity from 10 to 30 degree Celsius.
- Specification of the necessary input power supplies.
- Estimation of the power consumption.
- Estimation of the durability.
- Estimation of the cost.

III.9E Slow control and monitoring:

- Block diagram of the system.
- Specification of the protocol to controlling or monitoring.
- Schematics of the system.
- Circuit diagram of the system.
- Specification of the necessary power supplies.
- Estimation of the power consumption.
- Estimation of the durability.
- Estimation of the cost.

III.9F System control and network interface:

- Block diagram of the system.
- Schematics of the system.
- Circuit diagram of the system.
- Specification of the input and the output signals.
- Timing char of the input and the output signals.
- Specification of the necessary power supplies.
- Estimation of the power consumption.

- Estimation of the durability.
- Estimation of the cost.

III.9G Optical interfaces:

- Electrical interfaces.
- Optical interfaces.
- Electrical and optical characteristics of the optical transceiver.
- Electrical test results in lower pressure and in vacuum.
- Mechanical test results under 100% humidity.
- Appropriate cooling method in case of a moulded environment.
- Electrical test results in slower pulse transfer frequency.
- Estimation of the durability.
- Estimation of the cost.

III.9H Watertight case:

- The requirements for the case, including its size and weight.
- The material for the case.
- The mechanical drawings of the chassis.
- The module and cable installation method in the case.
- The method for mounting the case on the photosensor support structure in the tank.
- The mechanical test results under the pressure.
- The gas leak test results in the vacuum environment.
- The change of the humidity under the water.
- The heat deposition test results with the module.

III.9I Watertight connectors:

- Schematics of the connectors.
- Electrical characteristics of the connector.
- Material of the connectors.
- Electrical test results under the water pressure.
- Mechanical test results under the water pressure.
- Electrical test results in vacuum.
- Estimation of the durability.
- Estimation of the cost.

III.9J Low Voltage power supplies:

- Block diagram of the system.
- Specifications of the control protocol.
- Specifications of the monitoring protocol.
- Schematics of the system.
- Circuit diagram of the system.
- Specification of the necessary power supplies.
- Estimation of the power consumption.
- Estimation of the durability.
- Estimation of the cost.

III.9K GPS system:

- Block diagram of the system.
- Schematics of the system.

- Specification of the 1pps and the timecode output signals.
- Timing char of the the 1pps and the timecode output signals.
- Circuit diagram of the system if applicable.
- Specification of the necessary power supplies.
- Electrical test results in the room environment.
- Estimation of the power consumption.
- Estimation of the durability.
- Estimation of the cost.

Appendix B: Construction Costs

ACKNOWLEDGMENTS

Acknowledgments if any.